UiT
THE ARCTIC
UNIVERSITY
OF NORWAY

Department of Physics and Technology

Synthetic Aperture Radar Compact Polarimetry for Sea Ice Surveillance

Martine Mostervik Espeseth

EOM-3901 Master thesis in Energy, Climate and Environment

July 2015

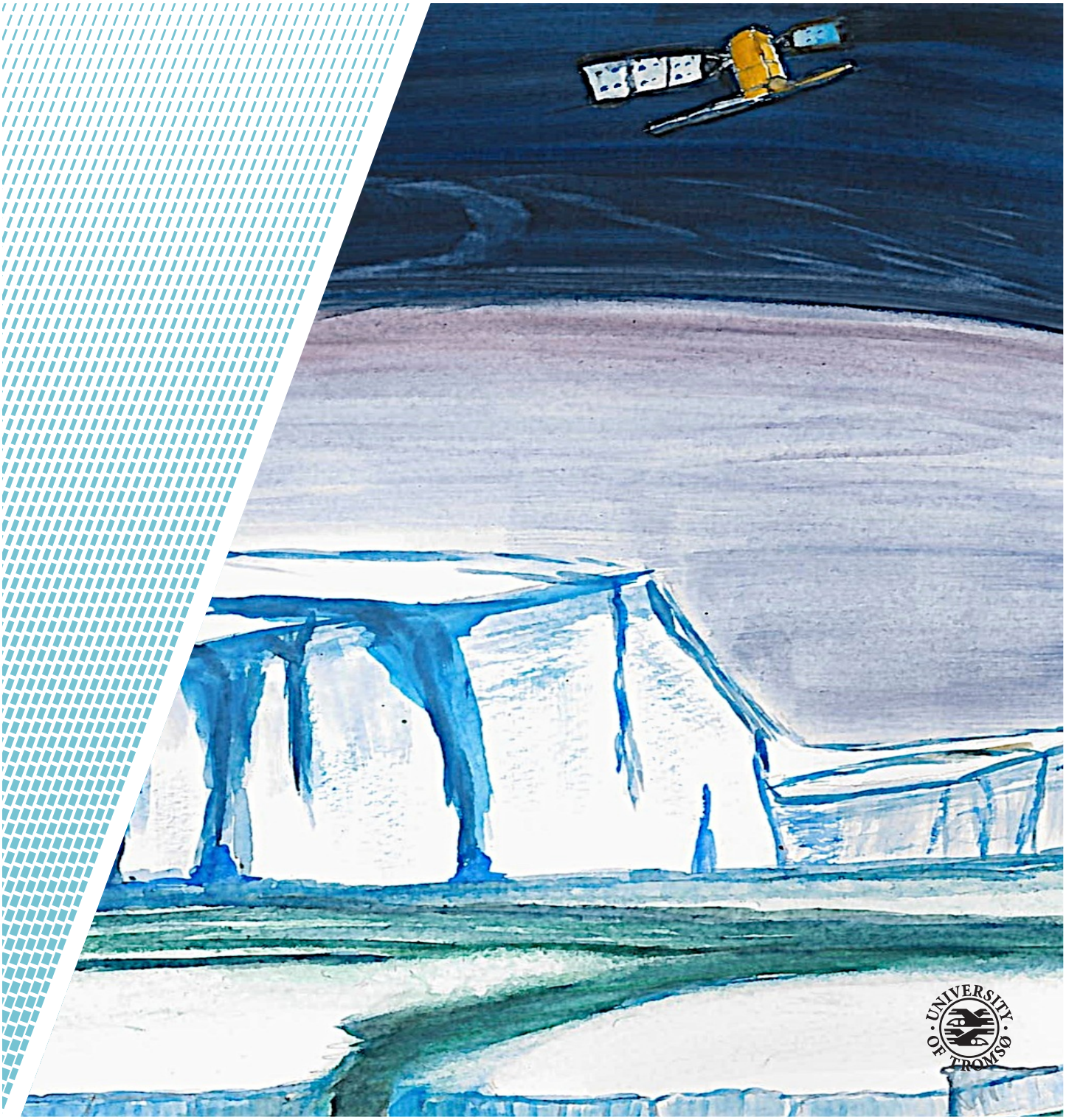

Abstract

The focus of this thesis is to investigate the use of synthetic aperture radar (SAR) compact polarimetry for studies of sea ice. Data obtained from quad-polarimetric SAR systems have already been studied extensively for sea ice monitoring. This thesis focuses on finding parallels to quad-polarimetric features from the compact-polarimetric data. This is achieved through the reconstruction of a pseudo quad-polarimetric sample covariance matrix.

The main contribution of this thesis is the suggestion of new reconstruction techniques for sea ice covered SAR scenes. Most of the estimated polarimetric features relevant to sea ice monitoring are successfully reconstructed. Furthermore, a comparison between the different reconstruction techniques is presented for different sea ice types. It is shown that the cross-polarization intensity can be reconstructed for different sea ice types, but that the performance is strongly affected by the choice of reconstruction method. The proposed modified Souyris' reconstruction technique turns out to be the best method for achieving high performance for different polarimetric features representing different sea ice types. Additionally, three other methods are suggested, namely a model-based, an eigenvalue-based, and a DoP-based reconstruction method. Each of these methods produce a higher accuracy than the existing reconstruction methods for most of the polarimetric features.

Remote sensing instruments have been extensively used as a tool for sea ice monitoring. Information about sea ice is important for multiple industries like oil and gas, fishing, research communities, and tourism. Full- and dual polarimetric SAR instruments have been used to extract useful information about the sea ice surface, but now a new polarimetric mode has been invented. In its infancy, the theoretical foundation of compact polarimetry was presented by Souyris, Nord, and later Raney with the hybrid-pol mode. However, compact polarimetry—especially the hybrid-pol mode—has proved valuable, and has in later years found its way into operational satellite systems such as the RISAT and the ALOS-2 satellites.

The work presented in this thesis adds to the on-going discussion on the potential of compact polarimetry, and is the first comprehensive analysis of reconstruction methods for specified application to sea ice.

Acknowledgements

First of all, I will like to thank my supervisors Camilla Brekke and Stian Normann Anfinsen for their inspiring feedback and discussions during this thesis. Especially thanks for proof-reading, and for pointing me towards interesting and relevant literature on the topic.

I am grateful to Gunnar Spreen and Sebastian Gerland at Norwegian Polar Institute (NP) for including me in the N-ICE project, and actually bringing me onto the sea ice. To get the opportunity of actually seeing sea ice "live" has been a life experience. Thanks to all at NP for learning me many interesting things when working on the ice. Also, thank you Gunnar for helping me labeling the sea ice scenes given in this work.

Many thanks to Boularbah Souissi for the inspiring discussions at your visit to UiT, you gave me a good "kick start" on the whole topic of compact polarimetry.

I would also like to thank my fellow students, EKM class '10 for five great years, and the master students in the neighbouring office for great jokes and coffee breaks.

To my family, parents, and brother: without your continuous love and support none of this would have been possible. A special thanks to my grandmother for painting the beautiful front page, and to my father for proof-reading the thesis.

Finally, to my boyfriend Jan-Ove Karlberg. Thank you for proof-reading this entire master thesis, your love, support, and for introducing me to your computer science LaTeX-gurus. You have been awesome!

Contents

List of Figures

List of Tables

List of Abbreviations

ALOS Advanced Land Observation Satellite

DCP dual circular polarization

H horizontal

LC left circular

MSE mean square error

PRF pulse repetition frequency

RAR real aperture radar

RC right circular

RISAT Radar Imaging Satellite

RMSE root mean square error

SAR synthetic aperture radar

SW swath width

V vertical

Nomenclature

A	Anisotropy
A_e	Effective area of antenna
A_g	Effective area of scatterer
$\boldsymbol{C}$	Covariance matrix
c	Wave's velocity
D_A	Antenna length
D_r	Antenna width
DoP	Degree of Polarization
d	Number of dimensions
$\overrightarrow{E}$	Electric field
$\overrightarrow{E}^{i}_{\text{sensor}}$	Transmitted electric field from sensor
$\overrightarrow{E}^{s}_{\text{sensor}}$	Measured electric field at sensor
$\overrightarrow{E}^{i}_{\text{surface}}$	Incident electric field at surface
$\overrightarrow{E}^{s}_{\text{surface}}$	Scattered electric field at surface
E_0	Amplitude of the wave
F_D	Power contribution from double-bounce scattering
F_S	Power contribution from surface scattering
F_V	Power contribution from volume scattering
G_g	Gain of scatterer
G_t	Gain of antenna
H	Entropy
$\overrightarrow{J}$	Jones vector
$\overrightarrow{s}_L$	Target vector in lexicographic basis
$\overrightarrow{s}_P$	Target vector in Pauli basis
k_i	Incident wave vector
k_s	Scattered wave vector
n	Refractive index
P_g	Incident power at ground
P_i	Pseudo Probabilities
P_r	Incident power at antenna
P_t	Transmitted power from antenna
PA	Polarization asymmetry

PF	Polarization fraction
PH	Pedestal height
q_0	Stokes vector: Total power
q_1	Stokes vector: Power in the linear horizontal or vertical polarization component
q_2	Stokes vector: Power in the linearly polarized components at tilt angles
q_3	Stokes vector: Power in the left- and right-handed circularly polarized component
r	Distance between sensor and surface
$\overrightarrow{\boldsymbol{r}}$	Propagation direction
$\boldsymbol{S}$	Sinclair matrix
s_h	Standard deviation of the height
T	Coherency matrix
T_R	Listening time
t	Time
$\boldsymbol{U}$	Special unitary group matrix
$\boldsymbol{u}$	Eigenvectors
α	Attenuation term
$\boldsymbol{\beta}$	Wave number in time domain
τ	Pulse length
Δx	Azimuth resolution
δ	Relative phase difference
δ_S	Width of the surface distribution
ϵ	Permittivity/dielectric constant
ω	Angular frequency of the wave
ψ	Orientation angle
χ	Ellipticity angle
λ	Wavelength
λ_i	Eigenvalue
ρ_{HHVV}	Coherence parameter
ρ_L	Shape parameter
σ	Radar cross section
θ	Incident angle
θ_B	Beam width
θ_i	Angle of Incident
θ_r	Reflection angle
μ	Conformity coefficient
μ_c	Circular cross polarization ratio

1 Introduction

In later years the focus on sea ice has intensified. Several different industries have shown their interest in investigating sea ice in relation to global climate change, oil and gas operations, and the fishing industries. These investigations require high quality data, which is quite challenging to acquire from the Arctic region. This is—apart from its shear size—because the Arctic region is remote, harsh, mostly cloud-covered, and dark for several months of the year. These factors will limit the data collection, especially for *in-situ* measurements and for optical space-borne sensors. However, space-borne microwave synthetic aperture radar (SAR) sensors have the advantage of being independent on the local weather conditions, since the microwaves can travel unaffected through the clouds, and it is not dependent on lightning conditions [Chuvieco and Huete, 2010, p. 51]. This instrument is extensively used to interpret sea ice, but it requires knowledge of the interaction mechanisms between the backscattered electromagnetic signal measured by satellite sensors, and the snow, ice, and ocean targets. The general expectation in the ice community is that multiple SAR frequencies, polarizations, and incidence angles, together with a higher frequency of repeat observations, will lead to greater understanding of the sea ice regime, better manual and automated interpretation of SAR scenes, and improved model performance [Falkingham, 2014].

SAR instruments employ various *acquisition modes* when collecting the images. The various acquisition modes have different resolution, and spatial coverage, i.e., swath width (SW). The resolution and the spatial coverage are dependent, meaning that a high resolution SAR scene will have a low spatial coverage and vice versa. Additionally, to gain large amount of polarimetric information about the backscattering properties of the targets within the SAR scenes, *quad-polarimetric* (pol) SAR mode can be used. Such

a SAR instrument transmits in two *polarizations*, and receives in two polarizations. The result of this polarization *configuration* is a narrow SW which limits coverage, but enables distinction of different scattering mechanisms as a consequence of the large amount of polarimetric information. The Canadian RADARSAT-2 SAR sensor has a maximum SW of 50 km using the wide quad-pol mode, and the highest resolution is 5.2 m for the wide fine quad-pol mode, and 9 m the standard wide quad-pol mode [MacDonald, Dettwiler and Associates Ltd, 2014]. The benefit of having more polarimetric information is a higher accuracy when interpreting the various sea ice phenomena within the SAR scenes, which, for example, could help in improving sea ice charts. One drawback of the quad-pol mode is the small spatial coverage, as the SW is only 50 km. Therefore, the dual-pol mode, with only one polarization at the transmitter and two polarizations at the receiver, will produce a SW that is twice of that obtained from a quad-pol system, and at the same time have a high resolution. As a result of the dual-pol mode, the amount of polarimetric information about the interaction mechanisms between the incoming wave and the target will be reduced. To be able to have both high spatial coverage and at the same time, a large amount of polarimetric information, the *compact polarimetry* SAR mode was introduced.

Over the last decade, compact polarimetry has emerged to provide a great opportunity for the radar industry in context of Earth Observation. The *compact polarimetry mode* is a SAR acquisition mode where only one polarization is transmitted, and two orthogonal polarizations are received. This configuration of polarization channels is also used in dual-polarimetric systems, but for compact polarimetric systems the choice of polarization for the transmitted and received channels is important. For dual-pol SAR systems the common polarizations are horizontal and vertical, while for compact-pol systems the polarizations are either circular or diagonal polarizations. This makes it possible to reconstruct an approximation of quad-pol data (also known for full-polarimetric data), i.e., *pseudo* quad-pol covariance matrix.

Many research communities have shown their commitment to investigating potential applications when using simulated compact-pol data, such as crop monitoring, oil-spill detection, and ship detection [Atteia and Collins, 2013, Souyris et al., 2005, Li et al., 2006]. The majority have concluded that the compact-pol mode is almost "as good" as quad-pol SAR systems. The reason for the large interest in the compact-pol mode is because this mode provides the benefits from both full- and dual-pol SAR systems; namely the double swath width from dual-pol systems, and the large amount of polarimetric information from quad-pol systems [Raney and Hopkins, 2011, Charbonneau et al., 2010]. The name originated from the fact that the compact-pol mode contains information that corresponds to quad-pol data, but in a compact manner, since a reduced number of polarimetric channels are being used.

1.1 Background on compact polarimetry

The main challenge of the compact polarimetric mode is that the interpretation of the parameters obtained from such a system is currently unknown. This differs from quad-pol data, where the different parameters have been extensively studied. There are mainly two sets of approaches that enable extraction of information from the compact-pol data.

The leading techniques are reconstruction methods proposed in [Souyris et al., 2005] and [Nord et al., 2009]. The output of the reconstruction methods is a pseudo quad-pol covariance matrix, which should resemble the covariance matrix obtained from quad-pol data. These data formats will be described later. The reconstruction methods rely on assumptions such as reflection symmetry, and that the area to be reconstructed is natural terrain. Using this approach will allow us to use existing techniques based on quad-pol parameters with known interpretations. For sea ice covered SAR scenes this is an important benefit, since current state of the art sea ice models and methods for extracting information about the sea ice utilize quad-pol parameters.

Another entrance to start the data analysis is through methods decomposing the compact polarimetry measurements directly, thereby avoiding the cumbersome reconstruction stage. The leading methods in this group were proposed in [Raney, 2007] and [Cloude et al., 2012].

Both these groups of methods, i.e., reconstruction and decomposition, have proven to be useful for applications such as oil-spill- and ship-detection, crop classification, and moon crater analysis. Note that decomposition also can be applied following a reconstruction.

1.2 Previous Work

The need to evaluate sea ice from a compact polarimetric perspective has been noted in many previous works, some of which are listed below.

- Contract report from Environment Canada, "Global Satellite Observation Requirements for Floating Ice - Focusing on Synthetic Aperture Radar", [Falkingham, 2014].

- Canadian Journal of Remote Sensing, "Compact Polarimetry Overview and Applications Assessment", [Charbonneau et al., 2010].

- ASPRS Annual Conference, "On the Classification of Sea Ice Types using Simulated Radarsat Constellation Mission (RCM) Compact Polarimetric SAR Parameters",

[Dabboor and Geldsetzer, 2014].

- The Cryosphere, "Comparison of feature based segmentation of full polarimetric SAR satellite sea ice images with manually drawn ice charts", [Moen et al., 2013].

1.3 Objective and contribution

The aim of this work is to test existing reconstruction methods and to find improved reconstruction methods specialized for sea ice SAR data. Even though a multitude of studies have been conducted on compact polarimetry, there is a lack of studies focusing on sea ice. From the sparse literature, the studies that have been conducted on sea ice mostly focus on compact polarimetric parameters for classification purposes, such as in [Dabboor and Geldsetzer, 2014]. If reconstruction of a pseudo quad-pol covariance matrix is performed, this will grant us access to the known quad-pol parameters, whose usage and interpretation is known.

To the author's knowledge there exists no study of reconstruction of a pseudo quad-pol covariance matrix for sea ice covered SAR scenes. The main contribution of this work is therefore to test various reconstruction techniques. Specifically, we want to expose which polarimetric features can be reconstructed from various subclasses of sea ice within the SAR scenes given in this work. In more detail, our immediate contributions to the research field are:

- Evaluation of existing reconstruction methods for first-year ice.
- Improved and modified reconstruction methods for first-year ice.
- Comparison between simulated compact polarimetric features and full polarimetric features for first-year ice.
- Overview of the information loss for sea ice covered SAR scenes using simulated compact-polarimetric data compared to quad-polarimetric data.

The main research question to be answered in this thesis is: *Can a pseudo quad-pol covariance matrix be reconstructed from simulated compact polarimetric data corresponding to sea ice covered SAR scenes, and if so, what are the desirable methods for achieving this?*

1.4 Limitation

Real compact-pol data was not available for this work. Therefore, quad-pol data from RADARSAT-2 was used to simulate compact-pol data. Hence, the results are carried out from simulated compact-pol data and not real compact-pol data.

1.5 Structure of the thesis

The thesis is structured in 8 chapters including the introduction.

Chapter 2 reviews some of the most important principles of SAR imaging, including the radar equation, geometry, frequency, and polarization. The last part of chapter 2 discusses scattering mechanisms for sea ice covered SAR scenes.

Chapter 3 briefly presents the theory of SAR remote sensing of Arctic sea ice, including physical properties and applications.

Chapter 4 contains information about the data that is used throughout this work, and also presents the labeling of the different sea ice types.

Chapter 5 introduces the key theory of compact polarimetry. This chapter is divided into two main parts. The first part is an introduction to the compact-pol mode, while the second part discusses different polarimetric parameters. Finally, a comparison between quad-pol and compact-pol parameters is conducted.

Chapter 6 describes the theory of reconstructing a pseudo quad-pol covariance matrix based on simulated compact-pol data. In this chapter, four new reconstruction methods are presented.

Chapter 7 presents the results obtained from the different reconstruction methods. This chapter also includes a comparison of the different reconstruction methods.

Chapter 8 summarizes the work and proposes some future work using compact polarimetry.

2

SAR Theory

This chapter presents the underlying theory of synthetic aperture radars (SARs). More specifically, the SAR principles, SAR geometry, acquisition principles, scattering mechanisms, and scattering target descriptors are all discussed throughout this chapter. Finally, compact polarimetry is introduced. Together, these concepts form the basis for the successive chapters.

2.1 SAR principles

SAR instruments are a type of system found in the broad class of radar instruments. SAR systems are usually mounted on either space-borne or air-borne platforms, and were invented to allow high resolution monitoring of the Earth's surface. SAR works by transmitting an electromagnetic (EM) pulse, and measuring the backscattered response from the surface. The backscattered response contains unique signatures that reflect the physical properties of a given surface element.

SAR is an active sensor, which transmits coherent EM pulses in the microwave region. These pulses are partially reflected back to the radar by targets within the antenna beam. Since SAR sensors operate in the microwave region, the transmitted signal can penetrate clouds and most weather conditions. SAR sensors do not require an external illumination source, such as the Sun, as apposed to optical sensors. Broadly, SAR sensors can be divided into two main categories; namely mono-static and bi-static radars. The former corresponds to a system where the transmitter and the receiver share the

same antenna, while the latter to a system where the transmitter and the receiver are separated by a considerable distance [Lee and Pottier, 2009, p. 23]. As the name implies, SAR instruments synthesize an aperture length in order to obtain a high resolution. This is achieved by utilizing the movement of the radar and further performing specialized signal processing to obtain a high resolution [van Zyl and Kim, 2010, p. 13]. As the platform travels and measure the response from a given target, the Doppler history will be considered for all the backscattered signals from this target. Therefore, SAR instruments have a *Doppler time delay format* [Elachi and van Zyl, 2006, p. 255].

The upcoming sections will describe the different concepts of the SAR theory. First, we will start by presenting the general theory of the EM field, and further presents the radar equation. This will help us understand the configuration of the power budget between the sensor and a target. Next, the SAR geometry is discussed, which describes how the sensor records responses from an area on the surface within the antenna beam. We will further discuss the EM spectrum, with a main focus on the frequencies that SAR sensors employ, before presenting the concept of polarization. With this theory in place, we will see how some polarimetric descriptors can be used on the SAR data.

2.1.1 Electromagnetic field

Radar systems transmit EM pulses towards the ground in an active manner. The basic laws of the EM field can be described using Maxwell's theory, where the EM wave consists of an electric and a magnetic field. When describing EM waves the assumption of a monochromatic plane wave is often made. This means the absence of sources, i.e., the propagation medium contains no mobile electrons [Lee and Pottier, 2009, p. 32]. This monochromatic plane wave with constant amplitude represented in time (t) and space ($\vec{\boldsymbol{r}}$) is given as:

$$\vec{E}(\vec{\boldsymbol{r}},t) = \Re\left[\vec{E}(\vec{\boldsymbol{r}})e^{j\omega t}\right] \tag{2.1}$$

where $E(\vec{\boldsymbol{r}}) = E_0 e^{-j\vec{\boldsymbol{k}}\vec{\boldsymbol{r}}}$ is the complex quantities of the electric field, $\Re(\ldots)$ denotes the real part operator, $\vec{\boldsymbol{k}}$ is the wave vector, $\vec{\boldsymbol{r}}$ denotes the propagating direction, and ω is the angular frequency [Lee and Pottier, 2009, p. 32-33]. Maxwell's theory yields the following expression for the wave vector:

$$\vec{\boldsymbol{k}} = \boldsymbol{\beta} - j\boldsymbol{\alpha} \tag{2.2}$$

where $\boldsymbol{\beta}$ acts like the wave number in the time-domain, and $\boldsymbol{\alpha}$ is the attenuation term. These terms are dependent on the complex dielectric constant[1], also known as the

1. The dielectric constant is a measure of the resistance of a material when interacting with EM waves.

permittivity [Lee and Pottier, 2009, p. 32]. The dielectric constant consists of a real and an imaginary part, i.e.:

$$\underline{\epsilon} = \epsilon' - j\epsilon'' \tag{2.3}$$

which describes the electrical properties of a medium, such as how a wave propagates and attenuates through a medium. The real part, ϵ', represents the contrast with regards to the permittivity of free space (vacuum), while the imaginary part, ϵ'', denotes the EM loss of the material [Elachi and van Zyl, 2006, p. 209].

A representation of the electric field in the orthogonal basis $(\hat{x}, \hat{y}, \hat{z})$, with $\hat{z}$ as the propagation direction, is given in equation 2.4.

$$\overrightarrow{E}(\overrightarrow{z}, t) = \begin{bmatrix} E_{0,x} e^{az} \cos(\omega t - kz + \delta_x) \\ E_{0,y} e^{az} \cos(\omega t - kz + \delta_y) \\ 0 \end{bmatrix} = \Re \left(\begin{bmatrix} E_{0,x} e^{j\delta_x} \\ E_{0,y} e^{j\delta_y} \\ 0 \end{bmatrix} e^{-jkz} e^{j\omega t} \right) \tag{2.4}$$

where δ is the relative phase term, and a is the attenuation term in the spatial domain, which was set to zero because of the independence of the wave polarization properties [Lee and Pottier, 2009, p. 33]. At a fixed time $t = t_0$, the electric field is composed of two orthogonal sinusoidal waves. Possible states of polarization are linear, circular, elliptical, or random [Cloude, 2010, p. 43-44]. The linear horizontal, linear vertical, and circular polarizations are illustrated in Figure 2.1.

The linear horizontal polarization (first figure) has zero magnitude in the linear vertical component. In the case of linear vertical polarization, the magnitude of the horizontal polarization component becomes zero. The circular polarization has equal magnitude of the electric field vectors in the horizontal and vertical directions, but are now 90° out of phase. The direction of the polarization is either to the left or right depending on which component of the electric field is leading in phase. Any polarization state can be described as the sum of two orthogonal linear polarization states [Lee and Pottier, 2009, p. 33].

2.1.2 Radar equation

The radar equation reflects the fundamental idea behind active radar systems. It establishes a link between the transmitted power, P_t, and the measured power, P_r. The total power incident on a given scatterer, P_g, must be considered in order to derive the radar equation, i.e., [Elachi and van Zyl, 2006, p. 241-242]:

$$P_g = \frac{P_t A_g G_t}{4\pi r^2} \tag{2.5}$$

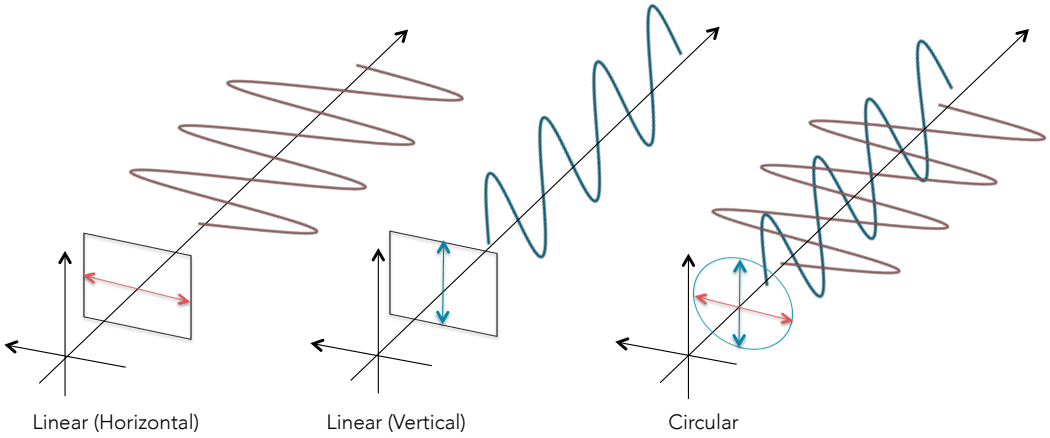

Figure 2.1: Spatial evolution of monochromatic plane wave components (illustrations based on Figures 2.1, 2.2, and 2.4 in [Lee and Pottier, 2009, p. 33-35]).

where P_g is the power incident on the ground, P_t is the power transmitted by the antenna, G_t is the gain of the antenna, A_g is the effective area of the scatterer (ground), and the factor $\frac{1}{4\pi r^2}$ represents the decrease in power density over the slant range r (see Figure 2.2) [Elachi and van Zyl, 2006, van Zyl and Kim, 2010, p. 241-242, p. 10-11]. The power incident on the antenna from the scatterer is given as:

$$P_r = \frac{P'_g A_e G_g}{4\pi r^2} \tag{2.6}$$

where P_r is the power at the antenna, P'_g is the re-radiated power by the scatterer, A_e is the effective area of the antenna $\left(\frac{G_t \lambda^2}{4\pi}\right)$, λ is the wavelength of the transmitted wave, and G_g is the gain of the ground (scatterer) in direction of the antenna (see Figure 2.2) [Elachi and van Zyl, 2006, p. 241]. The radar equation relates the power transmitted, P_t, and power received, P_r, in the following manner:

$$\frac{P_r}{P_t} = \frac{P'_g}{P_g} G_g A_g \frac{G_t A_e}{(4\pi r^2)^2} \implies P_r = \frac{G_t^2 \sigma \lambda^2}{(4\pi)^3 r^4} P_t \tag{2.7}$$

where σ is the radar cross section, i.e., a measurement of how detectable a given target is, and is expressed as:

$$\sigma = \frac{P'_g}{P_g} G_g A_g \tag{2.8}$$

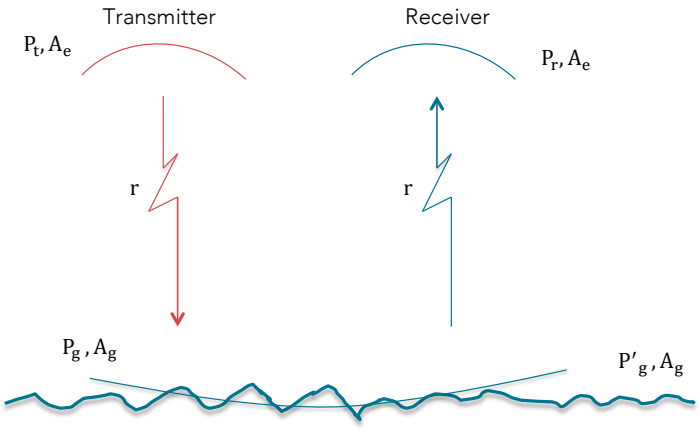

Figure 2.2: Configuration of transmitted and received power.

2.1.3 Radar geometry

SAR systems record the backscattered signal and create a two-dimensional image of the surface as it moves along a nominally straight line above the surface [van Zyl and Kim, 2010, p. 13]. One dimension corresponds to the time for the backscattered signal to be returned to the radar. This is referred to as the range direction. The 2nd dimension is proportional to the along track distance, and is called the azimuth direction [Cumming and Wong, 2005]. These two dimensions are illustrated in Figure 2.3. The parameters θ, β, θ_r, D_r, and D_A in Figure 2.3 represent the look angle, beam width, opening angle in range, antenna width, and antenna length respectively [Elachi and van Zyl, 2006, Lee and Pottier, 2009, p. 239-241, p. 6-7].

The time and the distance along range direction separate the reflected signal. Along the azimuth direction the Doppler effect separates the signals. This is because the Doppler effect is high when the satellite is moving towards a target and decreases as the satellite passes and moves away from the target [Cumming and Wong, 2005, p. 139-140].

Spatial resolution denotes "the minimum distance between two points on the surface that can still be separable" [Elachi and van Zyl, 2006, p. 239]. The resolution in range and azimuth direction is defined in two different ways. In the range direction, the time and distance are of essence, because two signals can only be separated if they arrive at different times at the sensor. Hence, for targets to be distinguishable, the smallest possible time difference between two signals defines the range resolution. This smallest time difference is equal to τ, where τ is the pulse length of the transmitted signal [Elachi and van Zyl, 2006, p. 239-240]. This indicates that short pulses provide higher resolution. However, this comes at a cost, and to overcome the noise effect the amplitude of the

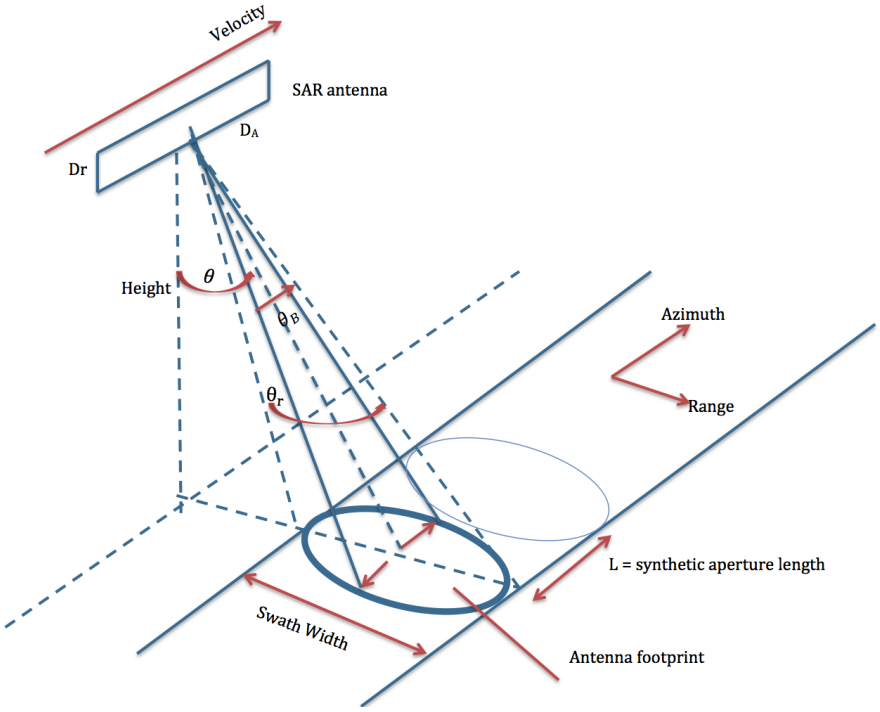

Figure 2.3: Illustration of the SAR geometry based on Figure 1.1 in [Lee and Pottier, 2009, p. 6].

signal must be high, which requires power. To overcome this problem, the chirp principle is used, which includes a frequency-modulated signal.

For SAR systems, the resolution in azimuth direction is defined by the different Doppler shifts that a scatterer reflects within the radar beam [Cumming and Wong, 2005, p. 8]. After processing, the azimuth resolution is equal to half of the antenna length (see Figure 2.3), i.e.:

$$\Delta x = \frac{D_A}{2} \tag{2.9}$$

As opposed to SAR systems, the azimuth resolution in real aperture radar (RAR) systems is given by the azimuth footprint. This is because all the signals from the targets along the azimuth direction arrive the sensor simultaneously. The azimuth footprint is defined as [Elachi and van Zyl, 2006, p. 241]:

$$L_{\text{footprint}} = \frac{r\lambda}{D_A \cos\theta} \tag{2.10}$$

where r is the distance between sensor and surface, λ is the wavelength of the transmitted signal, θ is the incident angle (see Figure 2.3), and D_A is the antenna length. To achieve a high resolution the antenna length must be large. This is in fact one of the disadvantages of RAR, since a large antenna length comes at a high cost. The main difference between SAR and RAR is therefore the way in which the azimuth resolution is achieved [van Zyl and Kim, 2010, p. 13]. By utilizing the Doppler effect to separate signals from targets within the antenna beam, higher resolution will be achieved.

2.1.4 Frequency

SAR instruments utilize different parts of the EM spectrum. SAR instruments can operate in a handful of different bands within the microwave region, and the choice of the band for a given SAR instrument is based on the purpose of the mission. The interaction mechanism between the incident wave and the surface depends, amongst other things, on the frequency of the incident wave. EM waves with long wavelength penetrate deeper into the surface compared to shorter wavelengths. Waves with shorter wavelengths detect roughness on a different scale than longer wavelengths. This is because waves interact strongly with objects with geometry that is of the same order of magnitude (scale) as the wavelength. Thus, small variations of the surface are more "visible" for waves with short wavelengths. The roughness is used to define the height variations within the target surface, and a common criterion for roughness is the Rayleigh criterion [Chuvieco and Huete, 2010]:

$$s_h \geq \frac{\lambda}{8} cos\theta_i \tag{2.11}$$

where s_h is the standard deviation of the surface height, λ is the wavelength of the transmitted waves, and θ_i is the radar incidence angle [Chuvieco and Huete, 2010]. If this equality holds, the surface is considered to be rough.

Figure 2.4 illustrates the EM spectrum, and a zoomed-in version of the microwave bands used in radar remote sensing. The Ka-, K-, and Ku-bands cover the short wavelengths. Interference from the atmosphere is prominent in these bands, and these bands are therefore not used in satellite borne radar systems. Bands containing longer wavelengths (X-, C-, S-, L-, and P-bands) have almost no influence from rain and clouds. The L- and P- bands are affected by the electrons in the ionosphere, which may results in changes of the polarization state of the transmitted waves [Souyris et al., 2005]. One example of space borne radar system operating in the C-band is RADARSAT-2, while TerraSAR-X operates in the X-band.

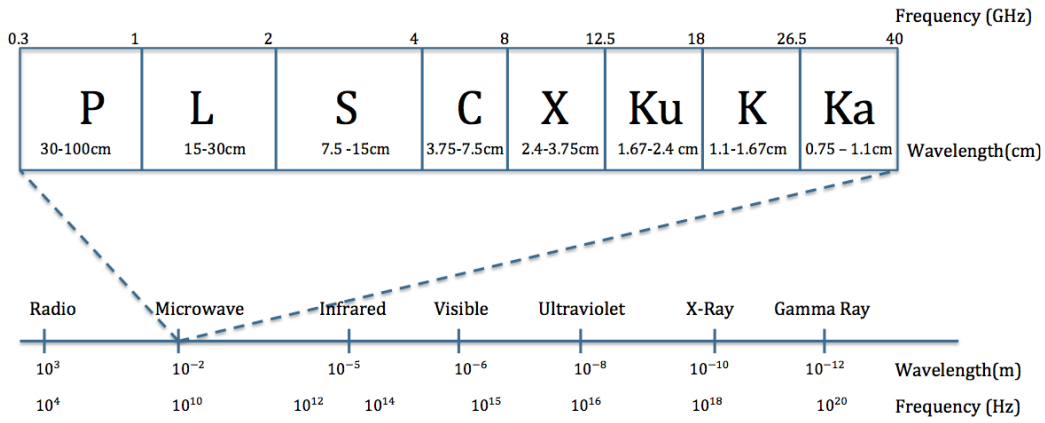

Figure 2.4: The figure illustrates the EM spectrum and a zoomed in version of the different bands in the microwave region (the illustration borrows elements from Figure 2.1 in [Chuvieco and Huete, 2010, p. 24]).

2.1.5 Polarization

Polarization is referred to as the orientation of the electric field, and it is contained in the elements of the vector amplitude of the electric field [van Zyl and Kim, 2010, p. 24]. In remote sensing, multiple polarizations are used to extend the information content that can be retrieved from a given target. This is because the type of polarization used will affect the signature from a target, and various polarizations have different sensitivity to the physical properties of the target.

SAR instruments can be divided into three groups depending on the choice of polarization. These are *quad-*, *dual-*, and *single-polarization (pol) SAR radars*. In a fully-polarized case, also referred to as quad-pol (from *quadrature polarization*), the radars transmit both horizontally and vertically polarized waves, and measure the response in both horizontal and vertical polarizations. As a result of this technique, four polarization combinations (also known as polarization channels) are generated, namely horizontal-horizontal (HH), vertical-horizontal (VH), HV, and VV. Dual-pol radars employ two channels, i.e., one polarization at the transmitter and two polarizations at the receiver. This yields the following polarization channels; HH and HV or VV and VH. Single-pol systems have one channel, i.e., only one polarization type at the transmitter and receiver.

When the linear horizontal (H) and vertical (V) polarizations are used the output of the system is often referred to as co(like)-pol and cross-pol. When the transmitter and the receiver have the same polarization, co-pol components are generated, i.e.: VV and HH. The cross-pol component is generated when the transmitter and the receiver have

different polarization modes, i.e.: HV and VH. For quad-pol systems all these scattering components are available, while for dual-pol systems only two of them are generated. For single-pol systems only one scattering component is generated. For compact-pol systems, the like- and cross-pol components are left out, since different polarizations are used at the transmitter and the receiver (except for circular transmit and circular receive polarimetric systems).

The advantage of providing one polarization at the transmitter is a larger swath width compared to two polarizations at the transmitter [Raney and Hopkins, 2011]. This is an important advantage when the goal is to monitor large areas for the purpose of for example large-scale sea ice surveillance.

Quad-polarimetric systems uses multiplexing when transmitting two signals with different polarizations [Raney and Hopkins, 2011]. This multiplexing is necessary to be able to capture the polarization of the transmitted waves [Touzi, 2009]. The different polarization architectures and the concept of multiplexing are discussed in chapter 5.

The choice of the polarization architecture for SAR instruments depend on the purpose of the mission. This is because the polarization affects the interaction mechanism between the surface and the incident field. Dual-pol systems provide a large swath width, and quad-pol systems provide complete polarimetric information. To combine the best of both worlds, a new mode named compact polarimetry was invented. The name comes from the fact that all the polarimetric information from quad-pol data are compacted in the compact-pol data. The compact-pol uses other polarization properties than the common horizontal and vertical ones, and different combinations of the polarization of the transmitter and the receiver have been suggested. The choice of polarizations at the transmitter are either left- or right-circular, or a diagonal polarization also known as $\frac{\pi}{4}$-pol which lies between horizontal and vertical polarization [Charbonneau et al., 2010]. The receiver measures the backscattered signals in two polarizations, either linear horizontal and vertical, or left- and right-circular polarizations. The latter combination is known as the dual circular polarization (DCP) if the transmitted wave is left- or right-circularly polarized [Charbonneau et al., 2010].

2.1.6 The Jones vector

The Jones vector is defined from the complex electric field, and is useful when transforming from one polarization basis to another [Taylor and Boerner, 2007]. The Jones vector describes the polarization properties in regards to the phase and amplitude [Lee and Pottier, 2009, p. 37-38]. Starting with equation 2.4, setting $\delta = \delta_y - \delta_x$, and fix

$z = z_0 = 0$ and $t = t_0 = 0$ yields the following normalized Jones vector:

$$\overrightarrow{J} = \frac{1}{\sqrt{(E_{0,x})^2 + (E_{0,y})^2}} \begin{bmatrix} E_{0,x} \\ E_{0,y} e^{j\delta} \end{bmatrix} \tag{2.12}$$

where the term in front of the matrix represents the amplitude. This form is known as the standard normalized Jones vector, which has a magnitude of 1 [Kliger et al., 1990]. The Jones vector takes various forms depending on the orientation of the electric field, and the upcoming sections discuss some of the common polarization types.

Linear polarization

In any linear orthogonal basis, the polarized wave can be represented in the horizontal and vertical plane, or by an orientation angle, ψ, relative to the horizontal and vertical basis [Lee and Pottier, 2009, p. 35-36]. In such cases, the Jones vector is given by the following equation:

$$\overrightarrow{J} = \frac{1}{\sqrt{(E_{0,x})^2 + (E_{0,y})^2}} \begin{bmatrix} E_0 \cos\psi \\ E_0 \sin\psi e^{j\delta} \end{bmatrix} \tag{2.13}$$

where $E_{x,0} = E_0 \cos\psi$, $E_{y,0} = E_0 \sin\psi$, $E_0 = \sqrt{(E_{0,x})^2 + (E_{0,y})^2}$, and the relative phase $\delta = \delta_y - \delta_x = 0$, which yields:

$$\overrightarrow{J} = \frac{E_0}{|E_0|} \begin{bmatrix} \cos\psi \\ \sin\psi \end{bmatrix} \tag{2.14}$$

If a wave has an orientation of 45° relative to the horizontal plane (diagonal polarization), then the following Jones vector represented in the horizontal and vertical basis is given on the left side in equation 2.15, while the Jones vector represented in the $\{45^\circ, 135^\circ\}$ basis will take the form on the right side of equation 2.15 [Taylor and Boerner, 2007].

$$\overrightarrow{J}^{\pi/4}_{\{\hat{h},\hat{v}\}} = \frac{1}{\sqrt{2}} \begin{bmatrix} 1 \\ 1 \end{bmatrix} \qquad \overrightarrow{J}^{\pi/4}_{\{45^\circ,135^\circ\}} = \begin{bmatrix} 1 \\ 0 \end{bmatrix} \tag{2.15}$$

Note that no phase difference exists between the components of a linear polarized wave.

Elliptical polarization

Circular polarization is a special case of the elliptical polarization, where the amplitudes in the two orthogonal bases are equal. An illustration of an elliptical polarization at a time-step t_0, and at a fixed point z_0 is given in Figure 2.5.

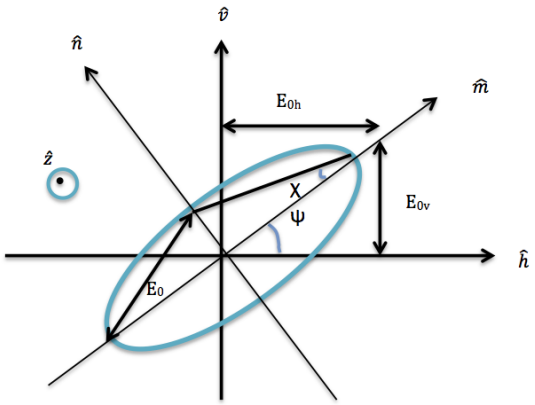

Figure 2.5: Elliptical polarized wave. Illustration based on Figure 2.5 in [Lee and Pottier, 2009, p. 35].

The angles χ and ψ represent the ellipticity and the orientation angle relative to the horizontal plane respectively [Lee and Pottier, 2009, p. 35-36]. The phase-term in equation 2.12 becomes $\delta = \delta_y - \delta_x = \frac{\pi}{2} + k\pi$ for an elliptically polarized wave, where k is the wave number [Lee and Pottier, 2009, p. 34]. Equation 2.12 can then be rewritten as:

$$\overrightarrow{J} = \frac{1}{\sqrt{(E_{0,x})^2 + (E_{0,y})^2}} \begin{bmatrix} E_{0,x} \\ E_{0,y} e^{j\frac{\pi}{2}} \end{bmatrix} = \frac{1}{\sqrt{(E_{0,x})^2 + (E_{0,y})^2}} \begin{bmatrix} E_{0,x} \\ jE_{0,y} \end{bmatrix} \tag{2.16}$$

Using the major axis denoted as $\hat{m}$, and the minor axis as $\hat{n}$ (see Figure 2.5), the Jones

vector can be represented in the $\{\hat{m}, \hat{n}\}$ basis as:

$$\overrightarrow{J}_{\{\hat{m},\hat{n}\}} = \frac{1}{\sqrt{(E_{0,m})^2 + (E_{0,n})^2}} \begin{bmatrix} E_{0,m} \\ jE_{0,n} \end{bmatrix} \tag{2.17}$$

where $E_{0,m} = E_0 \cos(\chi)$, and $E_{0,n} = E_0 \sin(\chi)$. Inserting this into equation 2.17 yields:

$$\overrightarrow{J}_{\{\hat{m},\hat{n}\}} = \frac{E_0}{|E_0|} \begin{bmatrix} \cos(\chi) \\ j \sin(\chi) \end{bmatrix} \tag{2.18}$$

Transforming from the $\{\hat{m}, \hat{n}\}$ to the $\{\hat{h}, \hat{v}\}$ basis, yields a rotation by an angle of ψ. The relation between the $\{\hat{m}, \hat{n}\}$ and the $\{\hat{h}, \hat{v}\}$ basis can be expressed as:

$$\begin{bmatrix} \hat{m} \\ \hat{n} \end{bmatrix} = \begin{bmatrix} \cos(\psi) & -\sin(\psi) \\ \sin(\psi) & \cos(\psi) \end{bmatrix} \begin{bmatrix} \hat{h} \\ \hat{v} \end{bmatrix} \tag{2.19}$$

where the matrix in front of $\{\hat{h}, \hat{v}\}$ is the rotational matrix. In the $\{\hat{h}, \hat{v}\}$ basis, the Jones vector for an elliptically polarized wave becomes:

$$\overrightarrow{J}_{\{\hat{h},\hat{v}\}} = \begin{bmatrix} \cos(\psi) & -\sin(\psi) \\ \sin(\psi) & \cos(\psi) \end{bmatrix} \begin{bmatrix} \cos(\chi) \\ j \sin(\chi) \end{bmatrix} \tag{2.20}$$

In the case of a left-circularly (LC) polarized wave, the phase becomes equal to $\frac{\pi}{2}$. The orientation angle becomes $\psi = 0$, and the elliptically angle becomes $\chi = \frac{\pi}{4}$. Using these parameters will result in the following expression for the Jones vector:

$$\overrightarrow{J}^{LC}_{\{\hat{h},\hat{v}\}} = \begin{bmatrix} 1 & 0 \\ 0 & 1 \end{bmatrix} \begin{bmatrix} \frac{1}{\sqrt{2}} \\ j\frac{1}{\sqrt{2}} \end{bmatrix} = \frac{1}{\sqrt{2}} \begin{bmatrix} 1 \\ j \end{bmatrix} \tag{2.21}$$

In the case of right-circularly (RC) polarized waves, the phase becomes $-\frac{\pi}{2}$, and the

Jones vector can be expressed as [Lee and Pottier, 2009, p. 37-38]:

$$\overrightarrow{J}^{RC}_{\{\hat{h},\hat{v}\}} = \frac{1}{\sqrt{2}}\begin{bmatrix}1\\-j\end{bmatrix} \tag{2.22}$$

A general expression of the Jones vector in the linear basis $\{\hat{h},\hat{v}\}$ for the different polarization types using the ellipticity and orientation angles, can then be formulated as:

$$\overrightarrow{J}_{\{\hat{h},\hat{v}\}} = \begin{bmatrix}\cos(\psi) & -\sin(\psi)\\ \sin(\psi) & \cos(\psi)\end{bmatrix}\begin{bmatrix}\cos(\chi)\\ \sin(\chi)e^{j\delta}\end{bmatrix} \tag{2.23}$$

Note that the ellipticity angle, χ, is always zero for linearly polarized waves.

2.2 Polarimetric target descriptors

The theory of polarimetry contains many different methods that can be useful when evaluating the information from satellite data. These methods can be based on the covariance matrix, coherency matrix (Jones matrix), the Kennaugh matrix, or the Stokes vector. These polarimetric descriptors have been thoroughly analyzed for quad-polarimetric systems, and it is therefore useful to convert the compact-pol data to the known basis vectors, namely horizontal and vertical basis. These polarimetric descriptors are used when reconstructing a pseudo quad-pol covariance matrix, and in decomposition theories, such as Cloude and Pottier's $H/A/\alpha$ decomposition [Lee and Pottier, 2009, p. 229-264]. These target descriptors are used throughout this work when testing different methods in terms of decomposition and reconstruction. The upcoming sections provide a general overview of different polarimetric descriptors.

2.2.1 The scattering coefficients

The scattering coefficients describe the transformation of an EM field as the result of the wave interaction with one or multiple scatterers at the target [Cloude, 2010, p. 47-48]. The interaction processes depend on the polarization, phase, power, and frequency of the wave. The target's properties may alter the properties of the incoming field, such that the scattered field contains an unique signature reflecting the properties of the target. These unique signatures are of special interest in remote sensing. The incident

field at the surface is defined as:

$$\overrightarrow{E}^{i}_{\text{surface}} = \frac{e^{-jk_i r}}{r}\overrightarrow{E}^{i}_{\text{sensor}} \tag{2.24}$$

where $\overrightarrow{E}^{i}_{\text{sensor}}$ is the transmitted field from the sensor, $\overrightarrow{E}^{i}_{\text{surface}}$ is the incident field at the surface, k_i is the wave vector, and $\frac{e^{-jk_i r}}{r}$ takes the propagation effects—both amplitude and phase—into account, and r is the distance from the sensor to the surface [Cloude, 2010, p. 46-47]. This is illustrated in Figure 2.6. The scattered field at the receiver is related to the scattered field at the surface in the following manner:

$$\overrightarrow{E}^{s}_{\text{sensor}} = \frac{e^{-jk_s r}}{r}\overrightarrow{E}^{s}_{\text{surface}} \tag{2.25}$$

The transformation between the incident field, $\overrightarrow{E}^{i}_{\text{surface}}$, and the scattered field, $\overrightarrow{E}^{s}_{\text{surface}}$, at the surface is through the so called scattering wave vector, and is expressed as:

$$\overrightarrow{E}^{s}_{\text{surface}} = \boldsymbol{S}\overrightarrow{E}^{i}_{\text{surface}} \tag{2.26}$$

Inserting for the $\overrightarrow{E}^{s}_{\text{surface}}$, yields:

$$\overrightarrow{E}^{s}_{\text{sensor}} = \frac{e^{-jk_s r}}{r}\boldsymbol{S}\overrightarrow{E}^{i}_{\text{surface}} \tag{2.27}$$

The scattering wave vector is often written as a scattering matrix ($\boldsymbol{S}$), that represents the relation between the polarizations of the incoming and outgoing waves. These relationships are referred to as scattering coefficients. For example, for quad-pol systems the relation between the transmitted fields and the measured fields is [Taylor and Boerner, 2007]:

$$\begin{bmatrix}\overrightarrow{E}^{s}_{H}\\ \overrightarrow{E}^{s}_{V}\end{bmatrix} = \frac{e^{jkr}}{r}\begin{bmatrix}S_{HH} & S_{HV}\\ S_{VH} & S_{VV}\end{bmatrix}\begin{bmatrix}\overrightarrow{E}^{i}_{H}\\ \overrightarrow{E}^{i}_{V}\end{bmatrix} \tag{2.28}$$

where H and V denotes horizontal and vertical polarizations. Solving for the transmitted

wave that is horizontally polarized yields:

$$\overrightarrow{E}^{s}_{H} = \frac{e^{jkr}}{r}\left(S_{HV}\overrightarrow{E}^{i}_{V} + S_{HH}\overrightarrow{E}^{i}_{H}\right) \tag{2.29}$$

where $S_{HV}\overrightarrow{E}^{i}_{V}$ represents the scattering of the incident horizontal component into the vertical polarization, and $S_{HH}\overrightarrow{E}^{i}_{H}$ represents the scattering of incident horizontally polarized wave into the same polarization state. S_{HH} is referred to as the co (like)-pol component, while S_{HV} is referred to as the cross-pol component.

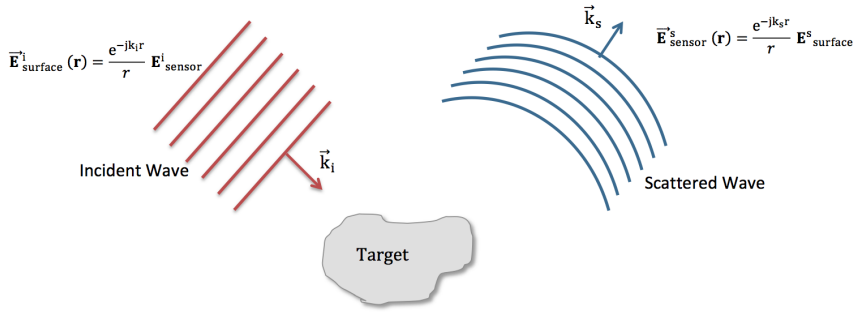

Figure 2.6: The figure illustrates the interaction of an EM wave and a target.

2.2.2 Polarimetric coherency and covariance matrices

The coherency and covariance matrices are frequently used to extract information about the surface of interest. These matrices are often used in decomposition theories, such as the Pauli decomposition, which uses the diagonal components in the coherency matrix to compose a RGB color image. The coherency and covariance matrices are defined as the Hermitian outer product of the scattering vector, where the scattering vector is represented in the lexicographic space for the covariance matrix or using the Pauli scattering vectors to create the coherency matrix. The sample covariance matrix is created by averaging over L pixels, i.e.:

$$\boldsymbol{C} = \langle \overrightarrow{s}_L \overrightarrow{s}^{\star T}_L \rangle = \frac{1}{L}\sum_{i=1}^{L} \overrightarrow{s}_L \overrightarrow{s}^{\star T}_L \tag{2.30}$$

where $\langle \ldots \rangle$ denotes spatial averaging, $\boldsymbol{T}$ denotes the transpose operator, $\star$ denotes the

complex conjugate, L is the number of pixels, and the scattering vector, $\overrightarrow{s}_L$, is defined as:

$$\overrightarrow{s}_L = [S_{HH}, S_{HV}, S_{VH}, S_{VV}]^T \tag{2.31}$$

where the subscript L denotes the lexicographic feature vector. The coherency matrix is defined as:

$$T = \langle \overrightarrow{s}_P \overrightarrow{s}_P^{\star T} \rangle = \frac{1}{L} \sum_{i=1}^{L} \overrightarrow{s}_P \overrightarrow{s}_P^{\star T} \tag{2.32}$$

where P denotes the Pauli feature vector, defined as:

$$\overrightarrow{s}_P = \frac{1}{\sqrt{2}} [S_{HH} + S_{VV}, S_{HH} - S_{VV}, S_{HV} + S_{VH}, j(S_{HV} - S_{VH})]^T \tag{2.33}$$

Both $\overrightarrow{s}_L$ and $\overrightarrow{s}_P$ contain four elements, but can be reduced to three elements if the *reciprocity assumption* is made. This means that the interaction between the target and the incident wave is equal for the two polarization cross-pol channels, namely HV and VH. Then the scattering wave vectors have the following expressions:

$$\overrightarrow{s}_L = [S_{HH}, \sqrt{2} S_{HV}, S_{VV}]^T \tag{2.34}$$

$$\overrightarrow{s}_P = \frac{1}{\sqrt{2}} [S_{HH} + S_{VV}, S_{HH} - S_{VV}, \sqrt{2} S_{HV}]^T \tag{2.35}$$

The sample covariance and coherency matrices are thus defined as [Lee and Pottier, 2009, p. 67-68]:

$$\boldsymbol{C}_3 = \langle \overrightarrow{s}_L \overrightarrow{s}_L^{\star T} \rangle = \begin{bmatrix} \langle |S_{HH}|^2 \rangle & \sqrt{2} \langle S_{HH} S_{HV}^{\star} \rangle & \langle S_{HH} S_{VV}^{\star} \rangle \\ \sqrt{2} \langle S_{HV} S_{HH}^{\star} \rangle & 2 \langle |S_{HV}|^2 \rangle & \sqrt{2} \langle S_{HV} S_{VV}^{\star} \rangle \\ \langle S_{VV} S_{HH}^{\star} \rangle & \sqrt{2} \langle S_{VV} S_{HV}^{\star} \rangle & \langle |S_{VV}|^2 \rangle \end{bmatrix} \tag{2.36}$$

and,

$$
\begin{aligned}
\boldsymbol{T}_3 &= \langle \overrightarrow{s}_P \overrightarrow{s}_P^{\star T} \rangle \\
&= \frac{1}{2} \begin{bmatrix}
\langle |S_{HH} + S_{VV}|^2 \rangle & \langle (S_{HH} + S_{VV})(S_{HH} - S_{VV})^\star \rangle & \\
\langle (S_{HH} - S_{VV})(S_{HH} + S_{VV})^\star \rangle & \langle |S_{HH} - S_{VV}|^2 \rangle & \cdots \\
2\langle S_{HV}(S_{HH} + S_{VV})^\star \rangle & 2\langle S_{HV}(S_{HH} - S_{VV})^\star \rangle & \\
\cdots\cdots\cdots & & \begin{matrix} 2\langle (S_{HH} + S_{VV}) S_{HV}^\star \rangle \\ 2\langle (S_{HV} - S_{VV}) S_{HV}^\star \rangle \\ 4\langle |S_{HV}|^2 \rangle \end{matrix}
\end{bmatrix}
\end{aligned}
\tag{2.37}
$$

Often, the total power measured by the sensor is used in the interpretation of the data. This is given as:

$$
\mathrm{P}_{\text{total}} = Tr(\boldsymbol{T}) = Tr(\boldsymbol{C}) = \langle |S_{HH}|^2 \rangle + 2\langle |S_{HV}|^2 \rangle + \langle |S_{VV}|^2 \rangle \tag{2.38}
$$

where $Tr(\cdot)$ denotes the trace of the matrix. The relationship between the covariance and the coherency matrix is given through the special unitary matrix, i.e.:

$$
\boldsymbol{U}_{L \to P} = \frac{1}{\sqrt{2}} \begin{bmatrix} 1 & 0 & 1 \\ 1 & 0 & -1 \\ 0 & \sqrt{2} & 0 \end{bmatrix} \tag{2.39}
$$

and is used in the following manner:

$$
\boldsymbol{T}_3 = \boldsymbol{U}_{L \to P} \boldsymbol{C}_3 \boldsymbol{U}_{L \to P}^{-1} \tag{2.40}
$$

Scattering symmetry properties

Throughout this work, we make multiple assumptions with respect to scattering symmetry. In this section we give a general overview of the three main symmetries; reflection,

rotational, and azimuthal symmetry. By assuming a certain symmetry the coherency and covariance matrices become less complex, and this will ease the reconstruction of a pseudo quad-pol covariance matrix from the compact-pol data. Scattering symmetry assumptions concern the distribution of elementary scatterers within the resolution cell, and can thus simplify and reduce the number of independent scattering elements in the covariance and coherency matrices [Moreria et al., 2013]. This section will only present the theory behind the different symmetries, which will be necessary for the successive chapters concerning the reconstruction process.

Reflection symmetry

Reflection symmetry can be assumed when the distributed target has two points (S_1 and S_2) with equal contributions [Cloude and Pottier, 1996]. The scatterer (S_1 and S_2) are mirrored to each other [Moreria et al., 2013]. This is demonstrated in Figure 2.7, where $u_\perp$ and $u_\parallel$ denotes the axis around the *line-of-sight* of the antenna. The equations in this figure demonstrate how the two scattering targets within the resolution cell (illustrated as the dark blue square) produce a decorrelation between the cross- and the co-pol scattering elements. The scattering elements are demonstrated with the a, b, and c symbols respectively.

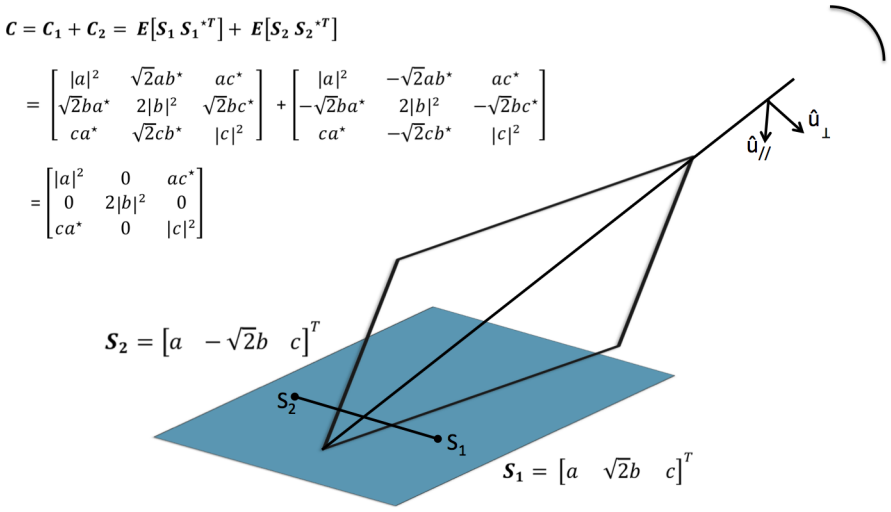

Figure 2.7: Reflection symmetry around the line-of-sight direction (illustration based on Figure 3.9 in [Lee and Pottier, 2009, p. 69]).

The following decorrelation takes place between the co- and cross-pol elements [Lee

and Pottier, 2009, p. 71-72]:

$$\langle S_{HH} S_{HV}^{\star} \rangle = \langle S_{VV} S_{HV}^{\star} \rangle = 0 \tag{2.41}$$

This means that the orientation distribution is symmetrical about the vertical direction [van Zyl and Kim, 2010, p. 61]. The sample covariance and coherency matrices have the following forms after this scattering symmetry configuration:

$$\boldsymbol{C}_3 = \begin{bmatrix} \langle |S_{HH}|^2 \rangle & 0 & \langle S_{HH} S_{VV}^{\star} \rangle \\ 0 & 2\langle |S_{HV}|^2 \rangle & 0 \\ \langle S_{VV} S_{HH}^{\star} \rangle & 0 & \langle |S_{VV}|^2 \rangle \end{bmatrix} \tag{2.42}$$

$$\boldsymbol{T}_3 = \langle \vec{s}_P \vec{s}_P^{\star T} \rangle$$

$$= \frac{1}{2} \begin{bmatrix} \langle |S_{HH} + S_{VV}|^2 \rangle & \langle (S_{HH} + S_{VV})(S_{HH} - S_{VV})^{\star} \rangle & \cdots \\ \langle (S_{HH} - S_{VV})(S_{HH} + S_{VV})^{\star} \rangle & \langle |S_{HH} - S_{VV}|^2 \rangle & \cdots \\ 0 & 0 & \\ \cdots\cdots\cdots & & \end{bmatrix} \tag{2.43}$$

$$\begin{matrix} 0 \\ 0 \\ 4\langle |S_{HV}|^2 \rangle \end{matrix} \Bigg]$$

Rotational symmetry

When a medium exhibits rotational symmetry, the covariance matrix will be invariant under the rotation around the line-of-sight by the angle θ (see Figure 2.8) [Nghiem et al., 1992]. This means that the elements in the covariance or the coherency matrices will generate equal response independent of the rotation angle [Cloude and Pottier, 1996, Souyris et al., 2005]. This is demonstrated in Figure 2.8. Here, α, β, and γ represent the target vectors in the Pauli basis space [Cloude and Pottier, 1996]. The rotational matrix $R_3(\theta)$ is a special unitary matrix. To enable a rotational invariant coherency matrix, the target vectors must be the eigenvectors ($\boldsymbol{u}$) of both the rotational and the coherency matrix (see equations in Figure 2.8) [Lee and Pottier, 2009, p. 71]. This means that the sample coherency and covariance matrices consist of only three independent scattering elements [Moreria et al., 2013].

If this assumption is made about a medium, the relationships among the coefficients in

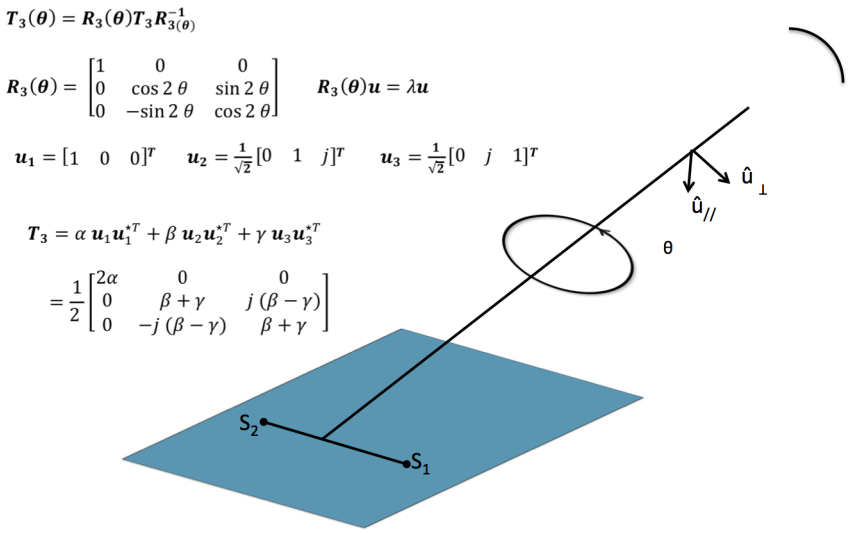

Figure 2.8: Rotation symmetry about the line-of-sight (illustration based on Figure 3.10 in [Lee and Pottier, 2009, p. 70]).

the scattering matrix becomes [Souyris et al., 2005]:

$$\langle S_{HH} S_{HH}^{\star} \rangle = \langle S_{VV} S_{VV}^{\star} \rangle \tag{2.44}$$

$$\Re\left(\langle S_{HH} S_{HV}^{\star} \rangle\right) = \Re\left(\langle S_{HV} S_{VV}^{\star} \rangle\right) = 0 \tag{2.45}$$

$$\Im\left(\langle S_{HH} S_{VH}^{\star} \rangle\right) = \Im\left(\langle S_{VH} S_{VV}^{\star} \rangle\right) \tag{2.46}$$

The sample covariance and coherency matrices for a medium that exhibits rotational symmetry have the following form:

$$C_3 = \begin{bmatrix} \langle |S_{HH}|^2 \rangle & \sqrt{2}\langle S_{HH} S_{HV}^{\star} \rangle & \langle S_{HH} S_{VV}^{\star} \rangle \\ \sqrt{2}\langle S_{HV} S_{HH}^{\star} \rangle & 2\langle |S_{HV}|^2 \rangle & -\sqrt{2}\langle S_{HV} S_{HH}^{\star} \rangle \\ \langle S_{VV} S_{HH}^{\star} \rangle & -\sqrt{2}\langle S_{HH} S_{HV}^{\star} \rangle & \langle |S_{VV}|^2 \rangle \end{bmatrix} \tag{2.47}$$

$$\boldsymbol{T}_3 = \frac{1}{2}\begin{bmatrix} \langle|S_{HH}+S_{VV}|^2\rangle & 0 & 0 \\ 0 & \langle|S_{HH}-S_{VV}|^2\rangle & 2\langle(S_{HV}-S_{VV})S_{HV}^{\star}\rangle \\ 0 & 2\langle S_{HV}(S_{HH}-S_{VV})^{\star}\rangle & 4\langle|S_{HV}|^2\rangle \end{bmatrix} \tag{2.48}$$

Azimuthal symmetry

Azimuthal symmetry includes both reflection and rotational symmetry [Lee and Pottier, 2009, p. 71-72]. The sample coherency and covariance matrices for such a scattering configuration take the following form:

$$\boldsymbol{C}_3 = \begin{bmatrix} \langle|S_{HH}|^2\rangle & 0 & \langle S_{HH}S_{VV}^{\star}\rangle \\ 0 & 2\langle|S_{HV}|^2\rangle & 0 \\ \langle S_{HH}S_{VV}^{\star}\rangle & 0 & \langle|S_{HH}|^2\rangle \end{bmatrix} \tag{2.49}$$

$$\boldsymbol{T}_3 = \frac{1}{2}\begin{bmatrix} \langle|S_{HH}+S_{VV}|^2\rangle & 0 & 0 \\ 0 & \langle|S_{HH}-S_{VV}|^2\rangle & 0 \\ 0 & 0 & \langle|S_{HH}-S_{VV}|^2\rangle \end{bmatrix} \tag{2.50}$$

Medium that exhibits this kind of symmetry will backscatter equal response in both the linear vertical and horizontal polarizations. For this symmetry to hold, the element $\frac{1}{2}\langle|S_{HH}-S_{VV}|^2\rangle$ must be equal to twice the cross-pol intensity.

2.2.3 The Stokes vector

The Stokes vector is a useful tool that describes the polarization of the EM wave in terms of the power distribution of the wave [Lee and Pottier, 2009, p. 43-44]. For a monochromatic plane wave, these four parameters are defined as [Elachi and van Zyl, 2006, p. 28]:

$$\boldsymbol{q} = \begin{bmatrix} q_0 \\ q_1 \\ q_2 \\ q_3 \end{bmatrix} = \begin{bmatrix} |E_H|^2 + |E_V|^2 \\ |E_H|^2 - |E_V|^2 \\ 2|E_H||E_V|\cos\delta \\ 2|E_H||E_V|\sin\delta \end{bmatrix} = \begin{bmatrix} A^2 \\ A^2\cos 2\psi\cos 2\chi \\ A^2\cos 2\psi\sin 2\chi \\ A^2\sin 2\chi \end{bmatrix} \tag{2.51}$$

A short description of the different parameters included in the Stokes vector are listed below [Elachi and van Zyl, 2006, p. 28]:

- E_H, E_V: The horizontal and vertical polarization components of a polarized EM wave.
- $|E_H|^2, |E_V|^2$: Amplitude squared = power of E_H and E_V.
- δ: Relative phase between horizontal and vertical EM wave, i.e., $\angle(E_H, E_V)$.
- A: Overall amplitude, i.e. $A = \sqrt{|E_H|^2 + |E_V|^2}$.
- ψ, χ: Orientation and ellipticity angle (see Figure 2.1).

The different parameters in the Stokes vector contain the following information [Lee and Pottier, 2009, p. 44]:

$q_0 \rightarrow$ Total power density of the wave.

$q_1 \rightarrow$ Power in the linear horizontally or vertically polarized component.

$q_2 \rightarrow$ Power in the linearly polarized components at tilt angles $\psi = 45°$ or $\psi = 135°$.

$q_3 \rightarrow$ Power in the left-hand and right-hand circularly polarized component in the plane wave.

For a fully polarized wave, these parameters are related in the following way [Lee and Pottier, 2009, p. 44]:

$$q_0^2 = q_1^2 + q_2^2 + q_3^2 \tag{2.52}$$

The Stokes vector have been utilized in compact-pol decomposition analysis to extract information about the backscattering properties of a given target, such as in the $DoP - \chi$ and $DoP - \delta$ decompositions proposed in [Raney, 2007]. DoP is the degree of polarization defined as [Raney, 2007]:

$$DoP = \frac{\sqrt{q_1^2 + q_2^2 + q_3^2}}{q_0} \tag{2.53}$$

The Stokes vector has also been used to perform a H/α decomposition on compact-pol data by relating the DoP to the entropy (H) [Cloude et al., 2012]. The degree of

polarization is used extensively throughout this work for both retrieval of compact-pol parameters (see chapter 5) and in the reconstruction of a pseudo quad-pol covariance matrix (see chapter 6).

2.3 Scattering mechanisms

When an EM pulse interacts with a surface element, the behavior of the outgoing radiation is dependent on several factors. These include EM properties of the medium, properties of the sensor, and the geometry of the surface element. The interaction between the surface element and the incident wave can be described through scattering mechanisms. There are three main scattering mechanisms; surface-, double bounce-, and volume scattering. Each of these will be discussed in the upcoming sections, focusing mainly on scattering from sea ice surfaces.

2.3.1 Surface scattering

Single bounce scattering occurs when the incident wave has been dispersed only once by the surface boundary between two media, often air and the surface element. Surfaces that exhibit single bounce scattering are reasonably flat relative to the wavelength of the incoming field. The response from a "single-bounce scattering element" is highest in the co-pol channels [Cloude, 2010, p. 115-117].

In the single-bounce case, the incident angle equals the angle of reflection, and the refracted wave follows Snell's law, which relates the transmission angle to the incident angle through a refractive index n. This index is given by Maxwell's relation as $n = \sqrt{\epsilon}$, where ϵ is the dielectric constant [Cloude, 2010, p. 116]. Figure 2.9 illustrates the concept of single bounce scattering, and a relation between the two media can be established through Snell's law in the following way [Elachi and van Zyl, 2006, p. 56]:

$$n_1 \sin(\theta_i) = n_2 \sin(\theta_r) \tag{2.54}$$

The reflection matrix in this scenario is [Cloude, 2010, p. 117]:

$$\boldsymbol{R}_{QP} = \frac{\boldsymbol{E}_r}{\boldsymbol{E}_i} = \begin{bmatrix} R_{HH} & 0 \\ 0 & R_{VV} \end{bmatrix} \implies \begin{aligned} R_{HH} &= \frac{\cos\theta_i - \sqrt{\frac{\epsilon_2}{\epsilon_1} - \sin^2\theta_i}}{\cos\theta_i + \sqrt{\frac{\epsilon_2}{\epsilon_1} - \sin^2\theta_i}} \\ R_{VV} &= \frac{\frac{\epsilon_2}{\epsilon_1}\cos\theta_i - \sqrt{\frac{\epsilon_2}{\epsilon_1} - \sin^2\theta_i}}{\frac{\epsilon_2}{\epsilon_1}\cos\theta_i + \sqrt{\frac{\epsilon_2}{\epsilon_1} - \sin^2\theta_i}} \end{aligned} \tag{2.55}$$

where QP denotes a quad-polarized system with horizontal and vertical polarizations, $\boldsymbol{E}_i$ is the incoming electric field, $\boldsymbol{E}_r$ is the reflected field, and R is the reflection coefficients. The coefficients on the right are given by Fresnel's equations [Cloude, 2010, p. 117]. No depolarization of the incident wave occurs for perfectly smooth surfaces (relative to the incident wave's wavelength) [Cloude, 2010, p. 123,133-134]. This means that the horizontally polarized wave will reflect as a horizontally polarized wave. As a consequence of the completely polarized reflected wave, there will be no response in the cross-pol channel.

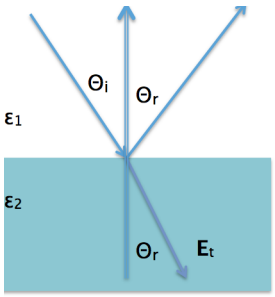

Figure 2.9: The concept of single-bounce scattering. The θ_i term represents the incident angle of the incoming wave, while the angle θ_r represent the reflection angle. The dielectric constants for the two media are represented by ϵ (illustration based on Figure 3.2 in [Cloude, 2010, p. 116]).

The roughness of the surface will also affect the backscattering properties, and is often described by the Rayleigh criterion. This criterion depends on the wavelength of the incoming wave (λ), the standard deviation of the height (s_h), and the angle of incidence (θ_i) (see equation 2.11). Figure 2.10 (a) illustrates the case when the incident wave's wavelength is much greater than the surface height variation, s_h, while Figure 2.10 (b) shows a situation where the wavelength of the incident wave has a slightly greater scale than the surface height. Finally, Figure 2.10 (c) illustrates the case where the wavelength of the incident wave is less or equal to the surface height [Chuvieco and Huete, 2010].

The backscattering properties can be divided into two components: a specular and a diffuse component. Perfectly smooth surfaces will have zero return, because the reflected wave is scattered away from the sensor (specular). If the surface is very rough compared to the incident wave, the surface tends to backscatter in a Lambertian fashion (diffuse part), meaning that the backscatter is independent of the incident angle. This will generate a response in all the polarization channels [Cloude, 2010, p. 133-134].

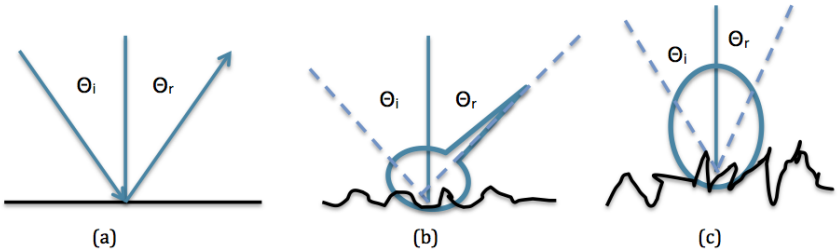

Figure 2.10: The figure illustrates three surface scattering scenarios, namely scattering for a smooth surface (a), a slightly rough surface (b), and a very rough surface (this illustration borrows elements from Figure 2.22 in [Chuvieco and Huete, 2010]).

Examples of media exhibiting single bounce scattering are flat surfaces (relative to the wavelength as judged by the Rayleigh criterion), for example calm water or smooth ice. Bragg scattering is also categorized as surface scattering, where the single bounce return from the ocean surface possesses the typical resonant scattering. This occurs when the incident wave's wavelength is in resonance with the wavelength of the ocean facet [Lee and Pottier, 2009, p. 326].

2.3.2 Double bounce scattering

Double bounce scattering is sometimes referred to as scattering from dihedral corner reflectors [Cloude, 2010, p. 54], and this kind of scattering arises when the incoming wave undergoes two bounces during the interaction process. Only the co-pol channels produce a response, and no responses are measured in the cross-pol channels for an ideal corner reflector [Cloude, 2010, p. 54]. If the transmitted signal is horizontally polarized, this signal will still be a horizontally polarized wave when arriving at the receiver. The vertical polarization component of the returned wave is mirrored with respect to the direction of the incident wave, which results in a phase shift of 180° in the measured signal in the vertical polarization channel [ESA, n.d.]. If the transmitted wave is left-circularly polarized, the outgoing wave will be right-circularly polarized (this is because the corner target will mirror the incident wave) [Charbonneau et al., 2010]. Double bounce return may be generated between smooth ice and deformed ice (see Figure 2.11) or along ice edges.

The two scattering mechanisms discussed, surface and double bounce scattering, may produce depolarized scattering scenarios. Depolarization of the incident wave may also occur due to surface slope or large scale roughness [Cloude, 2010, p. 133]. In this case, the backscattered wave is not completely polarized and consists of random polarization types, which will also produce a response in the cross-pol channels. This can occur for

rough and highly deformed sea ice [Eltoft et al., 2014].

2.3.3 Volume scattering

Volume scattering occurs within heterogeneous (varying particle density and particle distribution) bulk materials that contain local variations in the dielectric properties [Cloude, 2010, p. 142]. Figure 2.11 illustrates a typical scenario that exhibit volume scattering within a brine coated layer in the sea ice. Volume scattering within the sea ice structure is caused by inhomogeneity, for examples in the brine pockets (first-year ice), drainage structures, or in air bubbles (multi-year ice) [Winebrenner et al., 1989].

The penetration depth is dependent on the wavelength of the incoming wave as well as the dielectric properties (discussed in chapter 3). If the dielectric constant of the scattering material is large, there will be little transmission into the material and thus little or no volume scattering [Carsey, 1992, p. 42]. The depolarization in volume scattering is caused by two basic physical processes: particle anisotropy[2], or multiple scattering between particles [Cloude, 2010, p. 142]. Often, the cross-pol channel is used to represent the volume scattering, such as in Pauli basis vector. This is because the incident wave may change the polarization state when undergoing volume scattering, and a response will also be generated in the cross-pol channel. Considering compact polarimetry for this scenario may be challenging because the cross-pol term is mixed with the co-pol elements in the two compact-pol scattering elements (see chapter 5). Therefore, a variety of techniques, such as the reconstruction to quad-polarimetric data or decomposition theories, have been proposed to extract the cross-pol intensity or a measure of the depolarized effects from compact-pol data.

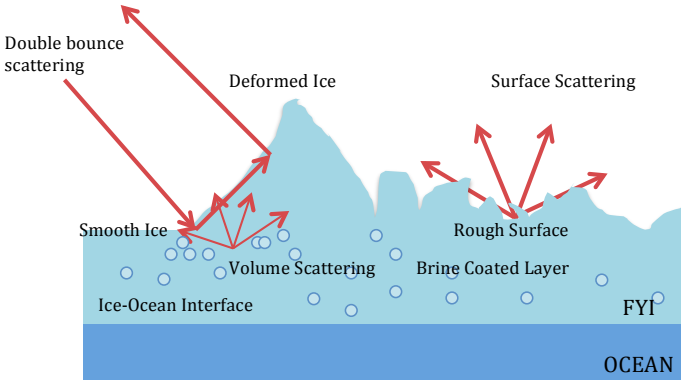

Figure 2.11: Scattering mechanism for first year ice (FYI), illustrating single bounce, double bounce, and volume scattering within a brine coated layer [Hossain, 2012].

2. A material that does not have the same behavior in all directions.

3

SAR Remote Sensing of Arctic Sea Ice

Sea ice covers approximately 25 million square kilometers of the Earth's surface, and is mostly located in the Polar regions [NSIDC, n.d.]. In the Arctic, there is a permanent ice cap above 72°N. Since the Polar regions are dark at least half the year—and often cloud covered—radar instruments such as SAR are very useful for monitoring these areas. It is important to monitor the sea ice and its cycles in order to obtain a deeper understanding of the effects of sea ice on climate change, and it is also an important tool when planning marine transportation, offshore operations, and for the fishing industry.

A thorough understanding of sea ice is important when attempting to analyze compact polarimetric data originating from such sea ice surfaces. This chapter includes an overview of sea ice and its properties in the context of remote sensing.

3.1 Introduction to sea ice

Although mostly consisting of frozen seawater, sea ice takes various forms depending on the season, weather, and ocean conditions. Often, the sea ice is labeled for interpretation and classification purposes. These types can be based on, e.g., different sea ice concentration levels, flow size distributions, thickness, snow cover, or in terms of the sea ice age [Onstott and Shuchman, 2004]. The World Meteorological Organization ([WMO-

No.574, 2010]) has derived a definition of sea ice in different stages of development (SoP), which is often used when classifying sea ice within SAR scenes.

The sea ice is given different names depending on its condition and age. The two main classes are *first-year ice* and *multi-year ice*. The former is sea ice that has grown (seawater freezing) during the current season, while multi-year ice has survived at least one melting season. The two main classes are further split into subclasses depending on the thickness and stage of development.

In the Arctic region, the sea ice growth normally starts around September and the ice usually reaches its maximum extent during February/March. Following these months, the sea ice starts to melt and withdraw. *New ice* is recently formed ice which includes *frazil ice*[1], *grease ice*[2], *slush* and *shuga*[3]. Grease ice exhibits little backscattering due to the soupy layer on the surface, and these regions appear relatively dark in SAR scenes [NSIDC, n.d., WMO-No.574, 2010]. In general, new ice has a high salinity content, and newly formed ice normally has very rough surfaces that often are wetted with seawater. As the temperature drops during the winter season the sea ice becomes thicker, and the *brine*[4] leaks out into the ocean. Nilas (< 5cm), grey (10−14cm), grey-white (15−30cm) and first-year (> 30cm) ice are names differentiating sea ice based on the thickness [WMO-No.574, 2010]. The backscattering from new ice ranges from strong for deformed and/or rough ice to weak for smooth and undeformed ice [Carsey, 1992, p. 43]. When the sea ice has reached a thickness of approximately 30 cm, it is considered to be first-year ice. If this sea ice survives one melting season it is from then on referred to as multi-year ice. This type of ice has grown for a long period, which often results in a relatively high thickness of approximately 2 meters. The backscattering from first-year ice tends to increase compared to newly formed ice due to lower brine volume, the consequently lower electromagnetic absorption, and increased roughness [Carsey, 1992, p. 43]. For multi-year ice, on the other hand, the backscattering signal increases due to multiple air bubbles and lower salinity content [Carsey, 1992, p. 44].

Another trait of long lived sea ice is a low salinity content. This is simply because the salt has been drained owe the entire life span of the ice. This will result in a large amount of gas bubbles populating the upper layer of this type of sea ice, which may alter volume scattering of microwaves. When the sea ice (often first-year ice) undergoes a deformation, the resulting ice is called *ridges* or *walls*. These formations occur when the sea ice is pressed together and form a vertical structure. *Open ice* occurs when the sea ice breaks and the floes no longer are in contact with one another, these cracks are called *leads*, which consists of open water or thin ice [WMO-No.574, 2010].

1. Frazil ice is fine spicules or plates of ice which is suspended in water [WMO-No.574, 2010].
2. Grease is has a very thin soupy laver of frail crystals which are clumped together [WMO-No.574, 2010].
3. Shuga is formed from grease or slush ice [WMO-No.574, 2010].
4. Brine is when salt in the sea ice accumulates into droplets [NSIDC, n.d.].

Figure 3.1 shows Photographs of different types of sea ice taken by the author during the N-ICE cruise in May 2015.[5] The different images illustrate the visual appearance of nilas, leads, ridges, floes, multi-year ice, and grey-white ice (soon to be first-year ice) discussed in the previous paragraphs.

In a SAR perspective there are several features that can be extracted. Sea ice type, thickness, and age are among other extremely important parameters to study. Sea ice is very complex in the microwave region, and the interaction mechanisms between the incident wave and the medium depend on the properties of the sea and the nature of the overlying snow pack. Such properties are temperature, salinity profile, density, size of air bubbles, brine inclusions, and other impurities [Falkingham, 2014].

5. More information about N-ICE project can be found on the following web-page: `http://www.npolar.no/en/projects/details?pid=b98886ce-590a-48a8-b113-4b96e98c65c8` (accessed on May 28th 2015).

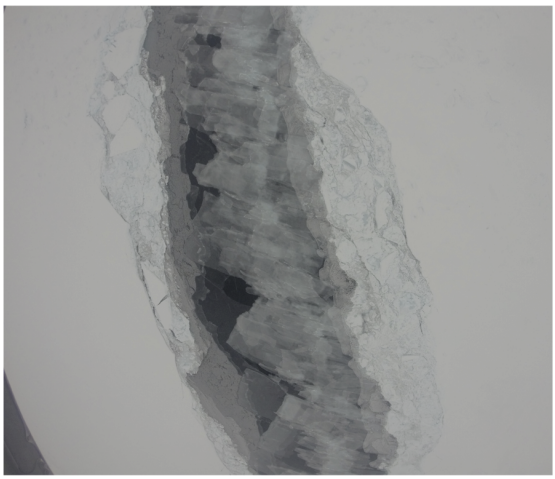

Nilas formed in calm water
Photograph acquired by Martine Espeseth, N-ICE 2015, Norwegian Polar Institute. Date: May 2015

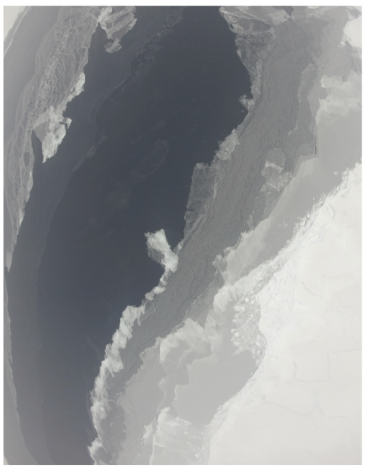

Lead
Photograph acquired by Martine Espeseth, N-ICE 2015, Norwegian Polar Institute. Date: May 2015

Ridges
Photograph acquired by Martine Espeseth, N-ICE 2015, Norwegian Polar Institute. Date: May 2015

Floes
Photograph acquired by Martine Espeseth, N-ICE 2015, Norwegian Polar Institute. Date: May 2015

Multi-year ice (left corner) and newly formed ice (right side of the photo)
Photographs courtesy Sebastian Sikora, UNIS, N-ICE 2015, Norwegian Polar Institute. Date: May 2015

Grey-white ice covered with 2-3 cm of snow (removed manually on the lower corner of the photo)
Photograph acquired by Martine Espeseth, N-ICE 2015, Norwegian Polar Institute. Date: May 2015

Figure 3.1: Photographs of different types of sea ice located in the Barents Sea. The images were taken by the author and Sebastian Sikora (employed at University of Svalbard), and was acquired during the N-ICE project managed by the Norwegian Polar Institute in May 2015.

3.2 Electromagnetic properties of sea ice

The collected signal backscattered from a given target contains information about the electromagnetic properties of target itself. These properties are interesting when studying sea ice effects on climate change, and also for other purposes like fishing and oil and gas industry. The backscattering field depends on the radar frequency, incident angle, polarization, wavelength, instrumental noise, and the scattering signatures of the illuminated area [Tucker III et al., 1992, Wackerman, 1992]. The scattering signatures of the illuminated area are influenced by the properties of the sea ice, i.e.:

- The complex dielectric constant, which refers to the basic electrical properties of material and determines the propagation, scattering, reflection and attenuation of the incoming electrical field [Onstott and Shuchman, 2004]. The complex dielectric constant is in turn dependent on the level of salinity, air pockets, snow covers, and sea ice age.

- Surface roughness relative to the length of the incoming electromagnetic wave [Onstott and Shuchman, 2004, Moen, 2014].

The properties listed above reflects the signature of the sea ice, and these are the ones of interest when interpreting a sea ice covered area.

3.3 Operational sea ice charting

Sea ice charts have been used extensively in several different industries. The oil and gas industry, for instance, frequently uses such ice charts to plan potential operations in the high North, where the charts are used to evaluate risks, and can affect the construction process of rigs and vessels.

Multiple services offer ice charts that illustrate sea ice types in terms of concentration, thickness and/or ice age. The Canadian Ice Service uses the SoP for their ice charts, in terms of an egg coding[6]. Other services, like the National Snow and Ice Data Center (NSIDC), and the Norwegian Metrological Institute (MET Norway) also offer ice charts. The former uses continuous sea ice concentration intervals, ranging from 0 (no ice) to 1 (high concentration). MET Norway operates with six main categorizes, which describes both the drift type and concentration level. Some selected ice charts from MET Norway are shown in Figure 3.2. These ice charts are from the same dates and location as the

6. The egg code contains information about the ice observation on a particular site, and is a tool in interpreting ice charts produced by the Canadian Ice Service. More information can be found on the following web page: `https://www.ec.gc.ca/glaces-ice/default.asp?lang=En&n=D5F7EA14-1&offset=1&toc=hide` (accessed on May 28th 2015).

dataset used in this work. These ice charts use color codes to represent the different types of sea ice. From these charts is can be seen that drift ice is present very close to the north east coast of Svalbard. This is indicated by a high percentage of sea ice cover across each pixel cell.

MET Norway's ice charts are high resolution sea ice concentration charts, and are created based on a manual interpretation of satellite data [MET Norway, n.d.]. The main satellite used in the labeling process is RADARSAT-2[7], which is a weather independent SAR system [MET Norway, n.d.]. It uses dual polarization mode, with horizontal or vertical polarization at the transmitter and receive at both horizontal and vertical polarizations. The main reason for using a dual-pol system is the large swath width (approximately 500 km for the ScanSAR wide swath in RADARSAT-2) [CSA, 2011]. This provides a resolution of approximately 100×100 m. Even though the resolution is low, this is reasonable as the goal is to monitor and map large areas of sea ice. If the fine quad-pol mode in RADARSAT-2 is used, the maximum swath width is 25 km, but more polarimetric information is provided and the ice charting will thus be more accurate. From these numbers, the importance of a compact-pol system can be inferred. Both the larger swath width and the additional polarimetric information about the backscattered field would be very useful. To the author's knowledge, no research has been conducted on estimating sea ice concentration levels using compact polarimetric data, and further study is thus warranted.

7. RADARSAT-2 is the second Canadian C-band SAR satellite, which was launched in December 14th in 2007.

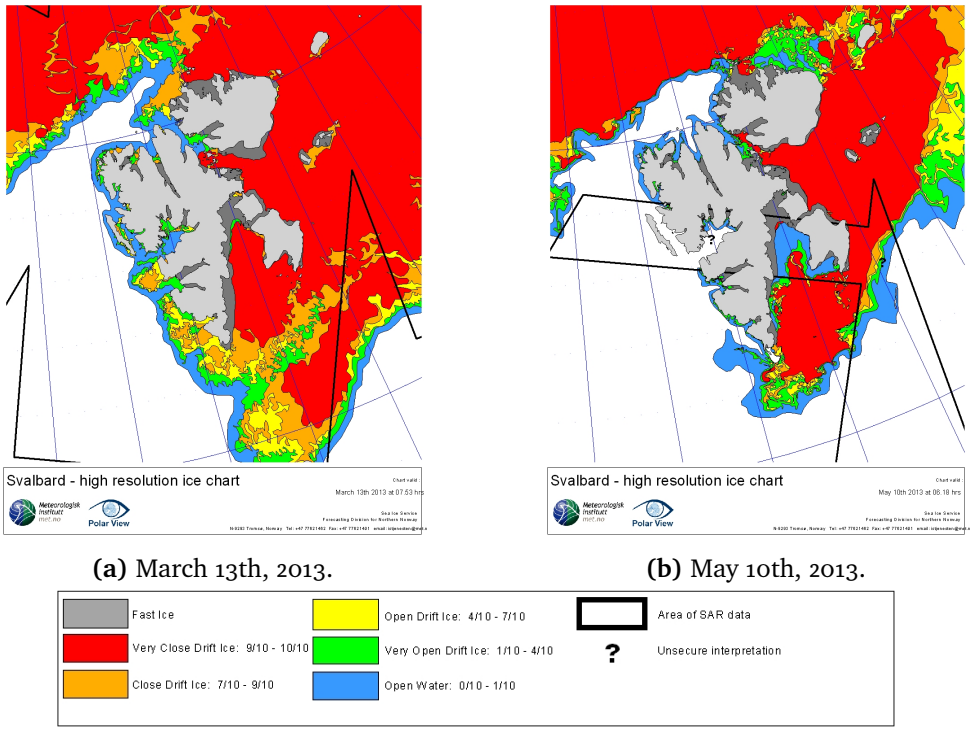

(a) March 13th, 2013.

(b) May 10th, 2013.

(c) Ice Categories.

Figure 3.2: Regional operational ice concentration chart from Svalbard area for 13th March, 14th March, 8th May and 9th May. 2013. *Image courtesy of the Ice Service at the Norwegian Meteorological Institute*.

3.4 Other applications

There are several other fields within the study of sea ice. Among them are ice classification, ice deformation, snow cover on sea ice, ice thickness and thickness distribution, ice drift/motion, melt and freeze onset, melt pond formation and evolution, leads, floe size distribution, and landfast ice. These areas have all been identified as needing further research [Falkingham, 2014]. Falkingham produced a report where he highlighted the different requirements for observing these areas by considering the frequencies, polarizations, incident angles, etc. Most of the study on these areas consider single- or dual-polarimetric SAR instruments, but he states that further research on quad-polarimetric SAR is warranted. Currently available quad-pol SAR instruments suffers from a narrow swath width which limits the coverage. However, using compact polarimetry, some of the existing methods for studying these applications could be improved, since compact polarimetric SAR data contain a higher level of polarimetric information than the regular single- and dual-polarimetric SAR systems.

4

Study Area and Data

This master thesis covers multiple methods for reconstructing a pseudo quad-pol covariance matrix based on the sample compact-pol covariance matrix. In order to test and explore the properties of these methods, real SAR data have been used. Specifically, four scenes covering sea ice from Storfjorden of the coast from Svalbard, are utilized. These four scenes have been acquired by RADARSAT-2 in quad-pol fine resolution mode. The data was collected at four different dates, namely March 13th, March 14th, May 8th, and May 10th 2013. The RADARSAT-2 data have been provided by Norwegian Space Centre/Kongsberg Satellite Services under the Norwegian-Canadian Radarsat agreement of 2013.[1]

4.1 Study area

Figure 4.1 shows the locations for each of the scenes, which are located around 17^o - 20^oE, 77^o - 78^oN. Figures 4.2 through 4.5 show the four scenes in the Pauli basis (see section 2.2.2) and their locations on a map. The two scenes from March contain approximately the same types of sea ice, but some of the ice has drifted between the two dates. This is also the case for the two scenes from May. The four scenes all contain first-year ice (see chapter 3) exclusively. Even so, there are significant differences between the first-year ice types from the March and May scenes. This difference might be due to sea ice growth, varying snow cover, or the fact the temperature and ocean conditions

1. RADARSAT-2 Data and Products ©MacDonald, Dettwiler and Associated Ltd., 2013 - All Right Reserved.

are different in March compared to May. The reasoning behind using four SAR scenes in this work is the varying sea ice cover and the presence of open water regions in two of the images. This will help when determining the performance of the different reconstruction methods for varying surfaces. The different scenes will be referred to based on the date of acquisition.

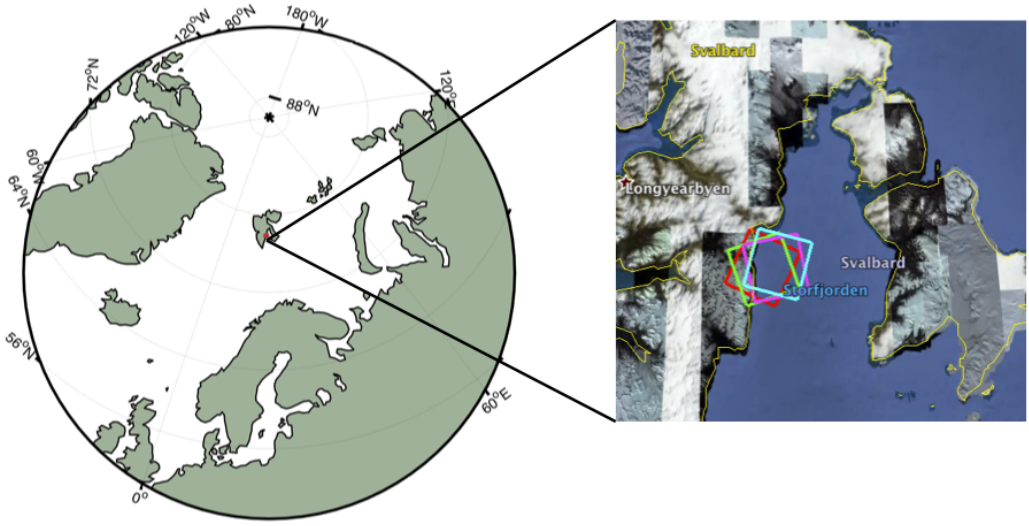

Figure 4.1: Polar stereographic map of the northern hemisphere showing the geographical location of the quad-pol scenes used in this work. The boxes inside the zoomed-in map are displayed with different colors. Each color indicates a date, and shows the location of the area shown in the largest map. Purple represent the SAR scene from March 13th, green is the scene from March 14, blue is May 8th, and red is the scene from May 10th.

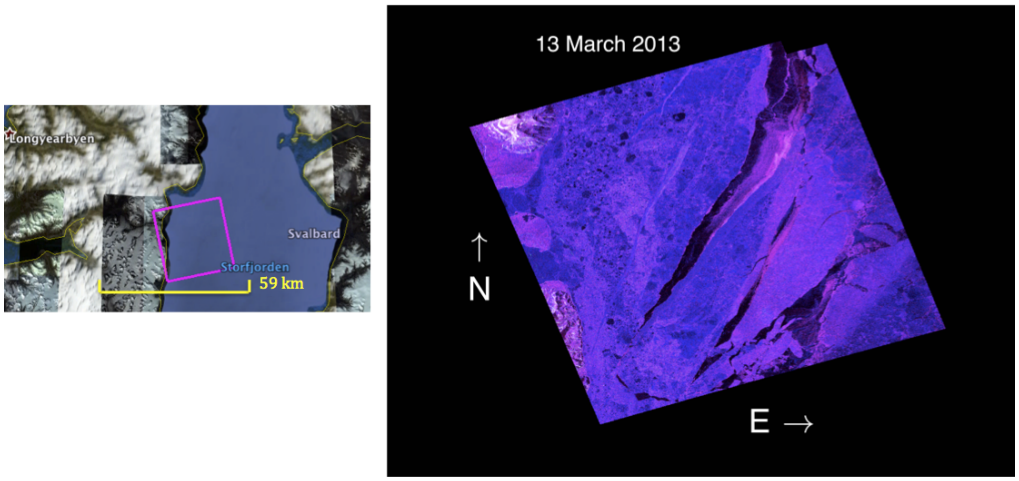

Figure 4.2: RADARSAT-2 scene from March 13th 2013. The scene is geocoded and the image is shown as a Pauli image, i.e.: Red = $\langle|S_{HH} - S_{VV}|^2\rangle$, Blue = $\langle|S_{HH} + S_{VV}|^2\rangle$, and Green = $2\langle|S_{HV}|^2\rangle$.

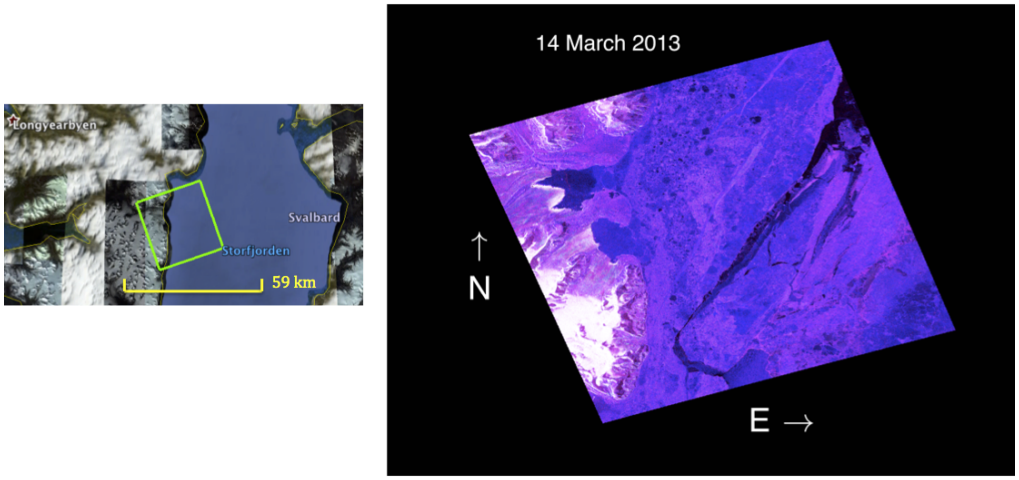

Figure 4.3: RADARSAT-2 scene from March 14th 2013. The scene is geocoded and the image is shown as a Pauli image, i.e.: Red = $\langle|S_{HH} - S_{VV}|^2\rangle$, Blue = $\langle|S_{HH} + S_{VV}|^2\rangle$, and Green = $2\langle|S_{HV}|^2\rangle$.

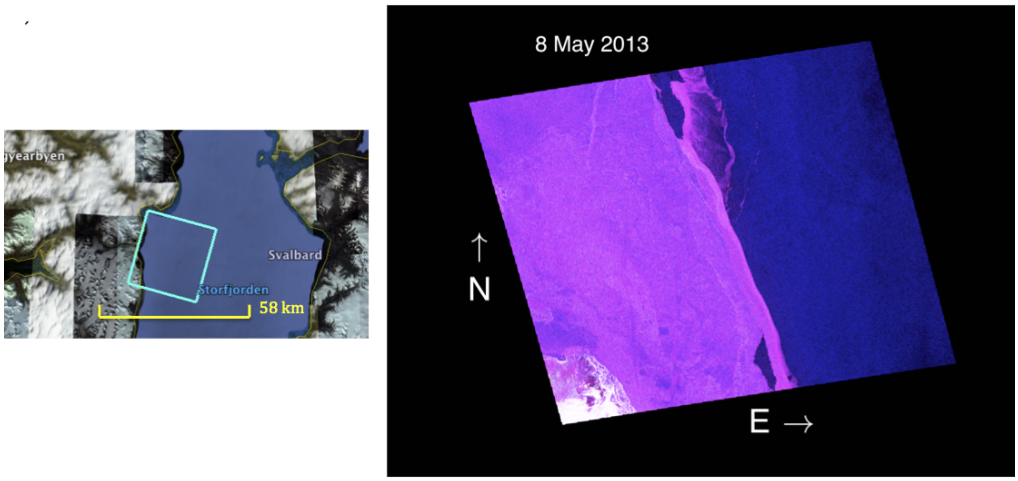

Figure 4.4: RADARSAT-2 scene from May 8th 2013. The scene is geocoded and the image is shown as a Pauli image, i.e.: Red = $\langle|S_{HH} - S_{VV}|^2\rangle$, Blue = $\langle|S_{HH} + S_{VV}|^2\rangle$, and Green = $2\langle|S_{HV}|^2\rangle$.

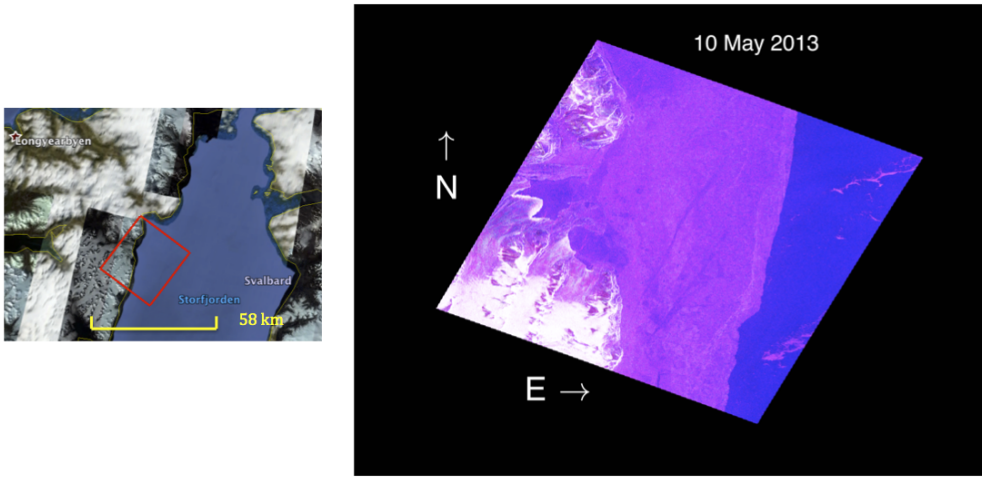

Figure 4.5: RADARSAT-2 scene from May 10th 2013. The scene is geocoded and the image is shown as a Pauli image, i.e.: Red = $\langle|S_{HH} - S_{VV}|^2\rangle$, Blue = $\langle|S_{HH} + S_{VV}|^2\rangle$, and Green = $2\langle|S_{HV}|^2\rangle$.

4.2 Properties of the data

Table 4.1 contains sensor properties of the four SAR scenes. The four scenes are acquired with the same quad-pol fine mode and with approximately the same resolution. The only parameter varying across the four scenes is the incident angle. The spatial resolution is high (approximately 5.7 m × 7.6 m) and the swath width is narrow (≈ 25 km) compared to other acquisition modes available for RADARSAT-2. This will enable extraction of detailed information about the sea ice. This dataset is especially well suited to this work because of the fine details present in each scene, but also because several distinct types of sea ice are present. All in all, this makes for a rich and realistic dataset on which to test existing and proposed reconstruction methods.

RADARSAT-2 (SLC product)	**March 13th 2013**	**March 14th 2013**	**May 8th 2013**	**May 10th 2013**
Product Id	1368109052	1368108853	1368166286	1368317557
Frequency	5.4 GHz	5.4 GHz	5.4 GHz	5.4 GHz
polarization	Quad-pol	Quad-pol	Quad-pol	Quad-pol
Resolution[a] (Rg × Az)	5.7 m × 7.6 m	5.7 m × 7.6 m	5.7 m × 7.6 m	5.7 m × 7.6 m
Scene size	25 km × 25 km	25 km × 25 km	25 km × 25 km	25 km × 25 km
Incidence angle	$46.1^o - 47.3^o$	$37.4^o - 38.9^o$	$42.0^o - 43.35^o$	$29.2^o - 30.93^o$
Bandwidth	30 MHz	30 MHz	30 MHz	30 MHz

Table 4.1: Properties of the SAR sensor modes investigated in this work. All scenes are acquired by RADARSAT-2 with the fine quad-pol mode. RADARSAT-2 is owned by the Canadian Space Agency (CSA) and operated by MacDonald Dettwiler and Associates Ltd (MDA) [MacDonald, Dettwiler and Associates Ltd, 2014]. [a] Range resolution is in radar slant range, and varies with incidence angle.

The data has been processed and collected by Kongsberg Satellite Services (KSAT). In this work, the polarimetric data has been multi-looked in order to reduce speckle and to make the axes of the scenes proportional to the ground length. The slant range resolution is approximately 5.2 m and azimuth resolution is 7.6 m for the four scenes, this means that the azimuth resolution is 1.5 times greater than the slant range resolution. To obtain a square resolution cell the averaging window size should have the same aspect ratio. For example; the scene acquired March 13th has 4208 pixels in range direction and 6095 pixels in azimuth direction, and a window size of 6 × 9 (range × azimuth) can therefore be used. This would yield a new image of size 702 × 678. The 6 × 9 window size is used for all the scenes, i.e., 6 pixels in the range and 9 pixels in the azimuth direction.

4.3 Sea ice labels

The labeling of sea ice was performed with help from an expert[2] at the Norwegian Polar Institute. This expert has substantial experience in interpreting sea ice SAR images, and has also visited this exact cite. The interpretation is also aided by EM-bird[3] measurements, which were taken at approximately the same time as the images were acquired.

The results of the labeling are shown in Figures 4.6 and 4.7, which also contain the class names. Only first-year ice is present in this area, and this is because most of the sea ice that is grown in Storfjorden will either drift out from the fjord or melt during the summer. There are two main classes of sea ice within the two SAR scenes; fast-ice and drifting ice. The former is sea ice that is attached to the shore, while the latter group is sea ice in motion. The separating border between these two classes is illustrated with a black dashed line in all the scenes. Further subclasses of sea ice are found within the two main groups. One such subclass is leads, which are located within the red ellipses in the two scenes from March. Another subclass is ridges, which is sea ice that has been deformed. This class can be observed within the orange ellipses in the SAR scenes acquired on March 13th and 14th. Another subclass is smooth or homogenous sea ice, which is located in the purple circle in the SAR scenes acquired in May. The yellow ellipses represent *sea ice objects* that have been drifting out from the landfast ice onto the fast ice, and thus produce a different backscatter response than the surrounding sea ice. Some rough sea ice may also be present in the two scenes from March. These areas are located inside the green ellipses, and are considered to be rough because the backscatter is higher compared to the smoother areas. The yellow dashed line in all the four scenes denotes the separation between land and landfast ice.

These classes are used as "ground truth" when evaluating the compact polarimetric data throughout this work.

2. Expert: Gunnar Spreen is employed as permanent research scientist for sea ice remote sensing at the Norwegian Polar Institute, Tromsø, Norway.
3. EM-bird: Electromagnetic induction sounding for measuring sea ice thickness.

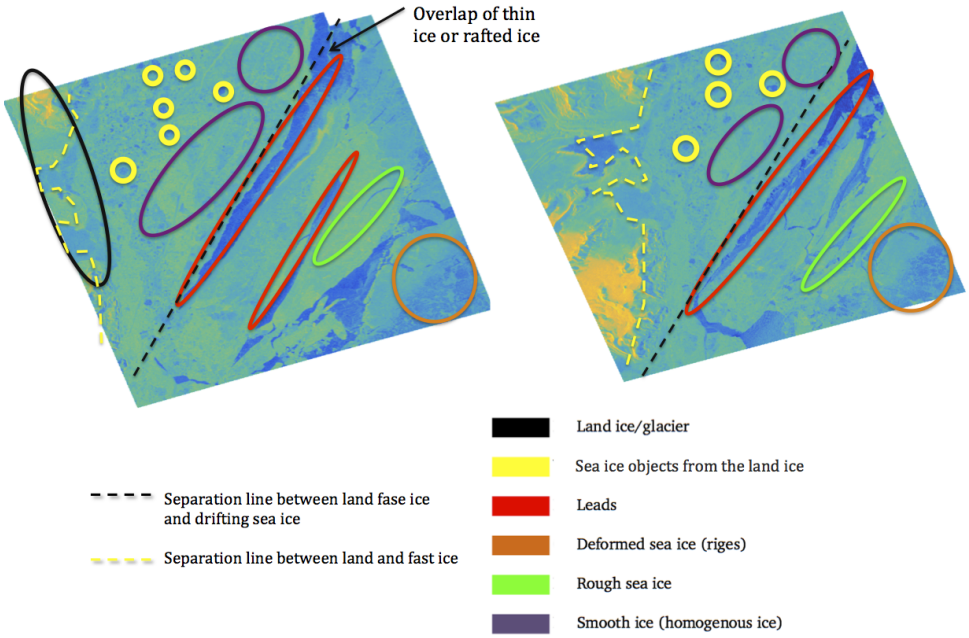

Figure 4.6: HH channel (in decibel) acquired March 13th (image to the left) and March 14th 2013 (image to the right) with segmentations of the different sea ice types.

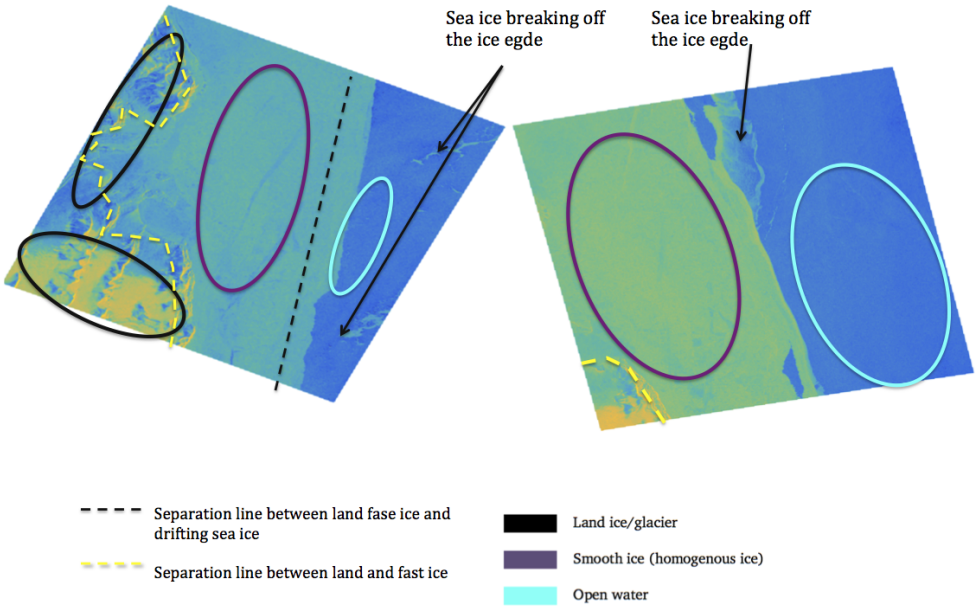

Figure 4.7: HH channel (in decibel) acquired May 10th (image to the left) and 8th 2013 (image to the right) with segmentations of the different sea ice types.

5

Compact Polarimetry

Over the last decade, compact polarimetry has emerged to provide a great opportunity in the radar industry in context of Earth Observation. The reason for the large interest in the compact-pol mode is because it provides the benefits from both full- and dual-pol SAR systems; namely the double swath width from dual-pol systems, and the large amount of polarimetric information from quad-pol systems [Raney and Hopkins, 2011, Charbonneau et al., 2010]. In its infancy, the theoretical foundation of compact polarimetry was presented by Souyris, Nord, and later Raney with the hybrid-pol mode. Compact polarimetry—especially the hybrid-pol mode—has proved valuable, and has in later years found its way into operational satellite systems such as the RISAT and the ALOS-2 satellites.

The first satellite that operated with the compact-pol mode was the Mini-SAR sensor. This sensor was launched on October 22th 2008 on the Chandrayaan-1 mission, and operated for nine months [Spudis et al., 2010]. The objective of this mission was to systematically map the surface polewards of 80° latitudes for both of the moons poles [Spudis et al., 2010]. The Mini-SAR operated in S-band using left-circular polarization transmits and received coherently in linear horizontal and vertical polarizations [Balabhavya, 2013]. RISAT was launched in April 2012, and this satellite provides several modes, such as hybrid-, dual-, single-, and quad-pol mode [NRSC, 2014]. The hybrid-pol mode is right-circularly polarized transmit and receives coherently in linear horizontal and vertical polarizations. ALOS-2 was launched in 2014 with the PALSAR-2 instrument, which has an experimental compact-pol mode. It can transmit on diagonal, left-circular and right-circular polarizations, while receiving on linear polarizations [JAXA, n.d.]. The objectives for this mission are maritime surveillance (ice, wind, oil pollution, and

ship monitoring), disaster management (mitigation, warning, response, and recovery), and ecosystem monitoring (forestry, agriculture, wetlands, and coastal change monitoring) [CSA, 2011]. The RADARSAT Constellation Mission, which is a follow-up to RADARSAT-1 and RADARSAT-2, is planned to launch in 2018. This mission will employ various modes, including the hybrid-pol mode.

Recall from section 2.1.5 that different polarization modes can be used in radar systems. The polarization mode defines the system with regards to the polarization of the transmitted and received electromagnetic field. Note that the "mode" term may also refer to different acquisition modes of SAR operation within a single system, such as *stripmap*, *scanSAR*, *Spotlight SAR*, and *Interferometric SAR*. In this work, mode will be used in terms of polarization and not the acquisition [Cumming and Wong, 2005, p. 12-13]. Note that radar systems are also characterized by the swath width, data rate, signal-to-noise ratio, frequency, and pulse repetition frequency (PRF).

The different polarization architectures can be divided into three categories. These are quad-pol (QP), dual-pol, and single-pol, which are illustrated in Figure 5.1. The box to the left in Figure 5.1 represents a quad-pol system, also known as a *full*-polarimetric system. This system transmits waves with two orthogonal polarizations and measures the response coherently in two orthogonal polarizations.

A dual-pol system is illustrated in the center box in Figure 5.1. Such a system transmits waves using only one polarization, and receives in two orthogonal polarizations. A compact polarimetric system is a subgroup of dual-pol system. In this system, the transmitted signal is either a circularly polarized wave, or a linear combination of a horizontally and a vertically polarized wave (known from the $\frac{\pi}{4}$-pol architecture [Souyris et al., 2005]). The backscattered signals are either recorded in the horizontal and vertical polarization basis, or left- and right-hand circular polarization basis. The dashed arrow (see Figure 5.1) from the compact-pol system to the quad-pol system indicates that information contained in the compact-pol data can be related to the quad-pol data in terms of the polarimetric information. This will be investigated in the upcoming sections. The last category, single-pol, transmits and receives only in one polarization channel. The single-pol system is illustrated in the box to the right in Figure 5.1.

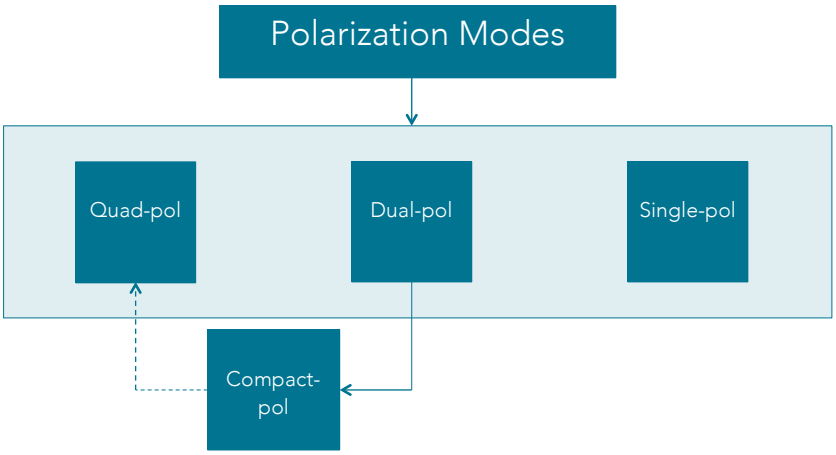

Figure 5.1: The different polarization architectures. The dashed line represent a partial connection, which is the case between a quad- and a compact-pol SAR system. The solid line between the dual- and compact-pol boxes indicate that the compact-pol is mainly a subgroup of dual-pol systems due to their equal number of polarization channels.

In radar systems, only a single polarized wave is transmitted at a time. Orthogonal transmitted polarizations must be interleaved (time-multiplexed) [Raney and Hopkins, 2011]. The time-multiplexing will affect the PRF, i.e., how many pulses per second the radar transmits. In dual- and single-pol systems only one polarization is used at the transmitter, meaning that the PRF is half of that of a system with two orthogonal polarizations [Raney and Hopkins, 2011]. Also, the spatial coverage will be affected by the number of channels used. The swath width is related to the listening time, and the listening time, T_R, is dependent on the length of the pulse transmitted (plus the delay), and the wave's velocity, c, when traveling towards the surface and back to the sensor. The relationship between the swath width and the listening time is:

$$\mathrm{SW} \approx T_R c \tag{5.1}$$

The concept of multiplexing, and how a quad-polarimetric system is related to a compact polarimetric system is illustrated in Figure 5.2.

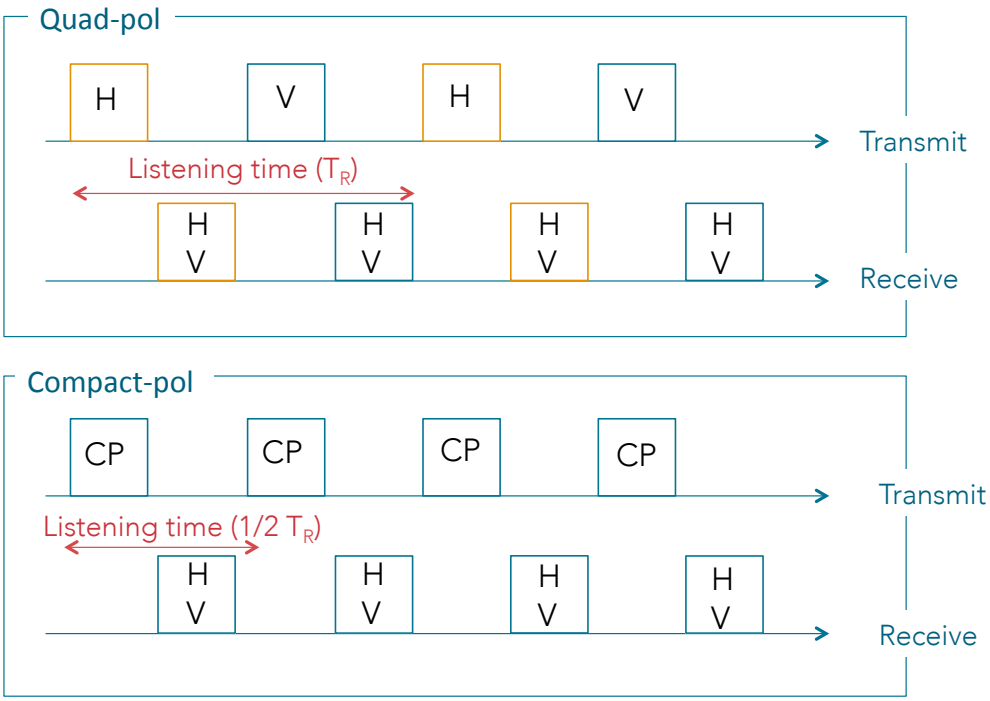

Figure 5.2: Concept of multiplexing in a full polarimetric SAR system, and how this is related to a compact polarimetric SAR systems (this figure is based on figure 4.9 in [Cumming and Wong, 2005, p. 134]).

The upper part of Figure 5.2 represents a quad-polarimetric system that utilizes both horizontal and vertical polarization channels. Such a system first transmits a horizontally polarized wave, and then waits for the response. After the antenna has received the response from the horizontally polarized wave, a vertically polarized wave is transmitted. The next time the horizontally polarized wave is transmitted, the listening time has doubled, because of the vertically polarized wave transmitted in between. In dual-, single-, and compact-pol systems, the multiplexing is left out, since only one type of polarization is used at the transmitter (see Figure 5.2). Hence, the swath width is doubled when using dual- or single-pol systems, compared to quad-pol systems.

Because of the two polarizations at the transmitter, quad-pol radars require twice the average power compared to dual- and single-pol systems [Raney and Hopkins, 2011]. The data rate, however, will not be doubled in dual/single-pol systems, even though the swath width is doubled. This is because quad-pol systems provide one additional polarization at the transmitter compared to dual- and single-pol systems. The data volume per pixel is doubled for quad-pol systems compared to dual-pol system [Raney

and Hopkins, 2011]. Hence, the dual- and the single-pol systems consume less power, and provide greater spatial coverage compared to quad-pol systems.

The different polarizations of the transmitted electromagnetic field provide different interaction properties with regards to the surface-wave and surface-atmosphere interactions. As discussed in section 2.1.1, the polarization state of the incoming electromagnetic waves will have significant impact on how the waves will interact with the surface element. By using a quad-polarimetric system, the backscattering properties can be described with great detail. The amount of polarimetric information decreases with the number of polarimetric channels. Compact-pol systems provide more polarimetric information than dual- and single-pol systems, but less than quad-pol systems.

We have now discussed some of the benefits of the compact-pol mode; namely the doubled swath width inherited from dual-pol systems, and the high amount of polarimetric information partly inherited from quad-pol systems. In the upcoming sections, we will present a more detailed overview of the different compact polarimetric modes and how these are related to the quad-pol system.

5.1 Compact polarimetric properties

There are three compact polarimetric modes discussed in the literature. The first of these—introduced by Souyris—was the linear diagonal polarization known as the $\frac{\pi}{4}$*-pol mode* [Souyris et al., 2005]. Such a radar system will transmit a pulse that is oriented at 45 degrees relative to the horizontal and vertical directions. This configuration is illustrated in Figure 5.3 A. The equation in Figure 5.3 A represents the transmitted signal, which is the superposition of linear horizontal and vertical polarizations, i.e., $H + V$ [Dubois-Fernandez et al., 2008b]. The receiver measures the incoming waves in two polarizations, namely H and V.

Following the theory from $\frac{\pi}{4}$-pol mode, Raney proposed to transmits circularly polarized pulses instead of transmitting diagonally polarized pulses [Raney, 2007]. The circular transmit and linear receive mode was introduced, and this type of configuration consists of two subclasses; left- and right-hand circular polarizations at the transmitter. This mode is also known as the hybrid-pol mode. This architecture transmits circularly polarized waves and receives in the two orthogonal linear polarizations H and V. The configuration of this mode is illustrated in Figure 5.3 B. The last polarimetric mode discussed is the DCP mode. Such a system transmits circularly polarized pulses, and receives coherently dual-circular polarizations (see Figure 5.3 C) [Raney, 2007].

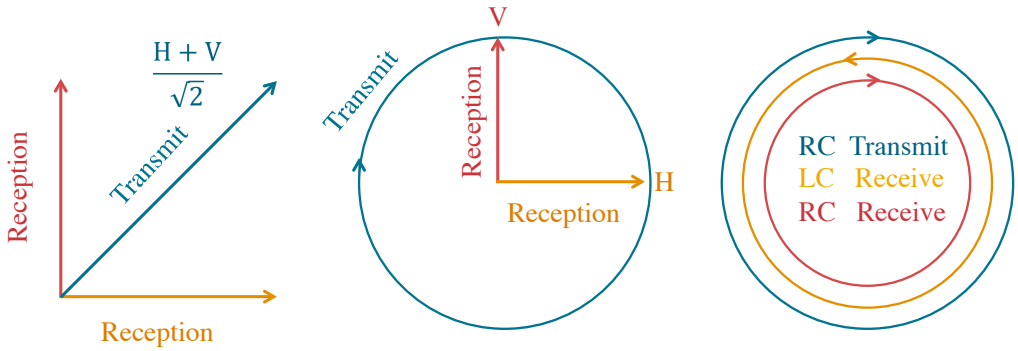

Figure 5.3: Polarimetric configurations of compact polarimetry: A: $\frac{\pi}{4}$-pol mode, B: hybrid-pol mode (transmitted field is right-circularly polarized), and C: DCP mode (transmitted field is right-circularly polarized) [Boularbah et al., 2012].

5.1.1 Scattering vector

The polarimetric target descriptors for the compact-pol modes deviate from the known target descriptors generated from quad-pol data (discussed in section 2.2). Both the hybrid-pol and $\frac{\pi}{4}$-pol modes have vertical and horizontal polarizations at the receiver. The transmitted electromagnetic pulse can be expressed as a function of the Jones vector in the linear basis space as:

$$\overrightarrow{E} = \begin{bmatrix} \cos(\psi) & -\sin(\psi) \\ \sin(\psi) & \cos(\psi) \end{bmatrix} \begin{bmatrix} \cos(\chi) \\ \sin(\chi)e^{j\delta} \end{bmatrix} \overrightarrow{E}_{h,v} \tag{5.2}$$

where h and v represent the linear $\{\text{H},\text{V}\}$ basis unit vectors, ψ is the orientation angle, and χ is the ellipticity angle [Lee and Pottier, 2009, p. 35-36]. The two matrices in front of $\overrightarrow{E}_{h,v}$ form the constitute Jones vector, which was discussed in section 2.1.6.

In the case of $\frac{\pi}{4}$-pol mode, the Jones vector becomes:

$$\overrightarrow{J}_{\frac{\pi}{4}} = \begin{bmatrix} \cos(\psi) \\ \sin(\psi) \end{bmatrix} \overset{\substack{\psi = 45^\circ \\ \chi = 0^\circ}}{=} \frac{1}{\sqrt{2}} \begin{bmatrix} 1 \\ 1 \end{bmatrix} \tag{5.3}$$

Combining the horizontal and vertical parts, the expression for the EM field is:

$$\overrightarrow{E}_{\frac{\pi}{4}} = \frac{\overrightarrow{E_h}\hat{h} + \overrightarrow{E_v}\hat{v}}{\sqrt{2}} \tag{5.4}$$

In the case of the hybrid-pol mode, the Jones vector for left circular (LC) and right circular (RC) becomes:

$$\overrightarrow{J}_{LC/RC} \overset{\substack{\psi=[-\frac{\pi}{2},\frac{\pi}{2}]\\ \chi=\pm 45^{o}}}{=} \frac{1}{\sqrt{2}}\begin{bmatrix}1\\ \pm j\end{bmatrix} \tag{5.5}$$

Here, j is the imaginary unit.

The incoming EM field interacts with a surface element, and the incident wave may scatter in all directions, one of which could be towards the sensor. The scattering matrix is used to relate the incoming and outgoing radiation in the following manner [Boularbah et al., 2012]:

$$\overrightarrow{E}_s = \boldsymbol{S}\overrightarrow{E}_i \tag{5.6}$$

where $\overrightarrow{E}_s$ is the electric field measured at the sensor, $\overrightarrow{E}_i$ is the incident field at the surface, and $\boldsymbol{S}$ is the scattering matrix (also known as the Sinclair matrix [Taylor and Boerner, 2007]). In the {H,V} basis, this is given as:

$$\boldsymbol{S} = \begin{bmatrix}S_{HH} & S_{VH}\\ S_{HV} & S_{VV}\end{bmatrix} \tag{5.7}$$

The scattering vector is the projection of the full backscattering matrix $\boldsymbol{S}$ (equation 5.7) on the transmitted polarization state (linear diagonal polarization) [Boularbah et al., 2012]. The relationship between these two vectors is given in equation 5.8 [Dubois-Fernandez et al., 2008b].

$$\overrightarrow{k} = \boldsymbol{S}\overrightarrow{J} \tag{5.8}$$

Inserting the Jones vector from equation 5.3 into equation 5.8 yields the following scattering vector for the $\frac{\pi}{4}$-pol mode:

$$\overrightarrow{k}_{\frac{\pi}{4}} = \begin{bmatrix}S_{\frac{\pi}{4}H}\\ S_{\frac{\pi}{4}V}\end{bmatrix} = \begin{bmatrix}S_{HH} & S_{VH}\\ S_{HV} & S_{VV}\end{bmatrix}\frac{1}{\sqrt{2}}\begin{bmatrix}1\\ 1\end{bmatrix} = \frac{1}{\sqrt{2}}\begin{bmatrix}S_{HH}+S_{HV}\\ S_{VV}+S_{VH}\end{bmatrix} \tag{5.9}$$

The scattering vector for the hybrid-pol mode can be constructed by applying the Jones

vector from equation 5.5, i.e.:

$$\vec{k}_{LC/RC} = \begin{bmatrix} S_{LH/RH} \\ S_{LV/RV} \end{bmatrix} = \begin{bmatrix} S_{HH} & S_{VH} \\ S_{HV} & S_{VV} \end{bmatrix} \frac{1}{\sqrt{2}} \begin{bmatrix} 1 \\ \pm j \end{bmatrix} = \frac{1}{\sqrt{2}} \begin{bmatrix} S_{HH} \pm jS_{HV} \\ \pm jS_{VV} + S_{VH} \end{bmatrix} \tag{5.10}$$

The term $\sqrt{2}$ is present to conserve the power [Souyris et al., 2005]. Often, the scattering coefficients S_{VH} and S_{HV} are assumed equal due to scattering reciprocity [Ainsworth et al., 2007], and this assumption is used throughout this work.

The target scattering vectors for transmitted waves that are left- or right-circularly polarized are calculated using the special unitary (SU(2)) group when transforming from $\{\text{H}, \text{V}\}$ to $\{\text{RC}, \text{LC}\}$ basis. Consider a quad-polarimetric system that transmits left- and right-circularly polarized waves, and measures the same polarization at the receiver. This scattering matrix can be defined as:

$$\boldsymbol{S}_{\text{circularly}} = \begin{bmatrix} S_{LL} & S_{LR} \\ S_{RL} & S_{RR} \end{bmatrix} \tag{5.11}$$

The elements in the above matrix can be transformed to the linear basis $\{\text{H}, \text{V}\}$ by using a special unitary transformation. It is important to preserve the power when transforming from one basis to another. If a special unitary transformation is not used, the power will change, and it may therefore affect the response obtained from a given target and cause misinterpretation of the polarimetric behavior. The Jones vector for a right-circularly polarized wave in the linear basis is $\frac{1}{\sqrt{2}}[1, -j]^T$, while for a left-circularly polarized wave the Jones vector becomes $\frac{1}{\sqrt{2}}[1, j]^T$. Combining these into a transformation matrix yields:

$$\boldsymbol{U} = \frac{1}{\sqrt{2}} \begin{bmatrix} 1 & 1 \\ j & -j \end{bmatrix} \tag{5.12}$$

The two criteria for a matrix to be special unitary are [Lee and Pottier, 2009, p. 38-39]:

$$(1)\ |\boldsymbol{U}| = +1 \qquad (2)\ \boldsymbol{U}^{-1} = \boldsymbol{U}^{\star T}$$

That is, the determinant ($|\cdot|$) must be equal to one, and the inverse of the special unitary matrix must be equal to the conjugate transpose. The transformation matrix above does not satisfy the first criterion, since the determinant is not equal to one, but $-j$. Hence, the power will not be conserved when performing a basis change. Thus, an alternative transformation is used that is special unitary. This is based on using two orthogonal

basis vectors of the form $L, L_\perp$, where L denotes the left-circular basis vector, and $L_\perp$ denotes a basis vector orthogonal to L [Lee and Pottier, 2009, p. 41-42]. The basis vector $L_\perp$ corresponds to the right-circular polarization basis vector. The difference between the left orthogonal and the right-circular basis is the phase difference [Lee and Pottier, 2009, p. 41]. The special unitary matrix in the $\{L, L_\perp\}$ basis space is:

$$\boldsymbol{U}_{SU} = \frac{1}{\sqrt{2}} \begin{bmatrix} 1 & j \\ j & 1 \end{bmatrix} \tag{5.13}$$

The general formula for transforming from one basis to another is [Cloude, 2010, p. 55-56]:

$$\boldsymbol{Y} = \boldsymbol{U}_{SU}\, \boldsymbol{X}\, \boldsymbol{U}_{SU}^{\star T} \tag{5.14}$$

where $\boldsymbol{X}$ is the scattering matrix obtained from a fully polarized linear basis system, and $\boldsymbol{Y}$ is the scattering matrix obtained from the fully polarized circular basis system. Inserting for $\boldsymbol{U}_{SU}$, $\boldsymbol{S}_{\text{circular}}$, and the scattering matrix from a quad-pol system, $\boldsymbol{S}$, yields [Cloude, 2010, p. 56]:

$$\begin{aligned} \boldsymbol{S}_{\text{circular}} &= \begin{bmatrix} S_{LL} & S_{LR} \\ S_{RL} & S_{RR} \end{bmatrix} = \frac{1}{\sqrt{2}} \begin{bmatrix} 1 & j \\ j & 1 \end{bmatrix} \begin{bmatrix} S_{HH} & S_{HV} \\ S_{VH} & S_{VV} \end{bmatrix} \frac{1}{\sqrt{2}} \begin{bmatrix} 1 & j \\ j & 1 \end{bmatrix} \\ &= \frac{1}{2} \begin{bmatrix} S_{HH} - S_{VV} + 2jS_{HV} & j(S_{HH} + S_{VV}) \\ j(S_{HH} + S_{VV}) & S_{VV} - S_{HH} + 2jS_{HV} \end{bmatrix} \end{aligned} \tag{5.15}$$

As can be observed from equations 5.9, 5.10, and 5.15, all the scattering coefficients in the new representations contain a blend of co- and cross-pol terms, as defined with respect to the linear basis.

5.1.2 Compact polarimetric covariance matrix

The sample covariance matrix for the compact-pol modes is given as the averaged Hermitian outer product of the target vectors. Equations 5.16, 5.17, and 5.18 show the sample covariance matrix for $\frac{\pi}{4}$-pol, hybrid-pol, and DCP mode with right-circular

polarization at the transmitter. Note that reciprocity is assumed.

$$\begin{aligned} C_{\frac{\pi}{4}} = \langle \vec{k}_{\frac{\pi}{4}} \vec{k}^{\star T}_{\frac{\pi}{4}} \rangle &= \frac{1}{2}\begin{bmatrix} \langle |S_{HH}|^2 \rangle & \langle S_{HH} S^{\star}_{VV} \rangle \\ \langle S_{VV} S^{\star}_{HH} \rangle & \langle |S_{VV}|^2 \rangle \end{bmatrix} + \frac{\langle |S_{HV}|^2 \rangle}{2}\begin{bmatrix} 1 & 1 \\ 1 & 1 \end{bmatrix} \\ &+ \frac{1}{2}\begin{bmatrix} 2\Re(\langle S_{HH} S^{\star}_{HV} \rangle) & \langle S_{HH} S^{\star}_{HV} \rangle + \langle S_{HV} S^{\star}_{VV} \rangle \\ \langle S^{\star}_{HH} S_{HV} \rangle + \langle S_{VV} S^{\star}_{HV} \rangle & 2\Re(\langle S_{VV} S^{\star}_{HV} \rangle) \end{bmatrix} \end{aligned} \tag{5.16}$$

$$\begin{aligned} C^{LC/RC}_{\text{Hybrid}} = \langle \vec{k}_{LC/RC} \vec{k}^{\star T}_{LC/RC} \rangle &= \frac{1}{2}\begin{bmatrix} \langle |S_{HH}|^2 \rangle & \mp j\langle S_{HH} S^{\star}_{VV} \rangle \\ \pm j\langle S_{VV} S^{\star}_{HH} \rangle & \langle |S_{VV}|^2 \rangle \end{bmatrix} \\ &+ \frac{\langle |S_{HV}|^2 \rangle}{2}\begin{bmatrix} 1 & \pm j \\ j & 1 \end{bmatrix} \\ &+ \frac{1}{2}\begin{bmatrix} \pm 2\Im(\langle S_{HH} S^{\star}_{HV} \rangle) & \langle S_{HH} S^{\star}_{HV} \rangle + \langle S_{HV} S^{\star}_{VV} \rangle \\ \langle S^{\star}_{HH} S_{HV} \rangle + \langle S_{VV} S^{\star}_{HV} \rangle & \mp 2\Im(\langle S_{VV} S^{\star}_{HV} \rangle) \end{bmatrix} \end{aligned} \tag{5.17}$$

$$\begin{aligned} C^{RC}_{DCP} &= \langle \vec{k}_{DCP} \vec{k}^{\star T}_{DCP} \rangle \\ &= \frac{1}{4}\begin{bmatrix} \langle |S_{VV} - S_{HH}|^2 \rangle & \langle -j(S_{VV} - S_{HH})(S_{HH} + S_{VV})^{\star} \rangle \\ \langle j(S_{VV} + S_{HH})(S_{VV} - S_{HH})^{\star} \rangle & \langle |S_{VV} + S_{HH}|^2 \rangle \end{bmatrix} \\ &+ \frac{1}{4}\begin{bmatrix} 4\langle |S_{HV}|^2 \rangle & 0 \\ 0 & 0 \end{bmatrix} \\ &+ \frac{1}{4}\begin{bmatrix} 4\Im(\langle (S_{VV} - S_{HH}) S^{\star}_{HV} \rangle) & 2\langle S_{HV}(S_{HH} + S_{VV})^{\star} \rangle \\ 2\langle (S_{HH} + S_{VV}) S^{\star}_{HV} \rangle & 0 \end{bmatrix} \end{aligned} \tag{5.18}$$

Here, $\Im(\cdot)$ and $\Re(\cdot)$ denote the imaginary and real parts respectively. The derivation of the sample covariance matrices is shown in Appendix A. The first matrix in equations 5.16, 5.17, and 5.18 contains only co-pol elements, while the second matrix contains only cross-pol elements. The last matrix contains a blend of both co- and cross-pol elements.

The sample covariance matrix can be used to evaluate the scattering properties of the surface. As discussed in the introductory part of this chapter, a quad-pol system gives complete description of the backscattering properties. The elements in the sample compact-pol covariance matrices can be obtained from the quad-pol covariance matrix (see section 2.2.2). Hence, one can see that the polarimetric information is somehow

compacted inside the compact-pol data.

Unfortunately, real compact-pol data were not available for this work (only quad-pol data from RADARSAT-2). Therefore, simulated compact-pol data were created from quad-pol data based on the above equations. Hence, the *noise-level*[1], resolution, and swath width will be the same for the quad-pol as for the simulated compact-pol data.

5.1.3 Some physical properties of the compact-pol

The geometry of a given target has a large impact on the total power that is backscattered. The total amount of power depends on the polarization of the incoming electric field. If the target is dominated by a horizontal structure, the power will be higher if a horizontally polarized wave is transmitted. If the target is dominated by a vertical structure, higher power is detected for vertically polarized wave. The transmitted wave will thus have "favorite" structures that provides maximum response [Cloude, 2010, p. 60-61]. This might cause some interpretation problems when evaluating a group of targets with different geometrical structure. If the transmitted wave is diagonally polarized, then a new "favorite" structure will take over, and the diagonally structured targets will generate the maximum response of the backscattered field. If the transmitted field is circularly polarized, "favorite" structures are no longer present, and the incoming field is agnostic to the orientation of the target in the plane of polarization (the orientation about the radar's line of sight) [Denbina, 2014]. This means that the amount of backscattered power does not depend on the orientation of the target, which is not the case for the horizontally, vertically, and diagonally polarized field. The independence of the orientation angle is one of the benefits of the hybrid-pol mode over the $\frac{\pi}{4}$-pol mode. This concept was proven in [Denbina, 2014], where the author used canonical scatterers to evaluate the orientation of the target and the polarization of the incoming field.

Effects from the atmosphere will also put their fingerprint on the transmitted signal. As the frequency of the wave falls into the microwave region, effects from clouds and aerosols are neglected (although tropospheric effects might influence SAR images acquired in X-band [Danklmayer et al., 2009]). However, the ionosphere may affect the incoming wave, and this is most critical in the L-band or at longer wavelengths [Souyris et al., 2005]. This effect is known as Faraday rotation. The Faraday rotation must be corrected for prior to evaluating the data, as it may cause additional noise. This effect has varying impact on the different compact-pol modes. The hybrid-pol mode will have the same polarization after passing through the ionosphere. It is thus independent of the Faraday rotation [Dubois-Fernandez et al., 2008a]. The atmospheric effect is only

1. Noise level, also referred to as *signal-to-noise ratio*, is the level of noise that is added to the receiving signal. It depends on the quality of the antenna, transmitted power, antenna gain, geometry of the target and the viewing, platform velocity, bandwidth, incident angle, system losses, and the target reflectivity [Wackerman, 1992].

limited to an absolute phase delay [Souyris et al., 2007], and will have no impact on the circular polarization. Hence, circularly polarized transmitted waves, will still be a circularly polarized waves when reaching the surface. In case of a $\frac{\pi}{4}$-pol mode, the transmitted wave will be affected by the atmosphere, and when the wave reaches the surface, the wave may no longer have a polarization of 45 degrees. This will cause limitations when using the $\frac{\pi}{4}$-pol mode in L-band.

5.2 Compact polarimetric approaches

Several different approaches have been suggested to study compact-pol data, and it is possible to divide these into three groups. The first group tries to reconstruct a pseudo quad-pol covariance matrix from the compact-pol data. Existing full-polarimetric methods can then be applied onto the pseudo quad-pol covariance matrix for further analysis, such as the three- and four-component scattering decomposition models. This group of methods has received most of the attention throughout this thesis, and several new approaches are presented in chapter 6. This group is illustrated as the left-most path in Figure 5.4. The second group of methods contains decompositions applied directly on the compact-pol data, such as the H/α-, $DoP - \delta$-, and $DoP - \chi$- decompositions (see right-most path in Figure 5.4). As in the quad-pol case, decomposition methods aim to decompose the data into multiple scattering types, such as surface, double bounce, and volume scattering. The H/α, $DoP - \delta$, and $DoP - \chi$ are methods for decomposing the compact-pol data through the Stokes vector. These methods were first suggested in [Cloude et al., 2012, Raney et al., 2012]. The third group (centre box in Figure 5.4) uses the compact-pol parameters available for interpretation and classification purposes directly, in applications such as oil-spill detection ([Shirvany et al., 2012]) or soil moisture retrieval ([Truong-Loi et al., 2009b]). This figure also provides an overview of the compact-pol theory which will be discussed throughout this thesis.

The upcoming sections present some polarimetric features and how these can be related to the compact-pol data. Quad-pol features have been thoroughly analyzed for sea ice covered SAR scenes, but polarimetric features for the compact-pol case have not. Therefore, the upcoming sections are devoted to finding selected compact polarimetric features, and also attempting to find an interpretation of these in the context of sea ice. The discussion in the next section covers the two boxes to the right in row two in Figure 5.4, while chapter 6 covers the left-most path.

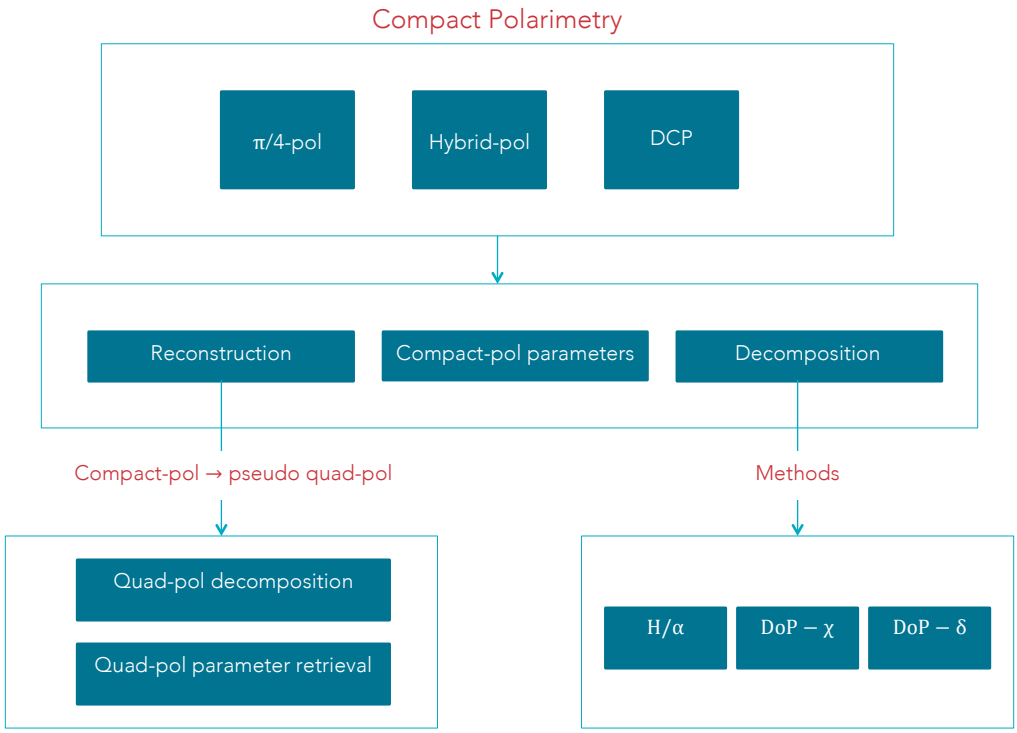

Figure 5.4: Compact polarimetry steps towards reconstruction or decomposition.

5.3 Retrieval of Compact polarimetric parameters

There are multiple polarimetric features that can be extracted from SAR data that are usable in sea ice analysis. Most of the commonly used quad-pol features discussed in the literature are listed in Table 5.1, with the corresponding nomenclature and formula. The cells above the first thick line contain features retrieved from the intensities and the correlation coefficients (the off-diagonal elements in the covariance matrix). The next table section contains eigenvalue and eigenvector parameters, while the last section shows the incoherent parameters, i.e.: parameters from the Stokes vector and combinations of these. The polarimetric features listed in Table 5.1 can help to provide an understanding of the backscattering properties for varying sea ice and snow covered areas. Most of these parameters are affected by sea ice thickness, salinity, water content, age, roughness, and composition. Most features retrieved from quad-pol systems have been thoroughly studied, such as in [Dierking, 2013, Moen, 2014, Onstott and Shuchman, 2004]. The corresponding compact-pol features have only been investigated to some extent in the context of sea ice [Geldsetzer et al., 2014, Dabboor and Geldsetzer, 2014]. The upcoming sections will highlight these polarimetric features computed from the

compact-pol data, and how these are used in context of sea ice.

Polarimetric feature	Name
$\langle \lvert S_{HH} \rvert^2 \rangle$	Co-polarization (HH-intensity)
$\langle \lvert S_{VV} \rvert^2 \rangle$	Co-polarization (VV-intensity)
$\langle \lvert S_{HV} \rvert^2 \rangle$	Cross-polarization (HV-intensity)
$\langle S_{HH} S_{VV}^\star \rangle$, $\langle S_{HV} S_{VV}^\star \rangle$, $\langle S_{HV} S_{HH}^\star \rangle$	Correlation coefficients
$\mathrm{SPAN}(\boldsymbol{C}) = \mathrm{Tr}(\boldsymbol{C})$	SPAN (total power)
$R_{VV/HH} = \frac{\langle \lvert S_{VV} \rvert^2 \rangle}{\langle \lvert S_{HH} \rvert^2 \rangle}$	Co-polarization ratio
$R_{HV} = \frac{\langle \lvert S_{HH} \rvert^2 \rangle + \langle \lvert S_{VV} \rvert^2 \rangle}{\langle \lvert S_{HV} \rvert^2 \rangle + \langle \lvert S_{VH} \rvert^2 \rangle}$	Cross-polarization ratio
$\rho_{HHVV} = \frac{\langle S_{HH} S_{VV}^\star \rangle}{\sqrt{\langle \lvert S_{HH} \rvert^2 \rangle \langle \lvert S_{VV} \rvert^2 \rangle}}$	Co-polarization correlation coefficient
$\mu = 2 \frac{\Re \langle S_{HH} S_{VV}^\star \rangle - \langle \lvert S_{HV} \rvert^2 \rangle}{\langle \lvert S_{HH} \rvert^2 \rangle + 2\langle \lvert S_{HV} \rvert^2 \rangle + \langle \lvert S_{VV} \rvert^2 \rangle}$	Conformity coefficient
$\mathrm{H} = -\sum_{i=1}^{d} P_i \log_d P_i$ d = number of dimensions	Entropy
$\mathrm{PF} = 1 - \frac{3\lambda_3}{\lambda_1 + \lambda_2 + \lambda_3}$	Polarization Fraction
$\mathrm{PH} = \frac{\min(\lambda_1, \lambda_2, \lambda_3)}{\max(\lambda_1, \lambda_2, \lambda_3)}$	Pedestal Height
$\mathrm{PA} = \frac{(\lambda_1 - \lambda_3) - (\lambda_2 - \lambda_3)}{(\lambda_1 - \lambda_3) + (\lambda_2 - \lambda_3)}$	Polarization Asymmetry
$q_0(\text{total power}), q_1, q_2, q_3$	Stokes vector
$\mu_C = \frac{q_2 - q_3}{q_2 + q_3}$	Circular polarization ratio
$\mathrm{DoP} = \frac{(q_1^2 + q_2^2 + q_3^2)^{\frac{1}{2}}}{q_0}$	Degree of polarization
$\sin 2\chi = -\frac{q_3}{DoP\ q_1}$	Ellipticity/circularity

Table 5.1: Selected polarization features from the literature.

5.3.1 Intensities

The intensities, also known as the backscattering coefficients, are given by the absolute value raised to the power of two for each polarization channel, i.e. $I_{XY} = \langle \lvert S_{XY} \rvert^2 \rangle$. Here, X denotes the polarization at the transmitter, and Y the polarization at the receiver. The backscattered *HH-intensity*, $X = Y = H$, is preferred over the *VV-intensity* for monitoring of sea ice, because ocean clutter is better suppressed with HH [Dierking,

2013]. This means that the HH-intensity will be better for ice-water discrimination. The backscattered intensities for a given surface element is affected by the incident angle of the incoming field. The HH-intensity will decrease faster with increasing incidence angle for smooth surfaces compared to the VV-intensity [Olsen et al., 1999]. Also, the wind conditions will affect the backscatter. A water surface will, in general, have higher backscatter in co-pol channels at higher wind speed, whereas it remains relatively dark in the cross-pol channels [Dierking and Pedersen, 2013].

The different polarization intensities have proven to be useful for discrimination of different sea ice types. For example, the cross-pol intensity (I_{HV}, I_{VH}) has been used to discriminate between level and deformed ice [Dierking, 2013]. This is because deformed sea ice result in strong depolarization effects [Dierking, 2013]. Also, discrimination between thin ice with rough surface and open water can be achieved better with the cross-pol compared to the co-pol intensities [Dierking, 2013]. Combinations of co- and cross-pol intensities have also been applied for sea ice discriminations, like discrimination of different types of multi-year and first-year ice [Geldsetzer and Yackel, 2009, Moen, 2014].

For a compact-pol system the intensities change with the mode. The hybrid-pol mode, with either right- or left-circular polarization at the transmitter and horizontal and vertical polarizations at the receiver, produces intensities on the form: $I_{RH} = \langle |S_{RH}|^2 \rangle$ and $I_{RV} = \langle |S_{RV}|^2 \rangle$. These two intensities contain information about both the co- and cross-pol elements. The *RH-intensity* has proven to be useful for discrimination between first-year ice, multi-year ice, and open water [Dabboor and Geldsetzer, 2014]. The vertical polarization can be found in the *RV-intensity*, and the horizontal polarization in RH-intensity. It is therefore expected that ocean clutter will be better suppressed in the RH-intensity. The cross-pol intensity is not accessible from the compact-pol intensities, and this might be problematic when attempting to distinguish between open water, level-, and deformed ice. The HH-, VV-, RH-, RV-, and RL-intensities are all dominated by surface scattering when compared to the other features in Table 5.1 [Geldsetzer et al., 2014].

Figure 5.5 shows box plots of the intensity range for the different combinations of polarizations. The data used for these box plots is from May 10th 2013 (see chapter 4), and covers sea ice from Storfjorden. The three boxes to the left show the intensities obtained from a quad-pol system. The remaining boxes are obtained from simulated compact-pol data. Note that all the compact-pol boxes are shifted down compared to the co-pol intensity boxes. This is due to the 3db power loss in the compact-pol system. One can also observe that the $\frac{\pi}{4}V$*-intensity* and RV-intensity are aligned, as for the $\frac{\pi}{4}H$*-intensity* and RH-intensity. In section 5.1.2 the compact-pol covariance matrices for the hybrid-pol and $\frac{\pi}{4}$-pol modes were found as a function of the quad-pol elements. The difference between the two compact-pol intensities is because of the last matrix in the compact-pol covariance matrix containing correlations between co- and cross-pol elements. In fact, the $\frac{\pi}{4}$-pol covariance matrix contains the real part of the co- and

cross-pol elements in the last matrix, while the hybrid-pol contains the imaginary part. If reflection symmetry is assumed, the elements in the last matrix becomes zero, and the diagonal intensities in the sample covariance matrix for $\frac{\pi}{4}$- and hybrid-pol are equal. From the box plots it is possible to observe that the real and imaginary parts of the co- and cross-pol elements are either equal, small compared to the co-pol intensities, or close to zero.

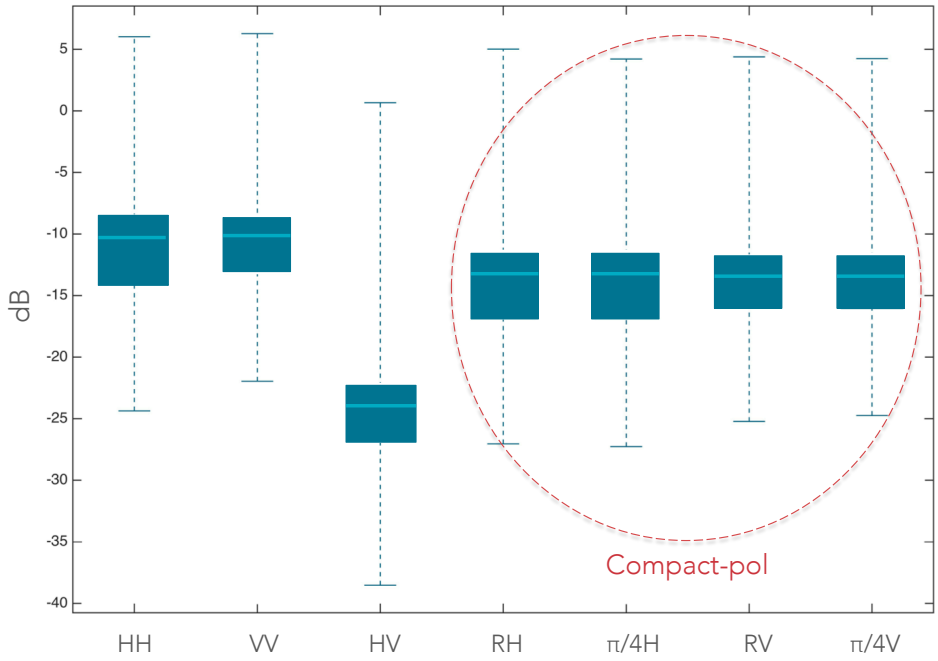

Figure 5.5: Intensity range in decibel for HH-, VV-, HV-, RH-, RV-, $\frac{\pi}{4}$H-, and $\frac{\pi}{4}$V-intensity illustrated in a box plot. The light blue line inside all the boxes denotes the median in the data. 50 % of all the data points falls within the dark blue box, while the remaining data points are spread along the dashed line (25 % on both sides). The data used in this box plot are from the May 10th scene.

A reconstruction must be performed to enable approximation of the co- and cross-pol intensities from the compact-pol data. As can be seen, the intensity is relatively low for the cross-pol, which might cause some difficulties when attempting to reconstruct the cross-pol intensity. This will be discussed further in chapter 6.

The total power can be calculated as the SPAN of the sample covariance matrix (see chapter 2) [Lee and Pottier, 2009, p. 64]. Gill and Yackel highlighted that the total power will increase with increasing surface roughness at all radar incidence angles [Gill and Yackel, 2013]. Furthermore, the total power from the quad-pol covariance matrix can easily be derived from the compact-pol covariance matrix if reflection symmetry is

assumed. This is demonstrated in chapter 6.

5.3.2 Phase difference

The benefit of polarimetric radar systems is the additional information about the phase difference. This information originates from the fact that the waves are received coherently. We say that the transmitted pulses are phase-coded [Cumming and Wong, 2005]. The phase difference is dependent on the dielectric constant and the scattering type [Drinkwater et al., 1992, Onstott and Shuchman, 2004]. The phase difference between the horizontally and vertically polarized wave at the receiver can aid in separating open water from sea ice [Onstott and Shuchman, 2004]. This parameter has also proven to be related to both salinity, incident angle, and level of deformation [Drinkwater et al., 1992, Gill and Yackel, 2013, Moen, 2014].

The co-pol phase difference is not directly accessible in compact-pol data. The works referred above state that the phase difference is an important parameter for sea ice analysis, and losing this information may therefore be critical for the compact-pol case. The phase difference between the horizontal and vertical polarizations (obtained from the quad-pol system) is defined as:

$$\phi_{HH-VV} = \operatorname{atan}\left(\frac{\Im(\langle S_{HH}S_{VV}^{\star}\rangle)}{\Re(\langle S_{HH}S_{VV}^{\star}\rangle)}\right) \tag{5.19}$$

This is also known as the co-pol phase difference. The circular-pol phase difference (obtained from the hybrid-pol system with right-circular transmits) is defined as:

$$\phi_{RH-RV} = \operatorname{atan}\left(\frac{\Im(\langle S_{RH}S_{RV}^{\star}\rangle)}{\Re(\langle S_{RH}S_{RV}^{\star}\rangle)}\right) \tag{5.20}$$

The $\frac{\pi}{4}$-pol phase difference (obtained from the $\frac{\pi}{4}$-pol system) is defined as:

$$\phi_{\frac{\pi}{4}H-\frac{\pi}{4}V} = \operatorname{atan}\left(\frac{\Im(\langle S_{\frac{\pi}{4}H}S_{\frac{\pi}{4}V}^{\star}\rangle)}{\Re(\langle S_{\frac{\pi}{4}H}S_{\frac{\pi}{4}V}^{\star}\rangle)}\right) \tag{5.21}$$

Finally, the double circular-pol phase difference (obtained from the DCP system)

is:

$$\phi_{RR-RL} = \text{atan}\left(\frac{\Im(\langle S_{RR}S_{RL}^{\star}\rangle)}{\Re(\langle S_{RR}S_{RL}^{\star}\rangle)}\right) \tag{5.22}$$

The four phase difference features are illustrated in Figure 5.6 for the co-pol phase, ϕ_{HH-VV} (green dashed line), circular-pol phase ϕ_{RH-RV} (red line), $\frac{\pi}{4}$-pol phase $\phi_{\frac{\pi}{4}H-\frac{\pi}{4}V}$ (blue line), and double circular-pol phase ϕ_{RR-RL} (purple line). The yellow dashed line denotes the circular-pol phase difference minus 90° degrees. The highest similarity to the co-pol phase difference is achieved by the $\frac{\pi}{4}$-pol phase. The double circular-pol phase difference is completely different than the co-pol phase difference. One can also observe that the circular-pol phase difference with −90° shift is very similar to the co-pol phase difference. Hence, by subtracting 90° from the circular-pol phase, one may obtain the same discrimination properties for sea ice as for the co-pol phase difference. This similarity can be shown mathematically. Considering hybrid-pol mode with right-circular polarization at the transmitter, one gets the following circular-pol phase difference:

$$\phi_{RH-RV} = \angle\langle S_{RH}S_{RV}^{\star}\rangle = \angle\left(\frac{j}{2}\langle S_{HH}S_{VV}^{\star}\rangle - \frac{j}{2}\langle|S_{HH}|^2\rangle + \frac{1}{2}\left(\langle S_{HH}S_{HV}^{\star}\rangle + \langle S_{HV}S_{VV}^{\star}\rangle\right)\right) \tag{5.23}$$

The reflection symmetry assumption yields:

$$\phi_{RH-RV} = \angle\left(\frac{j}{2}\langle S_{HH}S_{VV}^{\star}\rangle - \frac{j}{2}\langle|S_{HV}|^2\rangle\right)$$

If the assumption $\langle|S_{HV}|^2\rangle << \langle S_{HH}S_{VV}^{\star}\rangle$ is made as well, we can approximate:

$$\phi_{RH-RV} \cong \text{atan}\left(\frac{\Im(\langle S_{RH}S_{RV}^{\star}\rangle)}{\Re(\langle S_{RH}S_{RV}^{\star}\rangle)}\right) = \text{atan}\left(-\frac{\Re(\langle S_{HH}S_{VV}^{\star}\rangle)}{\Im(\langle S_{HH}S_{VV}^{\star}\rangle)}\right)$$

This assumption may be reasonable for sea ice, since the co-pol coefficients have higher response than the cross-pol coefficients (see Figure 5.5).

One can observe a relation between the circular-pol and co-pol phase difference (in equation 5.19) through the trigonometric identity:

$$\text{atan}(\theta + \frac{\pi}{2}) = -\text{cot}(\theta) = -\frac{1}{\tan\theta} \tag{5.24}$$

So the relationship becomes:

$$\tan(\phi_{RH-RV}) \cong -\frac{\Re(\langle S_{HH}S_{VV}^{\star}\rangle)}{\Im(\langle S_{HH}S_{VV}^{\star}\rangle)} \implies \frac{-1}{\tan(\phi_{RH-RV})} \cong \frac{\Im(\langle S_{HH}S_{VV}^{\star}\rangle)}{\Re(\langle S_{HH}S_{VV}^{\star}\rangle)}$$

$$\frac{\Im(\langle S_{HH}S_{VV}^{\star}\rangle)}{\Re(\langle S_{HH}S_{VV}^{\star}\rangle)} = \tan(\phi_{HH-VV})$$

$$\implies \frac{-1}{\tan(\phi_{RH-RV})} = \tan\left(\phi_{RH-RV} + \frac{\pi}{2}\right) \cong \tan(\phi_{HH-VV})$$

$$\phi_{RH-RV} + \frac{\pi}{2} \cong \phi_{HH-VV} \implies \underline{\underline{\phi_{RH-RV} \cong \phi_{HH-VV} - \frac{\pi}{2}}}$$

From Figure 5.6 and the above equations we have proven the similarity between the co- and circular-pol phase difference for the hybrid-pol mode. Some classification approaches for sea ice include the co-pol phase difference [Moen, 2014], and it would therefore be interesting to investigate the extension with the circular-pol phase or the $\frac{\pi}{4}$-pol phase difference in a similar classification approach.

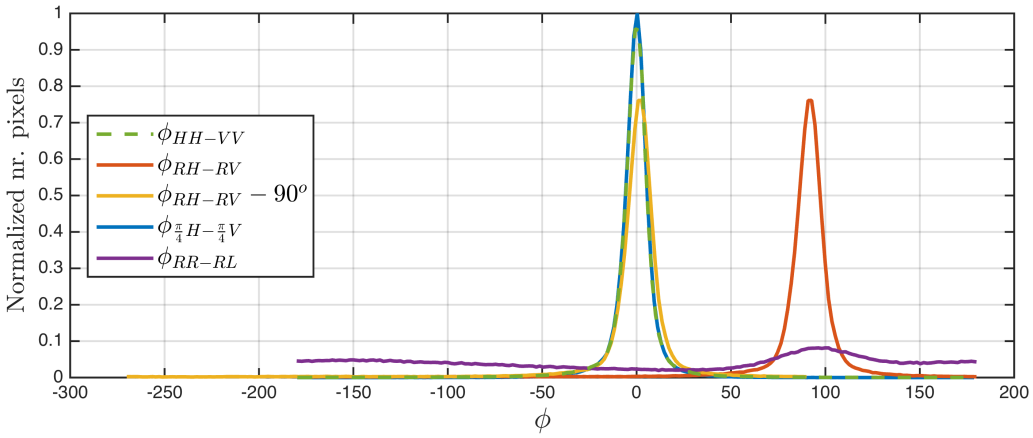

Figure 5.6: Histogram of the phase difference: blue = circular-pol phase difference under reflection symmetry assumption, red dashed line = true circular-pol phase difference, purple dashed line = true circular-pol phase difference with $-90°$ shift, and yellow = co-pol phase difference. The data used are from the May 10th scene, and covers sea ice, open water, and landfast ice from Storfjorden (see chapter 4).

5.3.3 Co-polarization ratio

The co-polarization ratio (co-pol ratio) is defined as [Taylor and Boerner, 2007]:

$$R_{VV/HH} = \frac{\langle|S_{VV}|^2\rangle}{\langle|S_{HH}|^2\rangle} \tag{5.25}$$

This ratio has proven to be sensitive to the dielectric constant of a given target [Moen, 2014]. This ratio is also sensitive to polarization differences in resonant Bragg scattering

[Geldsetzer et al., 2014]. Sea ice and water have very different dielectric constants, approximately 3 for sea ice and 80 for water [Elachi and van Zyl, 2006, p. 172], and can therefore aid in discriminating between the two [Scheuchl et al., 2001].

As can be observed from the co-pol ratio, both the HH and VV intensities are needed. These are not directly accessible in compact-pol data. Other ratios can be considered as replacements, for example the ratios between the intensities for each polarization channel. For the hybrid-pol mode with right-circularly polarized transmits, this ratio can be formulated as follows [Dabboor and Geldsetzer, 2014]:

$$R_{RV/RH} = \frac{\langle |S_{RV}|^2 \rangle}{\langle |S_{RH}|^2 \rangle} \overset{\text{Reflection symmetry}}{=} \frac{\langle |S_{VV}|^2 \rangle + \langle |S_{HV}|^2 \rangle}{\langle |S_{HH}|^2 \rangle + \langle |S_{HV}|^2 \rangle} \tag{5.26}$$

The $\frac{\pi}{4}$-pol mode has the following ratio:

$$R_{\frac{\pi}{4}V/\frac{\pi}{4}H} = \frac{\langle |S_{\frac{\pi}{4}V}|^2 \rangle}{\langle |S_{\frac{\pi}{4}H}|^2 \rangle} \overset{\text{Reflection symmetry}}{=} \frac{\langle |S_{VV}|^2 \rangle + \langle |S_{HV}|^2 \rangle}{\langle |S_{HH}|^2 \rangle + \langle |S_{HV}|^2 \rangle} \tag{5.27}$$

To analyze the similarity between the three ratios above, a line segment from the SAR images acquired on the March 13th and May 10th 2013 is visualized as a profile (in Figure 5.7). These line segments contain leads and deformed sea ice (March 13th) as well as glacier/landfast ice, thin sea ice, and open water (May 10th) (see chapter 4).

As expected, the co-pol ratio for pixels covering open water is high due to the higher dielectric constant. This is also true for the compact-pol ratios. The greatest similarity is observed for the compact- and co-pol ratios corresponding to open water pixels. This is because the cross-pol intensity is close to zero for open water. For the glacier/landfast ice regions, the hybrid-pol ratio has the highest deviation from the co-pol ratio, while the $\frac{\pi}{4}$-pol ratio is more similar. This is also the case for pixels covering thin sea ice. For pixels covering leads and deformed ice the difference between the co- and compact-pol ratios is large, especially for leads. Clearly, the compact-pol ratio can be used to discriminate open water from thin sea ice. This might also be possible for leads and deformed ice.

The difference in the ratios across the two scenes might be affected by the incident angle. The angle ranges across the profile from 29.2069° (glacier/landfast ice) to 30.9340° (open water), and 46.1° (leads) to 47.3° (deformed ice). As can be observed, both the compact-pol ratios can be used to distinguish between thin first-year ice and open water. However, problems might occur when attempting to distinguish between glacier ice and thin first-year ice using any of the three ratios.

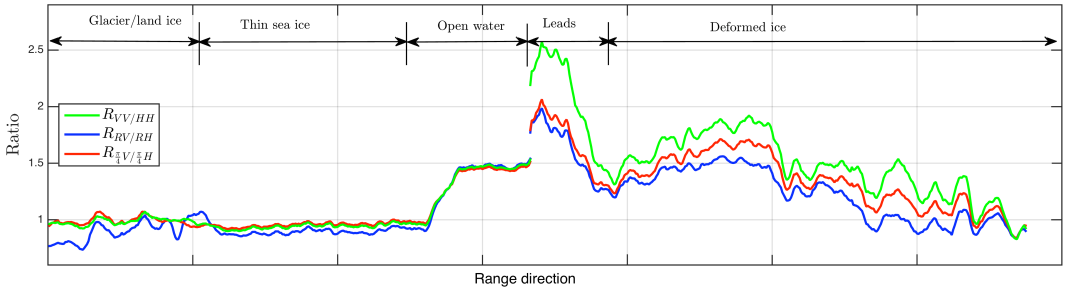

Figure 5.7: Line segment from Storfjorden SAR images (March 13th and May 10th 2013) visualised as a profile with the corresponding co-pol ratio values. The green line denotes the co-pol ratio, the blue line denotes the hybrid-pol ratio, and the red line denotes the $\frac{\pi}{4}$-pol ratio.

5.3.4 Cross-polarization ratio

The next ratio to be evaluated is the cross-pol ratio. This is defined here as:

$$R_{HV} = \frac{\langle|S_{HH}|^2\rangle + \langle|S_{VV}|^2\rangle}{\langle|S_{HV}|^2\rangle + \langle|S_{VH}|^2\rangle} \overset{\text{Reciprocity}}{=} \frac{\langle|S_{HH}|^2\rangle + \langle|S_{VV}|^2\rangle}{2\langle|S_{HV}|^2\rangle} \tag{5.28}$$

This ratio can be used to discriminate between different ice types, such as multi-year and first-year ice, and to determine the ice age [Onstott and Shuchman, 2004]. This ratio is also sensitive to depolarization effects [Geldsetzer et al., 2014].

Polarization channels needed in this ratio are HV, VV, and HH, which are all provided by quad-pol SAR systems. It is not possible to find this ratio in the compact-pol case, and again some replacement ratio must be found. The cross-pol ratio for compact-pol can be estimated if azimuthal symmetry is assumed. For the $\frac{\pi}{4}$-pol mode the double bounce power (from the Pauli basis) can be estimated directly, while the surface scattering power (also from the Pauli basis) can be estimated from the hybrid-pol mode. As a result of assuming azimuthal symmetry (see section 2.2.2), we can set the double bounce power equal to the cross-pol power, and further derive an estimation of the cross-pol ratio. This is performed in the following manner for the hybrid-pol mode with right-circularly polarized transmits:

$$\hat{R}_{HV}^{\text{Hybrid}} = \frac{\langle|S_{HH}|^2\rangle + \langle|S_{VV}|^2\rangle}{2\langle|S_{HV}|^2\rangle} \overset{P_{Total}=\langle|S_{HH}|^2\rangle+\langle|S_{VV}|^2\rangle+2\langle|S_{HV}|^2\rangle}{=} \frac{P_{Total} - 2\langle|S_{HV}|^2\rangle}{2\langle|S_{HV}|^2\rangle}$$
$$\overset{P_D=P_V=1/2\langle|S_{HH}-S_{VV}|^2\rangle=2\langle|S_{HV}|^2\rangle}{=} \frac{P_{Total} - P_D}{P_D}$$

where

$$P_{Total} = 2\langle|S_{RH}|^2\rangle + 2\langle|S_{RV}|^2\rangle$$

$$P_D = P_{Total} - P_S - 2\langle|S_{HV}|^2\rangle \overset{P_D=2\langle|S_{HV}|^2\rangle}{\Longrightarrow} 2P_D = P_{Total} - P_S$$

The same line segment from the SAR images acquired on March 13th and May 10th 2013 is visualized as a profile (see Figure 5.8) for the true cross-pol ratio and the estimated cross-pol ratios from the compact-pol data. The similarity between the estimated cross-pol ratios and the true ratio is large across pixels covering glacier/landfast ice, and the dissimilarity increase as the cross-pol ratio increases. The similarity between the cross-pol and estimated cross-pol (hybrid) ratio is also large for leads and deformed ice. High cross-pol ratio can be observed for open water and this is because of the low cross-pol power, which indicates high depolarization. The estimated cross-pol ratio (blue line) from the hybrid-pol data is closer to the true one (green line). Overall, the estimated cross-pol ratio deviates from the true ratio, and information concerning these parameters might be "lost" in the compact-pol data, unless a proper reconstruction of the cross-pol intensity is performed.

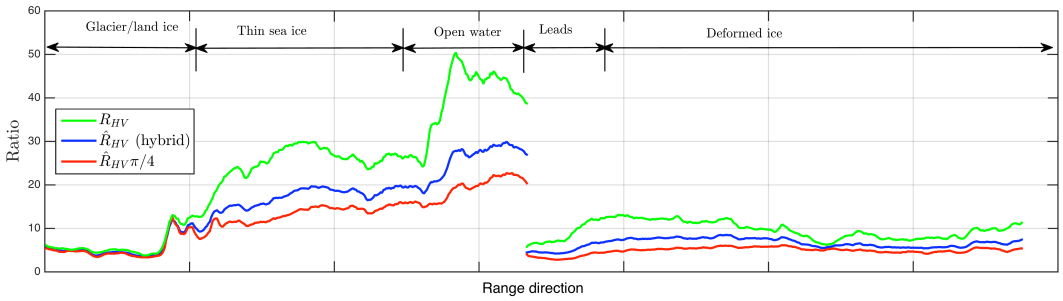

Figure 5.8: Line segment from Storfjorden SAR images (March 13th and May 10th 2013) visualised as a profile with the corresponding cross-pol ratio values. The green line denotes the cross-pol ratio, the blue line denotes the estimated cross-pol ratio from hybrid-pol data, and the red line denotes the estimated cross-pol ratio from $\frac{\pi}{4}$-pol data.

5.3.5 Co-polarization correlation coefficient

Polarizations needed to calculate the co-pol correlation coefficient are HH and VV, the cross-pol intensity is left out. This parameter is defined as [Taylor and Boerner, 2007]:

$$\rho_{HHVV} = \frac{\langle S_{HH}S_{VV}^{\star}\rangle}{\sqrt{\langle|S_{HH}|^2\rangle\langle|S_{VV}|^2\rangle}} \tag{5.29}$$

where $\langle S_{HH}S_{VV}^{\star}\rangle$ is a complex number, implying that ρ_{HHVV} is complex. Often, the absolute value is taken when using this parameter [Scheuchl et al., 2004, Moen, 2014]. This parameter is sensitive to incidence angle, salinity, and ice deformation [Drinkwater et al., 1992, Gill and Yackel, 2013]. The co-pol correlation coefficient can also be used to distinguish between first-year and multi-year ice. In [Drinkwater et al., 1992], the authors highlighted that at short wavelengths the co-pol correlation coefficient was high for first-year ice and low for multi-year ice.

This coefficient has also been used in a reconstruction method for a pseudo quad-pol covariance matrix from compact-pol data. This approach was first introduced in [Souyris et al., 2005], and has been tested by several researches, among others [Ainsworth et al., 2007, Boularbah et al., 2012]. This reconstruction approach is discussed in section 6.1.1.

It is possible to obtain an estimate of the co-pol correlation coefficient from the compact-pol data, but only if the cross-pol intensity is relatively low or small compared to the co-pol coefficients. For the hybrid-pol correlation coefficient this becomes [Salberg et al., 2014]:

$$\begin{aligned}\rho_{RHRV} &= \frac{-j\langle S_{RH}S_{RV}^{\star}\rangle}{\sqrt{\langle|S_{RR}|^2\rangle\langle|S_{RV}|^2\rangle}} \\ &\overset{\text{Reflection symmetry}}{=} \frac{-j/2(j\langle S_{HH}S_{VV}^{\star}\rangle - j\langle|S_{HV}|^2\rangle)}{\sqrt{1/2(\langle|S_{HH}|^2\rangle + \langle|S_{HV}|^2\rangle)1/2(\langle|S_{VV}|^2\rangle + \langle|S_{HV}|^2\rangle)}} \\ \rho_{RHRV} &\overset{\langle|S_{HV}|^2\rangle\approx 0}{=} \frac{\langle S_{HH}S_{VV}^{\star}\rangle}{\sqrt{\langle|S_{HH}|^2\rangle\langle|S_{VV}|^2\rangle}}\end{aligned} \tag{5.30}$$

Note that a similar equation can be derived for the $\frac{\pi}{4}$-pol mode. The hybrid-pol variant of this parameter was first suggested in [Salberg et al., 2014], where it was dubbed the *degree of coherence*, and used for oil-spill detection.

The results of the co-pol and compact-pol correlation coefficients are shown in Figure 5.9 for the same line segment as the previous figures in this chapter. The hybrid-pol correlation coefficient is less similar to the true co-pol correlation coefficient. The similarity between the hybrid- and co-pol correlation coefficient is highest for pixels covering open water and thin ice, and smallest for landfast ice, leads and deformed ice. The $\frac{\pi}{4}$-pol correlation coefficient is relatively close to the co-pol correlation coefficient. The hybrid-pol correlation coefficient has the same shape as the two other correlation coefficients, and can be scaled up in order to become more similar to the other two correlation coefficients. The glacier/landfast ice are rougher than the smooth ice, and one can observe that the correlation coefficient is different across this area compared

to the smooth ice. Based on the profile, the separation between open water and sea ice seems impossible for the three ratios, while separation might be possible for leads and deformed ice.

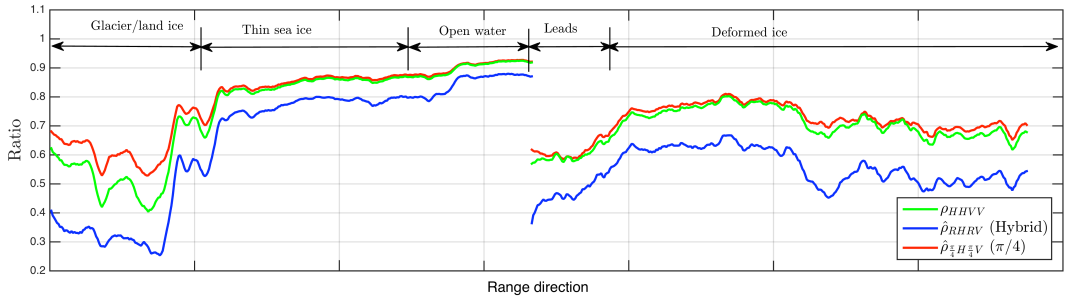

Figure 5.9: Line segment from Storfjorden SAR images (March 13th and May 10th 2013) visualised as a profile with the corresponding co-pol and compact-pol correlation coefficients. The green line denotes the co-pol correlation, the blue line denotes the hybrid-pol correlation, and the red line denotes the $\frac{\pi}{4}$-pol correlation coefficient.

5.3.6 Conformity coefficient

The conformity coefficient is defined under the reflection symmetry assumption as [Truong-Loi et al., 2009a]:

$$\mu = 2\frac{\Re\langle S_{HH}S_{VV}^{\star}\rangle - \langle|S_{HV}|^2\rangle}{\langle|S_{HH}|^2\rangle + 2\langle|S_{HV}|^2\rangle + \langle|S_{VV}|^2\rangle} = 2\frac{\Re\langle S_{HH}S_{VV}^{\star}\rangle - \langle|S_{HV}|^2\rangle}{P_{Total}} \tag{5.31}$$

The polarizations needed to calculate this parameter are HH, VV, and HV. The conformity coefficient is unfortunately not possible to calculate for the $\frac{\pi}{4}$-pol mode, but it is possible to find this parameter for the hybrid-pol case, which was first presented in [Truong-Loi et al., 2009a]. The conformity coefficient expressed in the hybrid-pol case can be formulated as follows:

$$\mu = -2\frac{\Re(j\langle S_{RH}S_{RV}\rangle)}{\langle|S_{RH}|^2\rangle + \langle|S_{RV}|^2\rangle} \tag{5.32}$$

Under the reflection symmetry assumption, the conformity coefficients are equal for both the hybrid- and quad-pol case. This parameter has been used to locate areas where surface, double bounce, or volume scattering are dominant within a scene [Truong-Loi et al., 2009a]. At longer wavelengths (approximately L-band) the Faraday-rotation (see section 5.1.3) can affect the signal. When transmitting circular pulses the effect of Faraday rotation can be neglected at these wavelengths, but this effect must be found

at the receiving signal from surface to the antenna [Truong-Loi et al., 2009a]. This can be achieved by considering the conformity coefficient for smooth surfaces under the reflection symmetry assumption [Truong-Loi et al., 2009a]. This is, in fact, one of the advantages of using the hybrid-pol as apposed to the $\frac{\pi}{4}$-pol mode.

5.3.7 Eigenvalue and eigenvectors parameters

The eigenvectors of the 3×3 Hermitian averaged coherency matrix, $\boldsymbol{T}_3$, represent a set of three uncorrelated targets [Lee and Pottier, 2009, p. 193]. The eigenvectors are the same for the covariance matrix, $\boldsymbol{C}_3$, and the coherency matrix, $\boldsymbol{T}_3$, because these are related through a special unitary matrix , $U(2)$, (see section 2.2.2). The eigenvalues and eigenvectors can be used to find the underlying scattering properties.

Entropy

The scattering entropy (H) is a statistical measure of the degree of randomness of the scattering process, and is defined as [Lee and Pottier, 2009, p. 237]:

$$H = -\sum_{i=1}^{d} P_i \log_d P_i \tag{5.33}$$

where d denotes the number of dimensions ($d = 3$ for quad-pol with reciprocity, and $d = 2$ for compact-pol). P_i corresponds to the pseudo-probabilities calculated from the eigenvalues [Lee and Pottier, 2009, p. 231], i.e.:

$$P_i = \frac{\lambda_i}{\sum_{i=1}^{d} \lambda_i} \tag{5.34}$$

where λ_i represent the eigenvalues, and these are assumed to be sorted, i.e.: $\lambda_1 > \lambda_2 > \lambda_3$. When the entropy is zero, no depolarization occurs, and the target is dominated by a single scattering mechanism [Moen, 2014]. As the entropy increases towards one, more depolarization is observed and the target exhibits a scattering process that is completely random (several scattering mechanisms). The entropy has been used to study roughness of the sea ice and to classify different sea ice types [Gill and Yackel, 2013, Uiboupin et al., 2009]. One advantage of the entropy is that is can be calculated for both dual- and quad-pol systems. The entropy can be used for water and ice discrimination, and for distinguishing ridges on sea ice surfaces [Uiboupin et al., 2009]. As quad-pol data have proven useful in these applications, it is interesting to check whether compact-pol data can serve as an alternative. The entropy can be calculated from the sample covariance

matrix obtained from the simulated compact-pol data. Consider the hybrid-pol sample covariance matrix:

$$\boldsymbol{C}_{\text{hybrid}} = \begin{bmatrix} C_{11} & C_{12} \\ C_{21} & C_{22} \end{bmatrix} = \begin{bmatrix} \langle |S_{RH}|^2 \rangle & \langle S_{RH} S_{RV}^{\star} \rangle \\ \langle S_{RV} S_{RH}^{\star} \rangle & \langle |S_{RV}|^2 \rangle \end{bmatrix} \tag{5.35}$$

This covariance can be expressed through the eigenvectors, $\boldsymbol{u}$, and eigenvalues, λ, in the following manner [Lee and Pottier, 2009, p. 229]:

$$\boldsymbol{C}_{\text{hybrid}} = \sum_{i=1}^{2} \lambda_i \boldsymbol{u}_i \boldsymbol{u}_i^{\star^T} \tag{5.36}$$

The compact-pol entropy can be calculated from the eigenvalues and the eigenvectors of this matrix. Since the compact-pol covariance matrix contains mixtures of co- and cross-pol elements, one should expect that the compact-pol entropy would have a different behavior than the quad-pol entropy. Another way to calculate the entropy based on quad-pol covariance matrix could be to reconstruct a pseudo quad-pol covariance matrix from the compact-pol data.

Often, the entropy is used together with a α angle to create a feature space for classification, i.e., H/α decomposition. The class boundaries of this space are already known for quad-pol data (see [Lee and Pottier, 2009, p. 239-243]). The entropy obtained from the compact-pol covariance matrix may have different class boundaries. These class boundaries may deviate from the ones for quad-pol entropy, and we must therefore keep in mind the deviations of these class boundaries for the compact-pol entropy when analyzing it for various surfaces.

The anisotropy feature is defined as the relative importance of the second and third eigenvalue, and is useful when the entropy is high and thus difficult to interpret [Lee and Pottier, 2009, p. 237-239]. This parameter is defined as:

$$A = \frac{\lambda_2 - \lambda_3}{\lambda_2 + \lambda_3} \tag{5.37}$$

Unfortunately, it is difficult to find an estimate for the anisotropy directly from the compact-pol data. This is because the two smallest (λ_2 and λ_3) eigenvalues are necessary. If a reconstruction of a pseudo quad-pol covariance matrix is performed, then an estimate of the anisotropy feature can be retrieved.

Polarization Fraction

The next parameter to be evaluated is the polarization fraction. This polarimetric feature is defined as [Lee and Pottier, 2009, p. 253]:

$$\mathrm{PF} = 1 - \frac{3\lambda_3}{\lambda_1 + \lambda_2 + \lambda_3} = 1 - \frac{3\lambda_3}{\mathrm{SPAN}\{\boldsymbol{C}\}} \tag{5.38}$$

Here, $3\lambda_3$ represents the completely depolarized power, and $\frac{3\lambda_3}{\mathrm{SPAN}\{\boldsymbol{C}\}}$ thus represents the fraction of the total power that is depolarized [Moen, 2014]. To calculate this feature, all the three eigenvalues of the coherency matrix, $\boldsymbol{T}_3$, are necessary. This is not accessible in the compact-pol data, but relationships can be found by considering the eigenvalues of the sample compact-pol covariance matrix. The calculation of the eigenvalues are shown in Appendix E, but the resulting eigenvalues of the quad-pol covariance matrix are:

$$\lambda_1 = \frac{1}{2}\left(\mathrm{H} + \mathrm{V} + \sqrt{(H+V)^2 - 4HV + 4PP^{\star}}\right) \tag{5.39}$$

$$\lambda_a = \frac{1}{2}\left(\mathrm{H} + \mathrm{V} - \sqrt{(H+V)^2 - 4HV + 4PP^{\star}}\right) \tag{5.40}$$

$$\lambda_b = 2X \tag{5.41}$$

where,

$$\lambda_2 = \begin{cases} \lambda_a & \text{if } \lambda_a > \lambda_b \\ \lambda_b & \text{if } \lambda_a < \lambda_b \end{cases} \qquad \lambda_3 = \begin{cases} \lambda_a & \text{if } \lambda_a < \lambda_b \\ \lambda_b & \text{if } \lambda_a > \lambda_b \end{cases} \tag{5.42}$$

A set of notational substitutions in the above equations were made to make it cleaner and easier to work with the different quad-pol elements. These substitutions are as follows:

$$H = \langle |S_{HH}|^2 \rangle \qquad V = \langle |S_{VV}|^2 \rangle \qquad X = \langle |S_{HV}|^2 \rangle \qquad P = \langle S_{HH} S_{VV}^{\star} \rangle$$

Note that these substitutions are used throughout this chapter, as well as in chapter 6.

For the sample compact-pol covariance matrix, the eigenvalues become:

$$\lambda_1^{CP} = \frac{1}{2}\left(C_{11} + C_{22} + \sqrt{(C_{11} + C_{22})^2 - 4C_{11}C_{22} + 4C_{12}C_{12}^{\star}}\right) \tag{5.43}$$

$$\lambda_2^{CP} = \frac{1}{2}\left(C_{11} + C_{22} - \sqrt{(C_{11} + C_{22})^2 - 4C_{11}C_{22} + 4C_{12}C_{12}^{\star}}\right) \tag{5.44}$$

$$\tag{5.45}$$

where C_{11}, C_{22}, C_{12} are the elements in the compact-pol covariance matrix (see section 5.1.2). Inserting the cross- and co-pol elements into the compact-pol elements, and assuming reflection symmetry, the eigenvalues from the hybrid-pol covariance matrix become:

$$\lambda_1^{CP} = \frac{1}{4}(H+V) + X + \frac{1}{2}\sqrt{\left(\frac{1}{2}(H+V) + 2X\right)^2 - (H+X)(V+X) + (jP - jX)(-jP^{\star} + jX)} \tag{5.46}$$

$$\lambda_2^{CP} = \frac{1}{4}(H+V) + X - \frac{1}{2}\sqrt{\left(\frac{1}{2}(H+V) + 2X\right)^2 - (H+X)(V+X) + (jP - jX)(-jP^{\star} + jX)} \tag{5.47}$$

One suggestion for the compact-pol polarization fraction could be:

$$\hat{\mathrm{PF}}_{CP} = 1 - \frac{2\lambda_2^{CP}}{\lambda_1^{CP} + \lambda_2^{CP}} \tag{5.48}$$

This fraction can only be similar to the quad-pol fraction if $\lambda_2 \approx \lambda_3 \approx 0$. If this is true, the compact-pol fraction becomes one, which will also be the case for the quad-pol fraction. Otherwise, the compact-pol fraction will represent a fraction between the highest and the lowest eigenvalues from the sample compact-pol covariance matrix. In this case, the lowest eigenvalue will be a mix of the depolarized and polarized power, which is not consistent with the minimum eigenvalue based on the pseudo quad-pol covariance matrix.

Since the polarization fraction is a function of the smallest eigenvalue, it will be difficult to find a similar feature from the compact-pol data, since the lowest eigenvalue is incorporated in the compact-pol data as observed in equations 5.46 and 5.47.

Pedestal Height

The pedestal height is very similar to the polarization fraction. The pedestal height, PH, is defined as the ratio between the minimum and maximum eigenvalue [Lee and Pottier, 2009, p. 254-255], i.e.:

$$PH = \frac{\lambda_3}{\lambda_1} \tag{5.49}$$

This polarimetric feature is a measure of the unpolarized scattering component in the average returned signal [Lee and Pottier, 2009, p. 255]. Again the minimum eigenvalue is needed, and a suggestion to a compact-pol variant of the pedestal height might be:

$$PH^{CP} = \frac{\lambda_2^{CP}}{\lambda_1^{CP}} \tag{5.50}$$

where λ_2^{CP} is the minimum eigenvalue of the sample compact-pol covariance matrix. PH^{CP} can be closely related to PH if the minimum eigenvalue of the sample quad-pol covariance matrix is equal to λ_b (not λ_a) from equation 5.39. Since λ_2^{CP} is a mix of depolarized and polarized power, this polarimetric feature will no longer represent the unpolarized scattering component in the average response from a scatterer, but rather the unpolarized *and* polarized scattering component in the average response.

5.3.8 Incoherent parameters

The next group of polarimetric parameters to be evaluated is the incoherent parameters. These parameters are generated from the power component, where the phase term is removed (hence the name incoherent).

The Stokes vector

The Stokes vector is a set of four real numbers that can be used to describe the polarization state of a wave [Denbina, 2014]. The parameters given in the Stokes vector are incoherent, because the phase dependency is removed. In [Geldsetzer et al., 2014] the third parameter in the Stokes vector, q_2, was found to be independent of both the incident angle and the wind speed. Recall that the third parameter defines the power in the diagonally polarized component. The first (total power) and the last (power in the circularly polarized component) were both found to be dominated by surface scattering. By combining the parameters from the Stokes vector, it is possible to generate various parameters which are characterized by the received scattered wave [Charbonneau et al.,

2010]. Raney suggested that the Stokes vector could be a useful tool for representing the data collected by the hybrid-pol mode [Raney, 2007]. The Stokes parameters for a dual-pol SAR were calculated in section 5.3.8, with the common horizontal and vertical polarizations. In the case of a compact-pol system, the polarization changes, and so does the value in the Stokes vector.

If the transmitted field is diagonally polarized $\left(\frac{\pi}{4}\right)$, the four Stokes parameters in the linear basis {H,V} at the receiver are:

$$\boldsymbol{q} = \begin{bmatrix} q_0 \\ q_1 \\ q_2 \\ q_3 \end{bmatrix} = \begin{bmatrix} |E_{\frac{\pi}{4}H}|^2 + |E_{\frac{\pi}{4}V}|^2 \\ |E_{\frac{\pi}{4}H}|^2 - |E_{\frac{\pi}{4}V}|^2 \\ 2\Re(E_{\frac{\pi}{4}H}E^{\star}_{\frac{\pi}{4}V}) \\ 2\Im(E_{\frac{\pi}{4}H}E^{\star}_{\frac{\pi}{4}V}) \end{bmatrix} \tag{5.51}$$

If the transmitted wave is either left- or right-circularly polarized, the Stokes parameters become [Raney, 2007]:

$$\boldsymbol{q}_{LC} = \begin{bmatrix} |E_{RH}|^2 + |E_{RV}|^2 \\ |E_{RH}|^2 - |E_{RV}|^2 \\ 2\Re(E_{RH}E^{\star}_{RV}) \\ 2\Im(E_{RH}E^{\star}_{RV}) \end{bmatrix} \qquad \boldsymbol{q}_{RC} = \begin{bmatrix} |E_{LH}|^2 + |E_{LV}|^2 \\ |E_{LH}|^2 - |E_{LV}|^2 \\ 2\Re(E_{LH}E^{\star}_{LV}) \\ -2\Im(E_{LH}E^{\star}_{LV}) \end{bmatrix} \tag{5.52}$$

The corresponding Stokes vector for the DCP mode is [Raney, 2007]:

$$\boldsymbol{q}_{RC} = \begin{bmatrix} q_0 \\ q_1 \\ q_2 \\ q_3 \end{bmatrix} = \begin{bmatrix} |E_{RL}|^2 + |E_{RR}|^2 \\ 2\Re(E_{RL}E^{\star}_{RR}) \\ 2\Im(E_{RL}E^{\star}_{RR}) \\ (|E_{RL}|^2 - |E_{RR}|^2) \end{bmatrix} \tag{5.53}$$

The elements in the Stokes vector vary depending on the polarization of the transmitted signal [Denbina, 2014]. q_1, q_2, and q_3 represent the amount of backscattered power within each of three polarization states (see section 5.3.8) [Denbina, 2014]. Also, the sign of the three parameters is related to the type of polarization at the receiving wave. For instance, a positive sign of q_1 represent horizontal polarization, and a negative value denotes vertical polarization [Denbina, 2014]. Note that the sign of the last Stokes

parameter, q_3, is dependent on the sign convention that is used. In this case we use the generally accepted sign convention within the SAR literature, namely the backwards scattering alignment [Lee and Pottier, 2009]. This indicates that the coordinate system is set with regards to the satellite and not the target, which yields a negative value of q_3 for right-circularly polarized and a positive sign of q_3 for left-circularly polarized waves.

There are multiple parameters that can be derived from the Stokes vector, and some of them are discussed in the upcoming sections.

Degree of polarization

In the compact-pol scenario, the most important parameter is the degree of polarization (DoP), which was emphasized in [Raney, 2007]. This is defined as the ratio of the polarized power of a wave to the total power of a wave, i.e.:

$$DoP = \frac{\sqrt{q_1^2 + q_2^2 + q_3^2}}{q_0} \tag{5.54}$$

When the DoP is one, the wave is considered fully polarized, and when DoP is zero, the wave is fully depolarized. In the eigenvalue and eigenvector section, multiple parameters were "lost" due to the need for the minimum eigenvalue, λ_3, which represents the depolarized power. The DoP can therefore help in finding a replacement measure for the depolarized effect of a given target which is not accessible from the compact-pol covariance matrix. This parameter is used frequently in chapter 6, when attempting to reconstruct a pseudo quad-pol covariance matrix.

Circular polarization ratio

The circular polarization ratio is defined as [Raney, 2007]:

$$\mu_c = \frac{q_0 - q_3}{q_0 + q_3} \tag{5.55}$$

To demonstrate the signature of μ_c on varying surface covers the circular polarization ratio was calculated from the scenes from March 13th and May 10th using the Stokes vector generated from both hybrid- (with right-circular polarization transmits) and $\frac{\pi}{4}$-pol data. The results are displayed in Figure 5.10.

The μ_c generated based on the hybrid-pol data is completely different from the one calculated from $\frac{\pi}{4}$-pol data. The μ_c from the hybrid-pol mode seems more sensitive to

water and the smooth sea ice compared to the μ_c from $\frac{\pi}{4}$-pol mode. The μ_c from the hybrid-pol data (March 13th) seems more sensitive to surface roughness, while the μ_c from $\frac{\pi}{4}$-pol looks to be more sensitive to ridges. The μ_c from $\frac{\pi}{4}$-pol data have a much lower value of the circular polarization ratio compared to the one generated from the hybrid-pol data. The μ_c from the hybrid-pol data manages to separate out the sea ice located in the open water areas.

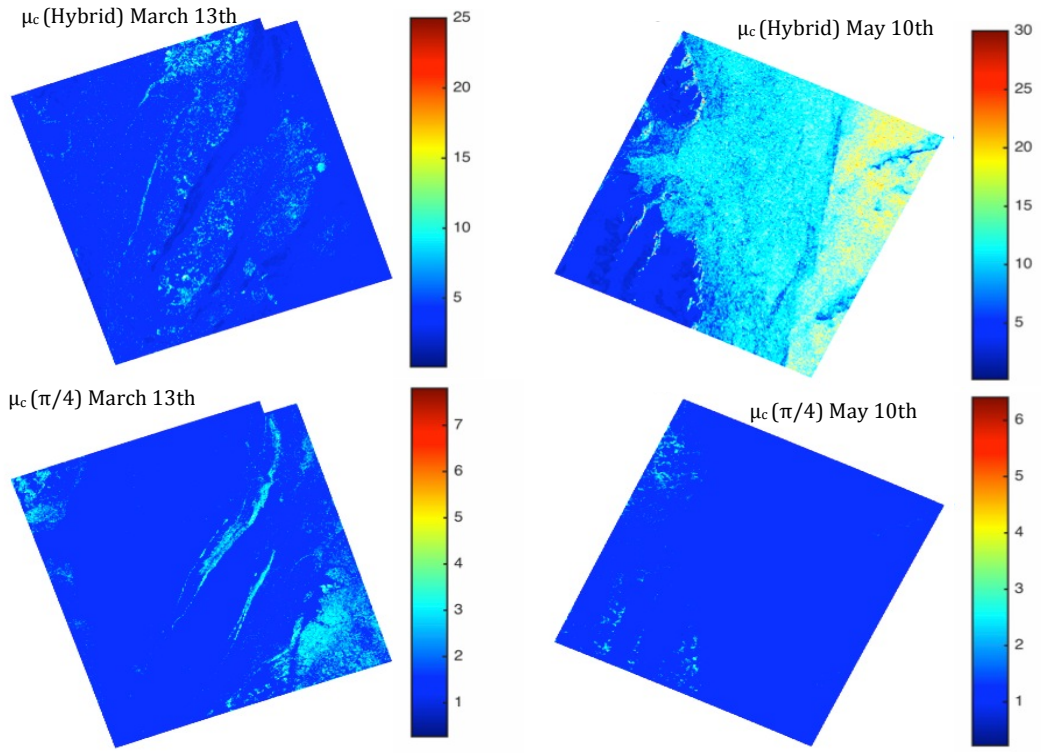

Figure 5.10: Circular polarization ratio calculated from both the simulated hybrid- and $\frac{\pi}{4}$-pol data acquired March 13th and May 10th 2013. The colorbar denotes the value of the circular polarization ratio.

Ellipticity/circularity

Raney proposed another way to express the Stokes vector through the degree of polarization, ellipticity angle, orientation angle, and the total power [Raney et al., 2012],

i.e.:

$$\boldsymbol{q}_{RC} = \begin{bmatrix} q_0 \\ q_1 \\ q_2 \\ q_3 \end{bmatrix} = \begin{bmatrix} q_0 \\ DoPq_0 \cos(2\psi)\sin(2\chi) \\ DoPq_0 \cos(2\psi)\sin(2\chi) \\ -DoPq_0 \sin(2\chi) \end{bmatrix} \tag{5.56}$$

This is the Stokes vector at the receiver, for right-circular polarization transmits and linear horizontal and vertical receive. From the Stokes vector above, the ellipticity is defined as [Raney et al., 2012]:

$$\chi = \frac{1}{2}\sin^{-1}\left(-\frac{q_3}{DoPq_0}\right) \tag{5.57}$$

where DoP is the degree of polarization defined in equation 5.54. The sign of this parameter has proven to be useful for distinguishing between double- and surface bounce scattering [Raney et al., 2012]. To locate where double bounce scattering may occur in the two SAR scenes from March 13th and May 10th, the idea presented in [van Zyl et al., 2011] can be used. The authors suggested that the sign of the real part of the two co-pol coefficients, S_{HH} and S_{VV}, can be used to determine if either double or surface scattering is the dominant form of scattering, i.e.:

$$\begin{aligned} \Re(S_{HH}S_{VV}^{\star}) > 0 &\implies \text{Surface scattering} \\ \Re(S_{HH}S_{VV}^{\star}) < 0 &\implies \text{Double bounce scattering} \end{aligned} \tag{5.58}$$

To find areas where surface and double-bounce scattering are located in the compact-pol case, the sign of the χ angle can be used [Charbonneau et al., 2010], i.e.:

$$\chi > 0 \implies \text{Surface scattering} \qquad \chi < 0 \implies \text{Double bounce scattering} \tag{5.59}$$

Figure 5.11 shows the sign of the ellipticity angle for the compact-pol, and the sign of the $\Re(S_{HH}S_{VV}^{\star})$ for the quad-pol data. Yellow corresponds to negative value (double-bounce scattering), while blue denotes positive value (surface scattering). The double bounce region seems to be overestimated for both the hybrid-pol and $\frac{\pi}{4}$-pol ellipticity angles compared to the areas obtained from the sign of the real part of the co-pol

correlation coefficient. However, the ellipticity angle generated from the hybrid-pol data seems more correct than the values generated from $\frac{\pi}{4}$-pol data. We can therefore confirm that the sign of the ellipticity angle (from the hybrid-pol mode) can be related to van Zyl's concept, but some overestimation is unfortunately present.

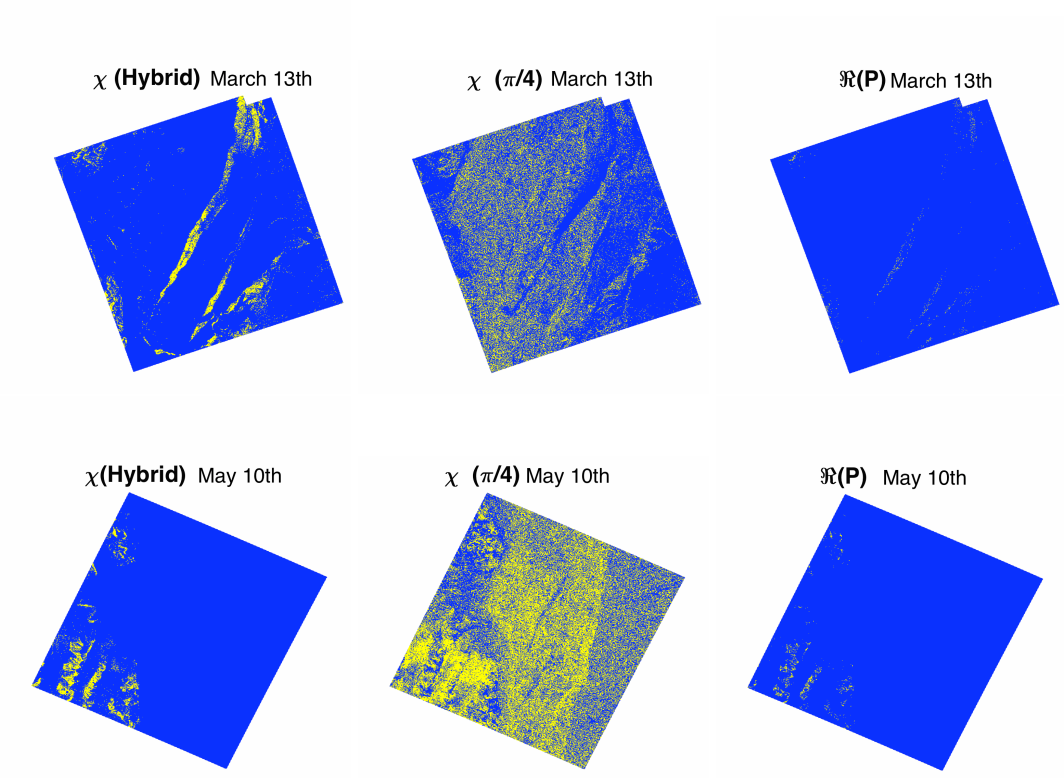

Figure 5.11: Ellipticity angle calculated from both the simulated hybrid- and $\frac{\pi}{4}$-pol data acquired March 13th and May 10th 2013. A positive value of the ellipticity angle is colored blue, while negative value is yellow. The real part of the co-pol correlation coefficient is calculated from the quad-pol data from the same dates. Again, negative values are yellow and positive values are blue.

5.4 Issues regarding information retrieval

The previous sections have covered interpretation of both the compact-pol features and their relationship to known quad-pol features. The quad-pol features are difficult to derive directly based on the compact-pol data, but some relationships have been found. The reason for the interest in finding relationships between the compact- and quad-pol features is because interpretations of sea ice are known and well established for the quad-pol case. Although it is difficult to reconstruct quad-pol features from the compact-pol data, some relevant information can still be obtained from the compact-pol

case for sea ice discrimination. The following compact-pol features were proven to be relatively similar to the quad-pol features in both shape and/or scale; co-pol ratio, co-pol correlation coefficient, and co-pol phase difference. These can help when distinguishing between open water and sea ice.

The cross-pol intensity is an important feature when distinguishing between smooth ice and open water. This is a "lost" parameter in the compact-pol case, i.e., it is not possible to extract directly. Hence, a reconstruction of the pseudo quad-pol covariance matrix would be useful, as this allows finding an estimate for this polarimetric feature. Also, the cross-pol ratio is "lost" in the compact-pol data, but by assuming azimuthal symmetry we were able to find an estimate for it. This turned out to fail for areas representing open water, rough, deformed, and thin sea ice. Again, a reconstruction could help in finding an estimate of the cross-pol ratio. The minimum eigenvalue (λ_3) from the sample quad-pol covariance matrix is impossible to extract from the compact-pol data. This feature is sensitive to depolarization effects, and is thus considered a "lost" polarimetric feature for the compact-pol case. This also affects the following polarimetric features; polarization fraction, polarization asymmetry, and pedestal height. However, the degree of polarization calculated from the Stokes vector might help in recovering a measurement of the depolarization effects from the compact-pol data. Therefore, the use of the Stokes vector (first proposed in [Raney, 2007]) is very important when analyzing depolarization effects within the sea ice structure.

Based on these observations, a reconstruction approach can help provide the missing information from the compact-pol data. We therefore dedicate the next chapter to reconstruction techniques.

5.5 The best compact polarimetric mode

Most of the upcoming and existing radars utilize the hybrid-pol mode with right-circularly polarized transmitted waves, which indicate that there is a benefit of this mode over the others. Both in [Raney, 2007] and [Souyris et al., 2005], the authors concluded that using circularly polarized transmitted waves will limit the effect of Faraday rotation in the ionosphere in the L- and P-band frequency domain. Also, it has been claimed that the calibration process is easier using the hybrid-pol mode, i.e., it is self-calibrated, and no point target is needed in the calibration [Raney, 2007]. Additionally, the amount of backscattered power does not depend on the orientation of the target if circularly polarized waves are transmitted. This was first highlighted in [Denbina, 2014]. The advantages for hybrid- over $\frac{\pi}{4}$-pol modes are:

- One can neglect the effects from Faraday's rotation if the hybrid-pol is used.
- Hybrid-pol makes for a simpler calibration process.

- Hybrid-pol is invariant to target rotations.

Since upcoming and existing radars utilize the hybrid-pol mode, the upcoming chapter will in general only consider the hybrid-pol with right-circular polarization at the transmitter. However, when found useful, the $\frac{\pi}{4}$-pol and DCP mode will also be discussed, albeit to a smaller extent.

6

Reconstruction Methods

The idea of reconstructing a pseudo quad-pol covariance matrix is not new, and a multitude of approaches and techniques have been studied [Souyris et al., 2005, Ainsworth et al., 2007, Boularbah et al., 2012]. In order to restore a pseudo quad-pol covariance matrix, some assumptions about the target must be made. Reflection symmetry (see section 2.2.2) and strong azimuthal symmetry are examples of such assumptions, and will enable reconstruction. The performance of the reconstruction will depend on the accuracy of these assumptions. Identifying the assumptions that will have the least negative impact on the restored polarimetric data is a key challenge when applying reconstruction methods.

The reason for reconstructing the elements in a pseudo quad-pol covariance matrix instead of the scattering coefficients in the Sinclair matrix (see section 2.2.1), is that the compact-pol scattering coefficients (see section 5.1) are a blend of co- and cross-pol elements that cannot be separated under the common assumption that they follow a joint complex and circular Gaussian distribution [Souyris et al., 2005]. It is therefore necessary to use second order statistics in the reconstruction process, namely the sample covariance matrix.

Some of the research on reconstruction concludes that the techniques used to estimate pseudo quad-pol covariance matrices lead to results that are not always similar to the true quad-pol covariance matrices they approximate. However, there are still reasons and motivations for performing such a reconstruction for sea ice covered SAR scenes. These reasons are summarized as follows:

- Promising results for reconstructing vegetation covered areas was presented in [Truong-Loi et al., 2010] and [Ainsworth et al., 2007]. Due to some similarities in backscatter behavior between vegetation and sea ice, such as dominance of volume and surface scattering from natural media, we believe reasonable reconstruction results can be obtained from sea ice covered SAR scenes as well.

- As discussed in chapter 5, different quad-pol parameters are important when extracting information about the sea ice. This is because the physical information is already known (to some degree) for the quad-pol case. Many of these parameters are lost in the compact-pol case. If a reconstruction is performed, this will provide an opportunity to estimate these quad-pol parameters.

- If a reconstruction is performed, known decomposition techniques such as the Freeman and Durden, Yamaguci, and Touzi decompositions, can be applied on the pseudo quad-pol covariance matrix. This might enable the location areas where surface, double bounce, or volume scattering dominate.

Clearly, quad-pol data contain a higher amount of polarimetric information than dual-, compact-, and single-pol data. If a good reconstruction technique is applied on the compact-pol data, the maximum potential of the compact-pol data—in terms of polarimetric information—can be achieved. To the author's knowledge there exists no studies on reconstructing the pseudo quad-pol covariance matrix specifically for sea ice covered SAR scenes. Because of this, we devote this chapter to the discussion of such reconstruction.

This chapter is composed of two main sections. The first of these contains an overview of the two most commonly used methods for reconstruction, namely Souyris' and Nord's methods. The second section covers new approaches for reconstruction.

6.1 Existing reconstruction methods

As mentioned in the previous paragraph, there are currently two main reconstruction methods; Souyris' and Nord's reconstructions. These methods have been tested on vegetation, open water, and urban areas [Nord et al., 2009, Boularbah et al., 2012, Souyris et al., 2005]. The upcoming section presents these two methods in more detail and we will also investigate the validity of these two methods for our dataset.

6.1.1 Souyris' reconstruction method

Souyris' method is aimed at *unpacking* the compact-pol data in order to reconstruct a pseudo quad-pol covariance matrix, which is the case for all the reconstruction methods.

This reconstruction process is done by assuming reflection symmetry, and that the compact-pol data represents natural surfaces. The first assumption; reflection symmetry, was discussed in section 2.2.2. This results in zero correlation between the cross- and co-pol scattering coefficients, i.e.:

$$\langle S_{HH}S_{HV}^{\star}\rangle = \langle S_{HV}S_{HH}^{\star}\rangle = 0 \qquad \langle S_{VV}S_{HV}^{\star}\rangle = \langle S_{HV}S_{VV}^{\star}\rangle = 0 \tag{6.1}$$

The sample quad-pol covariance matrix will then take the following form:

$$\boldsymbol{C}_3 = \begin{bmatrix} \langle |S_{HH}|^2\rangle & 0 & \langle S_{HH}S_{VV}^{\star}\rangle \\ 0 & 2\langle |S_{HV}|^2\rangle & 0 \\ \langle S_{VV}S_{HH}^{\star}\rangle & 0 & \langle |S_{VV}|^2\rangle \end{bmatrix} \tag{6.2}$$

The sample hybrid-pol covariance matrix (see section 5.1.2) has the following form after assuming reflection symmetry:

$$\boldsymbol{C}_{\text{Hybrid}}^{LC/RC} = \frac{1}{2}\begin{bmatrix} \langle |S_{HH}|^2\rangle & \mp j\langle S_{HH}S_{VV}^{\star}\rangle \\ \pm j\langle S_{VV}S_{HH}^{\star}\rangle & \langle |S_{VV}|^2\rangle \end{bmatrix} + \frac{\langle |S_{HV}|^2\rangle}{2}\begin{bmatrix} 1 & \pm j \\ j & 1 \end{bmatrix} \tag{6.3}$$

Compared to the sample hybrid-pol covariance matrix in equation 5.17, the last matrix containing the correlation between the cross- and co-pol elements is now cancelled out, which leaves us with fewer unknown elements.

However, assuming reflection symmetry alone will not help solving this system of equations, i.e., finding solutions to H, V, X, and P, since there are four unknowns and only three independent equations.

We must therefore introduce a new independent equation for linking the co- and cross-pol terms. In [Souyris et al., 2005], the following non-linear equation was suggested for this purpose:

$$\frac{X}{H+V} = \frac{1-|\rho_{HHVV}|}{4} \tag{6.4}$$

$$X = \langle |S_{HV}|^2\rangle \quad H = \langle |S_{HH}|^2\rangle \quad V = \langle |S_{VV}|^2\rangle \quad P = \langle S_{HH}S_{VV}^{\star}\rangle \tag{6.5}$$

where the *coherence parameter* is defined as [Li et al., 2006]:

$$\rho_{HHVV} = \frac{P}{\sqrt{H\,V}} \tag{6.6}$$

The relationship in equation 6.4 will be referred to as *Souyris' linking*. In the following, a set of notational substitutions has been made in order to make it easier to work with the different elements in the covariance matrix. These substitutions are given in equation 6.5.

The relationship given by equation 6.4 is extrapolated from the cases where the backscattered wave is either fully polarized or fully depolarized. The fully depolarized wave is often dominated by volume scattering (diffuse part of the backscattered field) [Dubois-Fernandez et al., 2008b]. Hence, using this method will only be strictly valid in the case of pure volume scattering, and problems will arise in case of double-bounce (urban areas) or surface scattering. Equation 6.4 is based on the following explanation [Souyris et al., 2005]:

- In case of a fully polarized wave: $\rho_{HHVV} = 1$, which yields a very low response in the cross-pol channel, i.e., $\langle |S_{HV}|^2 \rangle = X \approx 0$.

  Equation 6.4 becomes:

  $$\frac{X}{H+V} = \frac{1-|\rho_{HHVV}|}{4} \implies \frac{0}{H+V} = \frac{1-1}{4} \implies 0 = 0.$$

- In case of a fully depolarized system, the degree of coherence becomes equal to 0. Souyris stated that "for a fully depolarized backscattered wave, the average power collected by the receiving antenna does not depend on its polarization state", which will result in: $H = V = 2X$ [Souyris et al., 2005].

  Equation 6.4 becomes:

  $$\frac{X}{H+V} = \frac{1-|\rho_{HHVV}|}{4} \implies \frac{X}{2X+2X} = \frac{1-0}{4} \implies \frac{1}{4} = \frac{1}{4} \implies 1 = 1$$

Equation 6.4 originates from a calculation using the coherency matrix (see section 2.2.2) and will only be valid for natural surfaces. The volume scattering component for natural surfaces exhibit much stronger azimuthal symmetry, and it is only the presence of direct surface scattering or dihedral returns that will break this symmetry [Cloude, 2009]. In context of sea ice, we expect that highly deformed ice or leads will break this symmetry. The linking between the co- and cross-pol intensities in equation 6.4 is in fact derived from an azimuthal symmetric coherency matrix. This calculation is shown in Appendix C.

Following these two assumptions, equation 6.4 is added to the system of equations, and

we are left with four equations with four unknowns. The next task is to find solutions to H, P, V, and X by using an iterative approach, where the coherence parameter ρ_{HHVV} and X are updated every iteration step.

Iterative method

The goal for this method is to find an expression for the cross-pol intensity $\langle |S_{HV}|^2 \rangle = X$, so that all the unknown parameters can be found in the sample quad-pol covariance matrix in equation 6.7. For the hybrid-pol data with right-circular polarization at the transmitter, the system of equations is:

$$\boldsymbol{C}_{QP} = \begin{bmatrix} H & 0 & P \\ 0 & 2X & 0 \\ P^{\star} & 0 & V \end{bmatrix} = \begin{bmatrix} 2C_{11} - X & 0 & -2jC_{12} + X \\ 0 & 2X & 0 \\ 2jC_{12}^{\star} + X & 0 & 2C_{22} - X \end{bmatrix} \tag{6.7}$$

Note that C_{ij} represents the elements in a compact-pol covariance matrix. In our case, the hybrid-pol mode is considered, which has the following sample covariance matrix after assuming reflection symmetry:

$$\boldsymbol{C}_{\text{hybrid}} = \begin{bmatrix} C_{11} & C_{12} \\ C_{12}^{\star} & C_{22} \end{bmatrix} = \frac{1}{2} \begin{bmatrix} H + X & jP - jX \\ -jP^{\star} + jX & V + X \end{bmatrix} \tag{6.8}$$

The degree of coherence as a function of the scattering elements in the hybrid-pol covariance matrix is:

$$\rho_{HHVV} = \frac{P}{\sqrt{HV}} = \frac{-2jC_{12} + X}{\sqrt{(2C_{11} - X)(2C_{22} - X)}} \tag{6.9}$$

The following algorithm was first proposed in [Souyris et al., 2005]. In the **initial step** ($i = 0$), the cross-pol term is set to 0, i.e.:

$$X = \langle |S_{HV}|^2 \rangle = 0 \tag{6.10}$$

This implies that the coherence parameter has the following form:

$$|\hat{\rho}_{HHVV}^{(0)}| = \frac{|-jC_{12}|}{\sqrt{C_{11}C_{22}}} \tag{6.11}$$

Here, the superscript in $\hat{\rho}^{(i)}_{HHVV}$ indicates iteration number. By using equation 6.11 and the relationship in equation 6.4, an expression for $\hat{X}^{(0)}$ can be calculated:

$$\hat{X}^{(0)} = \frac{(H+V)\left(1-|\hat{\rho}^{(0)}_{HHVV}|\right)}{4}$$

Inserting the expressions for H and V from equation 6.8, yields:

$$\hat{X}^{(0)} = \frac{\left(2C_{11}+2C_{22}-2\hat{X}^{(0)}\right)\left(1-|\hat{\rho}^{(0)}_{HHVV}|\right)}{4}$$

Rearranging the above expression, one gets:

$$\hat{X}^{(0)}\left(3/2-1/2|\hat{\rho}^{(0)}_{HHVV}|\right) = \frac{\left(C_{11}+C_{22})(1-|\hat{\rho}^{(0)}_{HHVV}|\right)}{2}$$

$$\hat{X}^{(0)} = \frac{(C_{11}+C_{22})\left(1-|\hat{\rho}^{(0)}_{HHVV}|\right)}{2\left(3/2-1/2|\hat{\rho}^{(0)}_{HHVV}|\right)} = \frac{(C_{11}+C_{22})\left(1-|\hat{\rho}^{(0)}_{HHVV}|\right)}{3-|\hat{\rho}^{(0)}_{HHVV}|}$$

Following this, an **iterative process** is used to find an expression for X. The first iteration, $(i=1)$, can be expressed as follows:

$$\hat{\rho}^{(1)}_{HHVV} = \frac{-2jC_{12}+\hat{X}^{(0)}}{\sqrt{(2C_{11}-\hat{X}^{(0)})(2C_{22}-\hat{X}^{(0)})}}, \qquad \hat{X}^{(1)} = \frac{(C_{11}+C_{22})\left(1-|\hat{\rho}^{(1)}_{HHVV}|\right)}{3-|\hat{\rho}^{(1)}_{HHVV}|}$$

The relationship given by equation 6.4 is only an approximation, and thus the iterative approach may lead to errors. These errors are related to the fact that the $|\hat{\rho}^{(i)}_{HHVV}|$ term may become larger than one for certain pixels, or even that the expression in the square root can be a negative number. In these cases, the iterative process is halted, and the parameters used are corrected in the following manner: $|\hat{\rho}^{(i)}_{HHVV}| = 1$ and $|\hat{X}^{(i)}| = 0$. This is a supervised process, meaning that the user decides how many iterations are to be executed. Note that the number of iterations may affect the reconstruction performance. This is highlighted in section 7.4.1.

The general expressions for this iterative approach, and the resulting pseudo quad-pol covariance matrices for the three compact-pol modes, are given in Figure 6.1 [Nord et al., 2009].

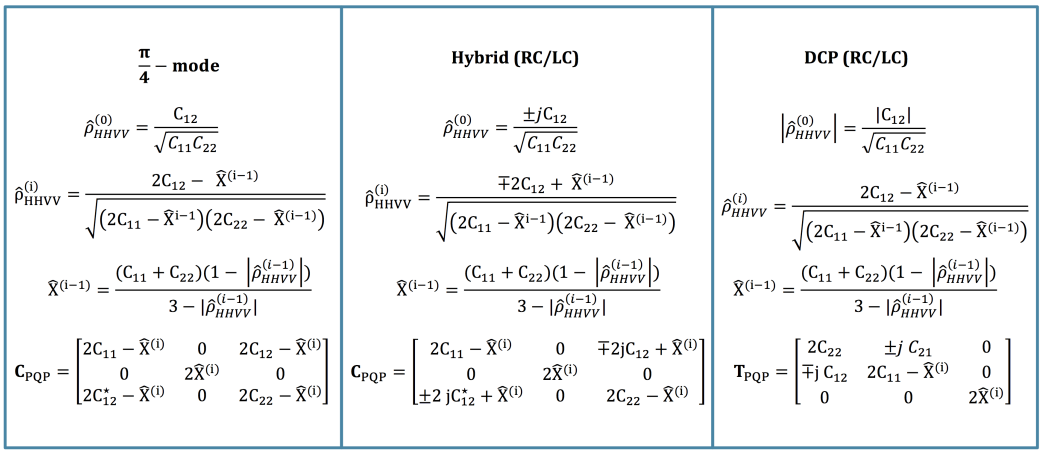

Figure 6.1: Overview of Souyris' reconstruction method for the three compact-pol modes.

As seen for the DCP mode in Figure 6.1, the coherency matrix is used instead of the covariance matrix. This is because the different terms in the scattering matrix from the circular mode are similar to the elements of the Pauli basis vectors, and it is thus more convenient to deal with the coherency matrix in this case.

The main limitation in the iterative process of Souyris' method is the initial step, i.e.: $X = 0$. The assumption that the cross-pol intensity is zero may cause significant errors in the reconstruction process following the iterations. One idea for resolving this problem is to find a better way to solve Souyris' system of equations. In section 6.2.4 we propose an alternative approach where we treat the determination of X as an optimization problem rather than using this iterative approach.

Another limitation to Souyris' method is the linking between the co- and cross-pol intensities (see equation 6.4). Only if this linking is valid, will the method produce a high accuracy approximation. To be able to observe whether Souyris' linking is reasonable for the sea ice scenes used in this work, one can study the difference between the left side $\left(\frac{X}{H+V}\right)$ and right side $\left(\frac{1-|\rho_{HHVV}|}{4}\right)$ of equation 6.4. We say that an overestimation occurs if the left side is greater than the right side of equation 6.4, and that an underestimation occurs if the right side is greater than the left side. Following this, let us say that we can afford to have a deviation (σ) between the two elements of 0.02. This empirical value is chosen to enable clear identification of areas of discrepancy between the right and left sides in Souyris' linking. This means that the equality in equation 6.4 is considered to hold if $\left(\frac{X}{H+V}\right)$ is equal to $\left(\frac{1-|\rho_{HHVV}|}{4}\right) \pm 0.02$. Figure 6.2 illustrates a color image displaying the difference between the two sides discussed, and scatter plots. The data are from March 13th and May 10th 2013, and the data points are selected randomly using a random number generator in Matlab. The color image is created in the following

way:

- Calculate the difference:

$$y = \frac{X}{H+V} - \frac{1-|\rho_{HHVV}|}{4} \tag{6.12}$$

- Find boundaries for under-, over-, and reasonable estimation.

$$\text{If } y < -\sigma \implies \text{underestimation } \left(\frac{X}{H+V} < \frac{1-|\rho_{HHVV}|}{4}\right) \rightarrow \text{blue}$$

$$\text{If } y > \sigma \implies \text{overestimation } \left(\frac{X}{H+V} > \frac{1-|\rho_{HHVV}|}{4}\right) \rightarrow \text{red}$$

$$\text{If } -\sigma < y < \sigma \implies \text{reasonable estimation } \left(\frac{X}{H+V} \approx \frac{1-|\rho_{HHVV}|}{4}\right) \rightarrow \text{green}$$

From Figure 6.2, overestimation occurs for areas around leads, sea ice objects, and some areas of the landfast ice and rough sea ice. Recall that the labeling of the different sea ice types was presented in chapter 4. The red (overestimated) areas are in fact very similar to the yellow colored areas shown in Figure 5.11. This figure showed the sign of the ellipticity angle calculated from the Stokes vector from a simulated hybrid-pol system. Recall that a yellow region corresponded to a negative sign of the ellipticity angle, and such a negative signed angle represents double bounce scattering. From this observation, we see that the double bounce regions correspond to the red regions in Figure 6.2, which might be due to violation of the azimuthal symmetry assumption and double bounce being the prominent scattering type mechanism.

Underestimation occurs for sea ice that is located in open water, some areas of smooth sea ice, as well as rough, and landfast sea ice. Underestimation may occur if the cross-pol intensity is low, or for low values of the coherence parameter. Souyris' linking seems valid for some areas of smooth sea ice, ridges, open water, and rough sea ice. One should therefore expect the green area to yield a high accuracy reconstruction of the quad-pol scattering components, while the others will not. Souyris' linking is reasonable when both $\frac{1-|\rho_{HHVV}|}{4}$ and $\frac{X}{H+V}$ are low, which occurs when $|\rho_{HHVV}|$ is high and the cross-pol intensity is low. This was also discovered for vegetation covered areas in [Souyris et al., 2005]. Overall, the most promising class to be reconstructed is smooth sea ice and open water.

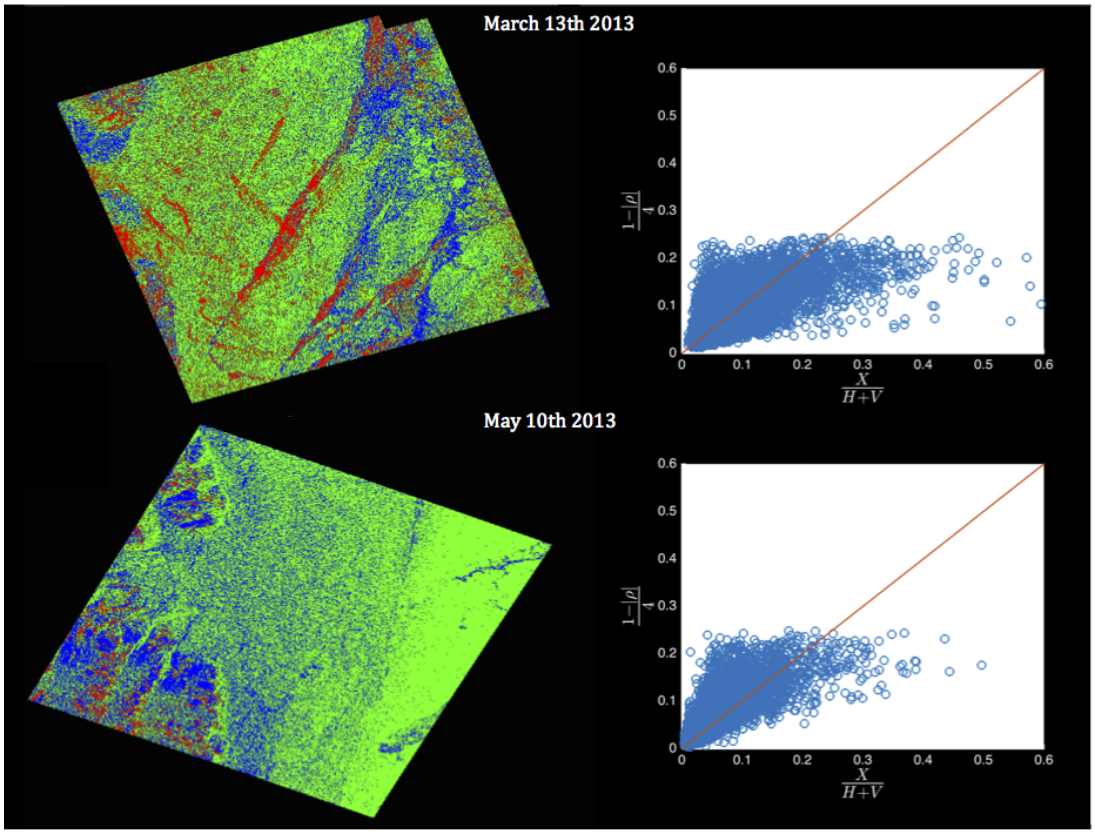

Figure 6.2: The figure shows a color image (column to the left) demonstrating Souyris' linking between the cross- and co-pol scattering coefficients. Red denotes overestimation, blue denotes underestimation, and green color represent when this linking is reasonable (reasonable estimation). The definitions of over-, under-, and reasonable estimation are explained in the introductory part of this section. The column to the right shows scatter plots of the two components.

Results of Souyris' reconstruction approach

Scatter plots are created to demonstrate the results of the cross-pol intensity reconstructed from the hybrid-pol mode. This is because the cross-pol intensity is the most delicate term to reconstruct due to its low radiometry (typically 7 – 10 dB below the co-pol intensities (see Figure 5.5)). Thus, the reconstructed co-pol components are left out in this section.

Since different classes of sea ice have different polarimetric behavior, scatter plots are created for each class (see chapter 4). The root mean square error (RMSE) and Pearson correlation coefficient (r) are calculated for each type of sea ice, and are displayed in

each figure. Note that the decibel scale is used when calculating the RMSE and Pearson correlation coefficient, and when displaying the estimated and true values in the scatter plots. The Pearson correlation coefficient is given in equation B.5 in Appendix B, while the RMSE is given in equation B.3. The RMSE with the decibel scale is used throughout this work (with some exceptions in chapter 7).

Such a RMSE measure is also used in previous work when evaluating the reconstruction performance of a pseudo quad-pol covariance matrix [Nord et al., 2009]. In our work, a high reconstruction performance is defined as having a correlation which is greater than 0.8, and a RMSE which is below 1dB.[1] A similar RMSE threshold was also used in [Nord et al., 2009] when determining the performance of the estimated co- and cross-pol intensities, which was based on the accuracy of geophysical parameter estimates. The RMSE considers the absolute error of the averaged difference, including both the variance and the bias (skewness), i.e.,

$$\text{RMSE} = \sqrt{\text{Var}(X - \hat{X}) + \left(\text{Bias}(X - \hat{X})\right)^2},$$

and it is therefore important to also consider the linear correlation between the estimated and true variables, which is independent on the scale within the data. The following interpretation of both the Pearson correlation coefficient and RMSE (in decibel) are:

- Pearson correlation coefficient is large and high RMSE $\implies$ High bias.
- Pearson correlation coefficient is low and low RMSE $\implies$ Small variation between the estimated and true values, but little correlation.
- Low Pearson correlation coefficient and high RMSE $\implies$ High bias and variance, and little correlation between the estimated and true values.
- High Pearson correlation coefficient and low RMSE $\implies$ High performance of the estimator.

These metrics will be used when evaluating the performance of the different reconstruction techniques throughout this work, and the above mentioned values are chosen to clearly identify the deviations from the true cross-pol intensity.

The reconstruction results of the cross-pol intensity obtained from simulated hybrid-pol data with right-circular polarization at the transmitter are shown in Figure 6.3. In these

1. A RMSE below 1dB indicates that the estimated value varying between ±1dB relative to the true value.

scatter plots, a high correlation coefficient is achieved for landfast ice, smooth level ice, and deformed sea ice. Little correlation is found for open water, leads, sea ice objects, and rough sea ice. Relatively high RMSE is found for all the classes—highest for open water and smooth ice. We believe the reason for this is the low response generated in the cross-pol channel for such areas. Note that the bias in the RMSE is high for smooth ice, deformed ice, and open water. We are aware that outliers might influence the values of the RMSE and Pearson correlation coefficient. Such outliers may occur due to manual selection of training samples for each class (see section 4.3). The scatter plots do not indicate that outliers are a problem in our case.

Figure 6.2 illustrated the validity of Souyris' linking, which we observed to be reasonable for areas covering open water and some areas covering smooth and deformed sea ice. The reconstructed cross-pol intensity for the open water class showed the opposite of the trend in Figure 6.2. In Figure 6.2, we observed that the left and right sides are closely similar for low radiometric values, while the deviation increases as the values of the left side increases. Open water produces low backscattering response. The low signal strength from such surface cover allows the left and right side to become equal. This implies that Souyris' linking is valid, but there is a relative discrepancy among the low radiometric values that are captured during the reconstruction of the cross-pol intensity. This might be the reason for the deviation of the estimated cross-pol intensity for the open water class.

Overall, Souyris' method manages to reconstruct areas where the backscattered response in the cross-pol intensity is high, and when the surface area is relatively smooth. It does, however, not handle complicated sea ice structures where the cross-pol intensity is low.

In chapter 7, the results of Souyris' method will be compared to the other reconstruction methods.

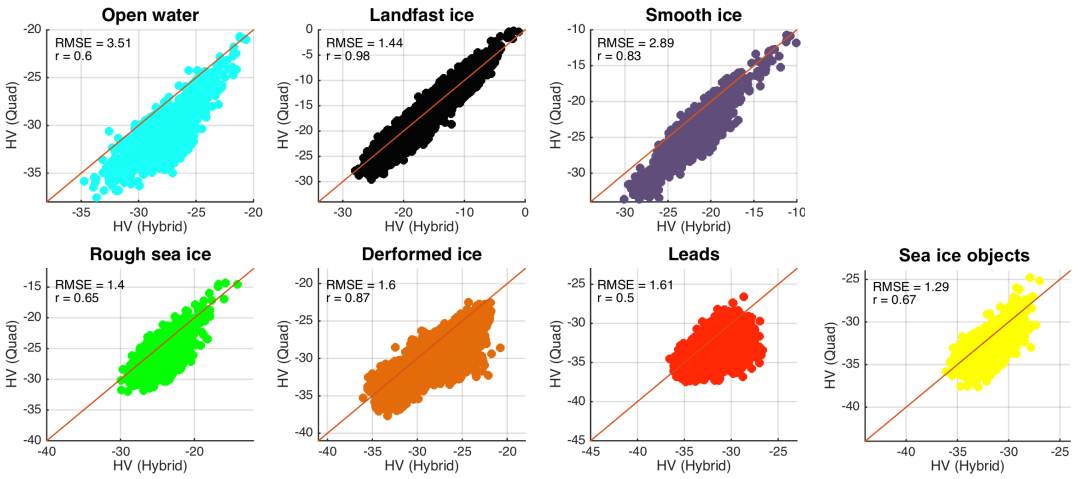

Figure 6.3: Results of Souyris' reconstruction for different types of sea ice for the simulated hybrid-pol mode with right-circular polarization at the transmitter. The RMSE and Pearson correlation coefficient for the true and estimated cross-pol intensity (in decibel) are displayed in each scatter-plot. The different sea ice types are selected from the scenes acquired March 13th and May 10th (see chapter 4).

6.1.2 Nord's reconstruction method

Souyris' method is well suited for surfaces that exhibit volume scattering. Nord alters this behavior by replacing the 4 with N in equation 6.4, N being a function of the ratio between the double bounce and volume scattering power. The method starts with the volume scattering component of the Freeman-Durden covariance model to calculate the degree of coherence [Nord et al., 2009]. Using Nord's method will, in theory, make it possible to account for double bounce scattering properties. This method is based on an inequality between the scattering elements in the covariance matrix. The process is described in Appendix D, and the final result of the calculation is:

$$\frac{X}{H+V} = \frac{1-|\rho_{HHVV}|}{N} \qquad N = \frac{\langle |S_{HH}-S_{VV}|^2 \rangle}{\langle |S_{HV}|^2 \rangle} \tag{6.13}$$

The case of $|S_{HH}-S_{VV}|^2 = 4|S_{HV}|^2$ implies that $N = 4$, i.e., Souyris' method. This would meen strong azimuthal symmetry, and Nord's method therefore tries to compensate for areas where no such symmetry exists. Unfortunately, the N term is unknown and must

be estimated. In the case of $\frac{\pi}{4}$-pol mode, one term can be found, i.e.:

$$\begin{aligned}\langle|S_{HH} - S_{VV}|^2\rangle &= \langle|S_{HH}|^2\rangle + \langle|S_{VV}|^2\rangle - \Re\left(\langle S_{HH}S_{VV}\rangle\right) \\ &= 2C_{11} - X + 2C_{22} - X - 2\Re\left(2C_{12} - X\right) \\ &= 2C_{11} + 2C_{22} - 2X + 2X - 4\Re\left(C_{12}\right) = 2C_{11} + 2C_{22} - 4\Re\left(C_{12}\right)\end{aligned}$$

Since $\langle|S_{HV}|^2\rangle$ is unknown, Nord et al. choose to start with Souyris' method, and then include the N term afterwards. The first iteration in Souyris' method is then used to find an expression for ρ_{HHVV}. Note that the initial estimate of the covariance matrix elements is based on $N = 4$. This may cause some deviation in the results, as the initial step assumes azimuthal symmetry for the data. One idea for improvement could therefore be to find a different initial step that does not rely on strong azimuthal symmetry. This has been studied in [Collins et al., 2013], where the authors explored a non-linear regression model for the N parameter. The authors concluded that the estimated N gave a high reconstruction performance for open water areas. The first iteration step in Nord's method is performed as follows (with initialization $N = 4$):

$$X^{(1)} = \frac{(H+V)\left(1 - |\rho^{(1)}_{HHVV}|\right)}{N} = \frac{(2C_{11} + 2C_{22} - 2X)\left(1 - |\rho^{(1)}_{HHVV}|\right)}{N}$$

Rearranging this, yields:

$$X^{(1)} = \frac{(2C_{11} + 2C_{22})(1 - |\rho^{(1)}_{HHVV}|)}{(N + 2(1 - |\rho^{(1)}_{HHVV}|))}$$

where

$$|\rho^{(1)}_{HHVV}| = \frac{(C_{11} + C_{22})(1 - |\rho^{(0)}_{HHVV}|)}{3 - |\rho^{(0)}_{HHVV}|} \qquad \rho^{(0)}_{HHVV} = \frac{|-2jC_{12}|}{\sqrt{C_{11}C_{22}}}$$

When the iteration is completed, the N parameter is calculated from the elements in the pseudo quad-pol covariance matrix, and X is updated.

Nord et al. presented promising results when using the hybrid-pol or DCP modes. The authors managed to reconstruct the cross-pol intensity representing grass, forest, and urban areas, although the latter was less accurate than the first two.

The N parameter is dependent on the surface of interest. In Souyris' method the N parameter was set to 4, indicating that the surface is natural and exhibits strong azimuthal symmetry. Hence, one should therefore expect the N parameter to be low for natural surfaces, and high for surfaces that exhibit double bounce scattering, i.e., urban areas. That is:

$$N = \frac{\langle |S_{HH} - S_{VV}|^2 \rangle}{\langle |S_{HV}|^2 \rangle} = \frac{H + V - 2\Re(P)}{X}$$

$$\text{Double bounce scattering: } \Re(P) < 0 \implies H + V - 2\Re(P) >> X$$

$$\implies H + V - 2\Re(P) >> \frac{H + V - 2\Re(P)}{N} \implies N >> 1$$

The effects of using the N term for sea ice may improve areas covered with more complicated sea ice structures such as deformed ice and leads.

To study the effect of changing the value from 4 in Souyris' method to N in Nord's method—the same color image and scatter plots are generated based on the true quad-pol data. This is illustrated in Figure 6.4. One can clearly see some improvements from Souyris' method. First of all, no underestimation has occurred. This can in fact be proved mathematically. Recall that overestimation is defined when $\frac{X}{H+V}$ is greater than $\frac{1-|\rho_{HHVV}|}{N}$. Since only overestimation or reasonable estimation occurs for this method, the following relation is always true:

$$\frac{X}{H+V} \geq \frac{1-|\rho_{HHVV}|}{N} \implies \frac{X}{H+V} \geq \left(\frac{1-|\rho_{HHVV}|}{H+V-2\Re(P)}\right) X$$

$$\frac{1}{H+V} \geq \left(\frac{1-|\rho_{HHVV}|}{H+V-2\Re(P)}\right) \implies 1 - \frac{2\Re(P)}{H+V} \geq 1 - |\rho_{HHVV}|$$

Subtract and multiply with -1 on both sides to yield:

$$\frac{2\Re(P)}{H+V} \leq \frac{|P|}{\sqrt{HV}} \implies 2\Re(P)\sqrt{HV} \leq |P|(H+V)$$

The arithmetic mean can further be used in the following manner:

$$\sqrt{HV} \leq \frac{H+V}{2}$$

and the following equality is also true:

$$\Re(P) \leq |P| = \sqrt{\Re(P) + \Im(P)}$$

Following this, we can further see that the right side will always be greater than the left side of this equation:

$$2\Re(P)\sqrt{HV} \leq |P|(H+V)$$

From these equations we have proven mathematically that underestimation will not occur for Nord's linking.

Also, Nord's linking seems to be valid for most of the smooth ice covered areas. The leads, rougher sea ice, and ridges seem to be overestimated, more than when $N = 4$ in Figure 6.2. Overall, Nord's method may be a better approach for smooth first-year ice than Souyris' method.

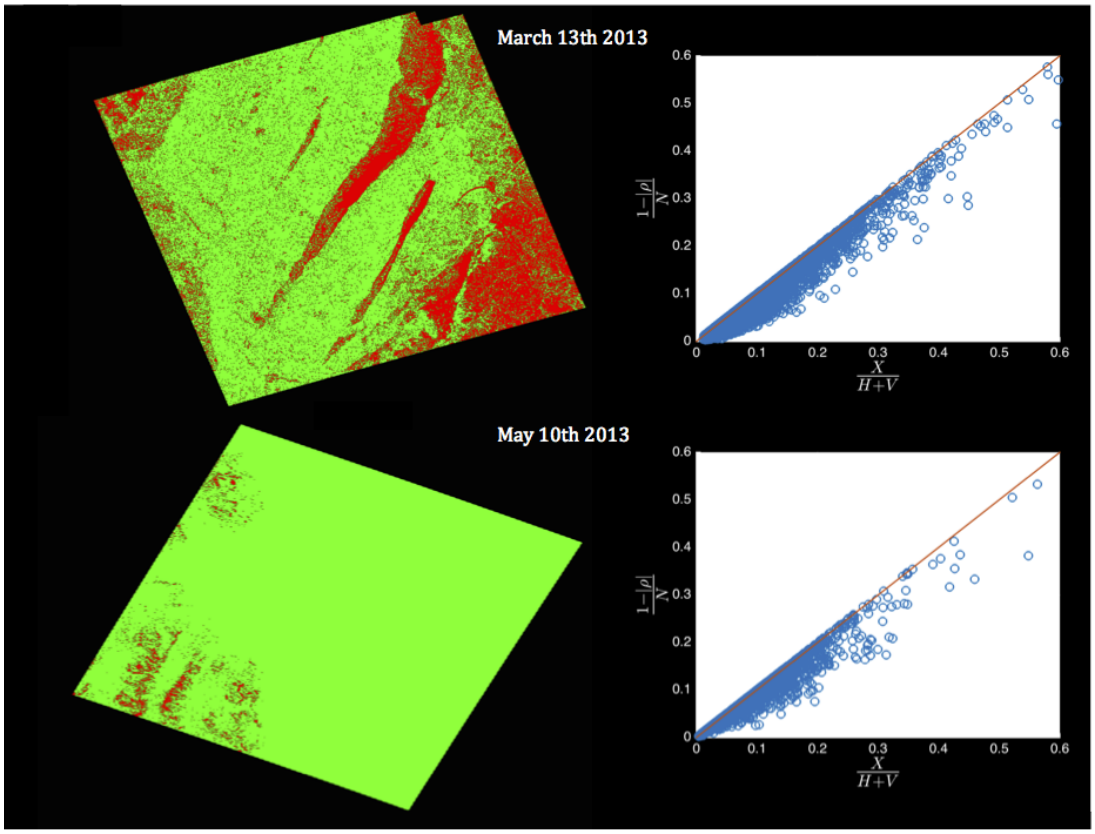

Figure 6.4: Figure shows a color image demonstrating Nord's linking between the cross- and co-pol components. Red color represents overestimation, blue color denotes underestimation, and green color represent when this linking is reasonable. The column to the right shows scatter plots of the two components. The data used are from the quad-pol SAR scenes acquired March 13th and May 8th 2013.

Results of Nord's reconstruction approach

The same scatter plots are created here as for the results obtained from Souyris' method. The results of the reconstructed cross-pol intensity based on simulated hybrid-pol data are shown in Figure 6.5. If the RMSE is considered, the reconstructed cross-pol intensity for pixels covering open water and smooth ice have improved compared to Souyris' algorithm. This however, is not the case if the Pearson correlation coefficient is

considered. In that case, Souyris' reconstruction method performs better than Nord's. One can also observe that for low values of the true cross-pol intensity, it becomes more difficult to reconstruct these elements, for example leads and the sea ice objects. This is more pronounced when using Nord's algorithm compared to Souyris' algorithm. Another important observation from these scatter plots is that all the classes seem to be slightly underestimated compared to Souyris' method. This observation is a result of including the N parameter in the algorithm, which has a high impact on the reconstruction results. The classes representing landfast-, rough-, and deformed ice, as well as the sea ice objects, all have RMSE values that are dominated by the bias (the opposite of the bias that was observed for Souyris). This indicates an underestimation of the cross-pol intensities representing these sea ice types. Overall, using Nord's method, we manage to improve the RMSE for pixels covering open water and smooth ice.

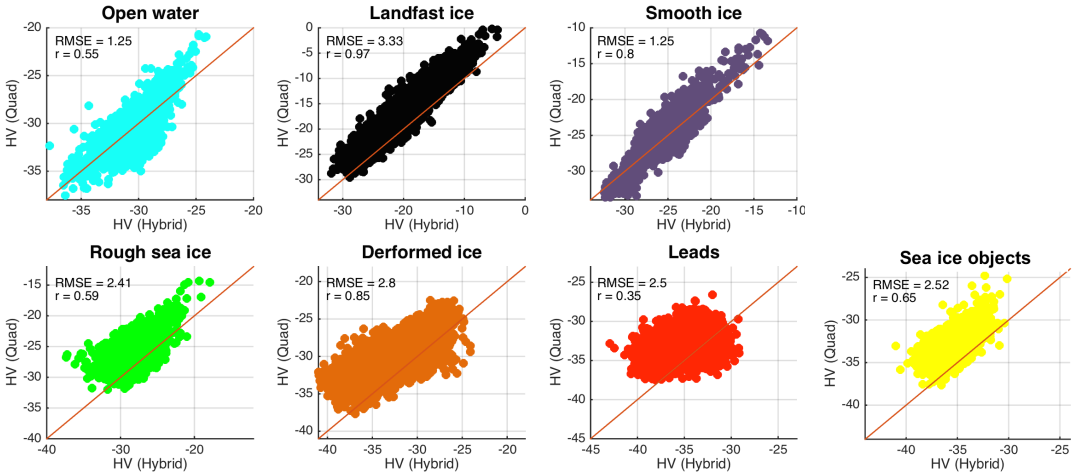

Figure 6.5: Results of Nord's reconstruction for different types of sea ice for the simulated hybrid-pol mode with right-circular polarization at the transmitter. The RMSE and Pearson correlation coefficient for the true and estimated cross-pol intensity (in decibel) are displayed in each scatter-plot. The different sea ice types are selected from the scenes acquired March 13th and May 10th (see chapter 4).

6.2 Suggestions to new methods

The upcoming sections outline a series of new reconstruction approaches, including a modification to Souyris' reconstruction technique.

6.2.1 DoP-based reconstruction

In this section, we describe a novel approach, DoP-based reconstruction. Souyris' method is not always the method best suited for reconstructing a pseudo quad-pol covariance matrix. This is because Souyris' linking (see equation 6.4) may not be valid for a particular surface (like deformed ice, rough sea ice, and leads). Instead of finding a link between the cross- and the co-pol term, one may attempt to use the degree of polarization in the reconstruction phase. The proposed method utilizes the degree of polarization calculated from the Stokes vector in the reconstruction process, hence its name. By considering the DoP in the reconstruction process, it is sometimes possible to achieve a higher reconstruction performance where azimuthal symmetry breaks down.

The DoP-based reconstruction can be performed on all the compact polarimetric modes. The goal is to find the depolarized power and further assign this power value to the power term in the cross-pol intensity, i.e., $\langle |S_{HV}|^2 \rangle$. Note that reciprocity must be assumed to be able to reconstruct a pseudo quad-pol covariance matrix. The variables needed in this method are the components from the Stokes vector and the sample compact covariance matrix.

Before presenting the algorithm, we must first answer an important question: Why is it reasonable to assign the depolarized power to the cross-pol intensity? Depolarized power originates mainly from two mechanisms; volume and surface scattering [Cloude, 2010, p. 142]. The volume scattering power is often estimated directly from the cross-pol power, such as in the Freeman-Durden decomposition [Freeman and Durden, 1998] and in the Pauli decomposition. This is because a response will most likely be generated in the cross-pol channel due to random scattering within the surface material [Elachi and van Zyl, 2006, p. 297]. In [Cloude, 2010] the author stated that all depolarization systems will cause a response in the cross-pol component but not *vice versa*. This means that if a response is generated in the cross-pol channel, it might originate from the depolarized system or other scattering phenomena such as scattering from dipoles with an orientation angle [Cloude, 2010, p. 71]. Surface depolarization might arise in natural surface scattering, such as scattering from rough surfaces. Some of these effects are related to the cross-pol return [Kim et al., 2011]. Based on these observations it may be reasonable to relate the degree of polarization to the cross-pol intensity. This will only hold if we assume that the dominant contribution to the cross-pol intensity is from depolarization effects. This is reasonable for a natural surface such as sea ice. Following this, dipole- and surface scattering are assumed to exhibit zero response in the cross-pol

channel.

There is one main limitation to this method; it assigns all the depolarized power to the cross-pol intensity. The cross-pol power could also be generated from polarized power due to the geometry of the surface [Cloude, 2010, p. 133-134]. Depolarized power might also be present in the co-pol components; since a depolarized system is related to "the coupling of energy from deterministic into stochastic modes of the field", rather than the polarization state of the incident field [Cloude, 2010, p. 72]. In section 6.2.2 we will try to minimize this limitation by considering a model-based technique, which include depolarization in both the co- and cross-pol components.

The concept of DoP-based reconstruction is shown in Figure 6.6, where the $\frac{\pi}{4}$- and hybrid-pol compact modes with right-circular polarization at the transmitter are used. Here, C_{11}, C_{22}, C_{12} and C_{21} represents the elements from the sample hybrid- or $\frac{\pi}{4}$-pol covariance matrix. These elements expressed for the hybrid-pol case are: $C_{11} = \langle |S_{RH}|^2 \rangle$, $C_{22} = \langle |S_{RV}|^2 \rangle$, and $C_{12} = \langle S_{RH} S_{RV}^{\star} \rangle$ (section 5.1.2).

The Stokes vectors in Figure 6.6 represents the Stokes vector generated at the receiver. The degree of polarization is calculated from all the parameters in the Stokes vector, and it is defined as [Raney, 2007]:

$$DoP = \frac{\sqrt{q_1^2 + q_2^2 + q_3^2}}{q_0} \tag{6.14}$$

The DoP is explained in the following manner [Lee and Pottier, 2009, p. 48]:

$DoP = 1$ The received electromagnetic wave is completely polarized, meaning that the polarization state is not random and does not have multiple polarization states [Elachi and van Zyl, 2006, p. 28-30].

$0 < DoP < 1$ The received electromagnetic wave is partially polarized.

$DoP = 0$ The received electromagnetic wave is completely depolarized.

The DoP is basis invariant for the receiving polarization basis, meaning that the same value of DoP is generated independent of the received basis space, i.e., circular, diagonal, or linear basis space [Lee and Pottier, 2009, p. 48]. Note that this is an important fact, as the same DoP value is found for the hybrid-pol and DCP mode.

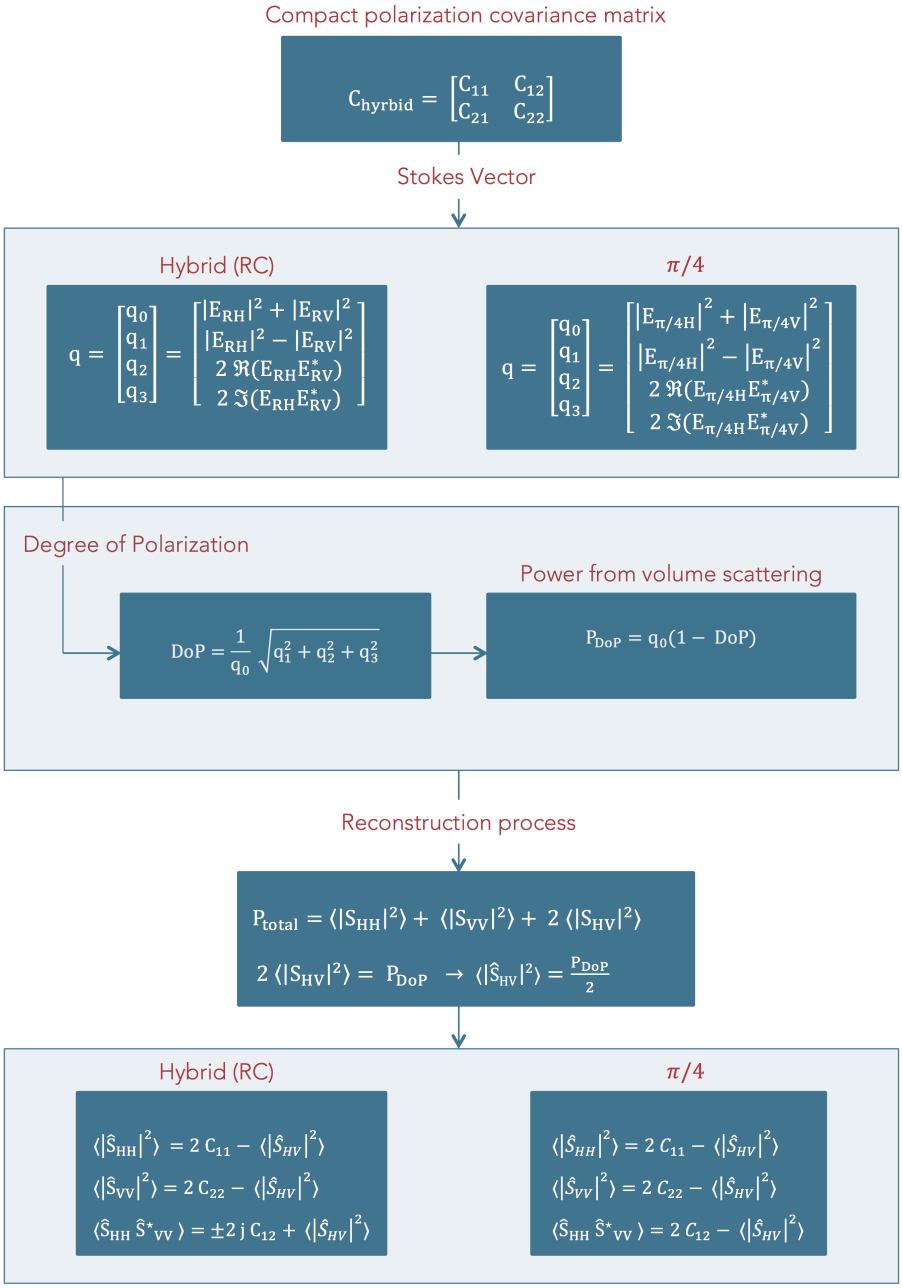

Figure 6.6: Overview of the DoP-based reconstruction method.

The total power generated from a full polarimetric system is [Lee and Pottier, 2009,

p. 65]:

$$P_{Total}^{FP} = \langle |S_{HH}|^2 \rangle + \langle |S_{VV}|^2 \rangle + 2\langle |S_{HV}|^2 \rangle \tag{6.15}$$

The total power generated from a compact-pol system is:

$$P_{Total}^{CP} = C_{11} + C_{22} \tag{6.16}$$

Here, C_{11} and C_{22} represent the diagonal elements in a compact-pol covariance matrix respectively. This power can further be expressed through the elements in the quad-pol covariance matrix as:

$$\begin{aligned} 2P_{Total}^{CP} &= 2C_{11} + 2C_{22} \\ &= \langle |S_{HH}|^2 \rangle + \langle |S_{VV}|^2 \rangle + 2\langle |S_{HV}|^2 \rangle - \Im(S_{HH}S_{HV}^{\star}) + \Im(S_{VV}S_{HV}^{\star}) \end{aligned} \tag{6.17}$$

The value 2 in front of the elements in the above equation originates from the fact that the total power from a full polarimetric system is half the power from a compact polarimetric system. Here, the hybrid compact mode is used, but the same is true for the $\frac{\pi}{4}$ and DCP compact polarization mode. This choice is arbitrary as the total power is the same for all the compact modes. If reflection symmetry is assumed, the total power becomes:

$$2P_{Total}^{CP} = \langle |S_{HH}|^2 \rangle + \langle |S_{VV}|^2 \rangle + 2\langle |S_{HV}|^2 \rangle = P_{Total}^{FP} \tag{6.18}$$

The equality between $2P_{Total}^{CP}$ and P_{Total}^{FP} is demonstrated in Figure 6.7, where the x-axis represents the total power for a quad-pol system, and the y-axis denotes twice the power from a simulated compact-pol system. The deviation in these scatter plots originates from the lack of validity of the reflection symmetry assumption. From these scatter plots the reflection symmetry seems to be a reasonable assumption, especially when the total power is high. Note that fewer data points are located in the region with high total power, which is—most likely—affecting the results.

The power of the depolarized scattering component can be calculated from the first parameter in the Stokes vector and the degree of polarization. This power is calculated in the following way:

$$P_{DoP} = (1 - DoP)q_0 \tag{6.19}$$

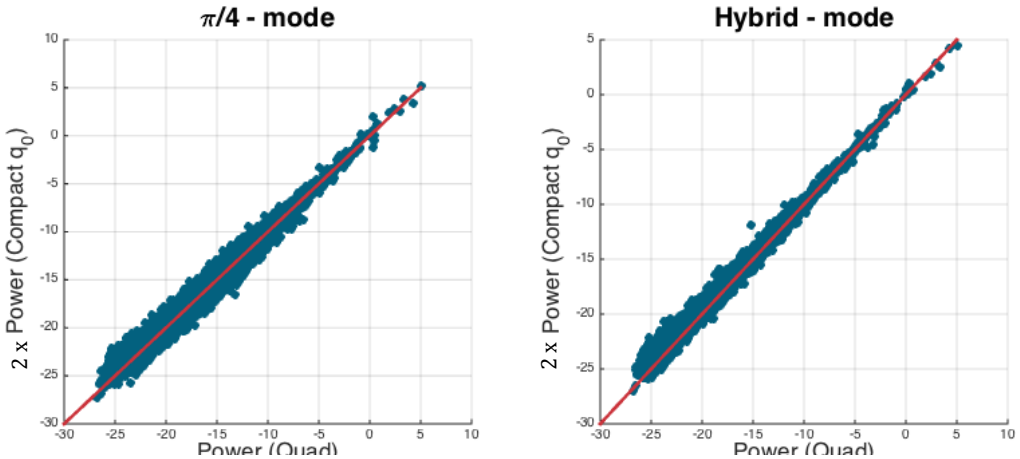

Figure 6.7: The equality between the total power from a full polarimetric system (x-axis) and twice the power from a simulated compact polarimetric system. The data used are the scene acquired March 13th 2013.

This power term was first suggested in [Raney et al., 2012], where it was assigned to the volume scattering power. The parameter q_0 can also be related to the total power calculated from the diagonal elements in the compact-pol and quad-pol covariance matrix, i.e.:

$$P_{DoP} = \frac{1}{2}(1 - DoP)P_{Total}^{FP} \tag{6.20}$$

The DoP is dependent on the polarization state of the system. This can be observed in Figure 6.8, which shows the DoP for different polarization states for compact- and dual-pol systems. The Stokes vector generated from the two dual-pol systems is used to demonstrate the difference from the ones generated from the compact-pol systems. The Stokes vector from the three compact-pol mode systems were discussed in section 5.3.8, and the Stokes vector obtained from the two dual-pol systems are:

- Dual-pol: H transmit, H and V receive. Denoted as {HH, HV}:

$$\boldsymbol{q}_{HH,HV} = \begin{bmatrix} q_0 \\ q_1 \\ q_2 \\ q_3 \end{bmatrix} = \begin{bmatrix} |E_{HH}|^2 + |E_{HV}|^2 \\ |E_{HH}|^2 - |E_{HV}|^2 \\ 2\Re(E_{HH}E_{HV}^{\star}) \\ 2\Im(E_{HH}E_{HV}^{\star}) \end{bmatrix} \tag{6.21}$$

- Dual-pol: V transmit, H and V receive. Denoted as {VV, VH}:

$$\boldsymbol{q}_{VV,VH} = \begin{bmatrix} q_0 \\ q_1 \\ q_2 \\ q_3 \end{bmatrix} = \begin{bmatrix} |E_{VV}|^2 + |E_{VH}|^2 \\ |E_{VV}|^2 - |E_{VH}|^2 \\ 2\Re(E_{VV}E_{VH}^{\star}) \\ 2\Im(E_{VV}E_{VH}^{\star}) \end{bmatrix} \tag{6.22}$$

The DoP calculated from the hybrid-pol and DCP modes are similar, and the DoP values in these two compact modes are lower across some areas compared to the DoP values from $\frac{\pi}{4}$-pol mode and the DoP generated from the dual-pol data. Since the DoP is lower for the hybrid-pol, the estimated cross-pol power will be higher for this mode compared to $\frac{\pi}{4}$-pol mode.

The last block in Figure 6.6 describes the reconstruction phase. The cross-pol intensity, $\langle|S_{HV}|^2\rangle$ is assigned to P_V in the following way:

$$\langle|\hat{S}_{HV}|^2\rangle = \left(\frac{1 - DoP}{2}\right) q_0 \tag{6.23}$$

If DoP is low, more power is assigned to the volume scattering component, meaning that a bigger portion of the wave is depolarized. A higher DoP indicates that a larger portion of the wave is polarized and less power is assigned to the cross-pol intensity.

To be able to find the other elements, $\langle|S_{HH}|^2\rangle$, $\langle|S_{VV}|^2\rangle$, and $\langle S_{HH}S_{VV}^{\star}\rangle$, the assumption of reflection symmetry is necessary. Then these elements can be found by subtracting the estimated cross-pol intensities from the elements in the sample compact covariance matrix. This is done in the following manner for the hybrid-pol mode with right-circular polarization at the transmitter:

$$\langle|S_{HH}|^2\rangle = 2C_{11} - \langle|S_{HV}|^2\rangle \qquad \langle|S_{VV}|^2\rangle = 2C_{22} - \langle|S_{HV}|^2\rangle$$
$$\langle S_{HH}S_{VV}^{\star}\rangle = -2jC_{12} + \langle|S_{HV}|^2\rangle$$

The reconstruction process for the $\frac{\pi}{4}$-pol mode is shown in the last block to the right in Figure 6.6.

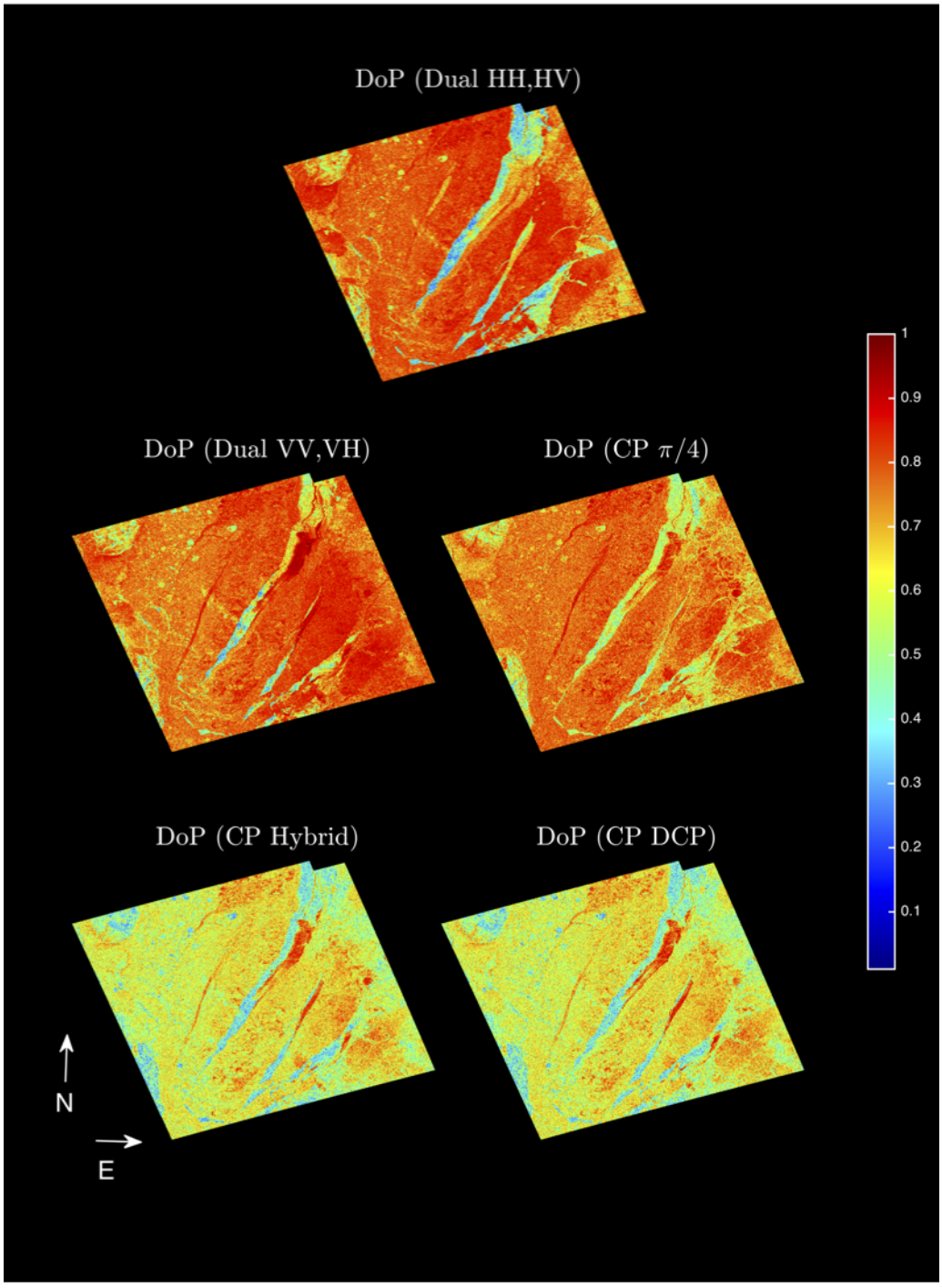

Figure 6.8: DoP calculated from the different sets of Stokes vectors; $\frac{\pi}{4}$-pol, hybrid-pol, DCP, and two dual-pol systems. The colorbar represent the values of the DoP. The SAR scene used is the one acquired March 13th 2013.

Results of DoP-based reconstruction

The same scatter plots are created here as for the results obtained from Nord's and Souyris' methods. The results of the reconstructed cross-pol intensity based on simulated hybrid-pol data are shown in Figure 6.9. If the Pearson correlation coefficient is considered, the pixels with low cross-pol intensity, such as the leads, deformed ice, and open water are improved compared to both Souyris' and Nord's reconstruction approach. High RMSE values, which are dominated by the bias due to high Pearson correlation coefficient, are found for all of them, and we can observe that the cross-pol intensity obtained is overestimated for all the classes. This observation is clearly a result of the last assumption made in this method, i.e., all depolarized power being assigned to the cross-pol intensity. The shapes of the different scatter plots are similar to those corresponding to Souyris' method. This might be becuase both Souyris' and DoP-based reconstruction use a measure of depolarization.

Overall, the cross-pol intensities obtained from the DoP-based reconstruction are mostly overestimated compared to the true cross-pol intensity. However, higher correlation coefficients are achieved for open water, deformed ice, and leads, compared to both Nord's and Souyris' reconstruction methods.

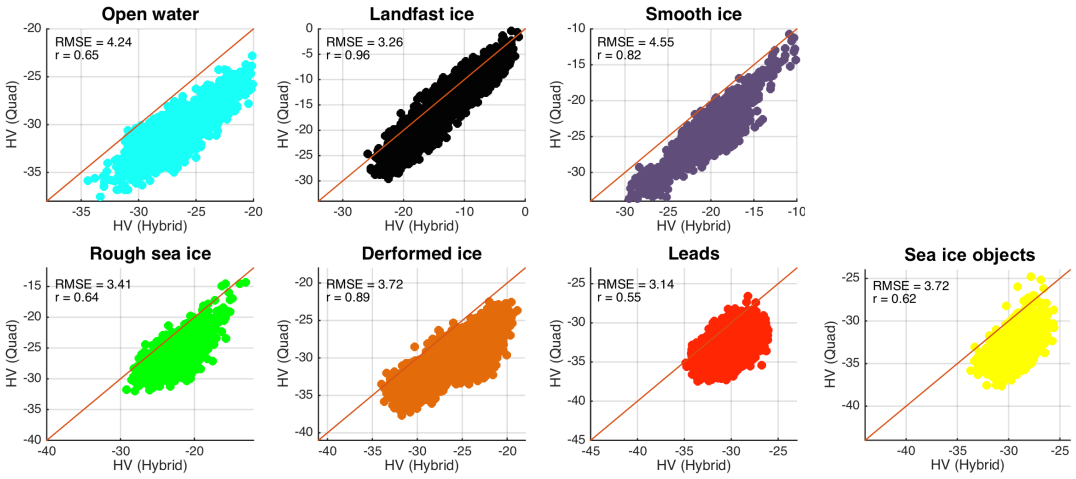

Figure 6.9: Results of DoP-based reconstruction for different types of sea ice for the simulated hybrid-pol mode with right-circular polarization at the transmitter. The RMSE and Pearson correlation coefficient for the true and estimated cross-pol intensity in decibel are displayed in each scatter-plot. The different sea ice types are selected from the scenes acquired March 13th and May 10th 2013 (see chapter 4).

Comparison between Souyris' and DoP-based reconstruction

In the previous section, one similarity between the DoP-based reconstruction and Souyris' methods becomes apparent; both utilize a measure of depolarization. Souyris suggests a linking between the co- and cross-pol scattering intensities in the following way:

$$\frac{X}{H+V} = \frac{1-|\rho_{HHVV}|}{4} \implies X_S = \frac{1-|\rho_{HHVV}|}{4}(H+V) \tag{6.24}$$

Here, X_S denotes the estimated cross-pol intensity obtained from Souyris' algorithm. The DoP-based reconstruction suggests the following algorithm:

$$X_{DoP} = \frac{1-DoP}{2}P^{CP}_{Total} = \frac{1-DoP}{4}P^{FP}_{Total} = \frac{1-DoP}{4}(H+V+2X) \tag{6.25}$$

$$X_{DoP} = \frac{1-DoP}{2\,(1+DoP)}(H+V) \tag{6.26}$$

Here, X_{DoP} denotes the estimated cross-pol intensity obtained from the DoP-based reconstruction algorithm. In case of a fully polarized wave, the degree of coherency becomes: $\rho_{HHVV} = 1$, which results in zero response in the cross-pol intensity. In the DoP-based reconstruction, the DoP becomes one, which will also provide zero response in the cross-pol intensity. If the wave is fully depolarized, the degree of coherency becomes equal to zero, and the estimated cross-pol intensity is:

$$X_S = \frac{1}{4}(H+V) \tag{6.27}$$

For a fully depolarized wave the degree of polarization becomes zero, and the cross-pol intensity is:

$$X_{DoP} = \frac{1}{2}(H+V) \tag{6.28}$$

The estimated cross-pol intensity obtained from DoP-based reconstruction is twice that of the cross-pol intensity obtained from Souyris' method.

6.2.2 Model-based reconstruction

As mentioned in the introductory part of the DoP-based reconstruction section; this method may fail if some of the depolarized power belongs to the co-pol components, which may be the case for surface effects related to rough and highly deformed ice. Recall that polarized power from surface scattering may also generate response in the cross-pol intensity. Then recall the assumption made in the DoP-based reconstruction; only depolarized power generates a response in the cross-pol channel. One way to remedy this assumption is to use a scattering decomposition model for sea ice. For example, in [Eltoft et al., 2014] the authors suggested to decompose the quad-pol covariance matrix into a volume and a surface contribution when analyzing sea ice covered SAR scenes. In the following, we propose a novel[2] *model-based* reconstruction technique that leverage this scattering decomposition model to find the necessary cross-pol intensity to obtain a pseudo quad-pol covariance matrix.

The upcoming theory highlights how these contributions are modeled for each scattering mechanism, and how we can utilize this model to find the desired cross-pol intensity.

The volume scattering matrix was modeled as [Eltoft et al., 2014]:

$$\boldsymbol{T}_V = \frac{P_V}{3-\rho_L}\begin{bmatrix} 1+\rho_L & 0 & 0 \\ 0 & 1-\rho_L & 0 \\ 0 & 0 & 1-\rho_L \end{bmatrix} \tag{6.29}$$

where ρ_L is the shape parameter describing the shape of the particles that causes the volume scattering (for example when $\rho_L = 1/3$ then the particles have a cylindrical shape, and for $\rho_L = 1$ then the particles are shaped spherically [Eltoft et al., 2014]). P_V is the total power generated from the volume scattering. The shape of the coherency matrix above indicates an assumption of azimuthal symmetry for the volume scattering case. This matrix also relies on the assumption that the scattering elements are randomly oriented described by the shape parameter. This indicates that the total backscattered signal from the randomly oriented scattering elements has no preferential direction [Hajnsek et al., 2009]. Further, the surface scattering matrix was modeled using an

2. In the Journal of Sensors, published May 2015, Yin et al. presented a similar mode-based reconstruction method. This method, however, is intended for oil-spill observation, and is based on a three-component scattering model integrated with Souyris' method [Yin et al., 2015]. Note that even though the naming of these techniques overlap, they have been developed independently without any relationship to each other.

X-Bragg model in the following manner:

$$\boldsymbol{T}_S = \frac{P_S}{1+|\beta|^2}\begin{bmatrix} 1 & \beta\text{sinc}(2\delta) & 0 \\ \beta^\star\text{sinc}(2\delta) & \frac{1}{2}|\beta|^2(1+\text{sinc}(4\delta)) & 0 \\ 0 & 0 & \frac{1}{2}|\beta|^2(1-\text{sinc}(4\delta)) \end{bmatrix} \tag{6.30}$$

where P_S is the total power generated for surface scattering. The roughness effect is accounted for by integrating a Bragg surface over the line-of-sight rotation angle distribution parameterized by the width δ of the distribution [Cloude, 2010, p. 133-138]. More information about the X-Bragg model and how to integrate a Bragg surface with a rotation angle distribution can be found in [Cloude, 2010, p. 133-138]. The δ is assumed to account for the amount of deformation of the scattering surface, where δ is close to zero for smooth surfaces, and δ is large for deformed ice [Eltoft et al., 2014]. This means that the δ accounts for surface slopes, and is referred to as the *surface slope angle*. β is a parameter based on Fresnel's equations [Cloude, 2010, p. 137]. I.e.:

$$\beta = \frac{R_{HH}-R_{VV}}{R_{HH}-R_{VV}},\quad R_{HH} = \frac{\cos\theta - \sqrt{\epsilon-\sin^2\delta}}{\cos\theta - \sqrt{\epsilon+\sin^2\delta}},\quad R_{VV} = \frac{(\epsilon-1)\sin^2\theta - \epsilon(1+\sin^2\delta)}{\cos\theta + \sqrt{\epsilon+\sin^2\delta}} \tag{6.31}$$

Here, θ is the incidence angle, R is the reflection coefficient, and ϵ is the dielectric constant (see chapter 3). Reflection symmetry is assumed for the surface scattering model, and that this matrix (equation 6.30) is rotated in the plane perpendicular to the scattering plane [Eltoft et al., 2014]. As can be seen, this model is built up based on surface roughness, dielectric constant, and surface slope [Cloude, 2010, p. 136-137]. Note that $\boldsymbol{T}_S$ is an average over the surface orientation angle which is assumed to be uniformly distributed. In [Eltoft et al., 2014] the authors argued that the double bounce (P_D) scattering return was low for sea ice and that surface and volume scattering mostly determined the response. This will also be assumed in this case in order to use this model. However, this may cause some problems for some areas close to leads, where double bounce scattering might occur between the leads and the surrounding smooth sea ice. The overall coherency matrix is then given as:

$$\boldsymbol{T} = \boldsymbol{T}_V + \boldsymbol{T}_S \tag{6.32}$$

Depolarization effects are considered in both the volume and surface scattering models, as depolarization in surface scattering is related to rough and highly deformed ice [Eltoft et al., 2014]. The solutions to the parameters in equations 6.29 and 6.30 are

[Eltoft et al., 2014]:

$$|\hat{\beta}| = \frac{|T_{22} - T_{33}|}{\cos(2\delta)\,|T_{12}|} \tag{6.33}$$

$$P_S = \frac{|T_{12}|}{|\hat{\beta}|\mathrm{sinc}(2\delta)} \tag{6.34}$$

$$P_V = P_{Total} - P_S \qquad P_D = 0 \tag{6.35}$$

$$\hat{\rho}_L = \frac{3S + (2 - |\hat{\beta}|^2)P_V}{S + (2 + |\hat{\beta}|^2)P_V} \tag{6.36}$$

$$S = |\hat{\beta}|^2(T_{11} - (T_{22} + T_{33})) \tag{6.37}$$

Here T_{ij} represents the elements in the coherency matrix (see section 2.2.2), i.e.:

$$\boldsymbol{T}_3 = \begin{bmatrix} T_{11} & T_{12} & T_{13} \\ T_{21} & T_{22} & T_{23} \\ T_{31} & T_{32} & T_{33} \end{bmatrix} \tag{6.38}$$

Next, the main challenge is to solve this non-linear system using the compact-pol data. If the quad-pol data were given, this would still be impossible to solve since there are four independent equations with five unknowns (β, ρ, δ, P_S and P_V). To enable solutions of this system, one parameter must be fixed or prior assumption is necessary. Hence, in [Eltoft et al., 2014] the authors suggested to fix the shape parameter to be able to solve this system. The purpose of using such a model for our case, is to enable an estimate of the cross-pol intensity. The estimated cross-pol intensity can be expressed as:

$$T_{33} = 2\hat{X} = T_{33}^S + T_{33}^V \tag{6.39}$$

Inserting the expression for T_{33}^S from equation 6.30 and the expression for T_{33}^V from 6.29 yields:

$$2\hat{X} = \frac{1}{2}|\beta|^2(1 - \mathrm{sinc}(4\delta))\frac{P_S}{1 + |\beta|^2} + \frac{1 - \rho_L}{3 - \rho_L}P_V \tag{6.40}$$

One can see that the contribution to the cross-pol originates from both surface and volume scattering. When $\delta = 0$; sinc(4δ) becomes equal to zero, and the estimated cross-pol intensity becomes:

$$2\hat{X} = \frac{1-\rho_L}{3-\rho_L} P_V \tag{6.41}$$

This results in contribution from the volume scattering model alone. When $\rho_L = 1$, the estimated cross-pol intensity becomes:

$$2\hat{X} = \frac{1}{2}|\beta|^2(1-\text{sinc}(4\delta))\frac{P_S}{1+|\beta|^2} \tag{6.42}$$

Here, the estimated cross-pol intensity will only be a function of the surface scattering model. The main challenge is to find the unknown parameters based on the compact-pol data. The following procedure is therefore suggested:

- From the hybrid-pol data, the following elements from the coherency matrix in equation 6.38 are available (under the reflection symmetry assumption):

$$\begin{aligned} T_{11} &= \frac{1}{2}\langle|S_{HH}+S_{VV}|^2\rangle = \frac{1}{2}(H+V+2\Re(P)) \\ &= C_{11}+C_{22}-X+\Re(-2jC_{12}+X) \\ &= C_{11}+C_{22}-X+\Re(-2jC_{12}+X) = C_{11}+C_{22}-2\Re(jC_{12}) \end{aligned} \tag{6.43}$$

$$\begin{aligned} T_{12} &= \frac{1}{2}\langle(S_{HH}+S_{VV})(S_{HH}-S_{VV})^\star\rangle = \frac{1}{2}(H-V-P^\star+P^\star) \\ &= \frac{1}{2}(H-V-2j\Im(P)) \\ &= C_{11}-X-C_{22}+X-j\Im(-2jC_{12}+X) = C_{11}-C_{22}+2j\Im(jC_{12}) \end{aligned} \tag{6.44}$$

  Since the cross-pol intensity is real, it becomes zero when the imaginary operator is applied. Recall that H, V, X, and P represent the elements in the quad-pol covariance matrix (see equation 6.5), and C_{11}, C_{22}, and C_{12} represent the elements in the hybrid-pol covariance matrix (see equation 6.8). The element T_{22} can be

expressed as a function of the cross-pol intensity, i.e.:

$$\begin{aligned} T_{22} &= \frac{1}{2}\langle |S_{HH} - S_{VV}|^2 \rangle = \frac{1}{2}(H + V - 2\Re(P)) \\ &= \frac{1}{2}(2C_{11} - X + 2C_{22} - X - 2\Re(-2jC_{12} + X)) \\ &= C_{11} + C_{22} + 2\Re(jC_{12}) - 2X \end{aligned} \tag{6.45}$$

- The surface scattering power is calculated as a function of δ in the following way:

$$P_S = \frac{|T_{12}|}{|\hat{\beta}|\text{sinc}\,(2\delta)} \tag{6.46}$$

- The volume scattering power is calculated as:

$$P_V = P_{Total} - P_S \tag{6.47}$$

- β is as a function of the compact-pol parameters, δ, and the cross-pol intensity, i.e.:

$$|\beta| = \frac{|T_{22} - T_{33}|}{\cos(2\delta)|T_{12}|} = \frac{|C_{11} + C_{22} + 2\Re(jC_{12}) - 4X|}{\cos(2\delta)|T_{12}|} \tag{6.48}$$

- Inserting for T_{11}, T_{22}, and T_{33} from equations 6.43 and 6.49, and substituting $T_{33} = 2X$ in equation 6.37, the parameter S becomes:

$$\begin{aligned} S &= |\beta|^2(T_{11} - (T_{22} + T_{33})) \\ &= |\beta|^2(C_{11} + C_{22} - 2\Re(jC_{12}) - (C_{11} + C_{22} + 2\Re(jC_{12} - 2X + 2X))) \\ &= -4|\beta|^2\Re(jC_{12}) \end{aligned} \tag{6.49}$$

- This expression for S can be inserted for the expression for the shape parameter, ρ_L, in equation 6.36.

- The cross-pol intensity is expressed as a function of δ, i.e:

$$2\hat{X} = \frac{1}{2}\frac{P_{Total} - P_V(\delta)}{1 + |\hat{\beta}(X)|^2}|\hat{\beta}(X)|^2(1 - \text{sinc}(4\delta)) + \frac{P_V(\delta)}{3 - \rho_L(X)}(1 - \rho_L(X)) \tag{6.50}$$

Following this, we are left with only one non-linear equation with two unknowns (cross-pol intensity and δ). This can be solved by considering this problem as an optimization problem where the non-linear cost function can be defined as:

$$\text{minimize } J_X(X) = 2X - \left(\frac{1}{2} \frac{P_S(\delta)}{1 + |\hat{\beta}(X)|^2} |\hat{\beta}(X)|^2 (1 - \text{sinc}(4\delta)) + \frac{P_V(\delta)}{3 - \rho(X)} (1 - \rho_L(X)) \right)$$

$$\text{subject to: } 0 < X < \frac{2}{3} C_{11}, \;\; 0 < X < \frac{2}{3} C_{22}, \;\; 0 < \delta < \frac{\pi}{4}$$

The boundary conditions of the cross-pol intensity is determined by the following reasoning:

$$2C_{11} = H + X \qquad 2C_{22} = V + X \tag{6.51}$$

Often, the cross-pol intensity is smaller than the co-pol intensities. We can therefore assume that the cross-pol intensity is at least half the power of the co-pol intensities (see box plot in Figure 5.5), i.e.:

$$\frac{1}{2} H \geq X, \qquad \frac{1}{2} V \geq X \tag{6.52}$$

Inserting for H and V:

$$2C_{11} - 2X \geq X \implies 0 \leq X \leq \frac{2}{3} C_{11} \tag{6.53}$$

$$2C_{22} - 2X \geq X \implies 0 \leq X \leq \frac{2}{3} C_{22} \tag{6.54}$$

It is physically impossible that the δ is smaller than zero because the surface slope will be negative, i.e.: below the ground. The reason that the δ is smaller than 45° is because of the expression for $|\beta|$ in equation 6.33. If δ was larger than 45°, the right-hand side of equation 6.33 would become negative, which is not possible since the left-hand side equals $|\beta|$ and must be non-negative.

The author has discovered a correlation between δ and the degree of polarization. This discovery might help when searching for a solution that will minimize our cost function. The "true" δ was calculated from the four SAR scenes from Storfjorden. This was done by searching for the δ that will minimize the cost function using the true cross-pol intensities. Note that the cost function will not have an unique minimum, but a bounded one [Eltoft et al., 2014]. Figure 6.10 illustrates the results of the "true" δ (in degrees) as

a function of DoP. The δ is between $20° - 25°$ when the values of the DoP is below 0.5. From the sea ice model, such values of δ indicates that the sea ice type is somewhere in between smooth and deformed sea ice [Eltoft et al., 2014]. When the values of the DoP are above 0.7, the values of δ fluctuate for the four scenes, but the δ increases towards $45°$ when DoP approaches 1. The δ as a function of DoP based on the data acquired March 13th deviates from the other three scenes, but the shape seems reasonable for DoP values below 0.8. The reason that δ and DoP are somehow related is mainly because both DoP and δ controls the depolarizations, as stated in [Hajnsek et al., 2009].

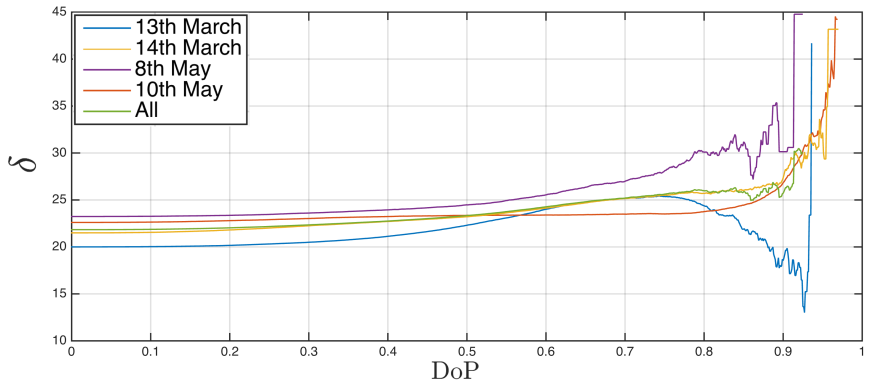

Figure 6.10: The "true" δ as a function of DoP calculated from the SAR scenes acquired March 13th (blue line), March 14th (yellow line), May 8th (purple line), and May 10th (red line). The green line denotes an average of the four δ calculated from the four scenes.

From this discovery, it is tempting to find an expression of δ as a function of the DoP. Following this, we can further develop an empirical model of δ from DoP as a polynomial, i.e.:

$$\hat{\delta} = \sum_{n=0}^{N-1} a_n DoP^n = a_0 + a_1 DoP + \ldots + a_{N-1} DoP^{N-1} \tag{6.55}$$

where DoP is the degree of polarization, and a_i for $i \in \{0, 1, \ldots, N\}$ are the coefficients of the polynomial. There are a number of limitations when using an empirical model. This is because the coefficients found may be dependent on several factors, such as the SAR scene, geographic location, weather, season, incident angle, frequency, sea ice condition, etc. The main concern is whether this model has a general validity. Since the behavior between DoP and δ seems to be consistent across the four SAR scenes given in this work, we can confirm the general validity on the SAR scene, weather, season, incident angle and sea ice condition, but not geographic location and frequency. This should, however, be tested. From this discovery, we can confirm that the ratio between

DoP and δ is partially general, but more tests should be carried out for another location and also other frequencies.

δ as a function of DoP is not a linear curve, which indicates that N must be higher than one. Several tests were conducted to find the N that mach this curve best. The coefficients are found based on a regression model called *polyfit* in Matlab, which is a N'th order polynomial regression model adapted by the least squares method. The data from March 14th and May 8th scenes are our training data. The test data are from March 13th and May 10th scenes. The reason for dividing the four scenes into test and training data is to make these coefficients as general as possible for sea ice, as well as scene independent.

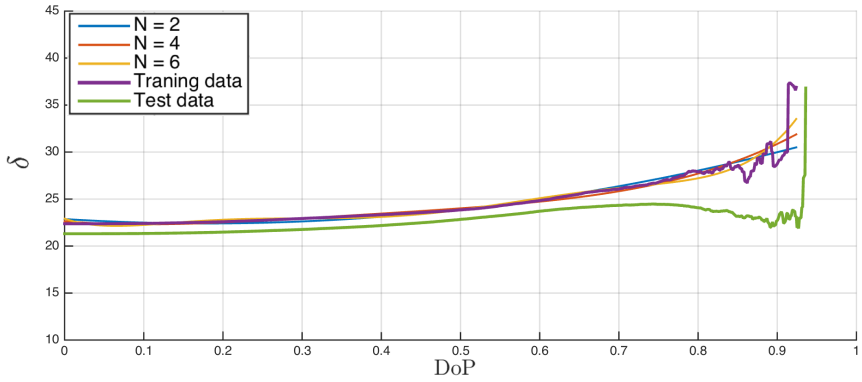

Figure 6.11: δ as a function of DoP, based on a regression model when $N = 2$ (blue line), $N = 4$ (red line), and $N = 6$ (yellow line). The purple line denotes the δ as a function of DoP based on the training data, while the green line is the test data.

From Figure 6.11, an appropriate order for the polynomial model seems to be 2. This yields a *quadratic* polynomial function on the form:

$$\hat{\delta} = a_0 + a_1 DoP + a_2 DoP^2 \tag{6.56}$$

The generated coefficients based on the training data are:

$$\boldsymbol{q} = \begin{bmatrix} a_0 \\ a_1 \\ a_2 \end{bmatrix} = \begin{bmatrix} 0.3992 \\ -0.0910 \\ 0.2545 \end{bmatrix} \tag{6.57}$$

By utilizing the relationship between the width of the surface distribution (δ) and the

degree of polarization, only the cross-pol intensity is unknown when minimizing the cost function, which becomes:

$$\text{minimize } J_X(X) = 2X - \left(\frac{1}{2} \frac{P_S(\delta)}{1 + |\hat{\beta}(X)|^2} |\hat{\beta}(X)|^2 (1 - \text{sinc}(4\delta(DoP))) + \frac{P_V(\delta)}{3 - \rho_L(X)} (1 - \rho_L(X)) \right)$$

$$\delta(DoP) = 0.3992 - 0.0910 DoP + 0.2545 DoP^2$$

$$\text{subject to: } 0 < X < \frac{2}{3} C_{11} \quad 0 < X < \frac{2}{3} C_{22}$$

The following optimization problem can be solved using *fmincon* in Matlab, which searches for a constrained minimum of a function of several variables with both linear and non-linear constraints. An initialization value is necessary, and is set to zero for the cross-pol intensity. The other elements (H,V, and P) in the quad-pol covariance matrix are then found by using equation 6.7, i.e., subtracting the estimated cross-pol intensity from the compact-pol intensities. This method is referred to as the model-based reconstruction.

Results of model-based reconstruction

The same scatter plots are created here as for the other reconstruction methods, and the results are displayed in Figure 6.12. The estimated cross-pol intensities obtained from the model-based reconstruction have improved compared to both Souyris' and Nord's methods for rough sea ice, deformed sea ice, and sea ice objects if the RMSE is considered. The Pearson correlation coefficients for all the types are similar to the ones obtained from Souyris' and DoP-based reconstruction methods, except for the open water class, where both the RMSE and the Pearson correlation coefficient are worse. Most of the values in the reconstructed cross-pol intensity based on DoP-based reconstruction were slightly overestimated. By introducing a model-based technique, the overestimation is reduced, and in some cases the values are underestimated (for leads and sea ice objects). Overall, the deformed sea ice class has improved compared to the other three methods discussed so far.

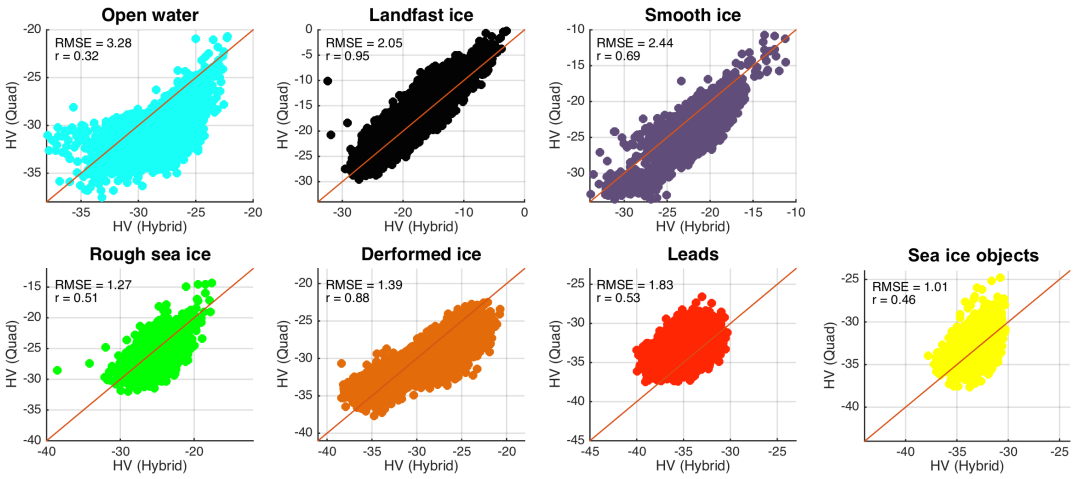

Figure 6.12: Results of model-based reconstruction for different types of sea ice for the simulated hybrid-pol mode with right-circular polarization at the transmitter. The RMSE and Pearson correlation coefficients for the true and estimated cross-pol intensity (in decibel) are displayed in each scatter-plot. The different sea ice types are selected from the scenes acquired March 13th and May 10th (see chapter 4).

6.2.3 Eigenvalue-based reconstruction

As was discovered in DoP-based reconstruction, the cross-pol power can be reconstructed based on the first parameter in the Stokes vector and the degree of polarization. This method attempts to find a fraction of the total power that belongs to the cross-pol intensity. This fraction can be found by considering a new novel approach, namely eigenvalue-based reconstruction. The fraction in the DoP-based reconstruction was based on $1 - DoP$, which is closely related to the entropy [Cloude et al., 2012]. Therefore, it is desirable to find a fraction of the total power that is zero when the cross-pol intensity is zero, and non-zero otherwise. Mathematically, this can be expressed as:

$$\langle |\hat{S}_{HV}|^2 \rangle = \frac{\gamma}{2} q_0 \tag{6.58}$$

Here, γ is the unknown variable that must be found. The suggested eigenvalue-based reconstruction postulates that this fraction can be determined from the eigenvalues generated from the Stokes vector. The eigenvalues of the 2×2 Hermitian sample covariance matrix can be found through the Stokes vector [Lee and Pottier, 2009, p. 49],

i.e.:

$$\lambda_1 = \frac{1}{2}\left(q_0 + \sqrt{q_1^2 + q_2^2 + q_3^2}\right) \tag{6.59}$$

$$\lambda_2 = \frac{1}{2}\left(q_0 - \sqrt{q_1^2 + q_2^2 + q_3^2}\right) \tag{6.60}$$

where $\lambda_1 \geq \lambda_2$. The author suggests that the γ can be approximated by:

$$\gamma = \frac{\lambda_2}{\lambda_1} \tag{6.61}$$

The reason that this may be reasonable is that when $\lambda_2 = 0$, the outgoing wave is completely polarized, and relatively little power is assigned to the cross polarization component. If, however, $\lambda_1 = \lambda_2$, the outgoing wave is completely unpolarized and power is generated in the cross-pol intensity [Lee and Pottier, 2009, p. 49]. The fraction between the two eigenvalues can be related to the compact-pol pedestal height (PH) (see section 5.3.7), where targets dominated by volume scattering or multiplelayer scattering have significant PH values [Jiao et al., 2011]. Figure 6.13 shows the true values of $2\frac{\langle|S_{HV}|^2\rangle}{q_0}$ and compares it with the γ values computed from the compact-pol data. Note that $\langle|S_{HV}|^2\rangle = I_{HV}$ is computed from the reference quad-pol data used to simulate compact-pol data, and is therefore constant. The q_0, however, depend on the compact-pol mode. Hence, so does the so-called true γ, i.e:

$$\gamma_{true} = 2\frac{\langle|S_{HV}|^2\rangle}{q_0} \tag{6.62}$$

From the images in Figure 6.13 the estimated γ value for both the hybrid-pol and DCP modes seems to be overestimated for smooth ice, rough ice, and ridges, while the leads seem to have a reasonable estimate (see Figure 4.6 for location of the different sea ice classes). The best estimates of γ seem to be generated from the $\frac{\pi}{4}$-pol mode.

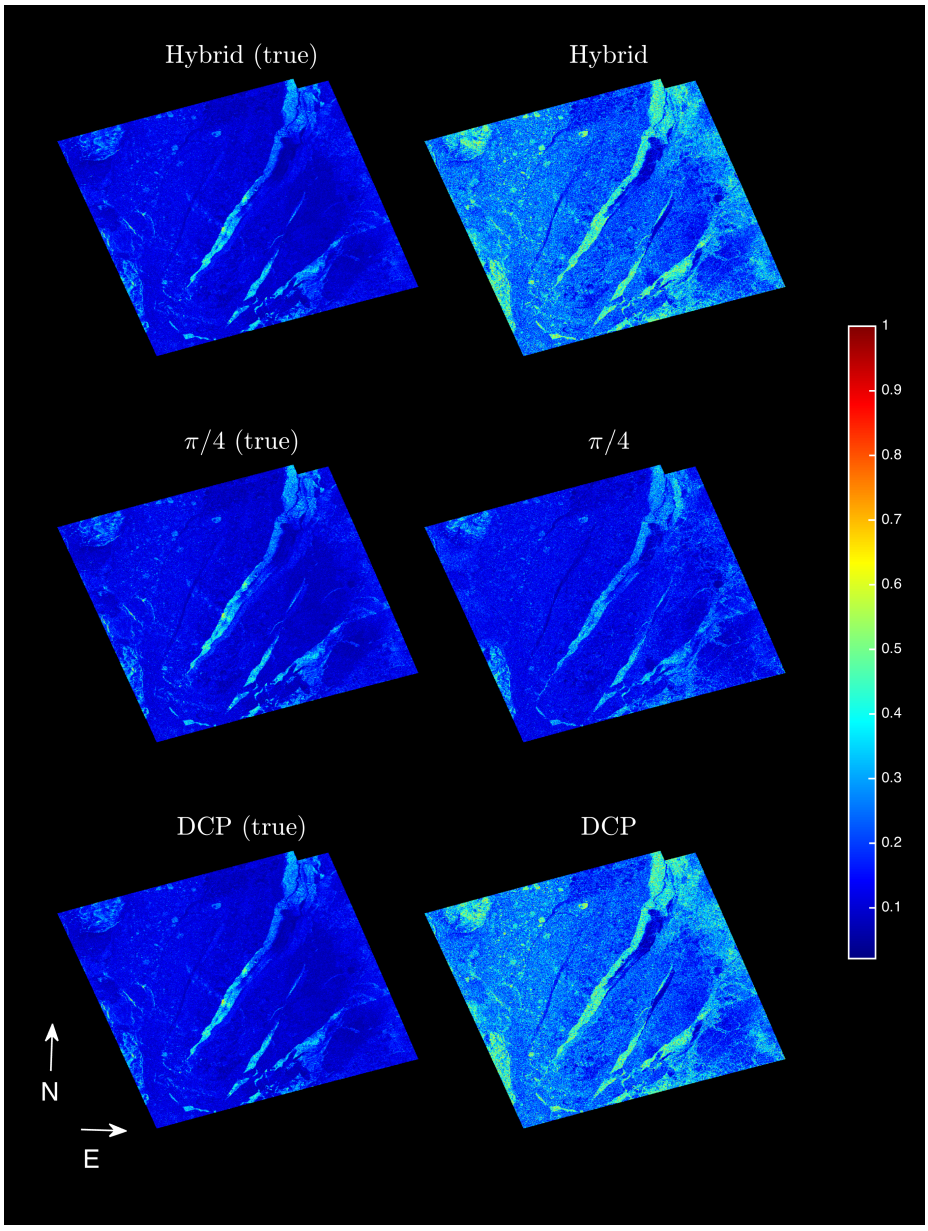

Figure 6.13: Comparison between the true γ calculated from the true cross-pol intensity (column to the left) and the proposed γ calculated from equation 6.63 using the three compact polarization modes when calculating the first parameter in Stokes vector (q_0) (column to the right).

The estimated cross-pol intensity obtained from the eigenvalue-based reconstruction

can be expressed using the degree of polarization (DoP), i.e.:

$$\langle|\hat{S}_{HV}|^2\rangle = \frac{\gamma}{2}q_0 = \frac{\lambda_2}{\lambda_1}\frac{q_0}{2} \tag{6.63}$$

Inserting for λ_1 and λ_2 from equations 6.59 and 6.60 yields:

$$\langle|\hat{S}_{HV}|^2\rangle = \frac{q_0 - \sqrt{q_1^2 + q_2^2 + q_3^2}}{q_0 + \sqrt{q_1^2 + q_2^2 + q_3^2}}\frac{q_0}{2} \tag{6.64}$$

Inserting for $\sqrt{q_1^2 + q_2^2 + q_3^2} = DoPq_0$ from equation 6.14 yields:

$$\langle|\hat{S}_{HV}|^2\rangle = \left(\frac{q_0 - q_0DoP}{q_0 + q_0DoP}\right)\frac{q_0}{2} = \left(\frac{1 - DoP}{1 + DoP}\right)\frac{q_0}{2} \tag{6.65}$$

The estimated cross-pol intensity from DoP-based reconstruction was defined as:

$$\langle|\hat{S}_{HV}|^2\rangle = \frac{1 - DoP}{2}q_0 \tag{6.66}$$

The fraction between the two eigenvalues is highly dependent on the degree of polarization as observed in equation 6.63. Changing from $1 - DoP$ in the DoP-based reconstruction to $\frac{1-DoP}{1+DoP}$ in the eigenvalue-based reconstruction may produce higher accuracy. This is because the fraction in front of the total power in equation 6.63 has been normalized. To study the effect of this approach, the RMSE between the estimated and the true cross-pol intensity is calculated for different intervals of the degree of polarization from both DoP-based and eigenvalue-based reconstruction. The results are illustrated in Figure 6.14, and is created from random sampling (using a random number generator in Matlab) from the cross-pol intensity data from March 13th and May 10th scenes, respectively.

Clearly, normalizing the fraction in front of the total power when estimating the cross-pol intensity seems to result in higher accuracy. The eigenvalue-based reconstruction is therefore considered as a better approach than the DoP-based reconstruction. The accuracy of the eigenvalue-based reconstruction increases with the degree of polarization, while the performance of the DoP-based reconstruction is relatively constant across the different values of the DoP. The other elements (H,V, and P) in the quad-pol covariance

matrix are then found by using equation 6.7, i.e., subtracting the estimated cross-pol intensity (in equation 6.63) from the compact-pol intensities.

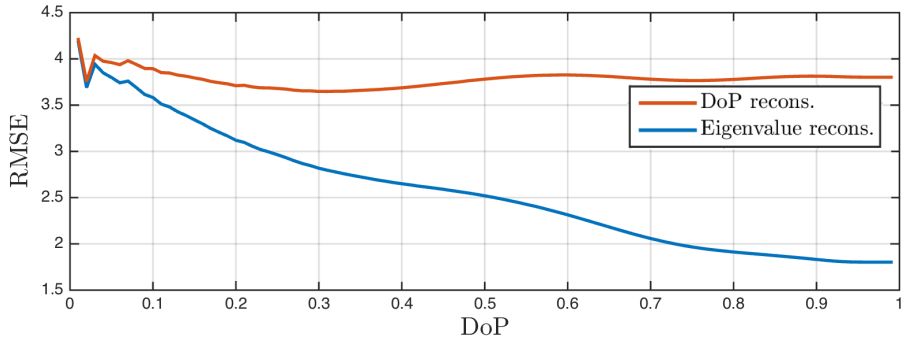

Figure 6.14: RMSE between the estimated and the true cross-pol intensity for the eigenvalue- (blue line) and DoP-based reconstructions (red line) as a function of the degree of polarization. The reconstruction is based on the simulated hybrid-pol data from the March 13th and May 10th scenes. The data are selected randomly using a random number generator in Matlab, and smoothed to avoid large fluctuations.

Results of eigenvalue-based reconstruction

The same scatter plots are created as for the other reconstruction methods, and the results are displayed in Figure 6.15. The estimated cross-pol intensity for pixels covering open water is the best so far, both with regards to the RMSE and the Pearson correlation coefficient. Reasonable results are achieved for landfast, deformed, and smooth ice. For low backscattering targets, the reconstruction shows similar results to model-based reconstruction and DoP-based reconstruction. In fact, the correlation coefficients are similar to the ones obtained from the DoP-based reconstruction, but the RMSE have improved drastically for the eigenvalue-based reconstruction. This indicates that the bias introduced by the previous reconstruction methods has been reduced.

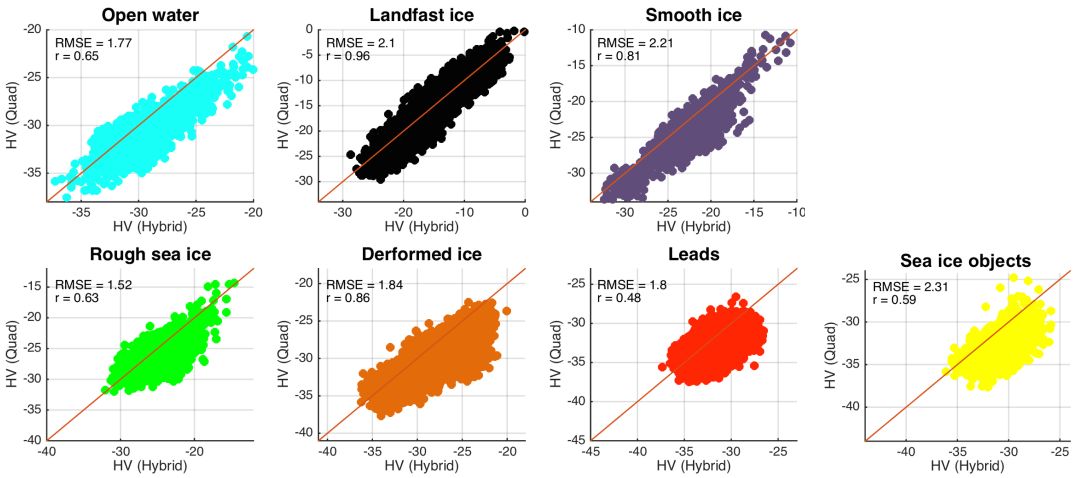

Figure 6.15: Results of eigenvalue-based reconstruction for different types of sea ice for the simulated hybrid-pol mode with right-circular polarization at the transmitter. The RMSE and Pearson correlation coefficient for the true and estimated cross-pol intensity (in decibel) are displayed in each scatter-plot. The different sea ice types are selected from the scenes acquired March 13th and May 10th (see chapter 4).

6.2.4 Modified Souyris' reconstruction method

This section presents a modified Souyris' reconstruction method. The challenges of Souyris' reconstruction method are to determine the number of iterations necessary to obtain a decent result, as well as the lack of a cost function. In this section, a novel approach is presented to improve this method in the reconstruction process by changing the iterative approach into an optimization problem.

The modified version approach results from changing Souyris' method in the following way:

- The linking proposed by Souyris is:

$$\frac{X}{H+V} = \frac{1-|\rho_{HHVV}|}{4} \tag{6.67}$$

- Inserting the elements from the sample hybrid-pol covariance matrix (with right-

circular polarization at the transmitter), i.e:

$$\langle C_{\text{hybrid}} \rangle = \begin{bmatrix} C_{11} & C_{12} \\ C_{21} & C_{22} \end{bmatrix} = \frac{1}{2} \begin{bmatrix} H+X & -jP+jX \\ jP^{\star}-jX & V+X \end{bmatrix} \tag{6.68}$$

into the linking in equation 6.67 yields:

$$4X = (1 - |\rho_{HHVV}|)(2C_{11} + 2C_{22} - 2X) \tag{6.69}$$

This equation is rearranged into

$$4X + 2X\,(1 - |\rho_{HHVV}|) = (1 - |\rho_{HHVV}|)\,(2C_{11} + 2C_{22}) \tag{6.70}$$

- The co-pol correlation coefficient can also be expressed through the compact-pol elements, i.e.:

$$|\rho_{HHVV}| = \frac{|P|}{\sqrt{HV}} = \frac{|-2jC_{12} + X|}{\sqrt{(2C_{11} - X)\,(2C_{22} - X)}} = \Omega\,(X) \tag{6.71}$$

- Inserting $\Omega\,(X)$ into equation 6.70, a cost function can be defined as:

$$J\,(X, \Omega(X)) = 2X\,(3 - \Omega(X)) - (1 - \Omega(X))\,(2C_{11} + 2C_{22}) \tag{6.72}$$

- The following optimization problem becomes:

$$\text{minimize} \quad J\,(X, \Omega(X)) = 2X\,(3 - \Omega(X)) - (1 - \Omega(X))\,(2C_{11} + 2C_{22}) \tag{6.73}$$

$$\text{subject to} \quad 0 \leq X \leq \frac{2}{3}C_{11} \quad \text{AND} \quad 0 \leq X \leq \frac{2}{3}C_{22} \tag{6.74}$$

- The constraints/boundary conditions above originates from the same reasoning as for the model-based reconstruction in section 6.2.2.

This optimization problem can be solved by searching for a solution of X that will minimize the cost function and at the same time be within the interval given above. The Matlab optimization toolbox contains a multitude of functions that can solve such

an optimization problem. Our cost function is not linear, but our constraint is, and thus the built-in Matlab function *fminbdn* or *fmincon* could help us find the solution.

Scatter plots are created to illustrate the improvement from Souyris general method to the modified approach. The scatter plots are shown in Figure 6.16 and are created based on the reconstruction of the cross-pol intensity, since this is the most difficult to reconstruct from the quad-pol covariance matrix. The data used are from May 10th 2013. These two scatter plots show that the modified version has the best reconstruction performance for the cross-pol intensity. This can also been seen from the RMSE value and Pearson correlation coefficient. The sea ice types used in this case is smooth ice, landfast ice, and open water.

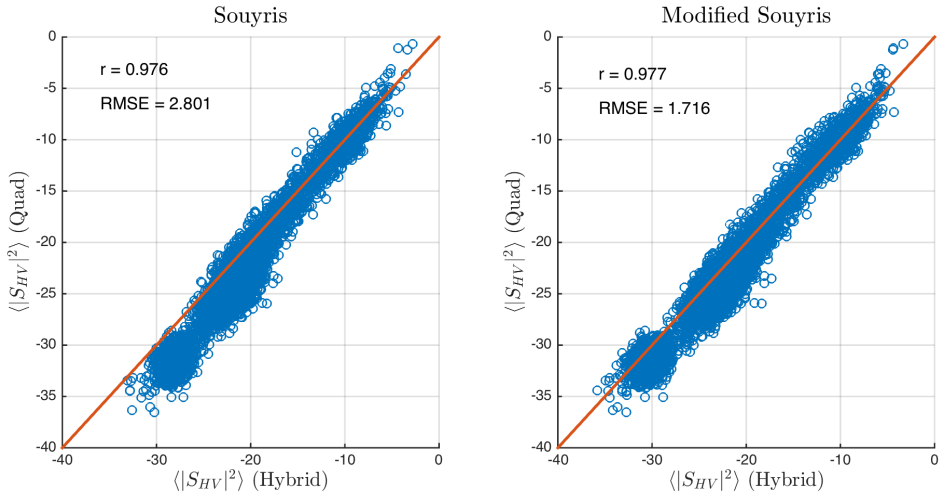

Figure 6.16: Scatter plots of the true (y-axis) and the estimated cross-pol (x-axis) component based on the general method of Souyris (to the left) and the modified approach (to the right). The reconstruction is based on the hybrid-pol data generated from the quad-pol data acquired May 10th 2013. The mean squared error and Pearson correlation coefficient between the estimated and true cross-pol intensity is calculated for each case.

Results of modified Souyris' reconstruction method

The same scatter plots are created here as for the other reconstruction methods, and the results are displayed in Figure 6.17. The results have improved compared to the other reconstruction methods that are tested in this section based on both RMSE and Pearson correlation coefficient. This is the first reconstruction method that produce RMSE values below 2 (some values are even close to our threshold of 1dB) for all the different types of sea ice and the open water class. This might indicate that the RMSE values are mostly dominated by the variance, and not the bias. The reconstruction of the cross-pol intensity of pixels covering rough sea ice, leads, and landfast ice generate

low RMSE values compared to the other reconstruction methods. Clearly, this method shows reasonable results for most of the classes, except for leads and the sea ice objects where the Pearson correlation coefficients are relatively low. Recall, however, that this also was the case for the other reconstruction methods.

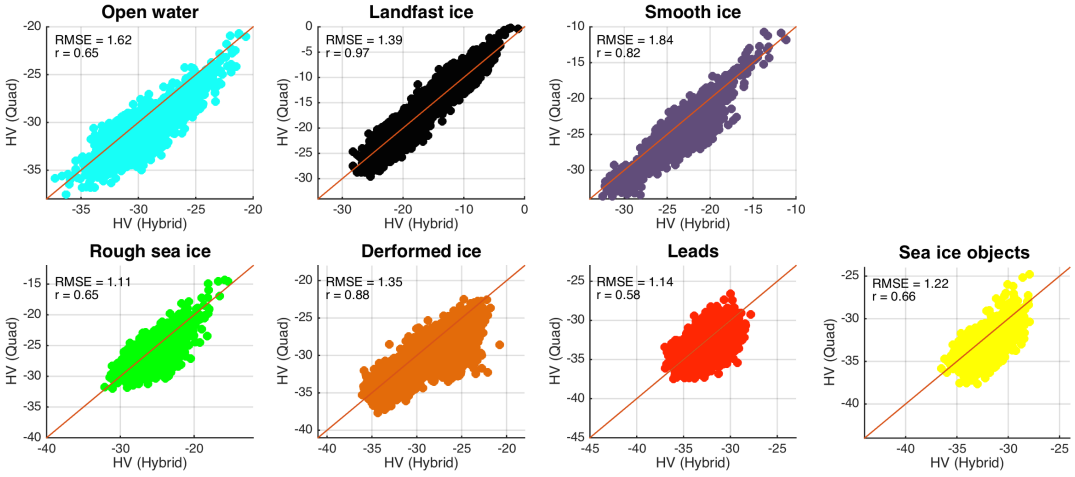

Figure 6.17: Results of the modified Souyris' reconstruction for different types of sea ice for the simulated hybrid-pol mode with right-circular polarization at the transmitter. The RMSE and Pearson correlation coefficient for the true and estimated cross-pol intensity (in decibel) are displayed in each scatter-plot. The different sea ice types are selected from the scenes acquired March 13th and May 10th (see chapter 4).

7

Results and Discussions

In this chapter, the results obtained from the different reconstruction methods are described in more detail. Recall from chapter 6 that the outcome of the reconstruction is a pseudo quad-pol covariance matrix. In chapter 5, a parameter study was conducted and the different polarimetric features presented are now estimated based on the pseudo quad-pol covariance matrix obtained from the different reconstruction methods. The upcoming sections include discussions and conclusions for the performance of the different reconstruction methods. The performance is evaluated based on the Pearson correlation coefficient and the RMSE for different polarimetric features and sea ice types. The effects of incidence angles, number of averaging pixels in the multi-looking window, and the number of iterations in the reconstruction process are also considered when determining the performance of the methods.

7.1 Results of the quad-pol parameter retrieval

In chapter 5 we looked at different polarimetric features than can be extracted from the compact-pol data, and features that are lost for sea ice covered SAR scenes. We discovered that the co-pol ratio, co-pol correlation coefficient, and co-pol phase difference could all be closely estimated from the compact-pol data. Problems occurred when attempting to find features that included the cross-pol intensity or the minimum eigenvalue (λ_3). This was one of the reasons for attempting to perform a reconstruction of a pseudo quad-pol covariance matrix. This section presents the results of the reconstruction of the polarimetric features discussed in chapter 5 based on the six methods that were

presented in chapter 6.

Since most of the polarimetric features that are based on the eigenvalues also include the minimum eigenvalue, the pseudo quad-pol covariance matrix reconstructed from simulated hybrid-pol data is used to find an estimate of this minimum eigenvalue. The results of this reconstruction are illustrated in Figure 7.1 for the data acquired on the March 13th, and in Figure 7.2 for the data acquired on the May 10th. The reason for using the two scenes is because they contain different types of sea ice (see chapter 4), and we can thus study the effect of the estimated minimum eigenvalue in terms of sea ice types. Note that the data points are selected randomly using a random number generator in Matlab, and thus represent various sea ice types. The data in the figures contain data points covering all the different classes of sea ice that are included in the two scenes.

Overall, the reconstruction methods that have Pearson correlation coefficients above 0.8 and RMSE close to 1 (see Appendix B) is the eigenvalue-based for the March 13th scene, and Nord's method for the May 10th scene. Souyris' method achieves a high correlation coefficient for the May 10th scene, but not for the scene from March 13th. Another important observation is that Nord's method is among the best if data from the May 10th scene are used, which is not the case for the March 13th scene. Consequently, Nord's method perform better for smooth ice than for more complicated sea ice types. The DoP-based reconstruction method scores the worst, followed by Souyris' method. The poor results from DoP-based reconstruction might be due to a large overestimation (large bias in the RMSE) of the cross-pol intensity, which was discovered in section 6.2.1. Overall, the best methods for reconstructing the minimum eigenvalue (measured by Pearson correlation coefficient) are modified Souyris' and the eigenvalue-based reconstruction methods. Note that the scatter plots created from modified Souyris' method seem to have a high bias since the correlation is high and the RMSE is low.

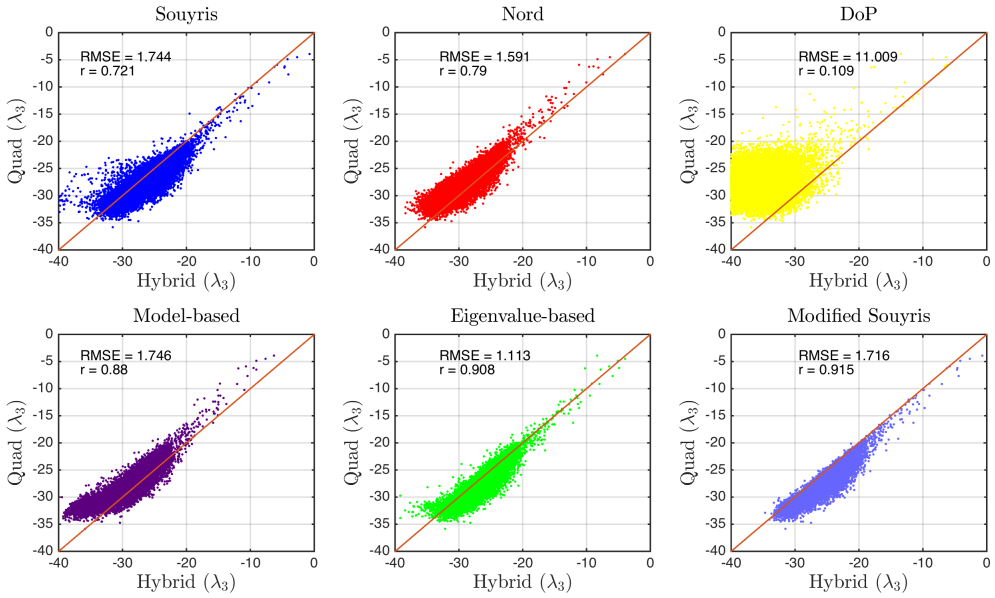

Figure 7.1: Results of the true and estimated minimum eigenvalue (in decibel) from the sample true and estimated covariance matrix for the six reconstruction methods. The data used are from the scene acquired March 13th 2013.

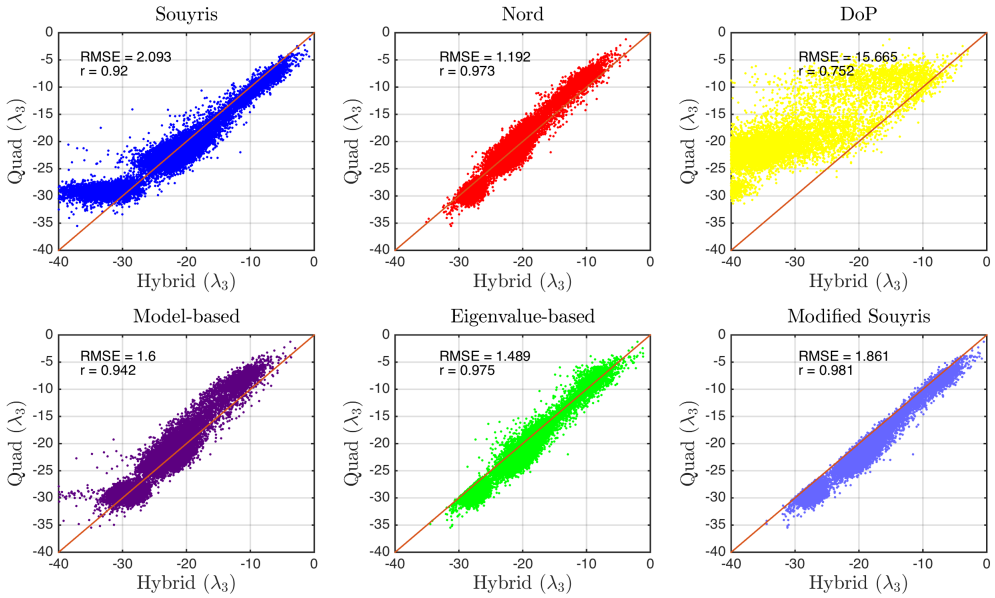

Figure 7.2: Results of the true and estimated minimum eigenvalue (in decibel) from the sample true and estimated covariance matrix for the six reconstruction methods. The data used are from the scene acquired May 10th 2013.

In the previous paragraph we observed that the minimum eigenvalue could be reconstructed, but that the performance of this estimation was somewhat affected by the SAR scene and the chosen reconstruction method. Following this, we attempt to estimate the other polarimetric features discussed in section 5.3 using the six reconstruction methods presented in chapter 6. This will provide us with additional information on which polarimetric features that can be reconstructed properly from the compact-pol data. Again, the two SAR scenes from March and May are used to demonstrate the results of this estimation. This is done to give a clear overview of the results on a per scene basis.

Tables 7.1 and 7.2 contain the results of the estimated polarimetric features. The blue colored cells represent the best reconstruction method, i.e., the one that achieves the highest score for a given polarimetric feature. Both the RMSE and Pearson correlation coefficients are calculated, and the interval of the true polarimetric feature is shown in the last column in both tables. 90% of the values falls within this interval (centered around the mean value) for each polarimetric features. This is done to remove the extreme data points. This indicates that 5% of the tails are left out. The reason for including the interval is that the RMSE is not a relative measure, and we can therefore compare it with regards to the interval given.

Polarimetric features that are computed from the co-pol scattering coefficients only include the co-pol ratio, co-pol correlation coefficient, the highest eigenvalue, and in some cases, the second eigenvalue (see Appendix E). These are all reconstructed with high correlation coefficients and relatively low RMSE. The one reconstruction method that does not accomplish this is Souyris' method. The cross-pol ratio is unfortunately badly reconstructed by all the methods for the data from the March 13th scene, but not for the data originating from May 10th. This might be due to more smooth sea ice in this scene, which might indicate that the results of the reconstruction is highly affected by the roughness of the surface.

Features that are highly influenced by depolarization effects are the anisotropy, polarization fraction, polarization asymmetry, minimum eigenvalue, and the pedestal height. In general, all the reconstruction methods utilize the depolarization concept to estimate the cross-pol intensity. If the polarimetric features are reconstructed properly, the Pearson correlation coefficient must be higher than 0.8 and for parameters that fall between 0 and 1, the RMSE should at least be below 0.05. The anisotropy feature is badly reconstructed by all methods based on both the Pearson correlation coefficient and the RMSE. The reason for this might be that the polarimetric anisotropy includes the difference between the two minimum eigenvalues, which are the most difficult features to estimate due to their low values. All reconstruction methods manage to reconstruct the entropy, while only the eigenvalue-based method manages to reconstruct the polarization fraction, as judged by both the correlation coefficient and RMSE, for the data from both the March 13th and May 10th scenes. All methods manage to reconstruct the polarization fraction calculated from the May 10th scene, except for the DoP-based

reconstruction method. Only the eigenvalue-based method yields a good reconstruction of the polarization asymmetry from the March 13th scene, while all methods manage to reconstruct this feature from the May 10th scene, except the model-based reconstruction. Finally, a satisfactory reconstruction of the pedestal height is achieved by all the methods except for the DoP-based reconstruction method.

Generally, all the polarimetric features are recovered well, with the exception of the polarimetric anisotropy. The results in Tables 7.1 and 7.2 show that what is the best reconstruction method vary depending on the SAR scene. Recall that rougher and more complicated sea ice structures are present in the March scene, while open water and smooth ice are present in the March scene. Nord's method scores highest for polarimetric features originating from the May 10th scene, while both the eigenvalue-based and the modified Souyris method score the best for the March 13 scene. Clearly, Souyris' and Nord's reconstruction methods seem to be the best for smooth surfaces that exhibit strong azimuthal symmetry. For other surface types with more complicated structure, the eigenvalue-based, model-based, and the modified Souyris methods seem to be the good choices for a reconstruction of these polarimetric features.

		RMSE and Pearson correlation coefficient						
		Souyris	Nord	DoP-based	Model-based	Eigenvalue-based	Modified Souyris	Value range
Co-pol ratio	RMSE	0.049	0.215	0.251	0.211	0.22	0.217	[0.617, 2.552]
	r	0.748	0.9	0.907	0.915	0.912	0.914	
Co-pol correlation coefficient	RMSE	0.081	0.06	0.248	0.061	0.096	0.059	[0.3927, 0.8672]
	r	0.853	0.911	0.704	0.903	0.85	0.919	
Cross-pol ratio	RMSE	9.354	19.671	16.178	8.309	9.464	7.494	[10.693, 47.615]
	r	0.585	0.476	0.68	0.487	0.68	0.697	
λ_1(dB)	RMSE	0.078	0.087	0.081	0.084	0.081	0.08	[-0.309, 29.378]
	r	0.999	0.999	0.999	0.999	0.999	0.999	
λ_2(dB)	RMSE	0.926	0.811	1.611	0.883	0.804	1.171	[3.289, 32.878]
	r	0.93	0.951	0.959	0.938	0.946	0.953	
λ_3(dB)	RMSE	1.744	1.591	11.009	1.746	1.113	1.716	[4.704, 35.405]
	r	0.721	0.79	0.108	0.88	0.908	0.915	
Entropy	RMSE	0.04	0.038	0.078	0.039	0.037	0.039	[0.367, 0.795]
	r	0.94	0.94	0.909	0.93	0.942	0.943	
Anisotropy	RMSE	0.246	0.194	0.556	0.233	0.17	0.306	[0.130, 0.566]
	r	-0.083	0.094	-0.02	-0.021	0.129	-0.007	
Polarization fraction	RMSE	0.084	0.062	0.16	0.073	0.052	0.096	[0.635, 0.903]
	r	0.763	0.749	0.572	0.581	0.801	0.809	
Polarization asymmetry	RMSE	0.13	0.084	0.202	0.104	0.078	0.158	[0.574, 0.952]
	r	0.304	0.740	0.771	0.631	0.81	0.446	
Pedestal height	RMSE	0.039	0.028	0.069	0.033	0.024	0.044	[0.037, 0.185]
	r	0.838	0.831	0.68	0.668	0.811	0.846	

Table 7.1: Results of reconstructed polarimetric features from simulated hybrid-pol data (with right-circular polarization at the transmitter). The Pearson correlation coefficient (r) and RMSE are calculated to measure the performance of the six reconstruction methods. The last column contains the range of the values for each polarimetric feature, and 90% of the values fall within this interval. This is done to remove the extreme data points introduced in each polarimetric feature. The data are from the March 13th scene (see chapter 4).

		RMSE and Pearson correlation coefficient						
		Souyris	Nord	DoP-based	Model-based	Eigenvalue-based	Modified Souyris	Value range
Co-pol ratio	RMSE	0.143	0.131	0.157	0.136	0.143	0.139	[0.711, 1.596]
	r	0.786	0.812	0.76	0.814	0.785	0.796	
Co-pol correlation coefficient	RMSE	0.065	0.038	0.164	0.054	0.062	0.038	[0.445, 0.943]
	r	0.965	0.957	0.722	0.949	0.903	0.963	
Cross-pol ratio	RMSE	28.648	15.679	36.57	24.915	19.49	17.044	[8.324, 118.780]
	r	0.858	0.822	0.858	0.241	0.858	0.862	
$\lambda_1(dB)$	RMSE	0.039	0.047	0.04	0.044	0.041	0.039	[0.976, 13.122]
	r	1.00	0.999	0.999	0.999	0.999	1.00	
$\lambda_2(dB)$	RMSE	0.787	0.780	1.596	0.907	0.99	1.288	[6.471, 26.753]
	r	0.986	0.988	0.99	0.978	0.988	0.99	
$\lambda_3(dB)$	RMSE	2.093	1.192	15.665	1.6	1.489	1.861	[8.840, 29.797]
	r	0.92	0.973	0.752	0.942	0.975	0.981	
Entropy	RMSE	0.029	0.028	0.059	0.03	0.027	0.027	[0.194, 0.827]
	r	0.984	0.982	0.974	0.98	0.984	0.985	
Anisotropy	RMSE	0.223	0.168	0.595	0.26	0.249	0.339	[0.145, 0.564]
	r	-0.017	0.003	0.149	-0.065	-0.066	-0.127	
Polarization fraction	RMSE	0.05	0.038	0.112	0.047	0.044	0.066	[0.591, 0.958]
	r	0.935	0.915	0.693	0.85	0.879	0.936	
Polarization asymmetry	RMSE	0.078	0.052	0.14	0.066	0.068	0.109	[0.607, 0.977]
	r	0.072	0.878	0.846	0.77	0.812	0.561	
Pedestal height	RMSE	0.024	0.019	0.048	0.021	0.02	0.029	[0.015, 0.219]
	r	0.941	0.924	0.734	0.87	0.891	0.94	

Table 7.2: Results of reconstructed polarimetric features from simulated hybrid-pol data (with right-circular polarization at the transmitter). The Pearson correlation coefficient (r) and RMSE are calculated to measure the performance of the six reconstruction methods. The last column contains the range of the values for each polarimetric feature, and 90% of the values fall within this interval. This is done to remove the extreme data points introduced in each polarimetric feature. The data are from the May 10th scene (see chapter 4).

7.2 Results of the reconstructed co-pol information

This section gives a more detailed presentation of the results of the reconstructed co-pol intensities and the absolute value of the co-pol correlation coefficient. These parameters are much "easier" to reconstruct compared to the cross-pol intensities. This is because the co-pol intensities have a higher response, and are the most dominate in the compact-pol intensities.

Tables 7.3, 7.4, and 7.5 contain the results of the reconstructed HH-intensity, VV-intensity, and the $|\langle S_{HH}S_{VV}^{\star}\rangle|$ component, respectively. All the reconstruction methods produce correlation coefficients and RMSE values that are higher than 0.8 and lower than 1.5. Three exceptions are Nord's, Souyris', and DoP-based reconstruction methods, which produce a high RMSE value for some classes in the estimated HH-intensity, VV-

intensity, and $|\langle S_{HH} S_{VV}^{\star} \rangle|$ component. The targets with relatively low backscattering response in the cross-pol channel, such as the sea ice objects and leads, have the lowest correlation among all the cases. This might be due to an overestimation in the cross-pol intensity. It is difficult to comment on the general performance of the different methods based on the co-pol intensities alone, since these values are relatively high compared to the cross-pol intensity, and will dominate the compact-pol intensities (see figure 5.5). Generally, all the six methods provide similar results, but the modified Souyris' method performs the best based on both the Pearson correlation coefficient and RMSE.

		Results (HH) Hybrid-pol mode					
		Souyris	Nord	DoP-based	Model-based	Eigenvalue-based	Modified Souyris
Open water	RMSE	0.29	0.23	0.33	0.28	0.23	0.23
	r	0.98	0.98	0.98	0.97	0.98	0.98
Landfast ice	RMSE	0.89	0.85	1.35	0.82	1.02	0.84
	r	0.99	0.99	0.98	0.99	0.99	0.99
Smooth ice	RMSE	0.28	0.28	0.38	0.28	0.28	0.27
	r	0.99	0.99	0.98	0.99	0.99	0.99
Rough ice	RMSE	0.42	0.37	0.67	0.39	0.44	0.4
	r	0.92	0.92	0.92	0.93	0.93	0.93
Deformed ice	RMSE	0.47	0.65	0.54	0.51	0.47	0.47
	r	0.99	0.99	0.99	0.99	0.99	0.99
Leads	RMSE	1.08	3.09	1.22	0.6	0.7	0.52
	r	0.88	0.92	0.92	0.93	0.92	0.93
Ice objects	RMSE	0.42	0.40	0.97	0.36	0.61	0.4
	r	0.93	0.93	0.91	0.92	0.91	0.93
Total	RMSE	0.41	0.39	0.62	0.37	0.42	0.37
	r	0.99	0.99	0.99	1.00	1.00	1.00

Table 7.3: Results of the reconstructed HH-intensity (dB) based on the six reconstruction methods presented in chapter 6. The blue colored cells represent the best reconstruction method based on the highest correlation and lowest RMSE value. The Pearson correlation coefficient (r) and RMSE are calculated for each class and the last column represent all the classes. The data are from the March 13th and May 10th scenes (see chapter 4).

		Results (VV) Hybrid-pol mode					
		Souyris	Nord	DoP-based	Model-based	Eigenvalue-based	Modified Souyris
Open water	RMSE	0.21	0.2	0.25	0.2	0.19	0.19
	r	0.99	0.99	0.98	0.98	0.98	0.98
Landfast ice	RMSE	0.85	0.86	1.25	0.89	0.94	0.86
	r	0.98	0.98	0.98	0.98	0.98	0.99
Smooth ice	RMSE	0.37	0.29	0.52	0.36	0.34	0.33
	r	0.98	0.98	0.98	0.98	0.98	0.98
Rough ice	RMSE	0.37	0.4	0.56	0.39	0.39	0.37
	r	0.94	0.95	0.94	0.94	0.95	0.95
Deformed ice	RMSE	0.58	0.37	0.97	0.53	0.63	0.55
	r	0.99	0.99	0.98	0.99	0.99	0.99
Leads	RMSE	0.42	0.39	0.81	0.43	0.57	0.43
	r	0.98	0.98	0.97	0.97	0.97	0.97
Ice objects	RMSE	0.47	0.48	1.12	0.46	0.65	0.46
	r	0.92	0.93	0.92	0.91	0.92	0.93
Total	RMSE	0.39	0.38	0.62	0.38	0.41	0.37
	r	0.99	0.99	0.99	0.99	0.99	1.00

Table 7.4: Results of the reconstructed VV-intensity (dB) based on the six reconstruction methods presented in chapter 6. The blue colored cells represent the best reconstruction method based on the highest correlation and lowest RMSE value. The Pearson correlation coefficient (r) and RMSE are calculated for each class and the last column represent all the classes. The data used are those acquired March 13th and May 10th 2013 (see chapter 4).

		Results ($\lvert\langle S_{HH}S_{VV}^{\star}\rangle\rvert$) Hybrid-pol mode					
		Souyris	Nord	DoP-based	Model-based	Eigenvalue-based	Modified Souyris
Open water	RMSE	0.15	0.1	0.24	0.15	0.12	0.09
	r	1.00	1.00	0.99	1.00	1.00	1.00
Landfast ice	RMSE	0.99	1.44	1.67	1.37	1.39	1.06
	r	0.99	0.97	0.98	0.97	0.98	0.98
Smooth ice	RMSE	0.18	0.14	0.37	0.16	0.17	0.13
	r	1.00	1.00	1.00	1.00	1.00	1.00
Rough ice	RMSE	0.19	0.24	0.57	0.19	0.23	0.16
	r	0.98	0.99	0.98	0.98	0.98	0.99
Deformed ice	RMSE	0.38	0.29	0.85	0.32	0.46	0.34
	r	0.99	0.99	0.99	0.99	0.99	1.00
Leads	RMSE	1.98	0.92	1.74	0.95	1.22	0.87
	r	0.96	0.92	0.94	0.92	0.93	0.94
Ice objects	RMSE	0.49	0.62	1.48	0.47	0.93	0.49
	r	0.94	0.93	0.93	0.93	0.93	0.94
Total	RMSE	0.3	0.28	0.69	0.28	0.36	0.25
	r	1.00	0.99	0.99	0.99	1.00	1.00

Table 7.5: Results of the reconstructed $\lvert\langle S_{HH}S_{VV}^{\star}\rangle\rvert$ component (dB) based on the six reconstruction methods presented in chapter 6. The blue colored cells represent the best reconstruction method based on the highest correlation and lowest RMSE value. The Pearson correlation coefficient (r) and RMSE are calculated for each class and the last column represent all the classes. The data are from the March 13th and May 10th scenes (see chapter 4).

7.3 Results of the reconstructed cross-pol intensity

The results of the cross-pol intensities for the six reconstruction methods were illustrated when each method were presented in chapter 6. This section presents all the results together in Table 7.6 for a comparison. The best reconstruction method is highlighted in blue.

From this table, there is only one method that achieves a RMSE below 2 for all the classes, namely the modified Souyris' method. The other methods also have, for some classes, low RMSE. However, non of these method achieve RMSE values that are below 1, but some values are relatively close to 1. If the correlation is considered only pixels covering landfast ice, smooth sea ice, and deformed ice are recovered well. The open water class has relatively low correlation (0.66), which is not satisfactory. This is most likely because the cross-pol return from open water is relatively low. The classes (besides open water) with high RMSE and low Pearson correlation coefficient are rough ice, leads, and the sea ice objects. All these classes have relatively low cross-pol intensity values, and represent more complicated sea ice structure, which may results in challenges when reconstructing the cross-pol intensities for these areas. Unfortunately, non of these methods achieve a RMSE below 1, but the proposed methods, however, are closest to achieve a perfect reconstruction.

The last row contains RMSE and correlation coefficient values obtained from all the pixels in the two scenes, and all the methods achieve correlations that are above 0.9. However, only the modified Souyris', model-based, and eigenvalue-based reconstruction methods achieve RMSE values below 2, and the modified Souyris' method has a RMSE value closest to our limit of 1. Later, we will study the effects of the reconstruction based on the values in the true cross-pol intensity.

Overall, the best method is clearly modified Souyris' method.

		Results (HV) Hybrid-pol mode					
		Souyris	Nord	DoP-based	Model-based	Eigenvalue-based	Modified Souyris
Open water	RMSE	3.51	1.25	4.24	2.46	1.77	1.62
	r	0.6	0.55	0.65	0.49	0.65	0.65
Landfast ice	RMSE	1.44	3.33	3.26	1.98	2.1	1.39
	r	0.98	0.97	0.96	0.95	0.96	0.97
Smooth ice	RMSE	2.89	1.25	4.55	2.17	2.21	1.84
	r	0.83	0.8	0.82	0.78	0.81	0.82
Rough ice	RMSE	1.4	2.41	3.41	1.28	1.52	1.11
	r	0.65	0.59	0.64	0.53	0.63	0.65
Deformed ice	RMSE	1.6	2.8	3.72	1.42	1.84	1.35
	r	0.87	0.85	0.89	0.89	0.86	0.88
Leads	RMSE	1.61	2.5	3.14	1.86	1.8	1.14
	r	0.5	0.35	0.55	0.52	0.48	0.58
Ice objects	RMSE	1.29	2.52	3.72	1.03	2.31	1.22
	r	0.67	0.65	0.62	0.44	0.59	0.66
Total	RMSE	1.96	2.04	3.8	1.58	1.8	1.34
	r	0.95	0.93	0.96	0.94	0.96	0.96

Table 7.6: Results of the reconstructed HV-intensity (dB) based on the six reconstruction methods presented in chapter 6. The blue colored cells represent the best reconstruction method based on the highest correlation and lowest RMSE value. The Pearson correlation coefficient (r) and RMSE are calculated for each class, and the last column represent all the classes. The data are from the March 13th and May 10th scenes (see chapter 4).

7.4 Effects on the reconstruction

We have now seen the results of the reconstruction for different polarimetric features. The results might be affected by different user specified parameters or the properties of the data. The upcoming sections highlight how this impacts the reconstruction. Specifically, we will consider the number of iterations, incidence angle, number of averaging pixels in the multi-looking window (see section 4.2), and power in the true cross-pol intensity.

7.4.1 Effects of number of iterations

Nord's and Souyris' reconstruction methods require one user input to their algorithms, namely the number of iterations. When these reconstruction techniques are used, the number of iterations will in practice be selected without much guidance. Figure 7.3 shows how the correlation and RMSE between the estimated and true cross-pol intensity vary as the number of iterations increases (using Souyris' algorithm). The data from the March 13th and May 10th scenes are used in this case to demonstrate this effect.

The effect of increasing the number of iterations of the Pearson correlation coefficient

is small (see the scale on the y-axis) for the data from May 10th scene. If the data from the March 13 scene is used, the correlation coefficient is highly affected by the number of iterations, and a high number of iterations is needed to reach convergence of the estimated cross-pol intensity for such sea ice types. This might be due to more complicated sea ice structures in this scene. Recall that this scene consists of open water and smooth ice, which may be the reason for the rapid convergence compared to the data from the March 13 scene. The RMSE values, however, reaches a faster convergent for the March scene compared to the May scene. This might indicate that there is a higher bias in the RMSE values in the May scene due to its high Pearson correlation coefficient.

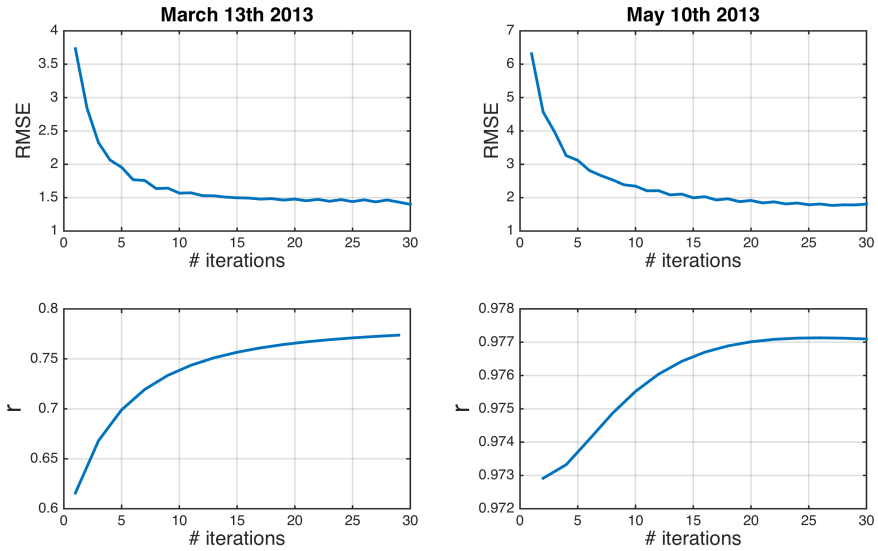

Figure 7.3: Results of Souyris' reconstruction method of the cross-pol intensity as a function of the number of iterations. The data used are the scenes acquired March 13th and May 10th 2013. Both the RMSE and Pearson correlation coefficient (r) are calculated.

7.4.2 Effects of incidence angle

The data from any given radar is acquired at different incidence angles. The incidence angle varies across the range direction as the radar collects the response from targets within the antenna beam. In this work, four different SAR scenes are used. These scenes cover a range of incidence angles (see Table 4.1, chapter 4). This section will therefore highlight the influence of the varying incidence angles for the different reconstruction methods.

The effect of the incidence angle on the reconstructed cross-pol intensity is shown in Figure 7.4. The graph to the left shows the data from the March 13th scene, while the

graph to the right shows that data from the May 10th scene. The data are collected along the range direction. The range profile will therefore transect different classes, such as rough sea ice, smooth ice, and deformed ice. The different colors in the line plots represent the six reconstruction methods.

The DoP-based reconstruction method has the highest RMSE values when compared to the other methods, which was also discovered in the previous section. It is difficult to observe whether the reconstruction results of the cross-pol intensity are affected by the incidence angle from the March 13th scene, as there is a larger variation across sea ice types. This effect is easier to observe from the May 10th scene, as the line segment contains smooth ice and open water from approximately 30.55°. For incidence angles covering open water, the RMSE decreases as the incidence angle increases. This is also observed for the smooth ice (30.1° - 30.55°), but to a smaller extent. All the methods are affected as the incidence angles vary across the range direction for open water, indicating that the backscatter response is highly dependent on the incidence angles, decreasing for higher incidence angles [Shokr and Sinha, 2015]. Nord's method is the one that is affected the least.

These figures also provide a good overview of which reconstruction method that is best suited for the March 13th and the May 10th scenes. The modified Souyris and the model-based reconstruction are clear "winners" when reconstructing the cross-pol intensity for more complicated sea ice structures (March 13th scene). On the other hand, Nord's reconstruction method is more suitable for the sea ice types located in the May 10th scene. Note that the modified Souyris scores high for both scenes combined, as does the eigenvalue-based method.

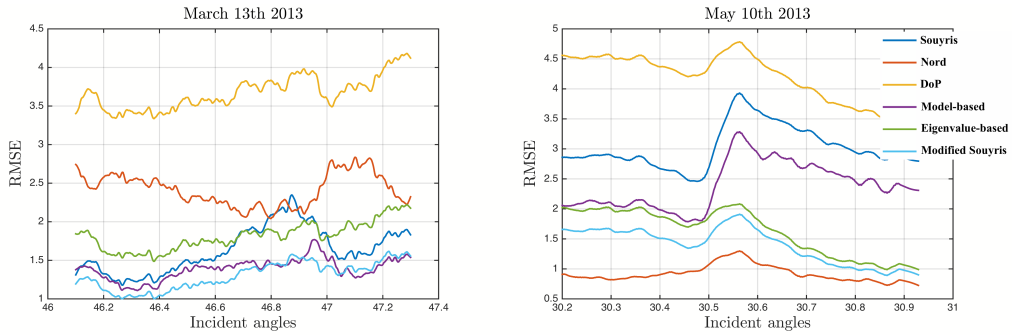

Figure 7.4: RMSE based on the true and estimated cross-pol intensity for varying incidence angle. The RMSE is calculated for the six reconstruction methods, and the data used are from the scenes acquired March 13th and May 10th.

7.4.3 Effects of multi-looking

Multi-looking is performed by averaging over a selected number of pixels to reduce the speckle effects present in SAR images. If a high number of averaging pixels are used, the different polarimetric parameters can become blurred due to averaging across class boundaries and over heterogeneous areas. If too few averaging pixels are used, a larger speckle effect is present. To observe the effects of averaging, one can plot the Pearson correlation coefficients and RMSE between the estimated and true cross-pol intensity as a function of number of averaging pixels. The same could be done using the estimated co-pol components, but since the cross-pol intensity is the most delicate term to reconstruct, the cross-pol intensity is used in this case.

The results of the different reconstruction methods are illustrated in Figure 7.5 through 7.10 for the different classes. As the number of averaging pixels increases, the correlation increases for all the classes. Recall that the highest correlation coefficient obtained from pixels covering open water was 0.65 (see Table 7.6). This was achieved when 54 (9×6) averaging pixels were used. If more averaging is performed, the estimated cross-pol intensities representing open water become more similar to the true cross-pol intensities when considering the correlation coefficients and RMSE. This behavior is consistent across all the methods except the model-based reconstruction technique. The latter method also produces poor results for the estimated cross-pol intensities for pixels covering smooth ice and open water.

Overall, both the RMSE and Pearson correlation coefficients are in favor of large multi-look factors. Recall that the rough sea ice class could not be reconstructed. Both Nord's and Souyris' reconstruction methods generates both high correlation coefficients and low RMSE values if the number of averaging pixels exceed at least 400. Such a heavy multi-looking factor is not unrealistic for certain sea ice image analyzing tasks, such as in [Moen et al., 2013], and segmentation, which the positive impact of extensive averaging has been demonstrated and explained [Doulgeris, 2012]. The model-based reconstruction is the best method for recovering the cross-pol intensities for areas covering deformed ice.

For the leads, only modified Souyris' and model-based methods achieve a good reconstruction of the cross-pol intensities. We also observe that the eigenvalue-based reconstruction and modified Souyris are methods that achieve good scores (compared to the other methods) for all the classes. The other methods tend to have varying results that are highly dependent on the surface cover.

For most of the classes and reconstruction methods, the Pearson correlation and RMSE converge when number of averaging pixels exceed approximately 200. Overall, the cross-pol intensities representing the different classes were reconstructed with high correlation coefficients and relatively low RMSE values.

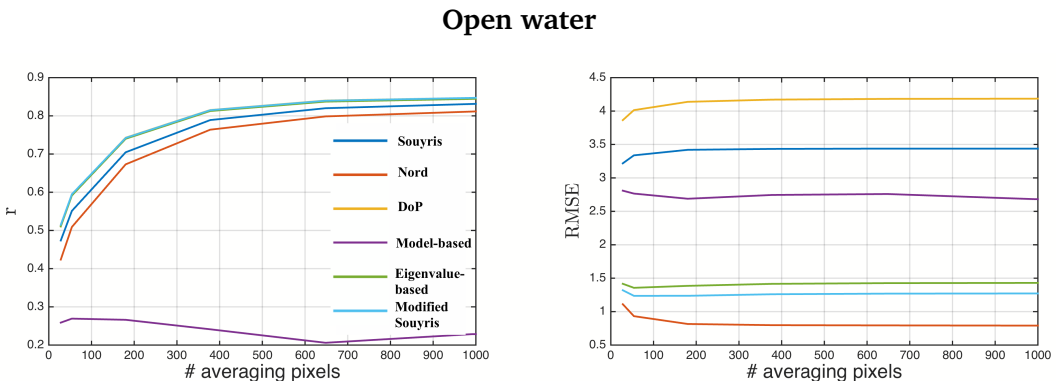

Figure 7.5: Results of the six reconstruction methods (for open water) as a function of varying number of pixels in the averaging window. RMSE and Pearson correlation coefficients are calculated between the true and estimated cross-pol intensity.

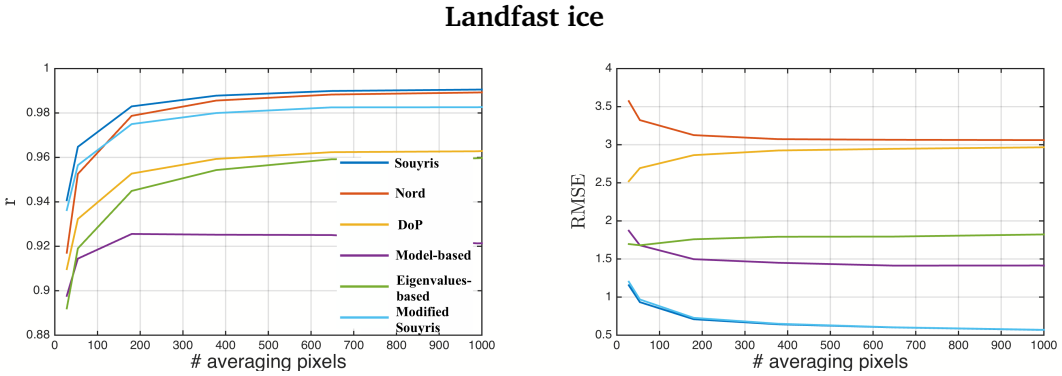

Figure 7.6: Results of the six reconstruction methods (for landfast ice) as a function of varying number of pixels in the averaging window. RMSE and Pearson correlation coefficients are calculated between the true and estimated cross-pol intensity.

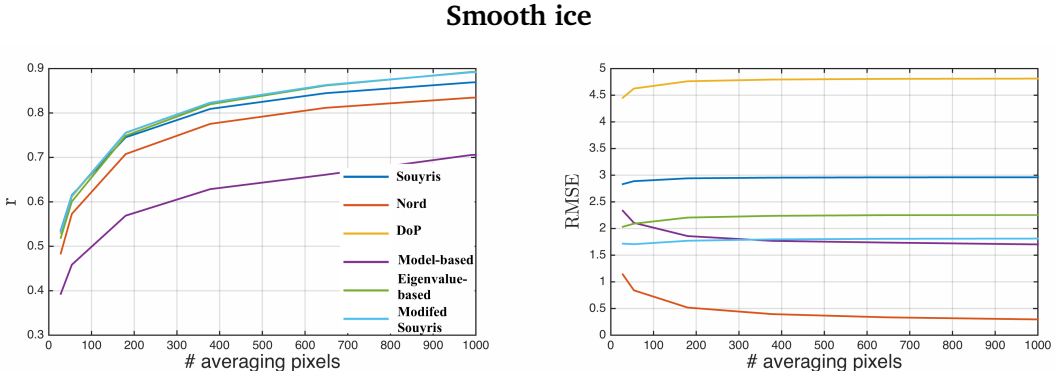

Figure 7.7: Results of the six reconstruction methods (for smooth sea ice) as a function of varying number of pixels in the averaging window. RMSE and Pearson correlation coefficients are calculated between the true and estimated cross-pol intensity.

Rough sea ice

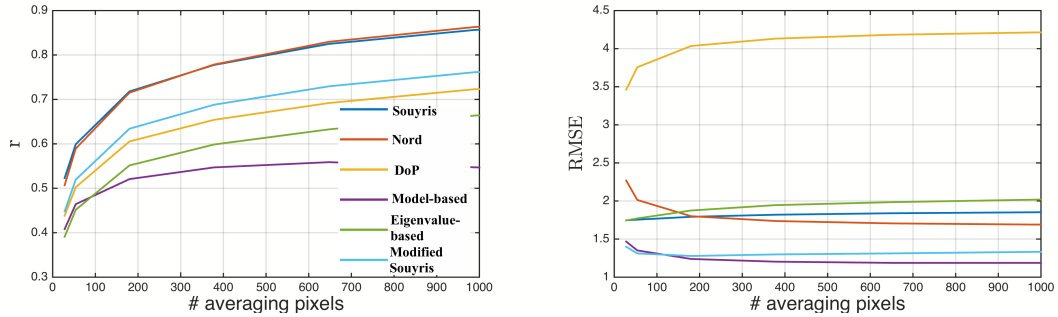

Figure 7.8: Results of the six reconstruction methods (for rough sea ice) as a function of varying number of pixels in the averaging window. RMSE and Pearson correlation coefficients are calculated between the true and estimated cross-pol intensity.

Deformed ice

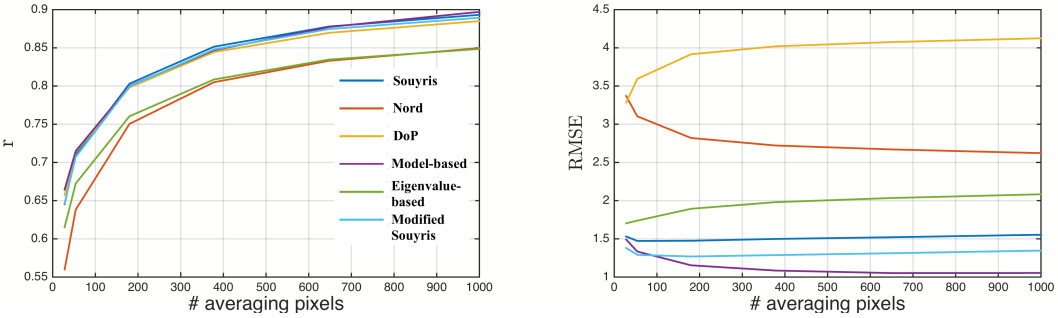

Figure 7.9: Results of the six reconstruction methods (for deformed ice) as a function of varying number of pixels in the averaging window. RMSE and Pearson correlation coefficients are calculated between the true and estimated cross-pol intensity.

Leads

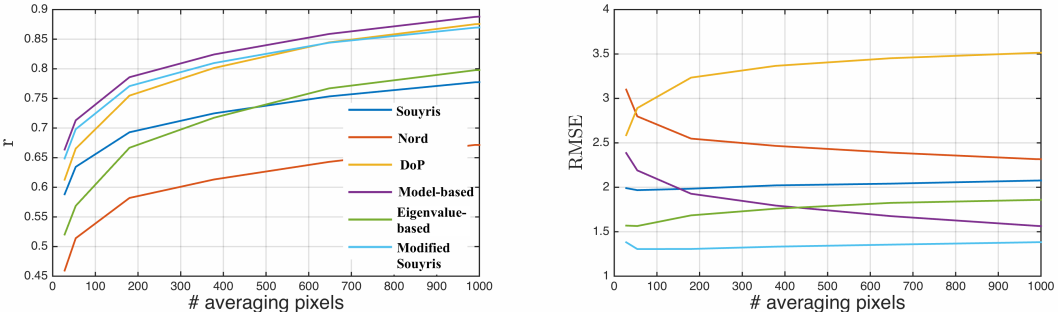

Figure 7.10: Results of the six reconstruction methods (for leads) as a function of varying number of pixels in the averaging window. RMSE and Pearson correlation coefficients are calculated between the true and estimated cross-pol intensity.

7.4.4 Effects of power in the cross-pol intensity

The signal strength of the cross-pol intensity might influence the reconstruction results. Low backscatter response in the cross-pol intensity is observed for the leads, sea ice objects, and open water, which were the classes that had the lowest reconstruction accuracy. The plots in Figure 7.11 demonstrate how the Pearson correlation coefficient and RMSE vary for the true cross-pol intensity.

These plots are created in the following manner:

1. Create a set of bins corresponding to values ranging from the minimum to the maximum values in the true cross-pol intensity.

2. Iterate through the bins, and find values corresponding to that bin.

3. A fixed number of samples are selected randomly, such that the results do not depend on the number of samples in each bin. In our case number of samples was set to 30.

4. Calculate the RMSE between the estimated cross-pol intensity obtained from each reconstruction method and the true cross-pol intensities that corresponds the bin. Note that if the number of samples do not satisfy our criteria, we will continue iterating, and skip the calculation of the RMSE. This will yield empty spaces in the RMSE array, but the RMSE values are interpolated when the iteration is completed.

5. Prior to visualizing the figures, the RMSE values are smoothed (using a simple averaging filter) and colored with the color representing the particular reconstruction method. Additionally, the original values of the RMSE are plotted behind the colored line in a light grey color.

Souyris' and the DoP-based reconstruction techniques exhibit similar behavior of the RMSE in Figure 7.11. The application of these two methods results in decreasing RMSE values as the true cross-pol intensities increase. Nord's reconstruction technique generate RMSE values that are relatively small for low values of the true cross-pol intensity, but large for high values of the true cross-pol intensity. This is an opposite trend compared to both Souyris' and DoP-based reconstruction methods. The model-based, eigenvalue-based, and the modified Souyris methods seem to be more stable for varying values of the true cross-pol intensity. This is especially pronounced for the eigenvalue-based reconstruction. These three methods have the lowest RMSE values across the entire x-axis. Souyris', Nord's, and DoP-based reconstruction generate varying RMSE values across the x-axis, and the reconstructed cross-pol intensity is therefore highly dependent on the true cross-pol intensity values.

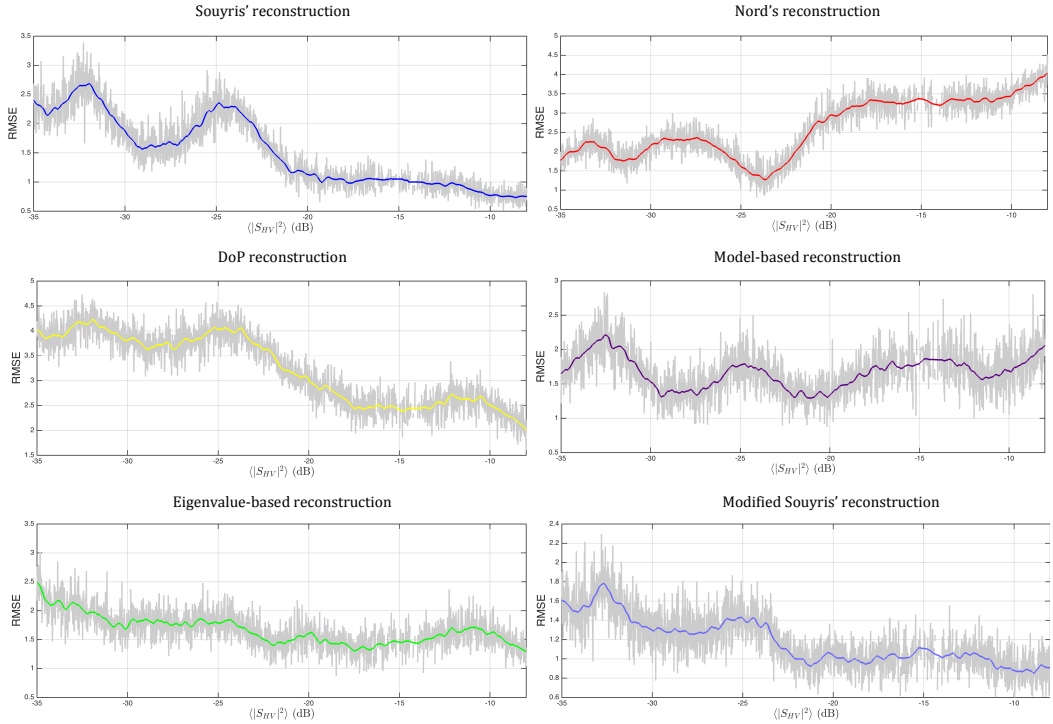

Figure 7.11: Pearson correlation coefficients and RMSE obtained from the six reconstruction methods as a function of the values in the true cross-pol intensity. The RMSE is calculated between the estimated and true cross-pol intensities. Data used in the scenes acquired March 13th and May 10th 2013.

7.5 Summary

The previous sections have covered different results of the six reconstruction methods. This section will summarize the different reconstruction methods in terms of their performance, and we will also attempt to find explanations for the achieved results. Table 7.7 shows a summary of the six methods in terms of the algorithms and the assumptions drawn to enable a reconstruction, the polarimatric features that could be recovered using the different reconstruction methods, and which SAR scene that gave the most promising reconstruction results.

Souyris' reconstruction method

Recall from section 6.1.1, that to enable an estimate of the cross-pol intensity, Souyris proposed the following equation:

$$\frac{X}{H+V} = \frac{1-|\rho_{HHVV}|}{4} \tag{7.1}$$

This is most likely to be true if the area to be reconstructed exhibit strong azimuthal symmetry. This equation was further tested, and the results were shown in Figure 6.2. The above equation is valid for surface areas that are relatively smooth, such as smooth sea ice. Tables 7.1 and 7.2 contain the results of reconstructed polarimetric features for the scenes acquired March 13th and May 10th, respectively. From the results in these two tables, the two highest eigenvalues, co-pol correlation coefficient, and the entropy were recovered well from both the scenes, while the polarization fraction, pedestal height, and the minimum eigenvalue were recovered only from the May scene. The reason for this is, most likely, that the May scene contains more smooth ice than the March scene, where more complicated sea ice structures are present and azimuthal symmetry is no longer valid.

In Table 7.6 the results of the reconstructed cross-pol intensities are presented. Only the smooth sea ice, deformed ice, and landfast ice areas had high correlation and relatively low RMSE between the estimated and true cross-pol intensities. This method was also highly influenced by the number of averaging pixels, where higher number of averaging pixels increased the correlation between the estimated and true cross-pol intensities. The number of iteration steps in the reconstruction process affects the reconstruction results. The number of iterations should at least exceed 10 in order to enable high correlation coefficients. An even higher number of iterations is needed for the cross-pol component to obtain a comparable accuracy for the scene acquired in March.

Another observation from Souyris' method was that it produced high RMSE values for high radiometric values of the true cross-pol intensity, but low RMSE when the cross-pol intensity was low. This was illustrated in Figure 7.11.

Nord's reconstruction method

Nord's method try to compensate for areas where azimuthal symmetry break down, and proposed the following equation (see section 6.1.2):

$$\frac{X}{H+V} = \frac{1-|\rho_{HHVV}|}{N} \qquad N = \frac{\langle|S_{HH}-S_{VV}|^2\rangle}{\langle|S_{HV}|^2\rangle} \tag{7.2}$$

The validity of this equation was also tested and visualized as a color image (see Figure 6.4). From this figure, the above equation seems to be more valid compared to Souyris' linking for smooth and rough sea ice areas. The author also proved that

the left side of the above equation was always higher or equal than the elements on the right side in the same equation. Following this, more overestimation will therefore occur for the estimated cross-pol intensity compared to Souyris' method (see section 6.1.2).

Some of the reconstructed polarimetric features extracted from the reconstructed pseudo quad-pol covariance matrix were improved compared to Souyris' method. These features were the co-pol ratio, co-pol correlation coefficient, cross-pol ratio, entropy, and the polarization asymmetry. Recall from section 6.1.2, that Nord's method enabled a higher reconstruction performance of the cross-pol intensity for open water and smooth sea ice (if RMSE was considered).

Nord's methods produced lower RMSE values for low backscattering values in the true cross-pol intensity, which is an opposite trend to the results obtained from Souyris' method.

DoP-based reconstruction method

The DoP-based reconstruction method is the first new method proposed in this work (see section 6.2.1). The proposed equation that enabling reconstruction is:

$$X = \left(\frac{1 - DoP}{2}\right) q_0 \tag{7.3}$$

As a consequence of this equation, all depolarized power is assigned to the cross-pol intensity. Using this approach, the reconstructed polarimetric features achieve similar results to both Nord's and Souyris' methods (if the correlation coefficients are considered). High RMSE is produced for most of the estimated polarimetric features. This is a consequence of assigning all depolarized power to the cross-pol intensity. Scatter plots demonstrating the relationship between the estimated and true cross-pol intensities were created in section 6.2.1. These showed that most of the sea ice classes suffered an overestimation of the cross-pol intensity, but that the correlation coefficient was relatively high. This indicates that all depolarized power will not only be generated in the cross-pol intensity, but also in the co-pol intensities. To solve this, the model-based reconstruction was introduced.

Model-based reconstruction method

The model-based reconstruction method was introduced to remove some of the limitations of the DoP-based reconstruction method. This method utilizes two model components; a surface and a volume scattering component. Recall that in this reconstruction method, depolarization effects are considered for both the co- and cross-pol scattering coefficients. This algorithm is shown in the fifth row in Table 7.7.

Recall from section 6.2.2 that some of the parameters included in the associated cost function can be found directly from the compact-pol (hybrid-pol) data, but more information is needed to enable a reconstruction. This was solved by introducing a relationship between the degree of polarization and the surface slope angle δ. This method managed to improve the reconstruction of some polarimetric features (compared to Souyris', Nord', and the DoP-based reconstruction methods), such as the co-pol ratio, co-pol correlation coefficient, and the minimum eigenvalue. The following polarimetric features could be reconstructed with high correlation ($>$ 0.8) and relatively low RMSE: co-pol ratio, co-pol correlation coefficient, all the eigenvalues, entropy, polarization fraction, and polarization height. Note that the latter two features could only be reconstructed if the data were from the May 10th scene. The model-based reconstruction achieved higher accuracy estimates of the cross-pol intensities when the number of averaging pixels in the multi-looking window increased. This method also scored the best when estimating the cross-pol intensity for areas covering deformed ice, and also the leads class if a high number of averaging pixels are used.

As opposed to Souyris', Nord's, and DoP-based reconstruction methods, the model-based reconstruction obtained relatively low RMSE values for varying values of the true cross-pol intensity. This means that the reconstruction results do not depend on the varying level of the backscattering cross-pol intensity.

Eigenvalue-based reconstruction method

Recall from section 6.2.3 that in the eigenvalue-based reconstruction we attempt to find a fraction of the total power when estimating the cross-pol intensity. The following equation was suggested:

$$X = \frac{\lambda_2}{2\lambda_1} q_0 \tag{7.4}$$

Here, λ_1 and λ_2 are the eigenvalues corresponding to the sample compact-pol covariance matrix. Specifically, the sample hybrid-pol covariance matrix was studied. Applying this method in the reconstruction process we mange to achieve relatively high reconstruction performance for the cross-pol intensities for all the classes. This method, as well as modified Souyris' are the two methods least dependent on the surface cover to be reconstructed. This can be observed in Table 7.6, where the values of the RMSE and Pearson correlation coefficient vary consistently. The four other methods discussed so far tend to generate either high correlation coefficients and RMSE, or low correlation coefficients and RMSE. This method was also the only capable of reconstructing the polarization asymmetry for the data from the March 13th scene. This method resulted in the highest correlation coefficient for the cross-pol intensity for the open water class given

that a large number of averaging pixels were used.

Modified Souyris' reconstruction method

Finally, the last method suggested was a modification of Souyris' reconstruction method. This modification replaced the iterative approach of Souyris with an optimization problem with a cost function and constraints. This algorithm is shown in the last row in Table 7.7. This method was by far the best method of those tested in this work. We attempted to reconstruct 15 polarimetric features; HH-intensity, VV-intensity, $|\langle S_{HH} S_{VV}^{\star} \rangle|$, cross-pol intensity, co-pol ratio, cross-pol ratio, co-pol correlation coefficient, entropy, the three eigenvalues, polarization fraction, pedestal height, polarization asymmetry, and the anisotropy. In total, the modified Souyris' reconstruction method managed to recover 12 of these from both the scenes from March and May. The cross-pol ratio, polarization asymmetry, and anisotropy where the only features that could not be recovered using this method.

	Assumptions	Equation	Polarimetric features	Best suited (SAR scene)
Souyris	1. Reciprocity ($S_{HV} = S_{VH}$) 2. Reflection symmetry 3. Natural media (exhibit strong azimuthal symmetry)	$\frac{X}{H+V} = \frac{1-\lvert\rho_{HHVV}\rvert}{4}$	ρ_{HHVV}, λ_1, λ_2 Entropy, PF^a, PH^a	May
Nord	1. Reciprocity ($S_{HV} = S_{VH}$) 2. Reflection symmetry	$\frac{X}{H+V} = \frac{1-\lvert\rho_{HHVV}\rvert}{N}$	$R_{VV/HH}$, ρ_{HHVV}, λ_1 λ_2, λ_3^a, Entropy PH^a, PA^a	May
DoP	1. Reciprocity ($S_{HV} = S_{VH}$) 2. Reflection symmetry 3. All the depolarized power is assign to the cross-pol intensity	$X = \left(\frac{1-DoP}{2}\right) q_0$	$R_{VV/FF}$, λ_1, λ_2 Entropy, PA^a	May
Model-based	1. Reciprocity ($S_{HV} = S_{VH}$) 2. Model assumptions: a. Reflection symmetry for the surface scattering model b. Azimuthal symmetry for the volume scattering model c. Surface orientation angle is uniformly distributed	$\min\ J_X(X) = 2X$ $-\left(\frac{1}{2}\frac{P_S}{1+\lvert\hat{\beta}(X)\rvert^2}\lvert\hat{\beta}(X)\rvert^2(1-\text{sinc}(4\delta))\right)$ $-\left(\frac{P_V}{3-\rho_L(X)}(1-\rho_L(X))\right)$ subject to: $0 < X < \frac{2}{3}C_{11}$ $0 < X < \frac{2}{3}C_{22}$	$R_{VV/HH}$, ρ_{HHVV}, λ_1 λ_2, λ_3, Entropy PF^a, PH^a	March
Eigenvalue-based	1. Reciprocity ($S_{HV} = S_{VH}$) 2. Reflection symmetry 3. Only depolarization effects generate response in the cross-pol channel	$X = \frac{\lambda_2}{2\lambda_1} q_0$	$R_{VV/HH}$, ρ_{HHVV}, λ_1 λ_2, λ_3, Entropy PA, PF^a, PH	March May
Modified Souyris	1. Reciprocity ($S_{HV} = S_{VH}$) 2. Reflection symmetry 3. Natural media (exhibit strong azimuthal symmetry)	$\min\ J(X, \Omega(X)) = 2X(3-\Omega(X))$ $-(1-\Omega(X))(2C_{11}+2C_{22})$ subject to $0 \le X \le \frac{2}{3}C_{11}$ $0 \le X \le \frac{2}{3}C_{22}$	$R_{VV/HH}$, ρ_{HHVV}, λ_1 λ_2, λ_3, Entropy PF, PH	March May

Table 7.7: Overview of the six reconstruction methods that include: the assumptions made in each reconstruction method, the algorithm to find a pseudo quad-pol covariance matrix, the polarimetric features that can be reconstructed, and which SAR scene that each particular reconstruction method works best on. ^{a} can only be reconstructed if the data used are from May 10th scene.

8 Conclusion

This thesis started by presenting the theory of SAR and compact polarimetry. Further, a parameter study was conducted and we investigated the different quad-pol features and how these are related to the compact-pol features. Consequently, in chapter 5, we discovered that several polarimetric features extracted from the quad-pol data were "lost" in the compact-pol case. Following this we suggested several new reconstruction methods, namely DoP-based, model-based, eigenvalue-based, and modified Souyris' reconstruction. To the author's knowledge, this is the first attempt to reconstruct a pseudo quad-pol covariance matrix for sea ice covered SAR scenes.

In the previous chapter, we presented results for reproducing several polarimetric features. Different types of sea ice were considered with respect to the results of the reconstruction; this to be able to see which classes could be reconstructed properly. Additionally, some results were also presented during chapters 5 and 6.

8.1 Contributions and Findings

There are several observations and scientific contributions made throughout this work, and we summarize these below:

- Chapter 5 contained information about the different polarimetric features obtained from a quad-pol SAR system. In this chapter we attempted to find estimates of these polarimetric features derived from simulated compact-pol data. We succeeded in

finding close estimates of the co-pol ratio, co-pol correlation coefficient, and co-pol phase difference. These polarimetric features could be closely estimated from simulated hybrid-pol data from sea ice covered SAR scenes (and also $\frac{\pi}{4}$-pol data). From the figures showing the line segment through the March 13th and May 10th scenes, we discovered that the estimated co-pol ratio could be used to distinguish open water from smooth ice, and distinguish leads from deformed ice areas. The estimated cross-pol ratio could also help in distinguishing open water from smooth sea ice. We also discovered an information loss for several polarimetric features corresponding to quad-pol data. These were the eigenvalues, polarization fraction, pedestal height, polarization asymmetry, entropy, polarization asymmetry, cross-pol ratio, and cross-pol intensity.

- In chapter 6 we discovered a relationship between Souyris' linking and the ellipticity angle proposed by Raney. We observed that when $\frac{X}{H+V} > \frac{1-|\rho_{HHVV}|}{4}$ (overestimation) this condition was closely related to negative values of the ellipticity angle calculated from the Stokes vector with simulated hybrid-pol data. Raney stated that a negative value of the ellipticity angle correspond to areas where double bounce scattering was most likely to occur. Souyris' linking is only valid for areas exhibiting strong azimuthal symmetry, where no double bounce scattering takes place. This corresponds well with our discovery since when an overestimation in Souyris' linking occurs the azimuthal symmetry assumption is invalid and double bounce scattering is likely to be the dominant form of scattering.

- The estimated cross-pol intensities representing the whole range of classes (different sea ice types and open water) could be reconstructed with high performance if a large number of averaging pixels were used in the multi-looking. However, this will yield poorer spatial resolution, and details within the sea ice will disappear.

- We also discovered a relationship between Souyris' and the DoP-based reconstruction technique in the limiting cases of zero and complete polarizations. This discovery revealed another link between Souyris' and Raney's methods, where the degree of polarization could be related to Souyris' linking.

- In Figure 7.4, we observed that the incident angle is affecting the results of the reconstructed cross-pol intensities for all the reconstruction methods. This is especially pronounced for homogenous areas, such as open water and the smooth sea ice.

- Souyris' and Nord's methods (see section 6.1.1) require a single user-input, namely the number of iterations when searching for the cross-pol intensity. This number is often chosen randomly when applying this method in the literature. This work also attempted to analyze how the number of iterations affected the reconstruction

results, especially for the cross-pol intensity. We observed that at least 10 iterations were necessary to obtain promising values of the Pearson correlation coefficients. Even higher numbers of iterations were needed to obtain a promising Pearson correlation coefficient for the data acquired March 13th. This is most likely because the sea ice in the March scene consists of more complicated sea ice structures. From these observations, we can conclude that a higher number of iterations is necessary if more complicated sea ice types are present in the SAR scenes, while smaller numbers of iteration can be tolerated if smoother sea ice types are present.

- Several of the polarimetric features investigated could be reconstructed with the proper choice of reconstruction method. We observed that the polarimetric features from the May 10th scene could be estimated with high accuracy based on both Nord's and Souyris' reconstruction methods. If the data from the March 13th scene were used, the best methods for reconstructing these polarimetric features were the eigenvalue-based and modified Souyris' methods.

- In section 7.4.4 we evaluated the values in the true cross-pol intensities, and how these affected the reconstructed cross-pol intensities for the six reconstruction methods discussed. The evaluation was based on figures showing the RMSE as a function of the true cross-pol intensities, and we observed that each method had different trends (compared to each other). Souyris' and DoP-based reconstruction generated high RMSE values for low cross-pol intensity values, while Nord's method generated low RMSE. The eigenvalue-based, model-based, and the modified Souyris reconstruction methods produced a more constant behaviour of the RMSE values. This finding indicates that these reconstruction methods are less dependent on the value in the true cross-pol intensities, which is a clear benefit over the two existing methods.

- 11 polarimetric features (see Table 7.1) were estimated using each of the individual reconstruction methods. The eigenvalue-based method managed to recover 9 of these, while the modified Souyris' method recovered 8.

- The model-based reconstruction is the first reconstruction method proposed that utilize a model-based technique to perform a reconstruction of a pseudo-quad pol covariance matrix. This method had problems when reconstructing polarimetric features from the May scene, but scored among the highest for the March scene. Especially, the estimated cross-pol intensities covering deformed ice and the ice objects could be estimated with relatively high performance when considering the Pearson correlation coefficient and RMSE.

- The proposed modified Souyris' and the eigenvalue-based reconstruction methods are, by far, the best methods for reconstructing most of the polarimetric features covering different classes of sea ice. These methods have the highest overall accuracy for all the polarimteric features, and were the least dependent on sea ice

type. This is considered the main contribution of this thesis, and justifies further research as indicated in the next section.

Overall, the existing method proposed by Nord can be used to reconstruct smooth sea ice with relatively high accuracy, while the proposed methods are best suited for more complicated sea ice structures.

8.2 Future Work

There are several possible improvements and extensions to the new reconstruction methods presented in this thesis, and the general topic of compact polarimetric imaging of sea ice covered SAR scenes. Some of these are:

- The model-based reconstruction includes several parameters that are related to the physical properties of the surface cover. A set of equations was given in this method, and the author observed a correlation between the surface slope angle and the degree of polarization. Following this, a solution to the cross-pol intensity could be calculated using an optimization technique. The results of this method were promising, especially when the number of averaging pixels was high. However, a deeper study on δ or the shape parameter ρ_L might provide even better reconstruction results. This study should include how these two physical parameters are affected by surface cover, incident angle, penetration depth, and frequency of the radar. Additionally, a study on δ in terms of it's sensitivity to the coefficients found in the empirical model should also be conducted. This should include how a small change in δ affects the estimated cross-pol intensity. Since the model-based reconstruction uses an empirical model, it should be further tested on other locations than Storfjorden and also for other frequency ranges. This to make sure that the model is as general as possible.

- Classification of different sea ice types based on the reconstructed polarimetric parameters should also be investigated. Can higher accuracy be achieved based on the reconstructed quad-pol parameters versus the compact-pol parameters?

- As discussed in chapter 3, MET Norway and NSIDC utilize dual-pol SAR data when creating sea ice charts. It is interesting to study whether the compact-pol data will improve the accuracy of these sea ice charts since more polarimetric information is given in compact-pol systems than in dual-pol systems, while the swath size is still extensive.

- The reconstruction methods tested in this thesis work well on sea ice covered SAR scenes, and it would be interesting to check if the newly proposed reconstruction methods could work on, e.g., vegetation covered SAR scenes.

- As observed during this work, the performance of the reconstruction is highly affected by the type of sea ice. All the types tested in this work are first-year ice, and it is therefore necessary to study if a reconstruction is possible for multi-year ice types.

- During this work we used simulated compact polarimetric data, and it is thus important to study how the methods proposed in this work can be used on real compact-pol SAR data. The best way to do so, is to have both quad-pol and compact-pol data from the same area acquired as close together in time as possible. Such a dataset was acquired over controlled oil slicks released at the Frigg field in June, and will be the subject of research in the next phase of this work.

8.3 Conclusion

The main question that was presented in the introductory part of this thesis was: *Can a pseudo quad-pol covariance matrix be reconstructed from simulated compact polarimetric data corresponding to sea ice covered SAR scenes, and if so, what are the desirable methods for achieving this?*

The answer is partially yes. From this work we can conclude that the co-pol components and some polarimetric features (listed in Table 7.1) representing different sea ice types can be reproduced with relatively high accuracy. The cross-pol intensity, however, is more problematic to estimate, especially for targets with low backscatter. Reproducing the cross-pol intensity in the limit suggested in [Nord et al., 2009] (0.8 dB) for the RMSE is not possible, but below 2dB is, however, possible. Our newly proposed methods managed to achieve higher accuracy compared to the existing reconstruction methods. We manage to achieve good results for the cross-pol intensity covering smooth, landfast-, rough-, and deformed ice, but there are still some challenges when reconstructing targets with relatively low response in the cross-pol channels, for example open water, sea ice objects, and leads. This can be remedied if a high number of averaging pixels is used in the multi-looking. Overall, the proposed modified Souyris' reconstruction technique is the best method for reconstructing a pseudo quad-pol covariance matrix, and for further estimating several polarimetric features.

Bibliography

[Ainsworth et al., 2007] Ainsworth, T. L., Preiss, M., Stacy, N., Nord, M., and Lee, J.-S. (2007). Analysis of Compact Polarimetric SAR Imaging Modes. *in Proc. POLinSAR, Frascati, Italy*.

[Atteia and Collins, 2013] Atteia, G. and Collins, M. J. (2013). On the use of Compact Polarimetry SAR for Ship Detection. *ISPRS Journal of Photogrammetry and Remote Sensing*, 80:1–9.

[Balabhavya, 2013] Balabhavya, K. (2013). Polarimetric modeling of lunar surface for scattering information retrieval using mini-sar data of chandrayaan-1. *Master of Science, The Netherlands*.

[Boularbah et al., 2012] Boularbah, S., Ouarzeddine, M., and Belhadj-Aissa, A. (2012). Investigation of The Capability of the Compact Polarimetry mode to Reconstruct Full Polarimetry mode using RADARSAT2 data. 1(1).

[Carsey, 1992] Carsey, F. D. (1992). Microwave Remote Sensing of Sea Ice. *Geophysical Monograph 68*.

[Charbonneau et al., 2010] Charbonneau, F. J., Brisco, B., Raney, R. K., McNairn, H., Liu, C., Vachon, P. W., Shang, J., DeAbreu, R., Champagne, C., Merzouki, A., and Geldsetzer, T. (2010). Compact Polarimetry Overview and Applications Assessment. *Canadian Journal of Remote Sensing*, 36(2):298–315.

[Chuvieco and Huete, 2010] Chuvieco, E. and Huete, A. (2010). *Fundamentals of Satellite Remote Sensing*. CRC Press Taylor and Francis Group.

[Cloude, 2009] Cloude, S. (2009). Dual versus Quadpol: A new test Statistic for Radar Polarimetry. *Workshop, POLinSAR, ESA*.

[Cloude, 2010] Cloude, S. (2010). *Polarisation Applications in Remote Sensing*. Oxford University Press.

[Cloude et al., 2012] Cloude, S., Goodenough, D., and Chen, H. (2012). Compact De-

composition Theory. *IEEE Transactions on Geoscience and Remote Sensing*, 9(1):28–32.

[Cloude and Pottier, 1996] Cloude, S. R. and Pottier, E. (1996). A Review of Target Decomposition Theorems in Radar Polarimetry. *IEEE Transactions on Geoscience and Remote Sensing*, 34(2):498–518.

[Collins et al., 2013] Collins, M. J., Denbina, M., and Atteia, G. (2013). On the Reconstruction of Quad-Pol SAR Data from Compact Polarimetry Data for Ocean Target Detection. *IEEE Transactions on Geoscience and Remote Sensing*, 51(2).

[CSA, 2011] CSA (2011). Satellite Characteristics, Canadian Space Agency. `http://www.asc-csa.gc.ca/eng/satellites/radarsat/radarsat-tableau.asp`, Accessed: 3 March 2015.

[Cumming and Wong, 2005] Cumming, I. G. and Wong, F. H. (2005). *Digital Processing of Synthetic Aperture Radar data*. Artech House.

[Dabboor and Geldsetzer, 2014] Dabboor, M. and Geldsetzer, T. (2014). On the Classification of Sea Ice Types using Simulated Radarsat Constellation Mission (RCM) Compact Polarimetric SAR Parameters. *ASPRS 2014 Annual Conference, Louisville, Kentucky*.

[Danklmayer et al., 2009] Danklmayer, A., Doring, B., Schwerdt, M., and Chandra, M. (2009). Assessment of Atmospheric Propagation Effects in SAR Images. *IEEE Transactions on Geoscience and Remote Sensing*, 47(20):3507–3518.

[Denbina, 2014] Denbina, M. (2014). Iceberg Detection Using Polarimetric Synthetic Aperture Radar. *P.h.D. Dissertation, University of Calgary*.

[Dierking, 2013] Dierking, W. (2013). Sea Ice Monitoring by Synthetic Aperture Radar. *Oceanography*, 26(2):100–111.

[Dierking and Pedersen, 2013] Dierking, W. and Pedersen, L. T. (2013). Monitoring Sea Ice using ENVISAT ASAR - A New Era Stating 10 Years Ago. *IEEE International Geoscience and Remote Sensing Symposium 2012*.

[Doulgeris, 2012] Doulgeris, A. P. (2012). Rethinking Statistical Based Segmentation of Sea Ice. *SeaSar*.

[Drinkwater et al., 1992] Drinkwater, M. R., Kwok, R., Rignot, E., Israelsson, H., Onstott, R. G., and Winebrenner, D. P. (1992). Chapter 24. Potential Applications of Polarimetry to the Classification of Sea Ice. *Microwave Remote Sensing of Sea Ice, Geophysical Monograph 68, American Geophysical Union*.

[Dubois-Fernandez et al., 2008a] Dubois-Fernandez, P., Angelliaume, S., Truong-Loi, M.-L., and Souyris, J.-C. (2008a). Compact Polarimetry Mode for a Low Frequency SAR in Space. *IEEE Transactions on Geoscience and Remote Sensing Symposium, IGARSS 2008*.

[Dubois-Fernandez et al., 2008b] Dubois-Fernandez, P., Souyris, J.-C., Angelliaume, S., and Garestier, F. (2008b). The Compact Polarimetry Alternative for Spaceborne SAR at Low Frequency. *IEEE Transactions on Geoscience and Remote Sensing*, 46(10).

[Edwards and Penney, 1988] Edwards, C. and Penney, D. (1988). *Elementary Linear Algebra*. PRENTICE HALL, Englewood Cliffs.

[Elachi and van Zyl, 2006] Elachi, C. and van Zyl, J. (2006). *Introduction to the Physics and Techniques of Remote Sensing*. John Wiley and Sons, Inc., Publication, second edition.

[Eltoft et al., 2014] Eltoft, T., Doulgeris, A. P., and Gran, J. (2014). Model-Based Polarimetric Decomposition of Artic Sea Ice. *EUSAR 2014*.

[ESA, n.d.] ESA (n.d.). Polarimetric Decompositions, European Space Agency - Earthnet Online Manuals. `http://earth.eo.esa.int/polsarpro/Manuals/`, Accessed: 15 February 2015.

[Falkingham, 2014] Falkingham, J. C. (2014). Global Satellite Observation Requirements for Floating Ice. *Contract report for Environment Canada: Dr. Chris Derksen, Scientific Authority*.

[Freeman and Durden, 1998] Freeman, A. and Durden, S. L. (1998). A Three-Component Scattering Model for Polarimetric SAR Data. *IEEE Transactions on Geoscience and Remote Sensing*, 36(3).

[Geldsetzer et al., 2014] Geldsetzer, T., Arkett, M., and Zagon, T. (2014). All Season Assessment of RADARSAT Constellation Mission Compact Polarimetry Modes for Canadian Ice Service Operational Implementation. *Geoscience and Remote Sensing Symposium (IGARSS), 2014 IEEE International*, pages 1560–1563.

[Geldsetzer and Yackel, 2009] Geldsetzer, T. and Yackel, J. J. (2009). Sea Ice Type and Open Water Discrimination using Dual Co-Polarized C-band SAR. *Canadian Journal of Remote Sensing*, 35(1):73–84.

[Gill and Yackel, 2013] Gill, J. P. S. and Yackel, J. J. (2013). Evaluating of C-band SAR Polarimetric Parameters for Discrimination of First-Year Sea Ice Types. *Department of Geography, University of Calgary, GeoCanadian Journal of Remote Sensing*, 38(3):306–323.

[Hajnsek et al., 2009] Hajnsek, I., Jaghuber, T., Schon, H., and Papathanassiou, K. P. (2009). Potential of Estimating Soil Moisture Under Vegetation Cover by Means of PolSAR. *IEEE International Geoscience and Remote Sensing*, 47(2).

[Hossain, 2012] Hossain, M. M. (2012). Polarimetric Synthetic Aperture Polarimetric Measurements of Snow Covered First-year Sea Ice. *Master of Science, University of Calgary*.

[JAXA, n.d.] JAXA (n.d.). About ALOS-PALSAR, ALOS Research and Application Project of Eorc, JAXA (Japan Aerospace Exploration Agency). `http://www.eorc.jaxa.jp/ALOS/en/about/palsar.htm`, Accessed: 9 January 2015.

[Jiao et al., 2011] Jiao, X., McNairn, H., Shang, J., Pattey, E., Liu, J., and Champagne, C. (2011). The Sensitivity of RADARSAT-2 Polarimetric SAR data to Corn and Soybean Leaf Area Index (LAI). *Canadian Journal of Remote Sensing*, 37(1):69–81.

[Kim et al., 2011] Kim, J.-W., jin Kim, D., and Hwang, B. J. (2011). Characterization of Arctic Sea Ice Thickness using Space-Borne Polarimetric SAR data. *Geoscience and Remote Sensing Symposium (IGARSS), 2011 IEEE International*, pages 2105–2108.

[Kliger et al., 1990] Kliger, D. S., Lewis, J. W., and Randall, C. E. (1990). *Polarized Light in Optics and Spectroscopy*. Academic Press.

[Lee and Pottier, 2009] Lee, J.-S. and Pottier, E. (2009). *Polarimetric Radar Imaging*. Number 42-45. CRC Press Taylor and Francis Group.

[Li et al., 2006] Li, Y., Zhang, Y., Chen, J., and Zhang, H. (2006). Improved Compact Polarimetric SAR Quad-Pol Reconstruction Algorithm for Oil Spill Detection. *IEEE Geoscience and Remote Sensing Letters*, 11(6).

[MacDonald, Dettwiler and Associates Ltd, 2014] MacDonald, Dettwiler and Associates Ltd (2014). Radarsat-2 product description. `http://gs.mdacorporation.com/products/sensor/radarsat2/RS2_Product_Description.pdf`, Accessed: 16 June 2015.

[MET Norway, n.d.] MET Norway (n.d.). Documentation - Satellite Data Used, MET Norway-Norwegian Meteorological Institute. `http://polarview.met.no/`, Accessed: 13 February 2015.

[Moen, 2014] Moen, M.-A. N. (2014). Analysis and Interpretation of C-band Polarimetric SAR Signatures of Sea Ice. *University of Tromso*, A dissertation for the degree of Philosophiae Doctor.

[Moen et al., 2013] Moen, M. A. N., Doulgeris, A. P., Anfinsen, S. N., Renner, A. H. H.,

Hughes, N., Gerland, S., and Eltoft, T. (2013). Comparison of feature based segmentation of full polarimetric sar satellite sea ice images with manually drawn ice charts. *The Cryosphere*.

[Moreria et al., 2013] Moreria, A., Prats-Iraola, P., Younis, M., Krieger, G., Hajnsek, I., and Papathanassiou, K. P. (2013). A Turorial on Synthetic Aperture Radar. *Microwaves and Radar Institute of the German Aerospace Center (DLR), Germany*.

[Nghiem et al., 1992] Nghiem, S. V., Yueh, S. H., Kwok, R., and Li, F. (1992). Symmetry Properties in Polarimetric Remote Sensing. *Radio Science*, 27(5):693–711.

[Nord et al., 2009] Nord, M. E., Aingworth, T. L., Lee, J.-S., and Stacy, N. (2009). Comparison of Compact Polarimetric Synthetic Aperture Radar Modes. *IEEE Transactions on Geoscience and Remote Sensing*, 47(1):634–646.

[NRSC, 2014] NRSC (2014). RISAT-1 Data Products Format, National Remote Sensing Centre Indian Space Research Organisation. `http://www.nrsc.gov.in/Data_Products_Services_Satellite_RISAT1.html`, Accessed: 24 May 2015.

[NSIDC, n.d.] NSIDC (n.d.). National Snow and Ice Data Center - All About Sea Ice. `http://nsidc.org/cryosphere/seaice/index.html`, Accessed: 3 February 2015.

[Olsen et al., 1999] Olsen, R., Wahl, T., and Engen, G. (1999). Expected performance of the ENVISAT ASAR for near real-time maritime applications. *Geoscience and Remote Sensing Symposium, 1999. IGARSS '99 Proceedings. IEEE 1999 International*, 2:962–964.

[Onstott and Shuchman, 2004] Onstott, R. G. and Shuchman, R. A. (2004). Chapter 3. SAR Measurements of Sea Ice. *Synthetic Aperture Radar Marine User's Manual*, `http://www.sarusersmanual.com/`, Accessed: 24 May 2015.

[Raney et al., 2012] Raney, K., Cahill, J. T. S., Patterson, G. W., and Bussey, D. B. J. (2012). The m-chi Decomposition of Hybrid Dual-Polarimetric Radar Data with Application to Lunar Craters. *Journal of Geophysical Research*, 117.

[Raney, 2007] Raney, R. K. (2007). Hybrid-Polarity SAR Architecture. *IEEE Transactions on Geoscience and Remote Sensing*, 45(11):3397–3404.

[Raney and Hopkins, 2011] Raney, R. K. and Hopkins, J. (2011). A Perspective on Compact Polarimetry. *IEEE Geoscience and Remote Sensing Newsletters*, `http://www.grss-ieee.org/wp-content/uploads/2010/03/ngrs_SeptForWeb.pdf`, Accessed: 17 March 2015.

[Salberg et al., 2014] Salberg, A.-B., Rudjord, O., and Solberg, A. H. S. (2014). Oil Spill Detection in Hybrid-Polarimetric SAR Images. *IEEE Transactions on Geoscience and*

Remote Sensing, 52(10).

[Scheuchl et al., 2001] Scheuchl, B., Caves, R., Cumming, I., and Staples, G. (2001). Automated Sea Ice Classification using Spaceborne Polarimetric SAR data. *IEEE International Geoscience and Remote Sensing Symposium (IGARSS)*, 7:3117–3119.

[Scheuchl et al., 2004] Scheuchl, B., Flett, D., Caves, R., and Cumming, I. (2004). Potential of Radarsat-2 data for Opertational Sea Ice Monitoring. *Canadian Journal of Remote Sensing*, 30(3):448–461.

[Shirvany et al., 2012] Shirvany, R., Chabert, M., and Tourneret, J.-Y. (2012). Ship and Oil-Spill Detection using the Degree of Polarization in Linear and Hybrid/Compact Dual-Pol SAR. *IEEE Journal of Selected Topics in Applied Earth Observations and Remote Sensing*, 5(3).

[Shokr and Sinha, 2015] Shokr, M. and Sinha, N. (2015). *Sea ice: Physics and Remote Sensing*. John Wiley and Sons, Inc.

[Souyris et al., 2005] Souyris, J.-C., Imboa, P., Fjørtoft, R., Mingot, S., and Lee, J.-S. (2005). Compact Polarimetry Based on Symmetry Properties of Geophysical Media: The $\pi/4$ Mode. *IEEE Transactions on Geoscience and Remote Sensing*, 43(3):634–646.

[Souyris et al., 2007] Souyris, J.-C., Stacy, N., Aingworth, T. L., Lee, J.-S., and Dubois-Fernandez, P. (2007). *SAR Compact Polarimetry (CP) For Earth Observation and Planetology: Concept and Challenges. A study case at P band.*

[Spudis et al., 2010] Spudis, P. D., Bussey, D. B. J., Butler, B., Carter, L., Chakraborty, M., Davis, J. G., Goswami, J., Heggy, E., Kirk, R., Neish, C., Nozette, S., Patterson, W., Robinson, M., Raney, R. K. ., Thompson, T., Thomson, B., and Ustinov, E. (2010). Result of the Mini-SAR Imaging RADAR, Chandrayyaan-1 Mission to the Moon. *41st Lunar and Planetary Science Conference*.

[Taylor and Boerner, 2007] Taylor, W. and Boerner, M. (2007). Basic Concepts in Radar Polarimetry. *PolSARpro Lecture Notes*, 3.

[Theodoridis and Koutroumbas, 2009] Theodoridis, S. and Koutroumbas, K. (2009). *Pattern Recognition Fourth Edition*. Elsevier.

[Touzi, 2009] Touzi, R. (2009). Compact-Hybrid Versus Linear-Dual and Fully Polarimetric SAR. *Canada Centre for Remote Sensing*.

[Truong-Loi et al., 2009a] Truong-Loi, M.-L., Dubois-Fernandez, P., Freeman, A., and Pottier, E. (2009a). The Conformity Coefficient or how to explore The Scattering behaviour from Compact Polarimetry mode. *Radar Conference, 2009 IEEE*, pages 1–6.

[Truong-Loi et al., 2010] Truong-Loi, M.-L., Dubois-Fernandez, P., Pottier, E., Freeman, A., and Souyris, J.-C. (2010). Potentials of a Compact Polarimetric SAR System.

[Truong-Loi et al., 2009b] Truong-Loi, M.-L., Freeman, A., Dubois-Fernandez, P. C., and Pottier, E. (2009b). Estimation of Soil Moisture and Faraday Rotation From Bare Surfaces Using Compact Polarimetry. *IEEE Transactions on Geoscience and Remote Sensing*, 47(11):3608–3615.

[Tucker III et al., 1992] Tucker III, W. B., Perovich, D. K., and Gow, A. J. (1992). *Chapter 2: Physical Properties of Sea Ice Relevant to Remote Sensing*. Number 73-104. Microwave remote sensing of sea ice.

[Uiboupin et al., 2009] Uiboupin, R., Sipelgas, L., and Raudsepp, U. (2009). Sea Ice Concentration and Type Analysis from Dual Pol Radarsat-2 and Modis Images in The Baltic Sea. *Geoscience and Remote Sensing Symposium, 2009 IEEE International, IGARSS 2009*, 2:II–590–II–593.

[van Zyl and Kim, 2010] van Zyl, J. and Kim, Y. (2010). *Synthetic Aperture Radar Polarimetry*. WILEY.

[van Zyl et al., 2011] van Zyl, J. J., Arii, M., and Kim, Y. (2011). Model-Based Decomposition of Polarimetric SAR Covariance Matrices Constrained for Nonnegative Eigenvalues. *IEEE Transactions on Geoscience and Remote Sensing*, 49(9):3452–3459.

[Wackerman, 1992] Wackerman, C. (1992). *Chapter 6: Digital SAR Image Formation*. Number 68. Microwave remote sensing of sea ice.

[Winebrenner et al., 1989] Winebrenner, D. P., Tsang, L., Wen, B., and West, R. (1989). Sea-ice Characterization Measurements needed for Testing of Microwave Remote Sensing Models. *IEEE Journal of Oceanic Engineering*, 14(2):149–158.

[WMO-No.574, 2010] WMO-No.574 (2010). Sea-ice Information Services in The World. *Technical Report 574, World Meteorological Organization*.

[Yin et al., 2015] Yin, J., Moon, W. M., and Yang, J. (2015). Model-Based Pseudo quad-Pol Reconstruction from Compact Polarimetry and Its Application to Oill-Spill Observation. *Journal of Sensors*.

A

Calculation of the Compact-pol Covariance matrix

This appendix highlights the calculation process of the compact-pol covariance matrix. To demonstrate the calculation of the compact-pol covariance matrix, the scattering vector obtained from the $\pi/4$-pol mode system is used. The scattering vector is given by equation A.1.

$$\overrightarrow{k_{\frac{\pi}{4}}} = [S_{HH} + S_{HV}, S_{VV} + S_{HV}]^T / \sqrt{2} \tag{A.1}$$

The covariance matrix has the following formula:

$$C_{\frac{\pi}{4}} = \langle \overrightarrow{k_{\frac{\pi}{4}}} \overrightarrow{k}^{\star T}_{\frac{\pi}{4}} \rangle = \langle \begin{bmatrix} S_{HH} + S_{HV} \\ S_{VV} + S_{HV} \end{bmatrix} / \sqrt{2} \times \left[(S_{HH} + S_{HV})^{\star}, (S_{VV} + S_{HV})^{\star} \right] / \sqrt{2} \rangle$$

$$= \frac{1}{2} \langle \begin{bmatrix} (S_{HH} + S_{HV})(S^{\star}_{HH} + S^{\star}_{HV}) & (S_{HH} + S_{HV})(S^{\star}_{VV} + S^{\star}_{HV}) \\ (S_{VV} + S_{HV})(S^{\star}_{HH} + S^{\star}_{HV}) & (S_{VV} + S_{HV})(S^{\star}_{VV} + S^{\star}_{HV}) \end{bmatrix} \rangle$$

The scattering matrix consist of one imaginary part and one complex part, hence, the scattering matrix can be written as:

$$S_{ab} = X_{ab} + jY_{ab}$$

where a and b the represent polarization state of the electromagnetic wave. The first expression in the matrix above can be calculated as:

$$(S_{HH} + S_{HV})(S^{\star}_{HH} + S^{\star}_{HV}) = S_{HH}S^{\star}_{HH} + S_{HH}S^{\star}_{HV} + S_{HV}S^{\star}_{HH} + S_{HV}S^{\star}_{HV}$$

From complex analyzis, the expression $S_{HH}S^{\star}_{HH}$ and $S_{HV}S^{\star}_{HV}$ can be rewritten as $|S_{HH}|^2$ and $|S_{HV}|^2$. The other two terms can be calculated as follows:

$$S_{HH}S^{\star}_{HV} + S_{HV}S^{\star}_{HH} = (X_{HH} + jY_{HH})(X_{HV} - jY_{HV}) + (X_{HV} + jY_{HV})(X_{HH} - jY_{HH})$$

$$= X_{HH}X_{HV}+Y_{HH}Y_{HV}+jX_{HH}Y_{HV}-jX_{HV}Y_{HH}+X_{HV}X_{HH}+Y_{HV}Y_{HH}+jX_{HV}Y_{HH}-jX_{HH}Y_{HV}$$

where all the complex part cancel each other out, yielding:

$$S_{HH}S^{\star}_{HV} + S_{HV}S^{\star}_{HH} = 2\Re(S_{HH}S^{\star}_{HV})$$

The other expression in the 2×2 matrix above will obtain a similar result for different polarization terms. After a similar calculation for the other terms, the covariance matrix has the following form:

$$\begin{aligned} \boldsymbol{C}_{\frac{\pi}{4}} = \frac{1}{2}&\begin{bmatrix} \langle|S_{HH}|^2\rangle & \langle S_{HH}S^{\star}_{VV}\rangle \\ \langle S_{VV}S^{\star}_{hh}\rangle & \langle|S_{VV}|^2\rangle \end{bmatrix} \\ &+ \frac{\langle|S_{HV}|^2\rangle}{2}\begin{bmatrix} 1 & 1 \\ 1 & 1 \end{bmatrix} + \frac{1}{2}\begin{bmatrix} 2\Re(\langle S_{HH}S^{\star}_{HV}\rangle) & \langle S_{HH}S^{\star}_{HV}\rangle + \langle S_{HV}S^{\star}_{VV}\rangle \\ \langle S^{\star}_{HH}S_{HV}\rangle + \langle S_{VV}S^{\star}_{HV}\rangle & 2\Re(\langle S_{VV}S^{\star}_{HV}\rangle) \end{bmatrix} \end{aligned} \tag{A.2}$$

The first matrix in equation A.2 characterizes the polarimetric behavior of co-polar channels, the second one is proportional to the cross polarization signature $|S_{HV}|^2$, and the last matrix is a residue matrix [Souyris et al., 2007], only correlation of co- and cross-pol.

B

Accuracy Assessment

During this work, several results are generated from the compact-pol data and compared against the quad-pol data. The Pearson correlation coefficient and root mean square error (RMSE) are considered when testing the performance of the different estimators (for example DoP reconstruction or Nord's reconstruction). By considering these two measurement techniques one can study both the correlation and the spread of the difference between the true and estimated data.

Root mean square error (RMSE)

Root mean square error is defined as:

$$RMSE = \sqrt{E[(X - \hat{X})^2]} \tag{B.1}$$

where $E[..]$ is the expectation operator, X is the true data, and $\hat{X}$ is the estimated data generated from an estimator. The expectation operator is often replaced by the average of the given product inside the expectation operator, i.e.:

$$RMSE = \sqrt{E[(X - \hat{X})^2]} \approx \sqrt{\frac{1}{N}\sum_{i=1}^{N}(X_i - \hat{X}_i)^2} \tag{B.2}$$

In our case, N is the total number of pixels, and X_i is the value on pixel location i.

RMSE measures the square root of the averaged squared difference between the true and estimated variable, and thus is a measure of the variability of the given estimator. By excluding the square root one end up with the mean square error (MSE) estimator. If a high RMSE (or MSE) is generated, this implies a high spread around the true value, and low RMSE indicates a low spread.

The values generated from the SAR data are low, and in most cases the decibel scale is used when visualizing the SAR data. When using the decibel scale the intensity in the different polarization channels may vary from −35dB to 0dB. If the decibel scale is used, the relative RMSE becomes:

$$RMSE = \sqrt{E\left[\left(10\log_{10}\left(\frac{X}{\hat{X}}\right)\right)^2\right]} \tag{B.3}$$

This is in fact an normalized absolute RMSE value, since this measure will only produce positive values. A major challenge is therefore to set a proper boundary on the RMSE, i.e., a limit on what is considered reasonable. In this thesis a promising RMSE is set to be below 1dB. This indicates that if the true variable, X, has a value of −10dB then a reasonable estimate will lie between −9dB and −11dB.

The RMSE considers both the variance within the data and the bias, i.e.:

$$RMSE = \sqrt{\mathrm{Var}(X - \hat{X}) + \left(\mathrm{Bias}(X - \hat{X})\right)} \tag{B.4}$$

Pearson correlation coefficient

The RMSE considers the absolute spread of the averaged difference, and it is therefore necessary to also consider a linear correlation between the estimated and true variables, which is independent on the scale within the data. The Pearson correlation coefficient is one way to do this. The Pearson correlation coefficient, also known as the Pearson product-moment correlation coefficient, measures the strength of the linear relationship between two variables, and whether there exists a linear association between them. The Pearson correlation coefficient is defined as:

$$r = \frac{(N\sum_{i=1}^{N} X_i\hat{X}_i - \sum_{i=1}^{N} X_i\hat{X}_i)}{\sqrt{(N\sum_{i=1}^{N} X^2 - \sum_{i=1}^{N} X_i)(N\sum_{i=1}^{N} \hat{X}^2 - \sum_{i=1}^{N} \hat{X}_i)}} \tag{B.5}$$

Here, r varies between −1 (negative correlation) and 1 (positive correlation). When

$r = 0$ no correlation between X and $\hat{X}$ exists. In this work, a Pearson correlation coefficient higher than 0.8 is considered as reasonable, and lower is considered as poor performance of the estimator used.

Scatter plots

The two accuracy measurements discussed above provide quantitative values for a given estimator. To visualize the results a scatter plot can be created to demonstrate both the spread (RMSE) and the correlation between the estimated and true variable. Very often during this work, scatter plots are used with both the RMSE (or MSE) and r (Pearson correlation coefficient) given in the figure. The scatter plots are created by plotting the true values along one axis (for example x-axis) and the estimated values along the other axis (for example y-axis). If the two variables are close, they should lie along a diagonal line.

Figure B.1 demonstrates how the RMSE, r, and scatter plots are used during this thesis. The figures also consider the cases when the results are varying from high (Figure A) to low performance (Figure F). In this thesis figures A to D are considered as reasonable when evaluating the performance of various estimated polarimetric features.

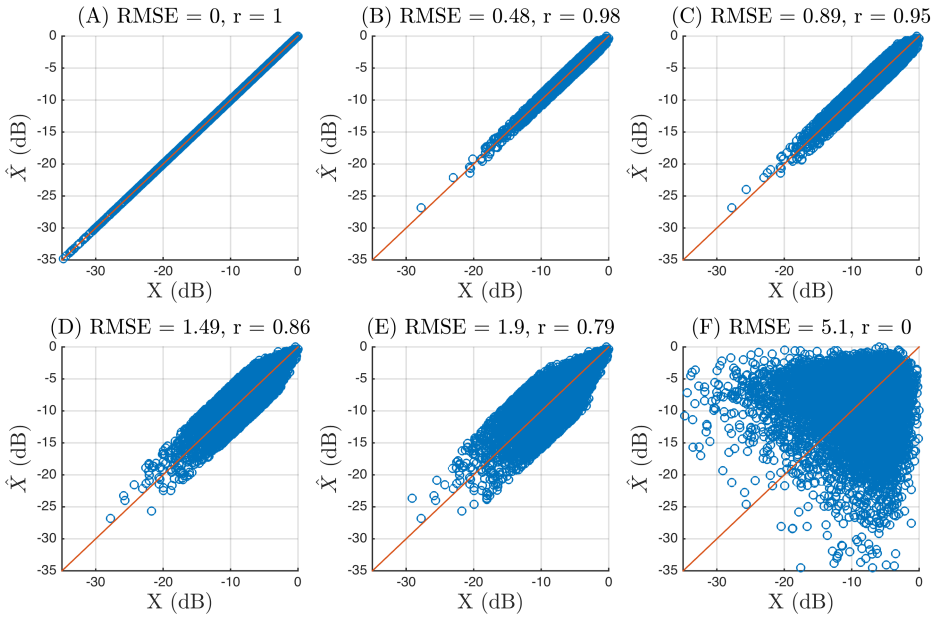

Figure B.1: Scatter plots of random distributed variables demonstrating varying values for RMSE and Pearson correlation coefficient.

When using the RMSE and the Pearson correlation coefficient together we can find

C

Sourys' Linking Between the Co- and Cross-pol Component

This appendix demonstrates the linking between the co- and cross-pol components that is used in Sourys' reconstruction method. The first step is to assume that the surface only exhibit pure volume scattering that has a strong azimuthal symmetry [Cloude, 2010], i.e.:

$$\boldsymbol{T}_V = \begin{bmatrix} t_{11} & 0 & 0 \\ 0 & t_{22} & 0 \\ 0 & 0 & t_{22} \end{bmatrix} \tag{C.1}$$

Then, a relation between the cross- and co-coherency parameter can be established, i.e. $t_{22} = t_{33}$. From this, the following expression follows:

$$\begin{aligned} &\langle |S_{HH} - S_{VV}|^2 \rangle = 4\langle |S_{HV}|^2 \rangle \\ &\implies \langle (S_{HH} - S_{VV})(S_{HH} - S_{VV})^\star \rangle = \\ &\langle |S_{HH}|^2 \rangle + \langle |S_{VV}|^2 \rangle - \langle S_{HH} S_{VV}^\star \rangle - \langle S_{VV} S_{HH}^\star \rangle \\ &= \langle |S_{HH}| \rangle + \langle |S_{VV}| \rangle - 2\Re\left(\langle |S_{HH} S_{VV}^\star| \rangle\right) \end{aligned} \tag{C.2}$$

Next, dividing by the term $\langle|S_{HH}|^2\rangle+\langle|S_{VV}|^2\rangle$ on both sides of the equal sign yields:

$$\frac{4\langle|S_{HV}|^2\rangle}{\langle|S_{HH}|^2\rangle+\langle|S_{VV}|^2\rangle} = \frac{\langle|S_{HH}|\rangle+\langle|S_{VV}|\rangle-2\Re\left(\langle|S_{HH}S_{VV}^{\star}|\rangle\right)}{\langle|S_{HH}|^2\rangle+\langle|S_{VV}|^2\rangle}$$

$$\frac{4\langle|S_{HV}|^2\rangle}{\langle|S_{HH}|^2\rangle+\langle|S_{VV}|^2\rangle} = 1-\frac{2\Re\left(\langle|S_{HH}S_{VV}^{\star}|\rangle\right)}{\langle|S_{HH}|^2\rangle+\langle|S_{VV}|^2\rangle}$$

because of the assumed strong azimuthal symmetry, $\langle|S_{VV}|^2\rangle = \langle|S_{HH}|^2\rangle$; the term to the left of the equal sign becomes:

$$1-\frac{2\Re\left(\langle|S_{HH}S_{VV}^{\star}|\rangle\right)}{\langle|S_{HH}|^2\rangle+\langle|S_{VV}|^2\rangle} = 1-\frac{2\Re\left(\langle|S_{HH}S_{VV}^{\star}|\rangle\right)}{2\langle|S_{HH}|^2\rangle} = 1-|\rho_{HHVV}|$$

and the final result is:

$$\frac{\langle|S_{HV}|^2\rangle}{\langle|S_{HH}|^2\rangle+\langle|S_{VV}|^2\rangle} = \frac{1}{4}(1-|\rho_{HHVV}|)$$

The key assumption is that this will be true even if a surface scattering component is added [Cloude, 2010], i.e.:

$$\boldsymbol{T} = \boldsymbol{T}_S + \boldsymbol{T}_V \tag{C.3}$$

This relation will entail some restrictions with regards to the surface of interest. One must be careful when making this assumption, as it only is valid if natural surfaces are evaluated [Cloude, 2010].

D

Calculation of the N-parameter

This appendix demonstrate the steps by chaining the value 4 in Sourys' method to N in Nord's method based on [Nord et al., 2009].

1. The starting point is the definition of the degree of coherence:

$$(1)\ |\rho_{HHVV}| = \frac{|\langle S_{HH} S_{VV}^{\star} \rangle|}{\sqrt{\langle |S_{HH}|^2 \rangle \langle |S_{VV}|^2 \rangle}}$$

2. The arithmetic mean is used for this purpose, and is given as:

$$(2)\ \frac{\langle |S_{HH}|^2 \rangle + \langle |S_{VV}|^2 \rangle}{2} \geq \sqrt{\langle |S_{HH}|^2 \rangle \langle |S_{VV}|^2 \rangle}$$

   This will always be true as the terms $\langle |S_{HH}|^2 \rangle$ and $\langle |S_{VV}|^2 \rangle$ are always real and positive numbers.

3. Inserting inequality (2) into (1) yields:

$$(3)\ \frac{\langle |S_{HH}|^2 \rangle + \langle |S_{VV}|^2 \rangle}{2} \geq \frac{|\langle S_{HH} S_{VV}^{\star} \rangle|}{|\rho_{HHVV}|}$$

$$(4)\ |\rho_{HHVV}|(\langle |S_{HH}|^2 \rangle + \langle |S_{VV}|^2 \rangle) \geq 2|\langle S_{HH} S_{VV}^{\star} \rangle|$$

This is equivalent to:

$$(5)\ \langle|S_{HH}|^2\rangle+\langle|S_{VV}|^2\rangle-|\rho_{HHVV}|(\langle|S_{HH}|^2\rangle+\langle|S_{VV}|^2\rangle) \leq \langle|S_{HH}|^2\rangle+\langle|S_{VV}|^2\rangle-2|\langle S_{HH}S_{VV}^{\star}\rangle|$$

4. After rearranging equation (3) into (5), a new relation is used: $|\langle S_{HH}S_{VV}^{\star}\rangle| \geq \Re\left(\langle S_{HH}S_{VV}^{\star}\rangle\right)$. Substituting this relation into (5), yields:

$$(6)\ (1-|\rho_{HHVV}|)(\langle|S_{HH}|^2\rangle+\langle|S_{VV}|^2\rangle) \leq \langle|S_{HH}|^2\rangle+\langle|S_{VV}|^2\rangle-2\Re\left(\langle S_{HH}S_{VV}^{\star}\rangle\right)$$

This will still hold, as the replacement is made by a smaller or equal value.

5. The following relation is true for complex numbers:

$$(7)\ \langle|S_{HH}|^2\rangle+\langle|S_{VV}|^2\rangle-\Re\left(\langle S_{HH}\rangle\langle S_{VV}\rangle\right)=\langle|S_{HH}-S_{VV}|^2\rangle$$

Inserting this relation into (6), yields:

$$(8)\ (1-|\rho_{HHVV}|)(\langle|S_{HH}|^2\rangle+\langle|S_{VV}|^2\rangle) \leq \langle|S_{HH}-S_{VV}|^2\rangle$$

where $S_{HH}-S_{VV}$ is actually one of the terms in the Pauli basis, which in general represents double bounce scattering.

6. Rearranging the inequality in (8) and multiplying both sides by $\langle|S_{HV}|^2\rangle$ yields:

$$(9)\ \frac{\langle|S_{HV}|^2\rangle}{\langle|S_{HH}|^2\rangle+\langle|S_{VV}|^2\rangle} \geq \frac{1-|\rho_{HHVV}|}{\left(\frac{\langle|S_{HH}-S_{VV}|^2\rangle}{\langle|S_{HV}|^2\rangle}\right)}$$

7. The assumption made by Souyris was: $\frac{\langle|S_{HV}|^2\rangle}{\langle|S_{HH}|^2\rangle+\langle|S_{VV}|^2\rangle}=\frac{1-|\rho_{HHVV}|}{4}$, which resembles the relation in (9) (except from the inequality sign).

8. A new variable, N, is introduced to relate the value 4 to the following expression:

$$N=\left(\frac{\langle|S_{HH}-S_{VV}|^2\rangle}{\langle|S_{HV}|^2\rangle}\right) \tag{D.1}$$

which is the ratio of the double bounce backscatter to the cross-pol (volume-like) backscatter [Nord et al., 2009]. When using this concept in the reconstruction, the inequality is replaced with an equality.

E

Calculation of the Eigenvalues

The eigenvalues of the sample covariance and coherency are equal since there exists a transformation between these two, i.e.:

$$U_{L\to P} = \frac{1}{\sqrt{2}}\begin{bmatrix} 1 & 0 & 1 \\ 1 & 0 & -1 \\ 0 & \sqrt{2} & 0 \end{bmatrix} \tag{E.1}$$

$$\boldsymbol{T}_3 = U_{L\to P}\boldsymbol{C}_3 U_{L\to P}^{-1} \tag{E.2}$$

$\boldsymbol{T}_3$ and $\boldsymbol{C}_3$ have real and positive eigenvalues if and only if these two matrices are positive definite[1] [Theodoridis and Koutroumbas, 2009]. This is in fact true for the covariance and coherency matrix. Both these two matrices are also symmetric which includes eigenvectors, which are orthogonal. Let considered the sample covariance for this example, $\langle \boldsymbol{C}_3 \rangle$. The following is true for the sample covariance:

$$\langle \boldsymbol{C}_3 \rangle \boldsymbol{e}_i = \lambda_i \boldsymbol{e}_i \qquad i = \{1,2,3\} \tag{E.3}$$

1. If a matrix A is called positive definite then for every nonzero vector $\boldsymbol{x}$ the following will be true:

$$\boldsymbol{x}^T A \boldsymbol{x} > 0$$

where $\boldsymbol{e}_i$ is eigenvector i with its corresponding eigenvalue λ_i. The eigenvalues can be found by considering the *characteristic equation* of the covariance matrix [Edwards and Penney, 1988], i.e.:

$$det\left(\langle \boldsymbol{C}_3 \rangle - \lambda \boldsymbol{I}\right) \tag{E.4}$$

Here, $\boldsymbol{I}$ is the identity matrix, and *det* is the determinant operator. The following steps are performed to find the three eigenvalues:

$$\boldsymbol{C}_3 = \begin{bmatrix} H & \sqrt{2}\langle S_{HH} S_{HV}^{\star} \rangle & P \\ \sqrt{2}\langle S_{HV} S_{HH}^{\star} \rangle & 2X & \sqrt{2}\langle S_{HV} S_{VV}^{\star} \rangle \\ P^{\star} & \sqrt{2}\langle S_{VV} S_{HV}^{\star} \rangle & V \end{bmatrix} \tag{E.5}$$

The substitutions made here are: $H = \langle |S_{HH}|^2 \rangle$, $V = \langle |S_{VV}|^2 \rangle$, $X = \langle |S_{HV}|^2 \rangle$, $P = \langle S_{HH} S_{VV}^{\star} \rangle$. Multiple times, the reflection symmetry assumption is made during this work. This implies the following form of the sample covariance matrix:

$$\boldsymbol{C}_3 = \begin{bmatrix} H & 0 & P \\ 0 & 2X & 0 \\ P^{\star} & 0 & V \end{bmatrix} \tag{E.6}$$

Inserting this expression into the characteristic equation yields:

$$\left(\begin{bmatrix} H & 0 & P \\ 0 & 2X & 0 \\ P^{\star} & 0 & V \end{bmatrix} - \lambda \begin{bmatrix} 1 & 0 & 0 \\ 0 & 1 & 0 \\ 0 & 0 & 1 \end{bmatrix} \right) \tag{E.7}$$

$$\det\left(\begin{bmatrix} H-\lambda & 0 & P \\ 0 & 2X-\lambda & 0 \\ P^{\star} & 0 & V-\lambda \end{bmatrix} \right) = 0 \tag{E.8}$$

$$(H-\lambda)(2X-\lambda)(V-\lambda) - P(2X-\lambda)P^{\star} = 0 \tag{E.9}$$

$$\lambda^3 - \lambda^2(H + V + 2X) + \lambda(2XH + HV + 2XV - PP^\star) + 2PP^\star - 2XHV = 0 \quad \text{(E.10)}$$

The three solutions to this equation are [van Zyl et al., 2011]:

$$\lambda_1 = \frac{1}{2}\left(H + V + \sqrt{(H+V)^2 - 4HV + 4PP^\star}\right) \quad \text{(E.11)}$$

$$\lambda_a = \frac{1}{2}\left(H + V - \sqrt{(H+V)^2 - 4HV + 4PP^\star}\right) \quad \text{(E.12)}$$

$$\lambda_b = 2X \quad \text{(E.13)}$$

Here, $\lambda_1 > \lambda_a$ AND λ_b. Either λ_a or λ_b is the second or the third eigenvalue. This is determined as follows:

$$\lambda_2 = \begin{cases} \lambda_a & \text{if } \lambda_a > \lambda_b \\ \lambda_b & \text{if } \lambda_a < \lambda_b \end{cases} \qquad \lambda_3 = \begin{cases} \lambda_a & \text{if } \lambda_a < \lambda_b \\ \lambda_b & \text{if } \lambda_a > \lambda_b \end{cases} \quad \text{(E.14)}$$

The eigenvalues of the sample compact-pol covariance matrix can be found by following the same procedure as for the sample quad-pol covariance matrix, i.e.:

$$\boldsymbol{C}_{CP} = \begin{bmatrix} C_{11} & C_{12} \\ C_{12}^\star & C_{22} \end{bmatrix} \quad \text{(E.15)}$$

$$\det\left(\begin{bmatrix} C_{11} - \lambda & C_{12} \\ C_{12}^\star & C_{22} - \lambda \end{bmatrix}\right) \quad \text{(E.16)}$$

$$(C_{11} - \lambda)(C_{22} - \lambda) - C_{12}C_{12}^\star = 0 \quad \text{(E.17)}$$

The eigenvalues for this equation are:

$$\lambda_1^{CP} = \frac{1}{2}\left(C_{11} + C_{22} + \sqrt{(C_{11} + C_{22})^2 - 4C_{11}C_{22} + 4C_{12}C_{12}^\star}\right) \quad \text{(E.18)}$$

$$\lambda_2^{CP} = \frac{1}{2}\left(C_{11} + C_{22} - \sqrt{(C_{11} + C_{22})^2 - 4C_{11}C_{22} + 4C_{12}C_{12}^\star}\right) \quad \text{(E.19)}$$

(E.20)

Here, $\lambda_1 \geq \lambda_2$. Note that when $X = 0$, then:

$$2\lambda_1^{CP} = \lambda_1 \qquad 2\lambda_2^{CP} = \lambda_a \tag{E.21}$$